

# **A polarimetric radar operator to evaluate precipitation from the COSMO atmospheric model**

THÈSE N° 8408 (2018)

PRÉSENTÉE LE 12 MARS 2018

À LA FACULTÉ DE L'ENVIRONNEMENT NATUREL, ARCHITECTURAL ET CONSTRUIT  
LABORATOIRE DE TÉLÉDÉTECTION ENVIRONNEMENTALE  
PROGRAMME DOCTORAL EN GÉNIE CIVIL ET ENVIRONNEMENT

ÉCOLE POLYTECHNIQUE FÉDÉRALE DE LAUSANNE

POUR L'OBTENTION DU GRADE DE DOCTEUR ÈS SCIENCES

PAR

**Daniel WOLFENSBERGER**

acceptée sur proposition du jury:

Prof. S. Takahama, président du jury

Prof. A. Berne, directeur de thèse

Dr U. Blahak, rapporteur

Dr O. Caumont, rapporteur

Prof. H. Wernli, rapporteur



ÉCOLE POLYTECHNIQUE  
FÉDÉRALE DE LAUSANNE

Suisse  
2018



# Remerciements

Je remercie avant tout Alexis Berne pour le temps précieux qu'il a consacré à cette thèse, pour sa confiance et pour ses conseils avisés. Je remercie aussi Jacopo Grazioli pour le traitement des nombreuses données radar en bande X utilisées dans le cadre de cette thèse et de manière plus générale pour toute son expertise dans le domaine, dont il m'a fait généreusement profiter. Mes sincères remerciements aussi à la division Radar, satellites et nowcasting de MeteoSuisse à Locarno, pour le partage des données radar opérationnelles et du composite radar. Pour terminer, je remercie tous mes collègues du LTE pour l'ambiance chaleureuse que j'ai tant appréciée, et pour tous les bons moments que nous avons passé au travail et en dehors.

*Lausanne, 28 Novembre 2017*

D. W.



# Abstract

Weather radars provide real-time measurements of precipitation at a high temporal and spatial resolution and over a large domain. A drawback, however, is that these measurements are indirect and require careful interpretation to yield relevant information about the mechanisms of precipitation.

Radar observations are an invaluable asset for the numerical forecast of precipitation, both for data assimilation, parametrization of subscale phenomena and model verification. This thesis aims at investigating new uses for polarimetric radar data in numerical weather prediction. The first part of this work is devoted to the design of an algorithm able to automatically detect the location and extent of the melting layer of precipitation, an important feature of stratiform precipitation, from vertical radar scans. This algorithm is then used to provide a detailed characterization of the melting layer, in several climatological regions, providing thus relevant information for the parameterization of melting processes and the evaluation of simulated freezing level heights.

The second part of this work uses a multi-scale approach based on the multifractal framework to evaluate precipitation fields simulated by the COSMO weather model with radar observations. A climatological analysis is first conducted to relate multifractal parameters to physical descriptors of precipitation. A short-term analysis, that focuses on three precipitation events over Switzerland, is then performed. The results indicate that the COSMO simulations exhibit spatial scaling breaks that are not present in the radar data. It is also shown that a more advanced microphysics parameterization generates larger extreme values, and more discontinuous precipitation fields, which agree better with radar observations.

The last part of this thesis describes a new forward polarimetric radar operator, able to simulate realistic radar variables from outputs of the COSMO model, taking into account most physical aspects of beam propagation and scattering. An efficient numerical scheme is proposed to estimate the full Doppler spectrum, a type of measurement often performed by research radars, which provides rich information about the particle velocities and turbulence. The operator is evaluated with large datasets from various ground and spaceborne radars. This evaluation shows that the operator is able to simulate accurate Doppler variables and realistic distributions of polarimetric variables in the liquid phase. In the solid phase, the simulated reflectivities agree relatively well with radar observations, but the polarimetric variables tend to be underestimated. A detailed sensitivity analysis of the radar operator reveals that, in the liquid phase, the simulated radar variables depend very much on the hypothesis about drop geometry and drop size distributions. In the solid phase, the potential of more advanced

## **Remerciements**

---

scattering techniques is investigated, revealing that these methods could help to resolve the strong underestimation of polarimetric variables in snow and graupel.

Key words: radar, polarimetric, COSMO, numerical weather prediction, melting layer, multi-fractals

# Résumé

Les radars météorologiques fournissent des mesures de précipitations en temps réel, à haute résolution spatiale et temporelle et ce, au-dessus d'une large zone. Ces mesures, toutefois, sont indirectes et nécessitent une interprétation minutieuse pour fournir une information pertinente sur les mécanismes de formation et d'évolution des précipitations.

Les données radars sont un atout indéniable dans l'estimation numérique des précipitations, tant pour l'assimilation de données que pour la paramétrisation de processus sous-maille et la vérification de modèles. L'objectif de cette thèse est de proposer de nouvelles utilisations de données de radars polarimétriques dans la prévision numérique du temps. La première partie de ce travail est dédiée au développement d'un algorithme permettant la détection automatique de la hauteur et de l'étendue de la couche de fusion des précipitations, une importante propriété de la précipitation stratiforme, à partir de scans radar verticaux. Cet algorithme est ensuite utilisé pour proposer une caractérisation détaillée de la couche de fusion dans plusieurs régions climatologiques ; une information utile pour la paramétrisation des processus de fusion et la validation de la hauteur de fusion simulée par le modèle.

Dans la seconde partie de ce travail, une approche multi-échelles basée sur la théorie des multifractales est utilisée pour évaluer les champs de précipitation simulés par le modèle de prévision COSMO avec des observations radar. Dans un premier temps, une analyse climatologique est effectuée afin de relier les paramètres multifractals à des descripteurs de la physique des précipitations. Ces résultats sont complétés par une analyse à courte-échelle sur trois événements caractéristiques. Les résultats indiquent la présence de ruptures de comportement scalant sur les précipitations simulées qui sont absentes des observations. Il est aussi constaté qu'un schéma microphysique plus complexe tend à générer une plus grande hétérogénéité et des extrêmes de précipitations plus prononcés, qui se rapprochent davantage des observations radar.

Enfin, dans la dernière partie de cette thèse, un nouvel opérateur radar polarimétrique, capable de simuler des variables radar réalistes à partir de sorties du modèle COSMO est proposé. Cet opérateur prend en compte les principaux aspects physiques de la propagation et de la rétrodiffusion du faisceau radar. Une méthode numérique efficace est proposée pour estimer le spectre Doppler, une mesure fréquente des radars de recherche, et qui fournit de riches informations sur la vitesse des particules et la turbulence. L'opérateur est évalué à l'aide de grands jeux de données issus de radars satellite et terrestres. L'évaluation indique que l'opérateur est capable de simuler des variables Doppler et des distributions de variables polarimétrique réalistes dans la pluie. En phase solide, la réflectivité simulée est en assez bon

## Remerciements

---

accord avec les observations mais les variables polarimétriques tendent à être sous-estimées. Dans la phase solide, la comparaison de plusieurs méthodes d'estimation de la rétrodiffusion indique que les méthodes les plus avancées pourraient permettre de résoudre le problème de sous-estimation de la signature polarimétrique dans la neige.

Mots clefs : radar, polarimétrique, COSMO, prévision numérique du temps, couche de fusion, multifractales



# Contents

<b>Remerciements</b>	<b>i</b>
<b>Abstract (English/Français)</b>	<b>iii</b>
<b>List of figures</b>	<b>xi</b>
<b>List of tables</b>	<b>xv</b>
<b>List of acronyms</b>	<b>xvii</b>
<b>List of variables used in Chapters 2-5</b>	<b>xix</b>
<b>1 Introduction</b>	<b>1</b>
1.1 Motivation . . . . .	3
1.2 Scientific background . . . . .	3
1.2.1 Microstructure of precipitation . . . . .	3
1.2.2 The COSMO model . . . . .	5
1.2.3 Basics of radar meteorology . . . . .	15
1.2.4 Quantitative precipitation estimation . . . . .	26
1.3 Thesis outline . . . . .	27
<b>2 Detection and characterization of the melting layer of precipitation</b>	<b>29</b>
2.1 Summary . . . . .	30
2.2 Introduction . . . . .	31
2.3 Data and processing . . . . .	33
2.3.1 Instruments . . . . .	33
2.3.2 Datasets . . . . .	34
2.3.3 Pre-processing of radar data . . . . .	35
2.4 Automatic detection of the ML . . . . .	37
2.4.1 Description of the algorithm . . . . .	37
2.4.2 Outputs . . . . .	41
2.4.3 Algorithm parameters . . . . .	42
2.5 Validation . . . . .	45
2.5.1 Vertical hydrometeor fall velocities . . . . .	45
2.5.2 Comparison with Payerne radiosoundings . . . . .	46

## Contents

---

2.5.3	Comparison with an algorithm adapted from PPI scans . . . . .	48
2.6	Characterization of the ML . . . . .	49
2.6.1	The ML attenuation effect . . . . .	50
2.6.2	Polarimetric signature of the ML . . . . .	53
2.6.3	Vertical profiles of polarimetric variables through the ML . . . . .	56
2.6.4	Geometry of the ML . . . . .	56
2.7	Correlation analysis of ML descriptors . . . . .	59
2.7.1	Factors controlling the ML thickness . . . . .	59
2.7.2	Principal component analysis . . . . .	63
2.8	Summary and conclusions . . . . .	64
<b>3</b>	<b>Multifractal evaluation of simulated precipitation intensities</b>	<b>67</b>
3.1	Summary . . . . .	68
3.2	Introduction . . . . .	69
3.3	Description of the data . . . . .	70
3.3.1	The COSMO model . . . . .	70
3.3.2	Climatological study . . . . .	71
3.3.3	QPE comparison . . . . .	72
3.4	The UM framework . . . . .	74
3.4.1	Multifractality . . . . .	74
3.4.2	Non-conservative fields . . . . .	76
3.4.3	Spatio-temporal analysis . . . . .	79
3.5	Climatological analysis of MF parameters . . . . .	79
3.5.1	Correlation study . . . . .	80
3.5.2	Hierarchical clustering . . . . .	80
3.5.3	Spatial structure of MF parameters . . . . .	83
3.6	Comparison of simulated precipitation with radar QPE . . . . .	86
3.6.1	Scaling analysis . . . . .	87
3.6.2	Spatio-temporal analysis . . . . .	91
3.6.3	Times series of UM parameters . . . . .	93
3.7	Summary and conclusions . . . . .	95
<b>4</b>	<b>A forward polarimetric radar operator for the COSMO NWP model</b>	<b>97</b>
4.1	Summary . . . . .	98
4.2	Introduction . . . . .	99
4.3	Description of the data . . . . .	101
4.3.1	COSMO model . . . . .	101
4.3.2	Radar data . . . . .	103
4.3.3	Precipitation events . . . . .	104
4.4	Description of the polarimetric radar operator . . . . .	104
4.4.1	Propagation of the radar beam . . . . .	105
4.4.2	Downscaling of model variables . . . . .	107
4.4.3	Retrieval of particle size distributions . . . . .	107

4.4.4	Integration over the antenna pattern . . . . .	109
4.4.5	Derivation of polarimetric variables . . . . .	112
4.4.6	Scattering properties of individual hydrometeors . . . . .	112
4.4.7	Simulation of the melting layer effect . . . . .	119
4.4.8	Retrieval of Doppler velocities . . . . .	124
4.4.9	Doppler spectrum . . . . .	125
4.4.10	Turbulence and antenna motion correction . . . . .	126
4.4.11	Attenuation correction in the Doppler spectrum . . . . .	128
4.4.12	Simulation of satellite swaths . . . . .	128
4.4.13	Computation time . . . . .	128
4.5	Evaluation of the operator . . . . .	129
4.5.1	Qualitative comparisons . . . . .	130
4.5.2	Doppler variables . . . . .	134
4.5.3	Polarimetric variables . . . . .	136
4.5.4	GPM swaths . . . . .	140
4.5.5	Effect of ice crystals . . . . .	141
4.6	Summary and conclusions . . . . .	143
<b>5</b>	<b>Sensitivity study of the polarimetric radar operator</b>	<b>145</b>
5.1	Summary . . . . .	145
5.2	Introduction . . . . .	146
5.3	Methods and data . . . . .	146
5.3.1	Scattering in the liquid phase . . . . .	147
5.3.2	Scattering in the ice phase . . . . .	147
5.3.3	Data . . . . .	150
5.3.4	Radar data . . . . .	150
5.3.5	Parsivel data . . . . .	151
5.4	Results . . . . .	151
5.4.1	Sensitivity in rain . . . . .	151
5.4.2	Sensitivity in the solid phase . . . . .	156
5.5	Summary and conclusions . . . . .	159
<b>6</b>	<b>Conclusions and further perspectives</b>	<b>161</b>
6.1	Summary . . . . .	161
6.2	Important contributions of this thesis . . . . .	163
6.3	Perspectives . . . . .	164
<b>A</b>	<b>Appendix of Chapter 2</b>	<b>167</b>
A.1	Spatial representation of all descriptors . . . . .	167
A.2	A visual example of box counting . . . . .	169
A.3	Visual example of the effect of multifractals on the structure of a field . . . . .	170
A.4	Comparison with the Köppen classification . . . . .	172

## Contents

---

<b>B Appendix of Chapter 3</b>	<b>173</b>
B.1 Trilinear downscaling . . . . .	173
B.2 Specificities of the two-moments scheme . . . . .	174
B.3 Polarimetric equations . . . . .	175
<b>Bibliography</b>	<b>195</b>
<b>Curriculum Vitae</b>	<b>197</b>

# List of Figures

1.1	Operational domains of COSMO . . . . .	5
1.2	Schema of a COSMO grid box volume . . . . .	11
1.3	Cloud microphysical processes flowchart . . . . .	14
1.4	Schematic of a pulse radar . . . . .	17
2.1	Example of melting layer signature . . . . .	33
2.2	Location and pictures of the four radar sites . . . . .	35
2.3	Flowchart of the preprocessing steps . . . . .	37
2.4	Gradients of $Z_H$ and $\rho_{hv}$ at the boundaries of the ML. Note that in the units of the vertical gradient, a pixel corresponds to $25 \times 25 \text{ m}^2$ (Section 2.3.3.1). . . . .	40
2.5	Flow diagram of the ML detection algorithm. . . . .	41
2.6	Two examples of ML detection overlaid on $\rho_{hv}$ (left) and $Z_H$ (right). . . . .	42
2.7	Distributions of $\rho_{hv}$ in the liquid and solid phases as well as in the identified ML. . . . .	42
2.8	Sensitivity of the algorithm to $T_{\text{grad, min}}$ . . . . .	44
2.9	Histogram of relative heights of the top and the bottom of the ML. . . . .	44
2.10	Normalized histogram of the distribution of gap sizes in the detected MLs . . . . .	45
2.11	Distributions of the hydrometeor vertical fall velocities . . . . .	46
2.12	$0^\circ\text{C}$ isotherm heights, radar vs soundings . . . . .	47
2.13	Schema of all melting layer descriptors . . . . .	49
2.14	Boxplots of the differences in $Z_H$ and $Z_{DR}$ across the melting layer . . . . .	52
2.15	Polarimetric signatures within the ML . . . . .	54
2.16	Distributions of polarimetric variables as a function of relative height in the ML . . . . .	57
2.17	Distributions and variograms of the melting layer thickness . . . . .	58
2.18	Event by event variability of the melting layer thickness on the HyMeX dataset . . . . .	59
2.19	Correlation plot of the melting layer descriptors . . . . .	60
2.20	Scatterplots of thickness vs. $Z_H$ and thickness versus distance between peak of $Z_H$ and minimum of $\rho_{hv}$ . . . . .	61
2.21	Biplot of the melting layer descriptors, using components 1 and 2 . . . . .	63
3.1	500 hPa geopotentials and pressure at mean sea level for the three considered events. Modified from <a href="http://www.wetterzentrale.de/de/default.php">http://www.wetterzentrale.de/de/default.php</a> . . . . .	72
3.2	Map of QPE extent and radar location . . . . .	73
3.3	Correlation plots in space and time of MF parameters and descriptors . . . . .	81

## List of Figures

---

3.4	Hierarchical clustering map . . . . .	82
3.5	Boxplots of MF parameters within the clusters . . . . .	83
3.6	Spatial representation of the MF parameters estimated in space for all areas . . . . .	85
3.7	Spectral analysis in space of the QPE products during the three event . . . . .	87
3.8	Scaling analysis of the QPE during the three events . . . . .	90
3.9	$\alpha$ , $C_1$ and $\gamma_s$ parameter values obtained with an analysis in time and space . . . . .	91
3.10	Time series of $\alpha$ and $C_1$ MF parameters and snapshots of precipitation fields . . . . .	94
3.11	Fraction of wet area during the event of the 13 August 2015. . . . .	95
4.1	Location of the five Swiss operational radars. . . . .	104
4.2	Forward operator workflow . . . . .	106
4.3	Schema showing the effect of atmospheric refraction and illustrating the integration quadrature method . . . . .	110
4.4	Bias and RMSE in terms of $Z_H$ during one day of stratiform of precipitation (around 120 RHI scans), for the five considered quadrature schemes. The exhaustive quadrature scheme is used as a reference. The other two events show similar results. . . . .	111
4.5	Fitted probability density functions for the inverse of the aspect-ratio and the canting angle . . . . .	115
4.6	Polarimetric variables as a function of the mass concentration for snow and graupel . . . . .	116
4.7	Trigonometric expression of the radial velocity . . . . .	125
4.8	Example of simulated and observed PPI at $1^\circ$ elevation during the 13 August 2015 convective event . . . . .	131
4.9	Example of simulated and observed PPI at $1^\circ$ elevation during the 8 April 2014 stratiform event . . . . .	132
4.10	Example of RHI showing the observed and simulated melting layer during the PARADISO campaign in Spring 2014 . . . . .	133
4.11	Comparison at several altitude levels between GPM radar observations and radar operator simulations . . . . .	134
4.12	Distributions of simulated and observed radial velocities during six days of precipitation . . . . .	135
4.13	Scatter-plot of overall agreement between simulated and observed radial velocities . . . . .	136
4.14	Simulated and measured average Doppler spectra at vertical incidence during six days of precipitation . . . . .	137
4.15	Observed and simulated distributions of polarimetric variables in the liquid phase . . . . .	138
4.16	Observed and simulated relationships between polarimetric variables in the liquid phase . . . . .	139
4.17	Comparison of reflectivities and QPE estimated by GPM and simulated with COSMO . . . . .	140
4.18	Distributions of polarimetric variables with and without ice crystals . . . . .	141
4.19	QQ-plots of reflectivities obtained with and without ice crystals . . . . .	142

5.1 Effect of the <i>shape</i> parameter $\mu$ on the raindrop size distribution for a constant mass concentration of $1 \text{ g m}^{-3}$ of rain . . . . .	148
5.2 Dependence of the polarimetric relations on canting angle, aspect-ratio and $\mu^{\text{rain}}$	152
5.3 Observed and simulated distributions of radar variables in rain for different values of $\mu^{\text{rain}}$ . . . . .	153
5.4 Distributions and relations between polarimetric variables obtained with the optimized DSD model . . . . .	155
5.5 Median measured and parameterized rain DSDs in Payerne . . . . .	155
5.6 Effect of the scattering method on the distributions of polarimetric variables in the solid phase . . . . .	157
5.7 Observed and simulated reflectivities at Ku and Ka bands for three scattering methods . . . . .	158
A.1 Map of all topographical and meteorological descriptors . . . . .	168
A.2 A visual example of box counting . . . . .	169
A.3 Effect of $\alpha$ and $C_1$ on random fields . . . . .	170
A.4 Effect of $H$ on random fields . . . . .	171
A.5 Köppen climate classification . . . . .	172
B.1 Schema of the trilinear downscaling . . . . .	174





# List of Tables

1.1	Parameters of the primitive equations of the atmosphere . . . . .	7
2.1	MXPOL properties and scanning strategy . . . . .	33
2.2	Description of the available RHI scans datasets . . . . .	35
2.3	Algorithm parameters and recommended values . . . . .	43
2.4	Bias and mean absolute error in the radar freezing level height . . . . .	47
2.5	Bias and mean absolute error in the radar freezing level height with an alternative detection method . . . . .	49
2.6	List of melting layer descriptors by category. For polarimetric variables, the average over the whole scan are taken, without consideration for the elevation angle. For $Z_{DR}$ , the elevation angles ( $45^\circ - 90^\circ$ ) are discarded (Section 2.3.3.1). . . . .	50
2.7	Statistics of the polarimetric variables within the melting layer . . . . .	55
3.1	List and description of all meteorological and topographical descriptors used in the MF characterization of the climatology of precipitation intensities. . . . .	71
3.2	Short description of the three precipitation events considered. . . . .	72
3.3	Overview of all MF parameters . . . . .	78
3.4	Values of the non-conservation parameter and the fractal dimension in time and space . . . . .	89
4.1	Parameters of the PSDs and power-laws for the one-moment and two-moment parameterizations . . . . .	102
4.2	Specifications of the ground radars used in the evaluation of the radar operator . . . . .	103
4.3	List of all events used for the comparison of simulated radar observables with ground radar observations. . . . .	105
4.4	Observed computation times for three types of scans . . . . .	129



## List of acronyms

2DVD	2-Dimensional Video Disdrometer
BB	Bright Band
COSMO	Consortium for Small-scale Modelling
DPR	Dual-frequency Precipitation Radar
DFR	Dual Frequency Ratio
DSD	Drop Size Distribution
DTM	Double Trace Moment
EDR	Eddy Dissipation Rate
EPFL	Ecole Polytechnique Fédérale de Lausanne
FFT	Fast Fourier Transform
GPM	Global Precipitation Measurement
HyMeX	Hydrological cycle in the Mediterranean Experiment
QPE	Quantitative Precipitation Estimation
QPF	Quantitative Precipitation Forecast
LTE	Laboratoire de Télédétection Environnementale
MAE	Mean Absolute Error
MANOVA	Multivariate Analysis of Variance
MASC	Multi-angle Snowflake Camera
MF	Multifractals
ML	Melting Layer
MXPol	Mobile X-band Polarimetric
NWP	Numerical Weather Prediction
PARADISO	Payerne Radar Disdrometers and Isotopes
Parsivel	Particle Size and Velocity (disdrometer type)
PCA	Principal Component Analysis
PIA	Path Integrated Attenuation
PPI	Plane Position Indicator
PSD	Particle Size Distribution
PRF	Pulse Repetition Frequency
RMSE	Root Mean Squared Error
RHI	Range Height Indicator

## List of acronyms

---

SNR	Signal to Noise Ratio
TKE	Turbulent Kinetic Energy
TM	Trace Moment
UM	Universal Multifractals
WGS84	World Geodetic System 1984

## List of variables used in Chapters 2-5

Symbol	Units	Description
$a_r$	[-]	Aspect-ratio (smallest over largest dimension)
$a$	[kg mm <sup>-b</sup> ]	Intercept parameter in the power-law mass-diameter relation
$a_v$	[m s <sup>-1</sup> mm <sup>-b<sub>v</sub></sup> ]	Intercept parameter in the velocity diameter power-law
$b$	[-]	Exponent parameter in the power-law mass-diameter relation
$b_v$	[-]	Exponent parameter in the velocity diameter power-law
$c$	[m s <sup>-1</sup> ]	Speed of light
$C$	[m] or [cm]	Forward scattering vector
$c_f$	[-]	Fractal codimension
$C_1$	[-]	Mean intermittency
$D$	[mm]	Particle diameter or reference size as a continuous variable
$[D]$	[mm]	Particle diameter or reference size as a discrete (binned) variable
$D_f$	[-]	Fractal dimension
$dr$	[m]	Radial resolution of the radar
$h$	[m] or [km]	Height above ground level
$H$	[-]	Non-conservation parameter in the multifractal framework
$f_{\text{wet}}$	[-]	Massic fraction of water
$k_H$	[dB km <sup>-1</sup> ]	Specific differential attenuation at horizontal polarization
$K$		Moment scaling function in the multifractal framework
$m$	[kg]	Mass of a given hydrometeor
$ML_{\text{Bot}}$	[m]	Altitude of the bottom of the melting layer
$ML_{\text{Thickness}}$	[m]	Thickness of the melting layer
$ML_{\text{Top}}$	[m]	Altitude of the top of the melting layer
$n$	[-]	Refractive index of the atmosphere
$N_0$	[mm <sup>-1-μ</sup> m <sup>-3</sup> ]	Intercept parameter in the gamma (or exponential) DSD/PSD
$N(D)$	[mm <sup>-1</sup> m <sup>-3</sup> ]	Drop or particle size distribution
$o$	[°]	Canting angle of an hydrometeor
$P_r$	[W] or [mW]	Power received by a radar
$P_t$	[W] or [mW]	Power transmitted by a radar

## List of variables

---

$Q_M$	[kg m <sup>-3</sup> ]	Mass concentration of a given hydrometeor
$Q_N$	[m <sup>-3</sup> ]	Number concentration of a given hydrometeor
$r$	[m] or [km]	Range distance
$R$	[mm hr <sup>-1</sup> ]	Precipitation intensity
$R^2$	[-]	Coefficient of determination in the multifractal TM analysis
$s$	[m] or [km]	Ground distance (along the Earth surface)
$S$	[m <sup>2</sup> ] or [cm <sup>2</sup> ]	Backscattering covariance matrix
$s_{hh}^b$	[m] or [cm]	Complex backward scattering amplitude at horizontal polarization
$s_{hh}^f$	[m] or [cm]	Complex forward scattering amplitude at horizontal polarization
$U$	[m s <sup>-3</sup> ]	Eastward wind component
$V$	[m s <sup>-3</sup> ]	Northward wind component
$V_f$	[-]	Volumetric fraction
$v_{\text{rad}}$	[m s <sup>-3</sup> ]	Radial wind velocity
$V_{\text{res}}$	[m <sup>3</sup> ]	Radar resolution volume
$v_t$	[m s <sup>-3</sup> ]	Hydrometeor terminal fall velocity
$W$	[m s <sup>-3</sup> ]	Vertical wind component
$Z_{\text{DR}}$	[dB]	Differential reflectivity
$Z_h$	[mm <sup>6</sup> m <sup>-3</sup> ]	Linear radar reflectivity factor at horizontal polarization
$Z_H$	[dBZ]	Radar reflectivity factor at horizontal polarization
$\alpha$	[-]	Multifractality index (Chapter 3)
$\beta$	[-]	Negative of the spectral slope (Chapter 3)
$\delta_{hv}$	[°]	Differential phase shift upon backscattering
$\epsilon$	[F m <sup>-1</sup> ]	Complex permittivity
$\epsilon_t$	[m <sup>2</sup> s <sup>-3</sup> ]	Eddy dissipation rate
$\mathcal{E}$	[-]	Normalized field in the multifractal framework
$\hat{\gamma}$		Empirical semivariance
$\gamma$	[-]	Multifractal singularity
$\gamma_s$	[-]	Maximum singularity
$\kappa$	[-]	Correction factor in the PSD model for melting hydrometeors
$\lambda$	[cm]	Radar wavelength
$\Lambda$	[mm <sup>-1</sup> ]	Slope parameter in the gamma (or exponential) DSD/PSD
$\lambda_r$	[-]	Observation scale in the multifractal framework (Chapter 3)
$\mu$	[-]	Shape parameter in the gamma DSD or PSD
$\nu$	[-]	Family parameter in the generalized gamma DSD/PSD
$\phi$	[°]	Azimuth angle of the incident radar beam
$\phi_{\text{dp}}$	[°]	Total differential phase shift upon propagation
$\psi_{\text{dp}}$	[°]	Total differential phase shift
$\rho$	[kg m <sup>-3</sup> ]	Volumetric mass density
$\rho_{hv}$	[-]	Copolar correlation coefficient
$\sigma$		Standard deviation

## List of variables used in Chapters 2-5

---

$\sigma^b$	[m <sup>2</sup> ] or [cm <sup>2</sup> ]	Radar backscattering cross section
$\sigma_h^b$	[m <sup>2</sup> ] or [cm <sup>2</sup> ]	Radar backscattering cross section at horizontal polarization
$\sigma_o$	[°]	Standard deviation of the Gaussian distribution of canting angles
$\sigma_v$	[m s <sup>-1</sup> ]	Spectrum width
$\tau$	[mS]	Radar pulse width
$\theta$	[°]	Elevation angle of the incident radar beam
$\theta_{3dB}$	[°]	3dB beamwidth of the radar antenna





# 1 Introduction

Precipitation is a key process in the water cycle, as well as a crucial resource to maintain suitable conditions for life on Earth (e.g., Jackson et al., 2001; Chahine, 1992). Absence or excess of precipitation have a strong direct social and economical impact on societies (Kunkel et al., 1999), and can lead to disastrous natural hazards (e.g. floods, avalanches, droughts). Precipitation is also related to many common economical activities, such as agriculture, drinkable water production and hydro-power generation. These impacts take place in a changing world, where climate change has led to additional uncertainties in the prediction of precipitation, both in terms of magnitude and location (e.g., Frei et al., 2006).

Because of its great importance in everyday life, people have tried to forecast weather for millennia with empirical, sometimes unrelated observations, such as the color of the sun, the position of stars or the pattern of winds. Scientific study of precipitation started in Ancient Greece (Aristotle and his pupil Theophrastus), and is still undergoing intense study today, as there is still a lot to be known. Indeed, precipitation is the result of complex interactions between turbulent atmospheric dynamics and cloud microphysics, that span from a few microns and seconds to thousands of kilometers and days (Lovejoy et al., 2008). Moreover, precipitation varies depending on the considered spatial and temporal scales (Fabry, 1996).

Nowadays, precipitation forecasts are performed with state of the art numerical weather prediction (NWP) models. Still, quantitative precipitation forecast (QPF) is considered as one of the most challenging tasks in NWP (Bauer et al., 2015). Although the dynamical processes governing the motions in the atmosphere and its thermodynamic state are well known, their numerical estimation is difficult, and is limited by the resolution of the model, which is typically in the order of a few kilometers for modern local-scale weather prediction. At these resolutions, numerical weather prediction and regional climate models are not able to fully resolve local processes, which occur at the sub-grid scale, especially over complex terrain. Such processes include, for example, exchange of heat and moisture between the surface and the atmosphere, local circulations over mountains and in valleys, and orographic precipitation. Processes that are too local or too complex are not explicitly resolved by the dynamics within the model, and are instead simplified and approximated with parameterizations based on

## Chapter 1. Introduction

---

empirical observations of the considered phenomena. Because of its complexity, QPF relies heavily on parameterizations, especially for heavy precipitation events associated with small-scale convection such as thunderstorms.

Another difficulty in NWP arises from the fact that, in order to predict the weather in the future, the present state of the atmosphere must be known as accurately as possible. Indeed, the dynamics of NWP rely on partial differential equations, which require initial and boundary conditions to be provided. This is done mostly with *data assimilation*, the process by which weather observations are incorporated into the model state. It is a key aspect of NWP, and offers major perspectives for overall weather prediction improvement (Rabier, 2005). Traditionally, assimilated data includes radio sounding profiles of temperature, humidity and pressure; synoptic stations measurements (wind, temperature, pressure and humidity) as well as data from vertical wind profilers.

At last, quantifying the performance of a NWP model is far from being a trivial task, especially in terms of QPF. Indeed, observations of precipitation are typically available at a different spatial and temporal resolution than the model. Traditional point-based verification scores are generally unable to provide sufficient information about the forecast quality, as they do not take into consideration the spatial structure of precipitation and are affected by the so-called “double penalty” (Gilleland et al., 2009). Indeed, small displacements in the simulated forecast features are penalized twice, once for missing the observation and again for giving a false alarm. The impact of this double penalty is related to the variability of the simulated fields, which tends to increase with the resolution of the model.

For all these reasons, improving the observations of precipitation is a crucial step in the development and improvement of QPF. Whereas collecting and measuring precipitation at the ground has a very long history dating back to the Ancient Greeks, the remote sensing of precipitation at altitude is only quite recent. It is only shortly after World War II, that the potential of the recently developed radar (RAdio Detection and Ranging), as a method to observe and describe precipitation, was recognized (Marshall et al., 1947). Radar technology has improved significantly since then and now most operational weather radar systems are equipped with dual-polarization and Doppler capabilities (polarimetric radars), which provide additional information about the type of precipitation (e.g. phase, homogeneity and shape of hydrometeors), and the radial component of the velocity of the precipitation field. Radars are able to deliver areal measurements of precipitation at a high temporal and spatial resolution. Unfortunately, these measurements are unavoidably indirect, and need to be carefully interpreted to yield any meteorological meaning.

This thesis focuses on new perspectives for the use of polarimetric radar data in NWP. These perspectives are threefold. First of all radar data can be used to improve and verify model parameterizations, by providing an insight into sub-grid scale processes, such as, for example, deep convection (Kumjian et al., 2014), the terminal velocity of snowflakes (Langleben, 1954), or the melting process (Zawadzki et al., 2005). Secondly, radar data can be used for assimilation.

However, this assimilation is necessary indirect: either the weather radar observations are first converted to atmospheric variables simulated by the NWP model (e.g., Chang and Holt, 1994; Davolio and Buzzi, 2004), or synthetic radar observations are generated based on the state of the atmosphere simulated by the model (e.g., Wang et al., 2013; Zeng et al., 2016). Finally, weather radars are essential for model validation. Traditionally, model validation has been performed with quantitative precipitation estimation (QPE) products retrieved from operational radar networks (e.g., Ebert, 2008; Wernli et al., 2008; Mittermaier et al., 2013). However, recent advances in radar meteorology make it possible to identify many more atmospheric features, which could also be used for model evaluation, albeit in a less direct and quantitative way. Examples of such features include hydrometeor types (e.g., Dolan and Rutledge, 2009; Grazioli et al., 2015; Besic et al., 2016), extent of the melting layer of precipitation and height of the freezing level (e.g., Das et al., 1993; Bandera et al., 1998; Giangrande et al., 2008), or wind patterns (Salonen et al., 2008).

## 1.1 Motivation

## 1.2 Scientific background

This section provides a basic overview of the physical and technical aspects of numerical weather prediction and radar meteorology, with an emphasis on meteorological applications. First, a short description of the particle size distribution will be given, as this key notion will be encountered on numerous occasions in this thesis. Then, the COSMO numerical weather prediction will be described, both in terms of atmospheric dynamics and sub-grid scale parameterizations. Finally, an introduction to radar meteorology will be given, where all polarimetric radar variables which are of major interest for meteorological purposes will be described.

### 1.2.1 Microstructure of precipitation

The microstructure of precipitation defines all measurable quantities of a population of hydrometeors within a given volume (Jameson, 1983). For meteorological applications, the microstructure is usually defined in terms of size distribution, shape, fall velocity and orientation (Thurai et al., 2009).

Knowledge of the precipitation microstructure is crucial to relate radar observables to meteorological information such as precipitation intensity or mass concentrations (Raupach and Berne, 2016), and to parameterize sub-grid scale precipitation in numerical weather prediction models (Seifert and Beheng, 2006).

Many established relations have been proposed to link microstructure quantities to the particle size, such as, for example, the mass (e.g., Locatelli and Hobbs, 1974; Heymsfield et al., 2004), the terminal fall velocity (e.g., Heymsfield, 1972; Locatelli and Hobbs, 1974; Beard, 1977) or the

aspect-ratio (e.g., Andsager et al., 1999; Thurai et al., 2007). Therefore, the characterization of the precipitation microstructure focuses on the estimation of the distribution of particle sizes within a given volume. The volumetric particle size distribution (PSD) or drop size distribution (DSD) in the case of rainfall, is a function that represents the number of hydrometeors  $N(D)$  per unit size (diameter  $D$ ) and volume. Usually, the PSD takes the units of  $\text{mm}^{-1} \text{m}^{-3}$ .

The PSD (or DSD for rain) is measured at the ground using disdrometers e.g. Parsivel (Löffler-Mang and Joss, 2000), POSS (Sheppard, 1990) or 2DVD (Schönhuber et al., 2008). Disdrometers take areal measurements of drop size distributions which can be converted to volumetric drop size distributions with the hydrometeor fall velocity.

$$N_A(D) = N(D)v_t(D) \quad (1.1)$$

where  $N_A$  is the areal PSD in  $\text{mm}^{-1}\text{m}^{-2}$ , and  $v_t(D)$  is the terminal fall velocity in  $\text{m s}^{-1}$  for a given particle diameter.

Defining a mathematical formulation for the PSD and DSD has been an evergoing debate in the scientific community (e.g., Joss and Gori, 1978; Ulbrich, 1983; De Michele and Ignaccolo, 2013). Agreeing on a reference model is difficult, mostly because the accuracy of disdrometer measurements is poorly known and depends very much on the instrument (e.g., Jaffrain and Berne, 2011; Raupach and Berne, 2015; Thurai et al., 2017).

For rain, the normalized gamma DSD proposed by Ulbrich (1983) is often used.

$$N(D) = \alpha N_t^* D^\mu \exp(-\Lambda D) \quad (1.2)$$

where  $N_t^*$  is a concentration [ $\text{m}^{-3}$ ],  $\mu$  a dimensionless *shape* parameter,  $\Lambda$ , a *slope* parameter [ $\text{mm}^{-1}$ ].  $\alpha$  is a normalization parameter that makes  $N_t^*$  an actual concentration:

$$\alpha = \frac{1}{\int_{D_{\min}}^{D_{\max}} D^\mu \exp(-\Lambda D) dD} \quad (1.3)$$

In numerical weather prediction, the prescribed DSD formulation varies from model to model. In its operational setup COSMO uses a gamma distribution, where  $\alpha N_t^*$  is replaced by  $N_0(\lambda)$  with units  $\text{mm}^{-\mu} \text{m}^{-3}$  (Seifert and Beheng, 2006). The value of  $N_0(\lambda)$  is based on a relation by Ulbrich (1983). Meso-NH uses a generalized gamma distribution, with an additional exponent on the diameter inside the exponential (Cohard and Pinty, 2000). In its non-operational two-moment scheme, COSMO uses also a generalized gamma distribution, but the concentration

of particles is defined as a function of mass and not diameter. Finally, WRF uses an exponential distribution, where  $\mu = 0$  (Chen and Sun, 2002).

### 1.2.2 The COSMO model

The COSMO model is a mesoscale limited area NWP model initially developed as the Lokal Modell (LM) at the Deutscher Wetterdienst (DWD). It is now operated and developed by various weather services in Europe, including Switzerland. Besides its operational applications, it is also used for scientific purposes in weather prediction and dynamics and for regional climate simulations. The COSMO model is a non-hydrostatic model based on the fully compressible primitive atmospheric equations in a moist atmosphere. The model uses a rotated coordinate system where the pole is displaced to ensure approximately horizontal resolution over the model domain. Sub-grid scale physical processes are taken into account with parameterizations.

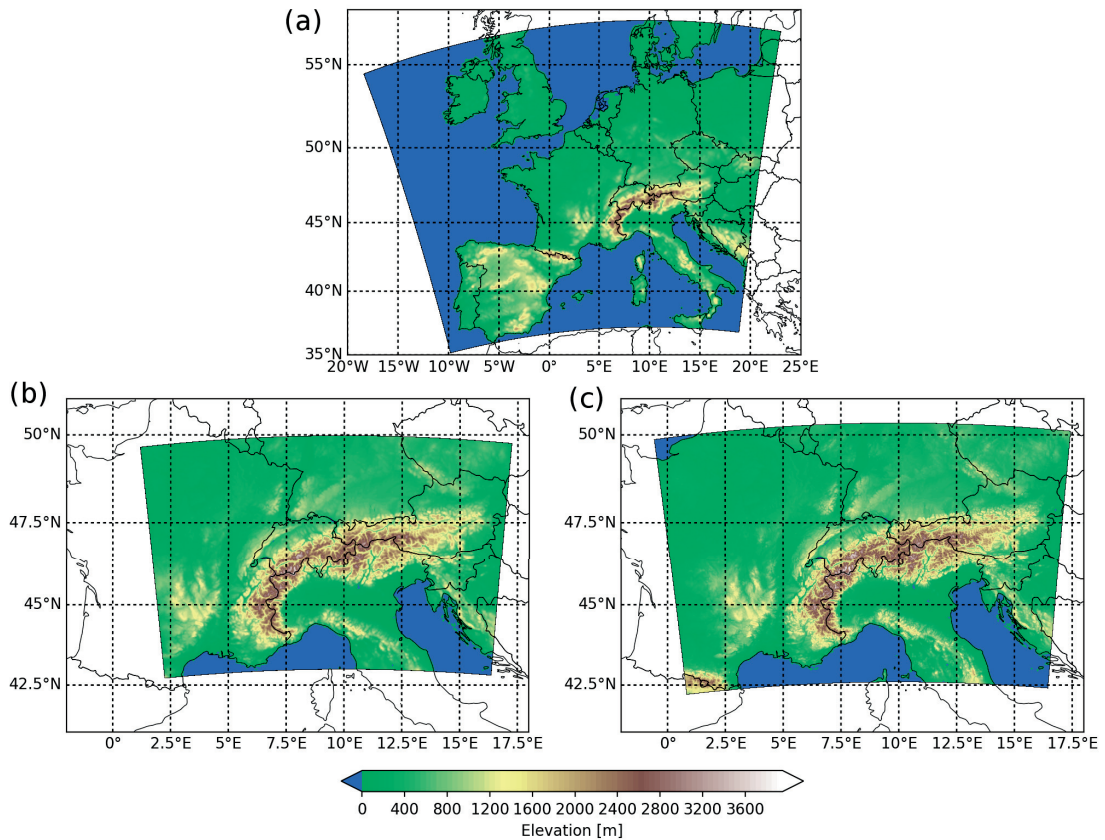


Figure 1.1 – Operational domains of COSMO-7 (a), COSMO-2 (b) and COSMO-1 (c).

Currently in Switzerland, COSMO is run operationally in two nested configurations: COSMO-7 and COSMO-1. COSMO-7 covers most of western Europe with  $393 \times 338$  grid points at a horizontal resolution of 7 km and 60 vertical levels. COSMO-1 covers Switzerland and part of its neighbouring countries with  $1158 \times 774$  grid points at a horizontal resolution of 1 km and 80

vertical levels. COSMO-1 has been operational only since 2016. Before this, the high-resolution version was COSMO-2 which covered a slightly smaller domain than COSMO-1 with  $520 \times 350$  grid points at a horizontal resolution of 2 km and 60 vertical levels. The areas covered by all three Swiss operational versions of COSMO are shown in Figure 1.1. In the context of this thesis, since most of the studied events happened before 2016, COSMO was used in the COSMO-2 configuration, with version 5.04a of the model. To simulate all precipitation events studied in this thesis, the COSMO model was set-up and run on EPFL's high-performance computing architecture<sup>1</sup>.

### 1.2.2.1 Model equations

The basic set of equations solved by COSMO comprises prognostic Eulerian equations for momentum, total mass, mass of water constituents, heat, and the equation of state (Doms and Baldauf, 2015). External effects on the system include gravity and Coriolis forces, while internal effects include heat, mass and momentum transfer as well as phase changes of water.

$$\rho \frac{d\mathbf{v}}{dt} = -\nabla p + \rho \mathbf{g} - 2\Omega \times (\rho \mathbf{v}) - \nabla \cdot \underline{\mathbf{t}} \quad (1.4)$$

$$\frac{dp}{dt} = -(c_p/c_v) p \nabla \cdot \mathbf{v} + (c_p/c_v - 1) Q_h + (c_p/c_v) Q_m \quad (1.5)$$

$$\rho c_p \frac{dT}{dt} = \frac{dp}{dt} + Q_h \quad (1.6)$$

$$\rho \frac{dq^x}{dt} = -\nabla \cdot \mathbf{J}^x + I^x \quad (1.7)$$

$$\rho = p [R_d(1 + \alpha) T]^{-1} \quad (1.8)$$

In the following, the superscript  $x$  represents a specific constituent of the mixture ( $x = d$ : dry air,  $x = v$ : water vapour,  $x = k$ : liquid water,  $x = f$ : ice). All parameters of Equations 1.4-1.7 are given in Table 1.1

Since the total mass is conserved, the rate of change of any given mass specific quantity  $\psi$  can be formulated as:

$$\rho \frac{d\psi}{dt} = \frac{\partial(\rho\psi)}{\partial t} + \nabla \cdot (\rho \mathbf{v} \psi) \quad (1.9)$$

In COSMO, dry air and water vapour behave like ideal gases, and liquid water and ice are incompressible substances.

---

<sup>1</sup><http://scitas.epfl.ch/hardware/deneb-and-eltanin>

$t$	time
$p$	pressure
$T$	temperature
$\mathbf{g}$	apparent acceleration of gravity
$\rho_x$	partial density of mixture constituent $x$
$\rho = \sum_x \rho_x$	total density of the air mixture
$\mathbf{v} = (u, v, w)$	barycentric velocity (relative to the rotating Earth)
$\mathbf{\Omega}$	constant angular velocity of Earth rotation
$\mathbf{t}$	stress tensor due to viscosity
$c_p, c_v$	heat capacities for constant pressure and volume
$Q_h$	adiabatic heat production per unit volume of air
$Q_m$	impact of changes in humidity constituents concentrations on the pressure
$q^x = \rho^x / \rho$	mass fraction (specific) content of constituent $x$
$I^x$	sources/sinks of constituent $x$
$\mathbf{J}^x$	diffusion flux of constituent $x$
$\alpha = (\frac{R^v}{R^d})q^v - q^l - q^f$	moisture term relating temperature to generalized virtual temperature. $R^d$ and $R^v$ are the gas constants of dry air and water vapour.
$\nabla$	gradient (Nabla) operator

Table 1.1 – Parameters of the primitive equations of the atmosphere (Equations 1.4-1.8).

Considering the large dimensions of the mesoscale meteorological circulations simulated by COSMO (horizontal scales up to 100 km and vertical scales up to 10 km), solving explicitly all model equations with a sufficiently small grid spacing is computationally impossible. It is thus necessary to average these basic equations over the relevant space and time scales. In COSMO, this is done by separating the meteorological variables into a mean value (at the temporal and spatial resolution of the model) and a deviation (at the subgrid scale), a process known as *Reynolds decomposition*. For velocity and mass specific variables of state, such as enthalpy, internal energy and concentrations  $q^x$ , another type of decomposition is performed, where the mean value is a mass weighted average. COSMO also considers some simplifications for the heat equation:

1. Since turbulent fluxes are dominant in the atmosphere, molecular fluxes are neglected except for the sedimentation fluxes of liquid and solid water.
2. The specific heat of moist air is approximated by the specific heat of dry air as in the atmosphere water constituents contribute very little to the total mass of any volume of air.
3. The impact on pressure due to  $Q_m$  and  $Q_h$  is neglected.
4. The effect of buoyant heat and moisture fluxes on the temperature is neglected.

## Chapter 1. Introduction

---

The primitive equations of the atmosphere are typically defined using spherical coordinates, since the Earth is nearly spherical. However, when considering large model domains, numerical problems arise from the convergence of meridians and the resulting pole singularities.

To overcome these issues, COSMO uses rotated spherical coordinates, in which the pole is tilted and positioned such that the equator runs through the center of the model domain. This rotated coordinate system is defined in terms of orthogonal spherical coordinates  $(\lambda, \phi, r)$ , where  $\lambda$  is the rotated longitude,  $\phi$  is the rotated latitude and  $r$  is the distance from the Earth center. Details about the transformation of the basic equations into this new coordinate system can be found in Dutton and Fichtl (1969).

COSMO also assumes the Earth to be spherical with constant radius  $a$ , which implies that the gravity acceleration is constant and perpendicular to surfaces of constant radius, and that the distance  $r$  from the Earth center can be replaced by the geometrical height above mean sea level  $z$ .

Moreover, in COSMO, the pressure  $p$  is represented as the sum of a base-state pressure and deviations from the base state, in order to improve the numerical accuracy. In COSMO the base state is horizontally homogeneous, time invariant, in hydrostatic equilibrium, as well as dry (no water) and at rest (no wind).

The rotated pole coordinate system is a curvilinear but orthogonal spherical coordinate system, where the vertical coordinate is the geometrical height above mean sea level  $z$ . When the model includes the surface terrain, the formulation of lower boundary conditions becomes very costly. Therefore, COSMO uses a nonorthogonal terrain-following coordinate system in the vertical, where the lowest level corresponds to the topography. In this coordinate system,  $z$  is replaced by a generalized vertical coordinate  $\zeta$ , which depends on  $\lambda, \phi$  and  $z$ . In order to keep the numerical formulation of the model equations independent from a specific choice of  $\zeta$ , a two-step coordinate transformation is performed. First, the vertical heights of all grid points are transformed into a user-specified terrain-following coordinate  $\hat{\zeta}$ . Then, all coordinates  $\hat{\zeta}$  are mapped to a regular discrete grid defined by the computational coordinates  $\zeta$  using a monotonic function  $\hat{\zeta} = m(\zeta)$ .

COSMO offers three options for the terrain-following coordinates  $\hat{\zeta}$ . The first one is a reference pressure based coordinate, the second one is a Gal-Chen height based coordinate system (Gal-Chen and Somerville, 1975), and the third one is the height-based SLEVE (Smooth Level Vertical) coordinate (Schär et al., 2002).

To summarize, four steps are needed to convert the primitive equations to a form that can be numerically solved: *Reynolds decomposition*, conversion to rotated pole coordinates, base-state deviation, and conversion to terrain-following coordinates. Applying all these modifications to the primitive atmospheric budget equations (Equations 1.4-1.8) gives the final set of model equations (Equations 1.10-1.17), which includes seven prognostic equations for horizontal wind velocity, vertical wind velocity, perturbation pressure, temperature, water



vapor, liquid and solid form of water, as well as one diagnostic equation for the total density of air.

*Horizontal wind velocity components*

$$\frac{\partial u}{\partial t} = - \left\{ \frac{1}{a \cos \phi} \frac{\partial E_h}{\partial \lambda} - v V_a \right\} - \dot{\zeta} \frac{\partial u}{\partial \zeta} - \frac{1}{\rho a \cos \phi} \left( \frac{\partial p'}{\partial \lambda} - \frac{1}{\sqrt{\gamma}} \frac{\partial p_0}{\partial \lambda} \frac{\partial p'}{\partial \zeta} \right) + M_u \quad (1.10)$$

$$\frac{\partial v}{\partial t} = - \left\{ \frac{1}{a} \frac{\partial E_h}{\partial \lambda} - u V_a \right\} - \dot{\zeta} \frac{\partial v}{\partial \zeta} - \frac{1}{\rho a} \left( \frac{\partial p'}{\partial \lambda} - \frac{1}{\sqrt{\gamma}} \frac{\partial p_0}{\partial \lambda} \frac{\partial p'}{\partial \zeta} \right) + M_v \quad (1.11)$$

*Vertical wind velocity*

$$\begin{aligned} \frac{\partial w}{\partial t} = & - \left\{ \frac{1}{a \cos \phi} \left( u \frac{\partial w}{\partial \lambda} + v \cos \phi \frac{\partial w}{\partial \phi} \right) \right\} - \dot{\zeta} \frac{\partial w}{\partial \zeta} - \frac{g}{\sqrt{\gamma}} \frac{p_0}{\rho} \frac{\partial p'}{\partial \zeta} + M_w \\ & + g \frac{\rho_0}{\rho} \left\{ \frac{T - T_0}{T} - \frac{T_0 p'}{T p_0} + \left( \frac{R_v}{R_d} - 1 \right) q^v - q^l - q^f \right\} \end{aligned} \quad (1.12)$$

*Perturbation pressure*

$$\frac{\partial p'}{\partial t} = - \left\{ \frac{1}{a \cos \phi} \left( u \frac{\partial p'}{\partial \lambda} + v \cos \phi \frac{\partial p'}{\partial \phi} \right) \right\} - \dot{\zeta} \frac{\partial p'}{\partial \zeta} + g \rho_0 w - \frac{c_p^d}{c_v^d} p \mathcal{D} \quad (1.13)$$

*Temperature*

$$\frac{\partial T}{\partial t} = - \left\{ \frac{1}{a \cos \phi} \left( u \frac{\partial T}{\partial \lambda} + v \cos \phi \frac{\partial T}{\partial \phi} \right) \right\} - \dot{\zeta} \frac{\partial T}{\partial \zeta} - \frac{1}{\rho c_v^d} p \mathcal{D} + Q_T \quad (1.14)$$

*Water vapour*

$$\frac{\partial q^v}{\partial t} = - \left\{ \frac{1}{a \cos \phi} \left( u \frac{\partial q^v}{\partial \lambda} + v \cos \phi \frac{\partial q^v}{\partial \phi} \right) \right\} - \dot{\zeta} \frac{\partial q^v}{\partial \zeta} - (S^l + S^f) + M_{q^v} \quad (1.15)$$

*Liquid and solid forms of water*

$$\frac{\partial q^{l,f}}{\partial t} = - \left\{ \frac{1}{a \cos \phi} \left( u \frac{\partial q^{l,f}}{\partial \lambda} + v \cos \phi \frac{\partial q^{l,f}}{\partial \phi} \right) \right\} - \dot{\zeta} \frac{\partial q^{l,f}}{\partial \zeta} - \frac{q}{\sqrt{\gamma}} \frac{\rho_0}{\rho} \frac{\partial P_{l,f}}{\partial \zeta} + S^{l,f} + M_{q^{l,f}} \quad (1.16)$$

*Total density of air*

$$\rho = p \left\{ R^d \left( 1 + (R^v / R^d - 1) q^v - q^l - q^f \right) T \right\}^{-1} \quad (1.17)$$

where  $\mathcal{D}$  is the divergence of the wind field and  $\dot{\zeta}$  is the contra-variant vertical velocity which are both diagnostic quantities within this set of equations,  $\sqrt{\gamma} = \frac{\partial p_0}{\partial \zeta}$  is the variation of reference pressure with  $\zeta$ ,  $E_h = \frac{1}{2} (u^2 + v^2)$  is the kinetic energy of horizontal motion,  $V_a$  is the vertical component of the absolute vorticity,  $S^l$  and  $S^f$  are cloud microphysical source and sink terms,  $P_{l,f}$  are precipitation fluxes and  $M_\psi$  indicates contributions from subgrid scale processes (e.g. turbulence, convection, radiation). Finally,  $Q_T$  is the diabatic heating rate due to these processes.

### 1.2.2.2 Numerical solving of the model equations

Equations 1.10-1.17 are solved by discretizing them spatially and temporally. For the spatial discretization, COSMO uses a regular computational grid with constant increments in the three dimensions ( $\Delta\lambda$ ,  $\Delta\phi$  and  $\Delta\zeta$ ). The computational  $(\lambda, \phi, \zeta)$  space is then represented by a finite number of grid points  $(i, j, k)$ , with  $i$  corresponding to the  $\lambda$ -direction,  $j$  to the  $\phi$ -direction and  $k$  to the  $\zeta$ -direction. The model variables are defined on a staggered Arakawa-C/Lorenz grid where the scalar quantities (temperature, pressure and humidity) are defined at the center of the grid box and the velocity components are defined on the box faces (Figure 1.2).

Acoustic waves, which propagate very fast, severely limit the maximum time step that can be used with explicit time integration schemes. To overcome this issue, the governing atmospheric equations are integrated in time with a mode-splitting time integration method. This technique is based on a separation of the prognostic equations into slowly varying processes and processes affected by acoustic waves, and only the later are solved with a small time step. This makes the explicit time integration scheme more efficient. Numerical integration is performed with a third-order Runge-Kutta scheme (Wicker and Skamarock, 2002) and slow tendencies are kept constant during the individual Runge-Kutta steps.

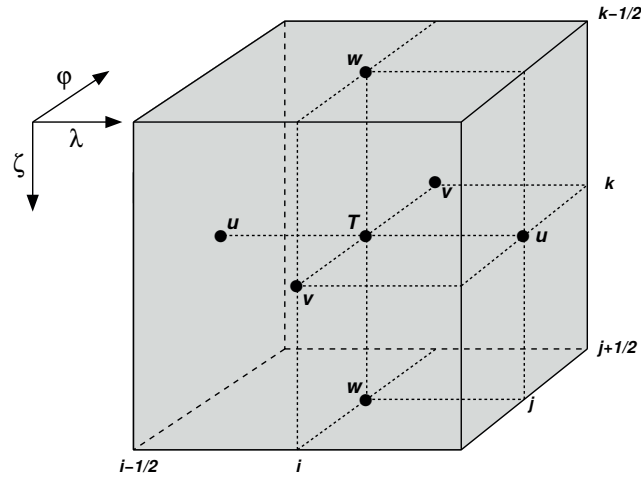


Figure 1.2 – A COSMO grid box volume, with Arakawa-C/Lorenz staggering of the model variables. Taken from (Doms et al., 2011)

### 1.2.2.3 Physical parameterizations

Because of the limited temporal and spatial resolutions of the model, not all atmospheric processes can be accounted for by the explicit solutions of the basic equations at grid scale. Subgrid scale processes include molecular processes such as radiation, cloud microphysics, as well as turbulence and convection. However, knowledge of these processes is crucial both for deriving the source and sink terms of the basic equations and for providing a complete characterization of the atmosphere. These processes are hence treated separately from the basic equations using physical parameterizations. COSMO includes many different parameterizations, which are summarized briefly in this section. Unless stated otherwise, only the parameterizations used operationally by MeteoSwiss will be indicated, even though more sophisticated schemes may be implemented in the model. More details will be given for the grid-scale clouds and precipitation parameterization since it is of high importance in this thesis. For a more exhaustive description of COSMO's physical parameterizations see Doms et al. (2011).

#### *Radiation*

The heating rate due to radiation is calculated with the two-stream parameterization scheme of Ritter and Geleyn (1992). This scheme considers three short wave (solar) and five long wave (thermal) spectral intervals, and takes into account the effect of absorption, emission and scattering of atmospheric particles on the radiative fluxes. However, this parameterization is very cost-intensive, and as such, is only called at hourly intervals. The radiative fluxes are kept constant in between.

## Chapter 1. Introduction

---

### *Turbulence*

In the operational set-up, the COSMO model uses a prognostic turbulent kinetic energy (TKE) closure at level 2.5 for the parametrization of atmospheric turbulence. This scheme is similar to Mellor and Yamada (1982), the main difference being the use of variables that are conserved under moist adiabatic processes: total cloud water and liquid water potential temperature. Additionally, a so-called “circulation term” is included which describes the transfer of non-turbulent sub-grid kinetic energy from larger-scale circulation towards TKE.

The TKE equation is extended to the ground by a surface layer scheme which introduces an additional laminar layer just above the surface that allows to differentiate model variables at the rigid surface from model variables at the roughness height.

### *Soil model*

The TERRA-ML (multilayer) soil model developed by Schrodin and Heise (2002) is used. The TERRA-ML model considers 8 soil layers as well as freezing and melting processes in the soil. The energy balance is computed with a direct solution for the heat conduction equation. The 8th layer is the so-called climate layer, where the annual mean 2 m-temperature is prescribed as a boundary value. The lower boundary condition at the bottom of the deep layer is free drainage. Soil water can drain from the lowest layer, but the flux due to diffusion is neglected. This means that ground water cannot moisten the soil by capillary rise from below.

### *Fractional Cloud Cover*

When calculating the radiative transfer and when interpreting model outputs in post-processing routines, it is useful to define a fractional cloud cover for the grid boxes where the relative humidity is less than 100%, but where no grid-scale cloud water exists. In COSMO, this fraction is estimated empirically as a function of relative humidity, height, convective activity and stability (Sommeria and Deardorff, 1977).

### *Moist convection*

For moist convection parameterization, MeteoSwiss uses a Tiedtke (1989) mass-flux convection scheme with equilibrium closure based on moisture convergence by, modified to consider only shallow convection.

### *Grid-scale clouds and precipitation*

For operational weather prediction, the COSMO model uses a one-moment microphysical scheme similar to Rutledge and Hobbs (1983) and Lin et al. (1983), with five hydrometeor categories: rain, snow, graupel, ice crystals and cloud droplets. Snow is assumed to be in the form of rimed aggregates of ice-crystals that have become large enough to have an appreciable fall velocity. In the version of COSMO that is being used, cloud ice is assumed to be in the form of small hexagonal plates that are suspended in the air and have no appreciable fall velocity. In later versions however (starting from 5.1), ice crystals are considered to have a bulk terminal

velocity, proportional to their mass concentration. The PSDs are assumed to be exponential for all hydrometeors except for rain where a gamma DSD is used:

$$N(D) = N_0 D^\mu \exp(-\Lambda \cdot D) \quad \text{m}^{-3} \text{mm}^{-1} \quad (1.18)$$

where  $D$  is the equivolume diameter,  $N_0$  is the *intercept* parameter ( $\text{m}^{-3} \text{mm}^{-1-\mu}$ ),  $\Lambda$  the *slope* parameter ( $\text{mm}^{-1}$ ) and  $\mu$  the dimensionless *shape* parameter. Note that the exponential PSD is just a special case of the gamma PSD where  $\mu = 0$ . For rain,  $N_0$  is a function of  $\mu$ , based on the relation of Ulbrich (1983):

$$N_0^{\text{rain}} = 0.1 N_0^0 \exp(3.2\mu) \quad (1.19)$$

where  $N_0^0 = 8e6 \text{ m}^{-4}$ .

In the operational one-moment scheme the only free parameter of the PSDs is the slope parameter  $\Lambda$  which can be obtained from the prognostic mass concentrations. The intercept parameter  $N_0$  is either assumed to be constant, or in the case of snow, to be temperature dependent. The scale parameter  $\mu$  is set to zero (exponential PSDs) for all hydrometeors except for rain where it can be chosen *a-priori* and is set to 0.5 by default.

In COSMO, the interaction of various microphysical processes and their feedback on the simulated flow fields are represented by a system of budget equations for  $q^x$ , the specific mass fraction in kg of hydrometeor  $x$  per kg of air.

$$\frac{\partial q^x}{\partial t} + \mathbf{v} \cdot \nabla q^x - \frac{1}{\rho} \frac{\partial P^x}{\partial z} = S^x - \frac{1}{\rho} \nabla \cdot \mathbf{F}^x \quad (1.20)$$

where  $S^x$  represents the microphysical sources and sink per unit mass of moist air,  $\mathbf{F}^x$  represent all non-microphysical tendencies (advection, turbulence) and  $P^x$  are the precipitation or sedimentation fluxes defined by  $P^x = \rho q^x v_t^x$ , where  $v_t^{(j)}$  is the terminal fall velocity of hydrometeor  $j$ . Microphysical sources and sinks for all six hydrometeor types are summarized in Figure 1.3.

A more advanced two-moment scheme, which adds hail as a sixth hydrometeor category, was developed for COSMO by Seifert and Beheng (2006) and extended by Blahak (2008) and Noppel et al. (2010). In this scheme all PSDs are assumed to be gamma distributions where the *intercept* and *slope* parameters are free parameters that can be obtained from the prognostic moments of order zero (number concentrations) and from the prognostic mass concentrations. This scheme allows a more versatile parameterization of the size distribution functions, but

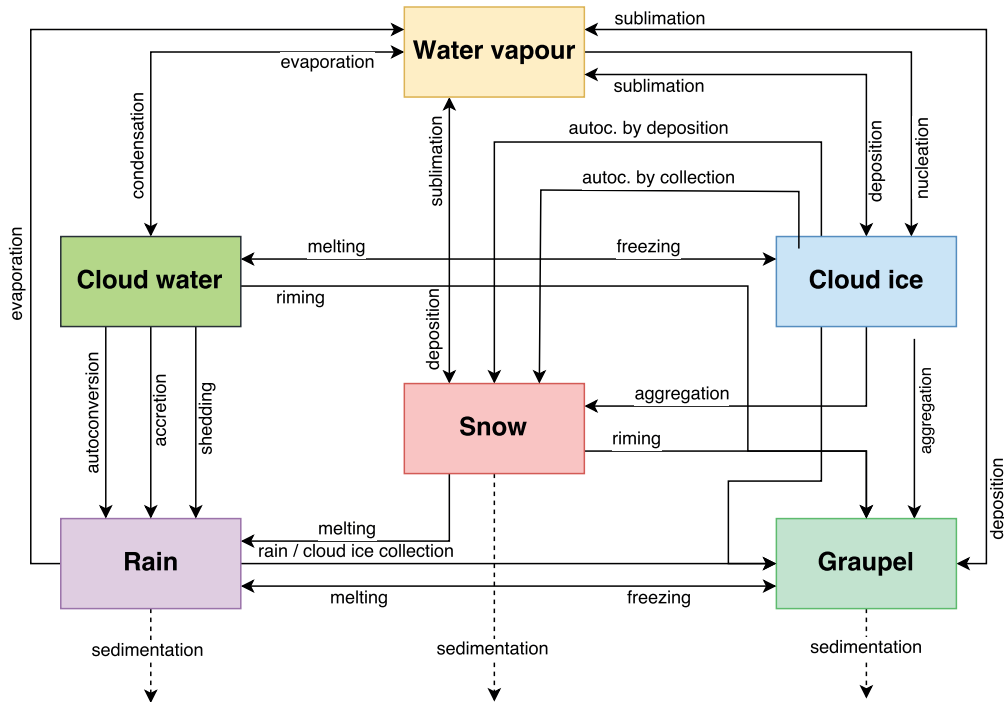


Figure 1.3 – Cloud microphysical processes considered in the operational one-moment scheme. Adapted from Reinhardt and Seifert (2006).

also increases significantly the overall computation time. Because of this, it is currently not used operationally.

The precipitation intensity at the ground is simply the sum of the sedimentation fluxes of all hydrometeors at the lowest model level. In terms of terminal velocities COSMO generally assumes power-laws:  $v_T = a_v D_v^b$ , where  $D$  is the particle diameter (equivolume diameter for rain and maximum diameter for solid hydrometeors). Note that in the two-moments scheme a more refined empirical relation by Rogers et al. (1993) is used for raindrops.

#### 1.2.2.4 Initial and boundary conditions

As any local model, COSMO needs to be initialized and driven on its lateral boundaries with a prescribed state of the atmosphere simulated by a global model or another larger scale local model. Since the resolution of the larger scale models is generally different from the one of COSMO, interpolation of the required variables has to be performed. Interpolation is a source of numerical noise which can propagate from the boundaries to the interior of the model domain (Davies, 1976). To alleviate this issue, COSMO defines a relaxation zone close to the boundaries, in which the simulated high-resolution variables are progressively blended with the coarser-resolution variables of the driving model. The influence of the driving model decreases exponentially with the distance to the boundaries.

In its operational setup, COSMO assumes open inflow/outflow lateral boundary conditions and non-slip (no mass-transfer) conditions at the highest vertical model layer for horizontal wind velocity, temperature and water substances. To avoid energy reflection at the upper boundary in case of orographically induced flows, the model uses a Rayleigh damping scheme which absorbs upward propagating wave disturbances.

Operationally, MeteoSwiss uses a nested procedure, COSMO-7 is first initialized and driven with simulations from the Integrated Forecast System (IFS) global model of the European Center for Medium-range Weather Forecasts (EMCWF) and the resulting COSMO-7 simulations are subsequently used to initialize and drive the COSMO model in its high-resolution set-up (now COSMO-1, previously COSMO-2). In the context of this thesis however, the first step of this nested scheme was skipped and all high-resolution runs were performed with initial and boundary conditions obtained from the COSMO-7 model runs done by MeteoSwiss in analysis mode<sup>2</sup>.

### 1.2.3 Basics of radar meteorology

This thesis makes use of a large selection of radar products from various research and operational radars. Therefore, this section provides a brief introduction to radar meteorology, with an exclusive focus on pulsed radars, since they represent the vast majority of weather radars, and are the only type of radars used in this work.

#### 1.2.3.1 A brief description of weather radars

Weather radars are a type of radar (RAdio Detection And Ranging) used to locate precipitation, measure its intensity and in some cases calculate its motion. Pulse weather radars send directional pulses of microwave radiation at a wavelength between 1 and 10 centimetres. Part of the energy of each pulse will be backscattered to the radar station by the hydrometeors in the atmosphere. At those frequencies Rayleigh scattering by the hydrometeors is the dominant process because the emitted signals have a wavelength in the order of ten times the diameter of the drops or ice particles. However, for weather radars emitting at small wavelengths (X to Ka bands: 8 to 40 GHz), Mie scattering can be important too. Differences between the transmitted and received powers can then be related to the amount of hydrometeors on the beam trajectory. Most operational radars cannot emit and receive simultaneously and thus switch to receiving mode between each emitted pulse.

---

<sup>2</sup>a mode in which the model is regularly corrected by assimilating measurements from various instruments (e.g. radio soundings, rain gauges, radars)

## Chapter 1. Introduction

---

Once the radar has received the backscattered signal, the range  $r$  (distance) to the target can be deduced from the time interval between emission and reception.

$$r = c \frac{\Delta_t}{2} \quad (1.21)$$

where  $c$  is the speed of light and  $\Delta_t$  is the elapsed time interval between the emission and the reception of the pulse.

The maximum unambiguous range  $r_{\max}$  of a radar is determined by the longest range to which a transmitted pulse can travel and return to the radar before the next pulse is transmitted. This range depends on the the pulse repetition frequency (PRF) of the radar.

$$r_{\max} = \frac{c}{2 \cdot PRF} \quad (1.22)$$

The range resolution  $dr$  of a radar depends mostly on its pulse width time  $\tau$ , which is the duration of a given radar pulse. The theoretical maximum range resolution of a radar system is equal to half of the distance corresponding to time  $\tau$ .

$$dr = \frac{c \cdot \tau}{2} \quad (1.23)$$

The angular resolution of a radar depends on the antenna characteristics. Indeed, radars use directional antennas which emit stronger radiation in one direction than in another, the radiation peak being in the direction pointed by the antenna. The angular resolution of a radar is usually approximated by the 3 dB beamwidth  $\theta_{3\text{dB}}$ , which is the angle between the half-power (-3 dB) point of the antenna pattern and the point of the main lobe with maximum power. In the following, a circular symmetric antenna pattern with the same beam width in azimuthal and elevational directions will be assumed.

As can be seen on Figure 1.4, the resolution volume  $V_{\text{res}}$  illuminated by a transmitted pulse along the radar beam can be approximated by a cylinder defined by the range  $r$ , the beam width  $\theta_{3\text{dB}}$  and the radial resolution  $dr = (c \cdot \tau)/2$ :

$$V_{\text{res}} \approx \pi \left( r \frac{\theta_{3\text{dB}}}{2} \right)^2 \frac{c\tau}{2} \quad (1.24)$$

It can be observed that the resolution volume increases with the square of the distance from the radar. This effect is called *beam-broadening* and is one of the reasons why the quality of radar measurements deteriorates with range (Ryzhkov, 2007). Another reason is that the



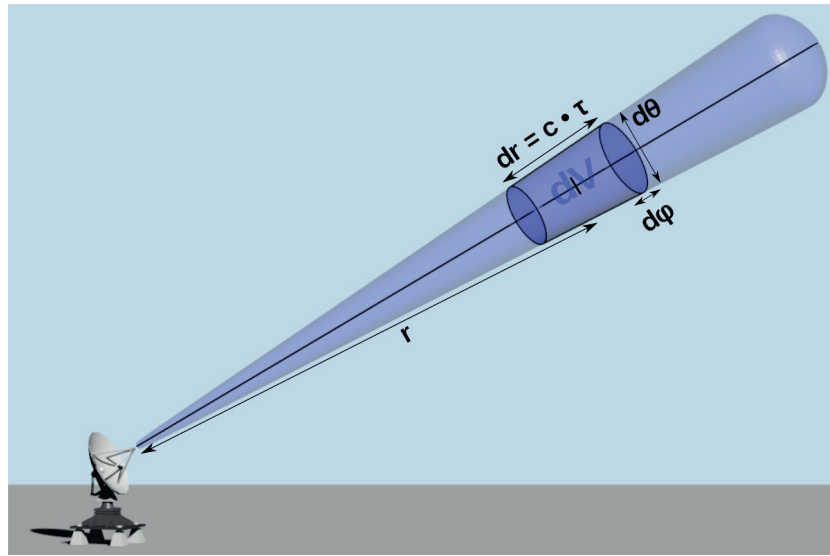


Figure 1.4 – Schematic of a pulse radar. At each range bin  $r$ , the radial resolution  $dr$  and the angular resolutions  $d\theta$  and  $d\phi$  define a volume of resolution  $V_{res}$ . The size of the volume of resolution is proportional to the square of the distance from the radar.

transmitted signal gradually weakens when going through precipitation, because of scattering in other directions than the radar and absorption of the incident wave by hydrometeors. This effect is known as *attenuation* and increases with the frequency of the radar and the intensity of precipitation.

Radars cover a large interval of frequencies. Generally the maximal range of the radar decreases with increasing frequency but radars operating at higher frequencies are smaller, generally less expensive and often have a higher radial resolution. Most operational weather radar radars operate at S-band (2 to 4 GHz) or C-band (4 to 6 GHz). Back-scattering by precipitation starts at S-band but the attenuation effect by hydrometeors at these wavelengths is still small. These radars have thus large maximal ranges (up to 250 km). Radars operating at X-band emit at a frequency between 8 and 12 GHz, where attenuation by precipitation is much larger. At X-band, radars have a much smaller antenna and a shorter range (up to 60 km), as such, they are generally restricted to research purposes.

The most common radar scanning mode is the Plane Position Indicator (PPI), which is often the only type of scanning performed by operational radars. In this mode, the radar performs a complete or partial azimuthal rotation at a fixed elevation angle. Data are acquired in polar coordinates (azimuth angle – radial distance). Since the elevation angle is usually higher than  $0^\circ$  (typically  $1$  to  $10^\circ$ ), the altitude of the range bin increases with its distance to the radar. Another type of scanning mode, often performed by research radars is the Range Height Indicator (RHI). In this mode, the radar performs a high-resolution scan along a vertical cut of the atmosphere at a fixed azimuth. Data are acquired in polar coordinates (elevation angle – radial distance).

## Chapter 1. Introduction

---

Localized information about the transmitted and received powers is of great interest since it can be related to the rain intensity. For a single body scatterer, the received power  $P_r$  is related to the transmitted power  $P_t$  by the radar equation (Doviak and Zrnić, 2006). For a monostatic radar (in which the receiver and the transmitter are collocated), which represents the vast majority of weather radars, the radar equation is:

$$P_r = \frac{P_t G^2 \lambda^2 \sigma^0}{(4\pi)^3 r^4} \propto \frac{\sigma^0}{r^4} \quad (1.25)$$

where  $P_r$  and  $P_t$  are the powers received, respectively, transmitted by the radar in W or mW,  $G$  is the total gain of the radar system (mostly the antenna gain),  $\lambda$  is the wavelength of the transmitted pulse,  $r$  is the distance to the target,  $\sigma^0$  is the radar cross-section of the target in units of squared distance. For a scattering object at a certain range, the radar (backscattering) cross-section  $\sigma^0$  is the cross-sectional area of an hypothetical isotropic scatterer located at the same range as the target, that would return the same power to the radar as the actual target. Note that in the present equation, the effect of attenuation by hydrometeors has, for now, been neglected.

In weather applications, there are many scattering bodies (hydrometeors) per unit volume and the radar equation has to be adapted. The total radar cross-section is the sum of all individual cross sections within the radar resolution volume.

$$\sigma^0 = V_{\text{res}} \int_{D_{\text{min}}}^{D_{\text{max}}} \sigma^b(D) N(D) dD = V_{\text{res}} \eta \quad (1.26)$$

where  $N(D)$  is the expected number of hydrometeors of diameter  $D$  per unit volume, as given by the particle size distribution,  $\sigma^b(D)$  is the radar cross-section of a single hydrometeor of size  $D$  and  $\eta$  is the *reflectivity*, the total radar cross-section per unit volume.

The weather radar equation can be obtained by substituting Equation 1.24 into Equation 1.26 (Probert-Jones, 1962). To account for the power density pattern of the antenna, a correction factor of  $1/(2 \ln(2))$  has to be applied to  $V_{\text{res}}$ . Note that this factor is only valid for a symmetrical circular Gaussian shape, but is generally considered as a realistic approximation for any real antenna.

$$P_r = \frac{P_t G^2 \eta c \tau \pi \lambda^2 \theta_{3\text{dB}}}{(4\pi)^3 r^2 16 \ln(2)} \propto \frac{\eta}{r^2} \quad (1.27)$$

In this equation, the received power depends on the square of the range, instead of the power four as with single targets. This is due to the fact that the radar resolution volume, and thus the number of hydrometeors that re-emit power towards the radar, increases with the square of the distance.

In the Rayleigh approximation, which is usually valid for diameters  $D \lesssim \lambda/16$ , the radar backscattering cross section of a single water drop increases monotonically with the diameter.

$$\sigma^{b,\text{Rayl}} = \frac{\pi^5}{\lambda^4} |K|^2 D^6 \quad (1.28)$$

where the superscript ‘‘Rayl’’ indicates Rayleigh scattering and  $K$  is the refractive factor of the hydrometeors with respect to the incident wave.  $K = (m^2 - 1)/(m^2 + 2)$ , with  $m$  being the complex refractive index. For liquid water  $|K_w|^2 \approx 0.93$  in the microwave regime.

Using Equation 1.28 in the definition of the *reflectivity*  $\eta$  gives:

$$\eta^{\text{Rayl}} = \frac{\pi^5}{\lambda^4} |K|^2 \int_{D_{\min}}^{D_{\max}} D^6 N(D) dD = \frac{\pi^5}{\lambda^4} |K|^2 Z_e^{\text{Rayl}} \quad (1.29)$$

where  $Z_e^{\text{Rayl}}$  is the sixth moment of the particle size distribution.  $Z_e$  is called the *reflectivity factor* and is expressed in units of  $\text{mm}^6 \text{m}^{-3}$ .

As a convention in radar meteorology, even when the Rayleigh approximation is not valid, the reflectivity factor is still defined in terms of  $\eta$ , as a Rayleigh ‘‘equivalent’’ *reflectivity factor*.

$$Z_e = \frac{\eta \lambda^4}{\pi^5 |K_w|^2} \quad (1.30)$$

Where a constant value of  $|K_w|^2 = 0.93$  is generally used even if the radar might be sampling ice-phase hydrometeors.

Because encountered values of  $Z_e$  commonly span many orders of magnitude, a logarithmic scale is often used:  $Z = 10 \log_{10}(Z_e)$ . Note that, though it is technically incorrect, by abuse of language  $Z$  is often simply referred to as the *reflectivity*.

At higher frequencies, as in the X-band, the observations of reflectivity factor are affected by along-path attenuation due to scattering and absorption by the hydrometeors. Part of the transmitted power will be lost because of two-way attenuation along the path, causing a decrease in the observed reflectivity factors.

## Chapter 1. Introduction

---

At a given range  $r$ , the observed (attenuated) reflectivity factor is:

$$Z^{\text{att}}(r) = 10 \log_{10} \left[ Z_e \exp \left( -2 \int_{r=0}^r k_e(s) ds \right) \right] \quad (1.31)$$

$$= Z - 8.6858 \int_{r=0}^r k_e(s) ds \quad (1.32)$$

where  $k_e(r)$  is the attenuation coefficient (in units of inverse length) at horizontal polarization and the factor 2 accounts for the fact that the radar pulse travels the same path twice. The term  $8.6858 k_e$  is often referred to as the specific attenuation  $k$ , expressed in units of  $\text{dB km}^{-1}$ .

The attenuation coefficient  $k$  can also be expressed in terms of the particle size distribution.

$$k(r) = 8.6858 \int_{D_{\min}}^{D_{\max}} \sigma^e(D) N(D) dD \quad (1.33)$$

where  $\sigma^e$  is the extinction cross-section which depends on the imaginary part of the complex permittivity.

Several methods for attenuation correction methods exist in the liquid phase. The simplest ones usually assume a power-law relation between  $k$  and  $Z$ , while others rely on other radar observables not affected by attenuation (Testud et al., 2000).

Most weather radars include a target tracking system based on the Doppler-Fizeau effect. In addition to reflectivity, these radars also gather information about the radial velocity component of the precipitation and its standard deviation. This allows to gain information about the rotational features within precipitation systems, and to improve the detection of ground echoes<sup>3</sup>, as they are generally characterized by a null velocity.

Dual-polarization radars transmit and receive horizontally (H) and vertically (V) polarized waves. As will be described in details in the next section, these radars give access to a whole set of derived variables which give relevant information about the type of precipitation and the shape of the hydrometeors. Weather radars that combine information about the phase (Doppler radars) and transmit in both vertical and horizontal polarizations are generally called polarimetric radars. In most radars, transmission at H and V polarizations is simultaneous, but for older radars and some research radars the transmission can be alternate.

---

<sup>3</sup> Strong backscattering caused by static elements of the relief such as building or rocks

In this work, data from three different pulse radar systems will be used. All systems are monostatic radars (collocated transmitter and receiver). All polarimetric radars that are used are simultaneous H and V transmitters.

- Operational polarimetric C-band radars of MeteoSwiss (5.6 GHz)
- Mobile polarimetric X-band radar operated by the LTE laboratory at EPFL, “MXPol” (9.41 GHz)
- Dual-Frequency Precipitation Radar (DPR, Furukawa et al. (2016)) on board the Global Precipitation Measurement (GPM, Iguchi et al. (2003)) mission Core Observatory satellite operating at Ku (13.6 GHz) and Ka bands (35.6 GHz)

More technical details about these radars will be given throughout the thesis.

### 1.2.3.2 Polarimetric radar observables

The present section provides a short description of the polarimetric variables of major interest for meteorological applications. The focus will be put on the relations between precipitation microphysics and radar observations, rather than on the signal processing aspects of radar observables acquisition. Note that all described radar observables are function of the range  $r$  (Equation 1.21), but for sake of conciseness, this is not indicated explicitly in their mathematical formulations.

The mathematical formulation of the radar observables involves the *scattering matrix*, which relates the scattered electric field  $\mathbf{E}^s$  to the incident electric field  $\mathbf{E}^i$  (Bringi and Chandrasekar, 2001) for a given scattering angle.

$$\begin{bmatrix} E_h^s \\ E_v^s \end{bmatrix} = \frac{e^{-ik_0 r}}{r} \begin{bmatrix} s_{hh} & s_{hv} \\ s_{vh} & s_{vv} \end{bmatrix}_{\text{FSA}} \begin{bmatrix} E_h^i \\ E_v^i \end{bmatrix} \quad (1.34)$$

where  $k_0$  is the wave number of free space ( $k_0 = 2\pi/\lambda$ ).

The scattering matrix is a  $2 \times 2$  matrix of complex numbers in units of  $\text{m}^{-1}$  (e.g., Bringi and Chandrasekar, 2001; Doviak and Zrnić, 2006; Mishchenko et al., 2002).

$$\mathbf{S}_{\text{FSA}} = \begin{bmatrix} s_{hh} & s_{hv} \\ s_{vh} & s_{vv} \end{bmatrix}_{\text{FSA}} \quad (1.35)$$

## Chapter 1. Introduction

---

The FSA subscript indicates the forward scattering amplitude convention, in which the positive  $z$ -axis is in the same direction as the travel of the wave (for both the incident and scattered wave). In the FSA convention, the scattering matrix is also called the *Jones* matrix (Jones, 1941). In the following the coefficients of the backscattering matrix (scattering towards the radar) will be denoted by  $s^b$ , and the coefficients of the forward scattering matrix (scattering away from the radar) by  $s^f$ .

Moreover, in the following, the term (complex) *permittivity* will be used for the relative dielectric constant of a given material. It is defined by:

$$\epsilon = \epsilon' + i\epsilon'' \quad (1.36)$$

where  $\epsilon'$  is the real part, related to the phase velocity of the propagated wave, and  $\epsilon''$  is the loss part, related to the attenuation of the propagated wave.

### Reflectivity factor at horizontal (vertical) polarization

The reflectivity factors at horizontal  $Z_H$  and vertical  $Z_V$  polarizations are simply the dual-polarization equivalents of  $Z$ .  $Z_H$  is defined in dB as ( $Z_V$  is strictly analogous):

$$Z_H = 10 \log_{10} \left[ \frac{\lambda^4}{\pi^5 |K_w|^2} \int_{D_{\min}}^{D_{\max}} \sigma^{b,h}(D) N(D) dD \right] \quad (1.37)$$

with the superscript  $h$  indicating the horizontal polarization. The backscattering cross-sections  $\sigma^b$  can be obtained from the backscattering matrix.

$$\begin{bmatrix} \sigma_h^b \\ \sigma_v^b \end{bmatrix} = 4\pi \begin{bmatrix} |s_{hh}^b|^2 \\ |s_{vv}^b|^2 \end{bmatrix} \quad (1.38)$$

For pure materials, where the bulk density is independent of size (e.g. raindrops) and when the Rayleigh approximation holds,  $Z_H$  is simply the sixth moment of the particle size distribution, expressed in decibel scale:

$$Z_H^{\text{Rayl}} = 10 \log_{10} \left[ \int_{D_{\min}}^{D_{\max}} D^6 N(D) dD \right] \quad (1.39)$$

Using measurements of received power, the possibly attenuated  $Z_H$  can be calculated by combining Equations 1.27 and 1.30.

$$Z_H = 10 \log_{10} \left[ \frac{P_{r,h}}{P_{t,h}} \frac{r^2 \lambda^2}{G^2 |K_w|^2 c \tau \theta_{3dB}} \frac{1024 \ln(2)}{\pi^3} \right] \quad (1.40)$$

$Z_H$  and  $Z_V$  depend on the particle size distribution, the incident wavelength, as well as, through  $\sigma^b$ , on the temperature and the dielectric properties of the hydrometeors.

For sake of simplicity, in what follows,  $Z_H$  and  $Z_V$ , expressed in units of dBZ, will sometimes be simply referred to as *horizontal* and *vertical reflectivities*. Though, not technically correct, this terminology is frequent, because the proper reflectivity  $\eta$  is rarely used in practical radar meteorology.

### Differential reflectivity

For oblate hydrometeors, for which the horizontal section is larger than the vertical section,  $Z_H$  is larger than  $Z_V$ . Intuitively, the reflectivity factors at both polarizations can be combined into a new variable that gives an indication of the particle shape: the differential reflectivity (in dB).

$$Z_{DR} = Z_H - Z_V \quad (1.41)$$

$Z_{DR}$  is generally independent of the concentration and tends to be influenced mostly by the largest particles, which have the highest reflectivity. In rain  $Z_{DR}$  is generally positive, since larger drops tend to fall faster and the air resistance flattens their base while falling. For ice crystals,  $Z_{DR}$  is slightly positive, whereas in hail it can be slightly positive, zero or negative depending on the orientation of the hail (Zrnic and Ryzhkov, 1999).  $Z_{DR}$  is close to zero at higher elevations because when illuminated from below all drops appear symmetrical.

### Copolar cross correlation coefficient

For a pulse radar,  $Z_H$  and  $Z_V$  are typically calculated as averages over several pulses separated by short time intervals (Bringi and Chandrasekar, 2001). This reduces the measurement noise and gives a more representative sampling of the resolution volume. Moreover it allows to calculate an additional variable, the copolar cross correlation coefficient  $\rho_{hv}$  which is estimated as the correlation between all backscattered echoes at horizontal and vertical polarizations (Bringi and Chandrasekar, 2001).

## Chapter 1. Introduction

---

With a very large number of pulses (exhaustive sampling of the resolution volume), the measured  $\rho_{hv}$  should converge to the expected  $\rho_{hv}$ , which in terms of microphysical parameters is equal to:

$$\rho_{hv} = \frac{\left| \int_{D_{\min}}^{D_{\max}} (s_{hh}^b(D))^* s_{vv}^b(D) N(D) dD \right|}{\sqrt{Z_h \cdot Z_v}} \quad (1.42)$$

where  $Z_h/Z_v$  is the horizontal/vertical reflectivity in linear units ( $Z_e$  in Equation 1.30), and  $s_{hh}^b/s_{vv}^b$  are the complex backscattering amplitudes at horizontal/vertical polarizations.

$\rho_{hv}$  is very sensitive to inhomogeneities in the hydrometeor population within the resolution volume. It is generally high in stratiform precipitation ( $> 0.95$ ) and ice clouds, and tends to be smaller in convective precipitation and aggregates (Matrosov et al., 2007).  $\rho_{hv}$  is often used for the discrimination of ground clutter and non-meteorological targets where it is particularly small (e.g., Rico-Ramirez and Cluckie, 2008; Berenguer et al., 2006), as well as for the detection of the melting layer of precipitation (e.g., Giangrande et al., 2008; Bandera et al., 1998; Wolfensberger et al., 2016).

### Specific differential phase shift on propagation

Besides reflecting part of the emitted power back towards the radar, hydrometeors also slow down the transmitted waves along the beam propagation path, which creates a shift in phase between the emitted and the received signal. For non-spherical scatterers, this phase shift is stronger for the waves polarized along their major dimension. The specific differential phase shift on propagation ( $K_{dp}$ ) is related to the difference in phase shift between both polarizations.

$$K_{dp} = \frac{180}{\pi} 10^3 \lambda \int_{D_{\min}}^{D_{\max}} \Re \left[ s_{hh}^f(D) - s_{vv}^f(D) \right] N(D) dD \quad (1.43)$$

where  $s_{hh}^f/s_{vv}^f$  in meters are the forward complex scattering amplitudes at horizontal/vertical polarizations and  $\Re$  indicates the real part of the complex number.  $K_{dp}$  has units of  $^{\circ} \text{km}^{-1}$  and represents the rate at which the difference in phase shift between horizontal and vertical polarizations increases.

Unfortunately,  $K_{dp}$  cannot be measured directly by the radar, as the phase shift can be measured only once the transmitted wave has been backscattered towards the radar. The observed quantity is thus the (range-integrated) differential phase shift on propagation  $\phi_{dp}$ .  $K_{dp}$  is the radial derivative of  $\phi_{dp}$ , which can be estimated numerically with a noise-robust estimator



such as the Kalman filter method by Schneebeli et al. (2014), or the moving window finite difference scheme of Vulpiani et al. (2012). Moreover, at higher frequencies (e.g. mostly starting from X-band), the differential phase shift on backscattering  $\delta_{hv}$ , which is the phase shift induced upon the backscattering process, is an additional source of error in the numerical estimation of  $K_{dp}$  (e.g., Trömel et al., 2013; Schneebeli et al., 2014). At these frequencies, the sum of  $\delta_{hv}$  and  $\phi_{dp}$  is called the total differential phase shift  $\Psi_{dp}$  and corresponds to the raw radar observations, from which  $K_{dp}$  has to be estimated.

Increases in  $K_{dp}$  imply the presence of large amounts of liquid water and/or the presence of highly oriented shapes.  $K_{dp}$  is linearly related to the specific attenuation and almost linearly related to the rain rate Zrnic and Ryzhkov (1999).  $K_{dp}$  is not affected by attenuation and as such is a robust indicator of rain intensity.

### Doppler variables

A Doppler capable radar is able to measure the phase of a received wave. The phase shift between the transmitted and the received waves is related to the radial component of the velocity of the target by the Doppler-Fizeau effect.

$$\Delta_{\Theta} = \left( \frac{4\pi v_{\text{rad}} \Delta_t}{\lambda} \right) \quad (1.44)$$

where  $\Delta_{\Theta}$  is the observed phase shift,  $v_{\text{rad}}$  is the radial component (relative to the radar beam) of the target velocity and  $\Delta_t$  is the time interval between emission and reception.

Most operational radars measure only the average radial velocity and its standard deviation within the radar resolution volume, by averaging over many different pulses emitted at short time intervals. The standard deviation of radial velocity is often referred to as the *spectral width* and depends on the wind shear, the particle size distribution and atmospheric turbulence. However, one must keep in mind that, since the volume of resolution increases with the distance from the radar (Equation 1.24), the spectral width is also sensitive to the beam-broadening effect.

Some radars are able to retrieve the full *Doppler spectrum*  $S(v)$ : the power-weighted distribution of radial velocities within the radar resolution volume. The value of  $S(v) dv$  represents the power returned to the radar by scatterers with radial velocity between  $v$  and  $v + \Delta_v$ . The resolution in velocity  $\Delta_v$  and the maximum and minimum bounds on  $v$  are defined by radar specific parameters such as the PRF and the length of the Fast Fourier Transform (FFT) used to convert the time-domain samples to the frequency-domain.

In terms of microphysical parameters the Doppler spectrum is equal to:

$$S(v) = \frac{\lambda^4}{\pi^5 |K_w|^2} \int_v^{v+\Delta v} v \sigma_h^b(v) dv \quad (1.45)$$

where  $\sigma_h^b(v)$  is the average horizontal backscattering coefficient of all scatterers having a radial velocity component equal to  $v$ .

The *average radial velocity* is simply the first moment of the normalized (divided by the total reflectivity) Doppler spectrum and the *spectral width* the square root of its second moment.

### 1.2.4 Quantitative precipitation estimation

Radar observables are well suited for quantitative precipitation estimation (QPE). The rain intensity  $R$  in  $\text{mm h}^{-1}$  can be related to  $Z_H$ ,  $Z_{DR}$  and  $K_{dp}$ . Most often, the rain intensity is simply related to the horizontal reflectivity by a power law:

$$R = a Z_H^b \quad (1.46)$$

where parameters  $a$  and  $b$  are chosen based on the parameters of the drop size distribution (DSD) obtained by disdrometers or by comparison with rain gauges measurements.

A wide range of  $Z - R$  relationships have been used in the literature, depending on the phase of precipitation (solid/liquid), the type of precipitation (stratiform/convective) and the climatology. A commonly used  $Z - R$  relationship is  $a = 200$ ,  $b = 1.6$  (Marshall et al., 1955), which is derived from the exponential Marshall-Palmer DSD model (Marshall and Palmer, 1948) and is valid for mid-latitude stratiform rainfall.

Several more sophisticated empirical methods have been proposed, that take advantage of the polarimetry. For example in the S-band, Ryzhkov et al. (2005) proposed a mixed approach combining the information from  $Z_H$ ,  $Z_{DR}$  and  $K_{dp}$ . In this method,  $Z_H$  is used only for weak precipitation intensity and  $K_{dp}$  only for strong precipitation intensities, where attenuation makes  $Z_H$  dubious.

### 1.3 Thesis outline

The main objective of this thesis is to develop new tools to evaluate numerical weather simulations using radar observations. Three broad topics, which correspond to three different ways to compare model and radar data, will be covered.

One way of comparison is to identify features on radar data that can be directly related to model variables. Hence, in the first part of this thesis, the polarimetric radar data will be used to retrieve the altitude and extent of the melting layer, an important feature of stratiform precipitation, which can be used to identify the height of the 0°C isotherm.

Another, more classical, method of comparison is to compare simulated precipitation with precipitation estimated from radar reflectivities. The second part of this thesis proposes a novel approach to this long-standing topic with the help of the multifractal framework, which allows a multi-scale characterization over a large range of scales.

An even more sophisticated approach is to simulate radar variables from model outputs, which can then be directly compared to observed radar data. Therefore, the third part of this thesis presents a forward radar operator able to simulate polarimetric radar observables from outputs of the COSMO NWP model. In the design of this operator, the knowledge gained in the two previous parts about the radar signature of precipitation will be crucial. This operator is carefully evaluated with radar data from various instruments and a sensitivity analysis of its main assumptions is performed.

This thesis is structured as follows: Chapter 2 is devoted to designing an automatic melting layer detection algorithm and providing an in-depth characterization of the polarimetric signature within the melting layer. Most existing melting layer detection techniques do not take advantage of the high vertical resolution offered by RHI scans and are quite rudimentary. A new method is thus proposed, in which the lower and upper boundaries of the melting layer are identified thanks to their strong vertical gradients in  $Z_H$  and  $\rho_{hv}$ . The capacity of the algorithm to separate high fall velocities in the liquid phase from small velocities in the solid phase is investigated. The proposed method is also validated with radio sounding measurements, offering a much better agreement than alternative methods. Finally, a detailed characterization of the melting layer in several climatological conditions is proposed, which shows that the distribution in thicknesses and the average polarimetric signature of the melting layer are rather climate-independent.

Chapter 3 focuses on the evaluation of the precipitation intensities simulated by the COSMO model with the universal multifractals framework. This framework allows to characterize a complex geophysical field over multiple scales with only a limited number of parameters. At first, a climatological study of five years of simulated precipitation at hourly resolution is performed. The relationship between multifractal parameters and meteorological and topographical descriptors is investigated, and it appears that the multifractal signature of rainfall differs significantly from one climatological region to the other. At second, a more

## Chapter 1. Introduction

---

local analysis is performed in which the precipitation intensities simulated by COSMO during three events, corresponding to typical synoptical situations over Switzerland, are compared with the Swiss QPE product, in terms of their multifractal parameters. It is shown that the COSMO simulations exhibit spatial scaling breaks that are not present in the radar data.

Chapter 4 presents the polarimetric radar operator and its evaluation. The implementation of the radar operator is described in details, from the propagation of the radar beam to the final estimation of the polarimetric variables and the Doppler spectrum. A special emphasis is put on three novel aspects: (1) a very efficient and simple method to simulate the full Doppler spectrum, (2) a local parameterization of solid hydrometeor properties with the help of a multi-angle snowflake camera and (3) a new diagnostic parameterization of the melting layer. The radar operator is then carefully evaluated both qualitatively and quantitatively. The qualitative evaluation focuses on a visual comparison with radar observations for a selection of events. The quantitative evaluation focuses on the comparison of the distributions of simulated polarimetric variables with real radar data. using large datasets from an X-band research radar, from the Swiss operational C-band radar network and from the spaceborne GPM-DPR.

Chapter 5 extends Chapter 4 with a sensitivity analysis of the main parameters and assumptions used in the radar operator. Here again the radar data is used as a reference. In the liquid phase, the effect of drop geometry and DSD model is tested, while in the solid phase, the simple T-matrix model is compared with two more sophisticated scattering estimation methods, one based on MASC observations, the other based on the discrete dipole approximation (DDA) and generalized multi-Mie method (GMM). It is shown that, in the liquid phase, the shape of the DSD considered by COSMO has a strong influence on the simulated polarimetric variables. A simple alternative DSD model is proposed that gives a significantly better match with observed radar variables. In the solid phase, T-matrix based methods tend to underestimate  $Z_H$ , especially at higher frequencies (Ka band). The DDA/GMM based methods tend to produce more realistic reflectivities, especially at higher frequency, but overestimate  $Z_{DR}$  and  $K_{dp}$ . Finally, Chapter 6 concludes this thesis and opens perspectives for future work.

## **2 Detection and characterization of the melting layer of precipitation**

This chapter is adapted from the following article:

1. Wolfensberger, D., Scipion, D. and Berne, A. (2016), Detection and characterization of the melting layer based on polarimetric radar scans. *Q.J.R. Meteorol. Soc.*, 142: 108–124. doi:10.1002/qj.2672

It presents a novel method for the automatic detection of the melting layer on RHI scans, as well as a characterization of the melting layer in different climatological regions.

### 2.1 Summary

Stratiform rain situations are often associated with the presence of a melting layer characterized by a strong signature in polarimetric radar variables. This layer is an important feature as it indicates the transition from solid to liquid precipitation. The melting layer remains poorly characterized, particularly from a polarimetric radar point of view. In this work a new algorithm to automatically detect the melting layer on polarimetric RHI radar scans using gradients of reflectivity and copolar correlation is proposed. The algorithm was applied to X-band polarimetric radar data and validated by comparing the height of the detected layer with freezing levels heights obtained from radio soundings and was shown to give both small errors and bias. The algorithm was used on a large selection of precipitation events (more than 4000 RHI scans) from different seasons and climatological regions (South of France, Swiss Alps and plains and Iowa-USA) to characterize the geometric and polarimetric signatures of the melting layer. The melting layer is shown to have a very similar geometry on average, independently of the topographical and climatological conditions. Variations in the thickness of the melting layer during and between precipitation events are shown to be strongly related to the presence of rimed particles, the vertical velocity of hydrometeors and the intensity of the bright band.

## 2.2 Introduction

The melting layer (ML) is an important feature of stratiform precipitation, associated with the melting of snowflakes and ice crystals below the freezing level, that can be seen on precipitation radar scans as a thin, nearly horizontal layer with a high reflectivity factor. This feature is known as the bright band (BB). The main cause of the BB effect is the fast increase in the dielectric constant of particles during the melting process, caused by the transition of the total water fraction within the ice-water mixture (Matrosov, 2008). The ML provides useful information about the vertical structure of precipitation since the base of the ML gives an indication of the vertical extent of liquid precipitation and the top of the ML is close to the altitude of the 0 °C isotherm. The detection of the ML has been a long-standing topic of interest for radar meteorologists, mainly for quantitative precipitation estimation (QPE), because mixed-phase hydrometeors may contaminate rainfall estimates at longer distances (Giangrande et al., 2008). Moreover, the detection of the ML makes it possible to separate liquid from solid precipitation, which is critical information for hydrometeor classification algorithms. Finally, the ML is characterized by an important attenuation effect at X-band and higher frequencies. Measurements at X-band by Bellon et al. (1997) showed that the attenuation effect of the ML could be 3 to 5 times larger than the one caused by the rain below.

On modern radars equipped with dual polarimetry, the ML is characterized by a very distinct polarimetric signature (Figure 2.1). Besides the presence of large values of  $Z_H$  due to the BB effect, one notable characteristic of the ML on polarimetric scans is the presence of distinctly smaller values of the copolar cross-correlation coefficient  $\rho_{hv}$ . Indeed,  $\rho_{hv}$  depends on the homogeneity in shape of the hydrometeors and is significantly lower in the ML where phases are mixed, than in stratiform rain or in solid precipitation (e.g. Matrosov et al. 2007). One should keep in mind that low values of  $\rho_{hv}$  can also be caused by non-meteorological echoes (e.g. insects, birds, aircraft). Additionally, the melting layer is also characterized by higher differential reflectivities  $ZDR$ , due to the transition between the solid phase, where  $ZDR$  is usually small (Doviak and Zrnić, 2006), and the liquid phase, where it is higher. To summarize, on polarimetric RHI scans, the ML is characterized by the combination of a layer of small  $\rho_{hv}$  values, a transition from high to low  $ZDR$ , and the presence of high values in  $Z_H$ .

Several operational algorithms for automatic detection of the ML on PPI scans have been proposed in the literature. Sánchez-Diezma et al. (2000) proposed an algorithm for BB detection from conventional operational radar scans based on the peak of reflectivity as well as the gradients of reflectivity between the BB and the liquid and solid phases. For polarimetric radars, Giangrande et al. (2008) proposed an algorithm for automatic ML detection in PPI scans, which searches for all range bins with low  $\rho_{hv}$  and classifies them as ML bins if the maxima of  $Z_H$  and  $ZDR$  fall within a specified range. Matrosov et al. (2007) proposed a simpler approach, again in PPI where the boundaries of the ML are detected using only  $\rho_{hv}$ , a method also used by Kalogiros et al. (2013). The ML can also be detected by using Doppler velocities. White et al. (2002) proposed a method using a wind profiler, which relies on the detection of the peak in reflectivity and zones where the gradient of reflectivity is negatively correlated

## Chapter 2. Detection and characterization of the melting layer of precipitation

---

with the vertical Doppler velocity. Few ML detection methods exist for RHI scans. Bandera et al. (1998) designed an algorithm that detects the ML based on the identification of strong vertical gradients in ZH and in the linear depolarization ratio (LDR), and assumes higher heterogeneity of radar variables within the ML.

Apart from its radar signature, the ML is also an important process as such. Some studies focused on the seasonal and geographical variability of the height of the ML. For example, Das et al. (1993) measured the variability of the ML height during 3 years in two different climatological regions of India. Although very common, the ML is still a relatively poorly known phenomenon and limited work has been done to date to study its scattering and geometric signatures. Fabry and Zawadzki (1995) analyzed vertical Doppler X-band radar and wind profiler data to quantitatively characterize the structure of the radar signature from melting precipitation. They suggested that the main cause of the BB were shape and density effects, as well as the change in the refractive index of hydrometeors during melting. Zawadzki et al. (2005) developed a model for the melting snow and its radar reflectivity. A relationship between a large increase in velocity through the ML and a small reflectivity difference between the BB and the rain below was derived from the model and confirmed with vertically pointing radar observations. Durden et al. (1997) studied scans from a polarimetric airborne radar operated in the context of the TOGA COARE experiment over the Pacific ocean near New Guinea. The authors found some relation between the BB intensity and the distance between the maximum of reflectivity and the freezing level, which they explained by the latent cooling effect of melting. Additionally, they found a positive correlation between the BB intensity with both  $\rho_{hV}$  and the vertical fall velocity within the ML.

These studies generally focused on one specific region and as such they might not be representative of the general characteristics of the ML. As an example, in tropical regions, the seasonal variations in thickness and altitude of the ML are expected to be weaker than at higher latitudes. Previous studies can also be complemented with the use of a hydrometeor classification scheme to gain a deeper understanding of the main factors that contribute to the ML variability.

Taking advantage of the strong polarimetric gradients at the ML boundaries, we propose a new algorithm for automatic ML detection on RHI polarimetric scans that is able to detect the height of boundaries of the ML all along the RHI. This algorithm is used to provide a more complete characterization and analysis of the structure and the polarimetric signature of the ML by using large datasets of polarimetric radar observations from different climatological regions (South of France, Western Switzerland, Swiss Alps and Iowa-USA). This study is completed with an in-depth analysis of the relationship between different characteristics of the ML.

This chapter is structured as follows: in Section 2.3 the instruments and the datasets are described as well as all pre-processing operations transforming polar radar data into inputs to the ML detection algorithm. The algorithm is explained in detail in Section 3 and is validated



in Section 4. Results of the characterization of the ML are given in Section 5, which is divided into four parts focusing respectively on the attenuation effect, the vertical structure, the polarimetric signature and the geometry of the ML. These results are discussed in more details in Section 6, which focuses on the relationship between ML descriptors, with an emphasis on the ML thickness. Finally, Section 7 gives a summary of the main results and concludes this work.

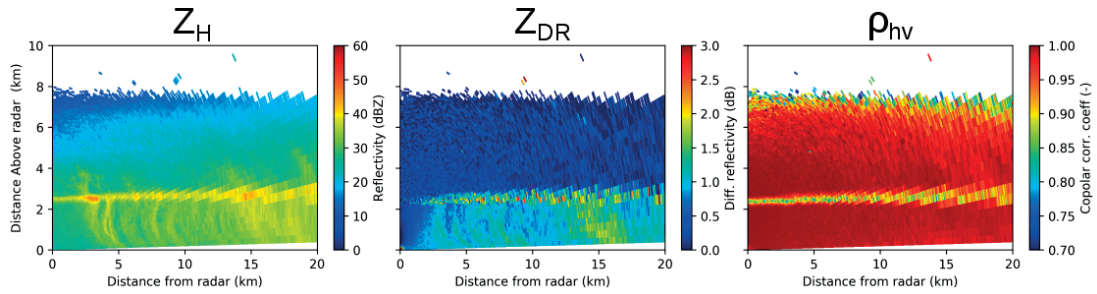


Figure 2.1 – Example of the ML signature in  $Z_H$ ,  $Z_{DR}$  and  $\rho_{hv}$  in a typical stratiform rain situation collected in the south of France (29.09.2012 12:24).

## 2.3 Data and processing

### 2.3.1 Instruments

The radar measurements used in this work come from the EPFL-LTE X-band polarimetric radar, called MXPoL, as well as from a nearly identical radar system operated in the context of the NASA IFloodS (Iowa Flood Studies) program (Domaszczyński, 2012). Information about the characteristics of the polarimetric radar as well as its scanning strategy are given in Table 2.1.

Frequency	9.4 GHz
Range	40 km
3dB beamwidth	1.45°
Rad. Resolution	75 m
Polarization	Simultaneous H-V
Scanning sequence	PPIs at different elevations, 2 RHIs and a vertical PPI (for $Z_{DR}$ calibration)
Scanning mode	Interleaved pulse pair mode (PPI), Full Doppler Spectrum (RHI and vert. PPI)

Table 2.1 – MXPoL properties and scanning strategy

## Chapter 2. Detection and characterization of the melting layer of precipitation

---

For validation, data from the Swiss operational radio soundings are used. These soundings are performed twice daily (0 and 12 UTC) from Payerne in western Switzerland and include measurements of temperature, pressure and relative humidity, recorded every second. This corresponds to a vertical resolution of 5 to 10 meters depending on the ascending velocity of the radiosonde.

### 2.3.2 Datasets

Since 2009, MXPoI recorded a large amount of high resolution polarimetric data during several measurement campaigns. In this work four datasets from different topographical and climatological regions are used; they are described in Table 2.2 and their respective locations are illustrated in Figure 2.2.

An interesting aspect is the high climatological diversity of the available data. The Ardèche region is characterized by a Mediterranean climate according to Köppen's climate classification (Peel et al., 2007). This climate is associated with warm summers and occasionally strong convective showers. Heavy precipitation events caused by the orographic updraft of wet air coming from the sea occur frequently in Autumn. An overview of the climate of the Ardèche region and of the HyMeX (Hydrological Cycle in the Mediterranean experiment) program is given in Drobinski et al. (2013) and Ducrocq et al. (2014).

The region around Davos, in the Swiss Alps has a subarctic climate (Peel et al., 2007), with long and cold winters and mild summers. Precipitation occurs mostly in summer and early autumn due to orographic lifting and convection.

Iowa is part of the Midwestern United States and is characterized by a humid continental climate (Peel et al., 2007) with marked seasonal variations. Summers are very warm and wet and are often associated with strong convection, which can lead to the formation of supercells and tornados.

Finally, the last dataset was recorded in Western Switzerland near the town of Payerne where the largest Swiss meteorological station is located. The radar set-up took place in the context of the PARADISO programme (PAYERne RADar and ISOtopes) which aims to study the segregation of isotopes in precipitation using combined sensors (disdrometers, radars, profilers). Compared with the Davos region, the Payerne region corresponds to a more oceanic climate (Peel et al., 2007) typical of western Europe with limited seasonal temperature variability, and milder winters. Precipitation occurs all over the year with a maximum in late summer and autumn.

## 2.3. Data and processing



Figure 2.2 – Location and pictures of the four radar sites

Site	Season	Context	Altitude	Coords.	Topography	Scans
<b>Ardèche</b> (South of France)	Fall 2012, Fall 2013	Data collected during the SOP1 (special observation period) and SOP2 of the HyMeX program (Hydrological Cycle in the Mediterranean experiment).	605 m a.s.l.	4.55°E 44.61°N	Small hills and riverbeds, between 400 and 800 m a.s.l	1763 RHI with ML
<b>Davos</b> (Swiss Alps)	Spring 2010 to summer 2011	Data collected in Davos, eastern Switzerland at high altitude to study mixed phase and solid precipitation.	2133 m a.s.l	9.84°E 46.79°N	Complex terrain, crossing of two valleys, altitudes between 1500 and 3000 m a.s.l	816 RHI with ML
<b>Iowa</b> (Mid-western United States)	Spring 2014	Data collected during the IFloodS NASA campaign (Assess the capability of flood forecasting by using satellite precipitation data).	379 m a.s.l	91.86°W 43.18°N	Very smooth and flat terrain with altitudes between 200 and 400 meters m a.s.l	380 RHI with ML
<b>Payerne</b> (Swiss Plateau)	Spring 2014	Data recorded during the PARADISO campaign (Payerne Radar and Isotopes), which aims at studying the segregation of isotopes in precipitation.	500 m a.s.l	6.94°E 46.81°N	Flat plateau in between the Jura and Alps mountain ranges with altitude between 450 and 700 m a.s.l	507 RHI with ML

Table 2.2 – Description of the available RHI scans datasets

### 2.3.3 Pre-processing of radar data

#### 2.3.3.1 Radar variables and projections

In the context of this work, five polarimetric variables are used: the reflectivity factor at horizontal polarization  $Z_H$  [dBZ], the unitless copolar correlation coefficient  $\rho_{hv}$ , the differential reflectivity  $Z_{DR}$  [dB], the specific differential phase shift on propagation  $K_{dp}$  [ $^{\circ}\text{km}^{-1}$ ], and the radial velocity  $v_{rad}$  [ $\text{m s}^{-1}$ ]. Only RHI scans are used, meaning that all variables are originally in

## Chapter 2. Detection and characterization of the melting layer of precipitation

---

polar range-elevation coordinates. Only measurements at a range shorter than five kilometres are used, in order to limit the effect of beam-broadening, and to consider only data with the highest signal to noise ratio. The choice of 5 km range can be justified by the fact that, at this distance, the diameter of the radar bin is approximately one third of the average ML thickness, which should still allow resolution of the ML with sufficient accuracy. The proposed approach should remain valid at longer ranges, but will suffer from beam broadening.

$K_{dp}$  is estimated from the total differential phase shift  $\Psi_{dp}$  [°] using a method based on Kalman filtering (Grazioli et al., 2014a; Schneebeli and Berne, 2012). This approach is designed to ensure the independence between  $K_{dp}$  estimates and other polarimetric variables, and to capture the fine scale variations of  $K_{dp}$ . Since this estimation of  $K_{dp}$  does not depend on  $Z_H$ , it remains unaffected by the strong effect of the ML on  $Z_H$ . All polarimetric variables are censored with a mask of signal-to-noise ratio of 8 dB. Measurements at very low elevation angles ( $0 - 2^\circ$ ) are removed in order to avoid possible interferences from ground echoes.  $Z_{DR}$  measurements at high elevation angles ( $45^\circ - 90^\circ$ ) are discarded, as they are strongly biased by the high angle of incidence of the radar beam.

The ML detection algorithm takes  $Z_H$  and  $\rho_{hv}$  projected onto a two-dimensional Cartesian grid as input. Projection from polar to Cartesian coordinates is done by simply assigning the value of the nearest radar bin to every cell of the Cartesian grid. If several radar bins fall into one Cartesian grid cell they are averaged (in linear values). In the context of this work, a small cell size of  $25 \times 25 \text{ m}^2$  is used to account for the higher density of radar bins at short range. This cell size has been chosen as a compromise between calculation time and accuracy of the Polar to Cartesian projection. Tests showed that changing the interpolation grid size between 25 and 75 m does not bias the results presented in Section 2.6.

### 2.3.3.2 Attenuation correction

In the liquid phase, the attenuation correction for  $Z_H$  and  $Z_{DR}$  is directly calculated in polar data according to Testud et al. (2000), using the relations linking  $K_{dp}$ ,  $Z_H$ , the specific horizontal attenuation  $A_H$  ( $\text{dB km}^{-1}$ ), and the specific differential attenuation  $A_{DR}$  ( $\text{dB km}^{-1}$ ). The power laws linking the variables were obtained using simulated realistic drop-size distribution fields (Schleiss et al., 2012). Since the attenuation properties in the melting layer are not known precisely, the attenuation correction is calculated only in the liquid phase and the correction is simply propagated further above, using the ML detection algorithm (Section 2.4) as reference to detect the base of the ML. Neglecting the attenuation in the solid phase should be acceptable since it is usually much smaller than in the liquid phase (Doviak and Zrnić, 2006). The situation is quite different in the ML where significant attenuation may occur (Bellon et al., 1997). More information about the ML attenuation effect is provided in Section

### 2.3.3.3 Hydrometeor classification

In order to gain a better understanding of the ML signature, a hydrometeor classification is performed in the solid phase above the detected ML using the classification algorithm of Grazioli et al. (2014b). This algorithm takes  $Z_H$ ,  $Z_{DR}$ ,  $\rho_{hv}$  and  $K_{dp}$  as well as an estimation of the freezing-level height as input and classifies every pixel into one of seven classes, light rain (LR), rain (R), heavy rain (HR), melting snow (MS), ice crystals/small aggregates (CR), aggregates (AG) and rimed particles (RI). In the context of this study, the height of the top of the detected ML is used as an estimation of the freezing-level height.

A flowchart summarizing all the pre-processing steps is shown in Figure 2.3.

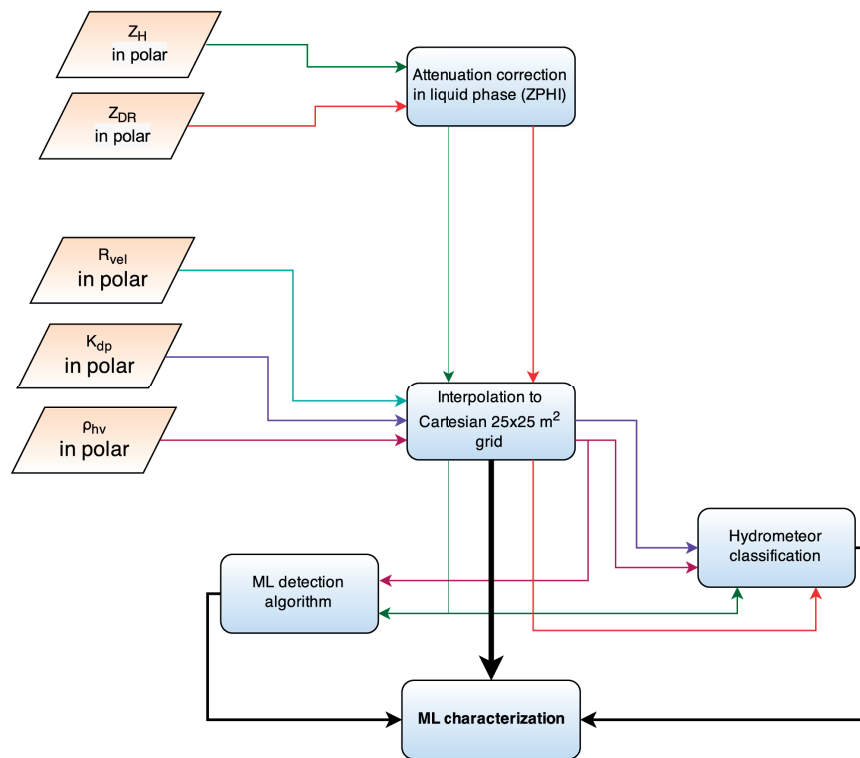


Figure 2.3 – Flowchart of the preprocessing steps

## 2.4 Automatic detection of the ML

### 2.4.1 Description of the algorithm

Instead of simply adapting an algorithm designed for PPI scans, a new algorithm was designed that works directly in RHI scans by taking advantage of the fact that vertical gradients in  $\rho_{hv}$  and  $Z_H$  are usually large and well defined.  $Z_{DR}$  is not used in the current algorithm because it is ill-defined at high elevation angles and because no improvement was observed when adding  $Z_{DR}$  as a third input variable.

## Chapter 2. Detection and characterization of the melting layer of precipitation

---

The main advantage of this algorithm is that it estimates the ML boundaries all along the vertical profile at a high resolution. As the main motivation of the present work is the characterization of the ML, we only consider radar data at short range (5 km max), in order to have reliable high-resolution observations not affected by beam broadening.

The algorithm is divided in two parts. First, an initial estimation of the ML is obtained by using both  $Z_H$  and  $\rho_{hv}$  and by assuming that the ML is a more or less horizontal structure. This first part of the algorithm is similar to Bandera et al. (1998), the main difference being the use of  $\rho_{hv}$  instead of LDR.

This initial estimation, which corresponds mostly to the layer of low  $\rho_{hv}$ , can sometimes underestimate the extent of the ML. Indeed,  $Z_H$  starts to increase when the ice crystals start to melt, i.e. when they are still large but contain a significant amount of liquid water; however  $\rho_{hv}$  decreases significantly only when the mixture between ice crystals and drops is already quite heterogeneous. This happens at a lower altitude, when sufficient melting has already occurred. Generally the distance between the maximum in  $Z_H$  and the minimum in  $\rho_{hv}$  increases with the concentration of hydrometeors (e.g. Giangrande et al. (2008)). In the case of intense precipitation, the top of the ML may thus be above the layer of lower values of  $\rho_{hv}$ . The second part of the algorithm aims to alleviate this effect: the top of the ML is estimated using the same procedure but with gradients in  $Z_H$  only.

All steps of the algorithm are explained in details below. Justification for the chosen values for parameters of the algorithm will be given in Section 2.4.3.

### Part 1: initial estimation

1.  $Z_H$  and  $\rho_{hv}$  are normalized:  $[10, 60]$  dBZ  $\rightarrow [0, 1]$  for  $Z_H$  and  $[0.65, 1] \rightarrow [0, 1]$  for  $\rho_{hv}$ , in order to give a similar weight to both variables. These boundaries correspond to the range of values expected in precipitation. Experiments showed that changing this range slightly, e.g. using  $[0, 60]$  instead of  $[10, 60]$ , does not change the output of the algorithm.
2. The normalized variables are then combined into a single image:

$$IM_{\text{comb}} = Z_H \cdot (1 - \rho_{hv})$$

Note that since the ML is characterized by high values of reflectivity and small values of  $\rho_{hv}$ , the complement of  $\rho_{hv}$  is used in the product.

3. The vertical gradient of the image is computed using a classical vertical Sobel filter<sup>1</sup>:

$$h_{\text{Sobel}} = \begin{bmatrix} -1 & -2 & -1 \\ 0 & 0 & 0 \\ 1 & 2 & 1 \end{bmatrix}$$

To decrease the noise, the image is filtered with a moving average of length  $L_{\text{filt, grad}}$  (in practice a length of 75 m is used, which corresponds to 75 m x 75 m, i.e. a window of 3 x 3 pixels).

4. The gradient image is thresholded. All pixels with absolute value exceeding  $T_{\text{grad, min}}$  (set to 0.02) are kept, whereas all others are set to 0. This step is done in order to detect only gradient extremes that are strong enough to correspond to a potential ML edge.
5. The image is scanned column by column (i.e. a vertical profile). The minimum and maximum of the vertical gradient are detected for each column. The lower edge of the ML is associated with the maximum and the upper edge with the minimum.
6. The median height of the upper boundary of the ML in meters ( $\text{Med}_{\text{ML,bot}}$ ) and the median height of the lower boundary of the ML in meters ( $\text{Med}_{\text{ML,top}}$ ) are computed at the end of this step.
7. Step 5 is run again but this time after discarding the gradient image above  $(1 + f_{\text{ML,height}}) \cdot \text{Med}_{\text{ML,top}}$  and below  $(1 - f_{\text{ML,height}}) \cdot \text{Med}_{\text{ML,bot}}$ , assuming the ML is a relatively flat structure. This helps to remove the possible contamination by ground echoes or small embedded cells of intense rainfall. The chosen value for  $f_{\text{ML,height}}$  is 0.3.

### Part 2: correction of the ML top

8. The vertical gradient is calculated as in Step 3, but on the normalized  $Z_H$  image only. Note that there is no thresholding this time.
9. For every vertical column the gradient image is cut below the top of the ML calculated in Part 1 (Figure 2.4, point 2) and above the first local maximum in the gradient in the solid phase (Figure 2.4, point 4).
10. Using this new gradient image, the top of the ML is detected again as in Steps 5 to 7 of Part 1.
11. (Optional): small gaps in the ML are filled if their size is smaller than 250 m (see Section 2.4.3). Interpolation is done separately on the lower and upper boundaries of the ML using shape-preserving piecewise Hermite interpolation polynomials (“pchip” in Matlab).

<sup>1</sup>Compared with a simple 1D finite difference, the Sobel operator is less sensitive to isolated high intensity point variations thanks to the local horizontal averaging over sets of three pixels (Wenshuo et al., 2010).

## Chapter 2. Detection and characterization of the melting layer of precipitation

An illustration of the behaviour of the gradient of  $Z_H$ ,  $\rho_{hv}$  and  $Z_H \cdot (1 - \rho_{hv})$  along a vertical profile is given in Figure 2.4. Point 1 corresponds to a positive peak in the gradient of  $Z_H \cdot (1 - \rho_{hv})$  and is associated with the bottom of the ML. Point 2 corresponds to a negative peak in the gradient of  $Z_H \cdot (1 - \rho_{hv})$  and a positive peak in the  $\rho_{hv}$  gradient. It marks the upper edge of the layer of low  $\rho_{hv}$  values. Points 1 and 2 are detected at the end of the first part of the algorithm (step 7). Point 3 corresponds to a negative peak in the  $Z_H$  gradient, which marks the upper bound of the BB and is closer to the real height of the freezing level. This point is considered as the top of the ML and is detected at the end of the second part of the algorithm (step 10).

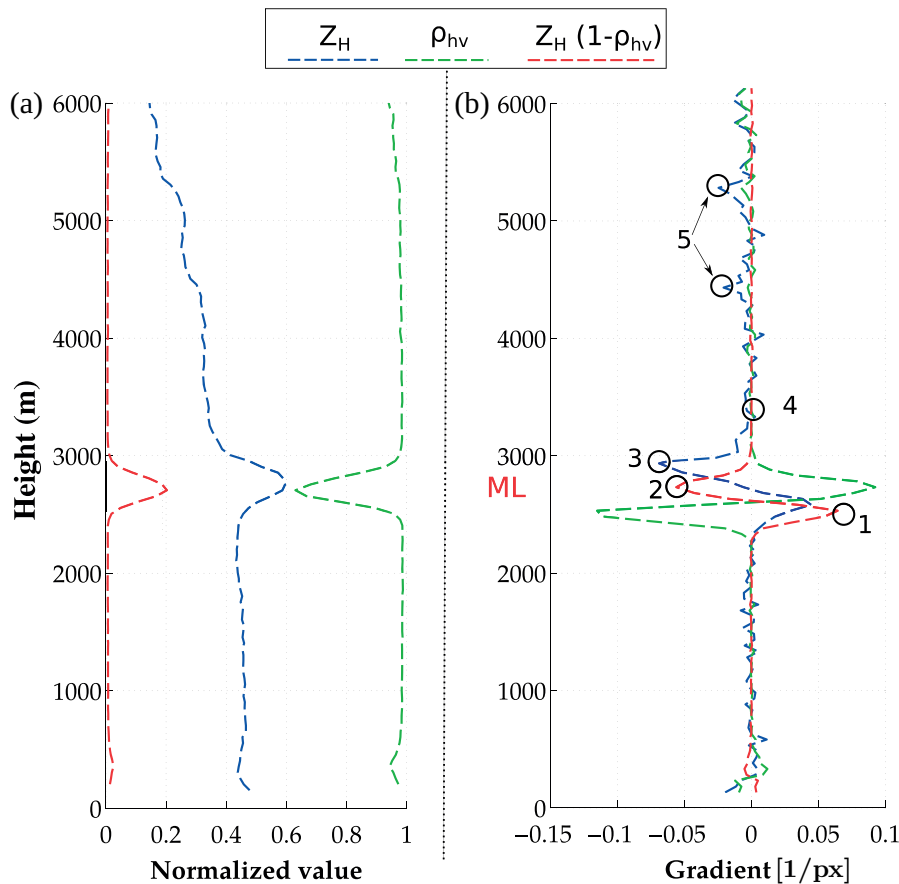


Figure 2.4 – Gradients of  $Z_H$  and  $\rho_{hv}$  at the boundaries of the ML. Note that in the units of the vertical gradient, a pixel corresponds to  $25 \times 25 \text{ m}^2$  (Section 2.3.3.1).

The gradient of  $Z_H$  is generally low in the solid phase and oscillates around zero, while it is highly variable in the liquid phase. The gradient of  $\rho_{hv}$  is mostly 0 in the liquid and solid phases. Points 4 and 5 illustrate why the gradient is cut above the first local maximum in step 9 of the algorithm; it can happen that, when a layer of higher  $Z_H$  is present in the solid phase (in case of riming for example), the gradient decreases again to reach a secondary minimum as in the points 5. Clearly these values do not correspond to the ML top and may in some very rare cases be even stronger than the  $Z_H$  gradient signature of the ML top. To alleviate this



effect, the search for the minimum is stopped as soon as a first local maximum (point 4) is encountered.

Figure 2.5 presents a flow chart of the proposed algorithm. In summary,  $Z_H$  and  $\rho_{hv}$  are first normalized and combined. The vertical gradient of the combined image is then calculated and thresholded. In a first approximation, the upper and lower boundaries of the ML are identified by the minimum and the maximum of the vertical gradient. This first approximation is then refined by detecting again the upper boundary based on the gradient of  $Z_H$  only.

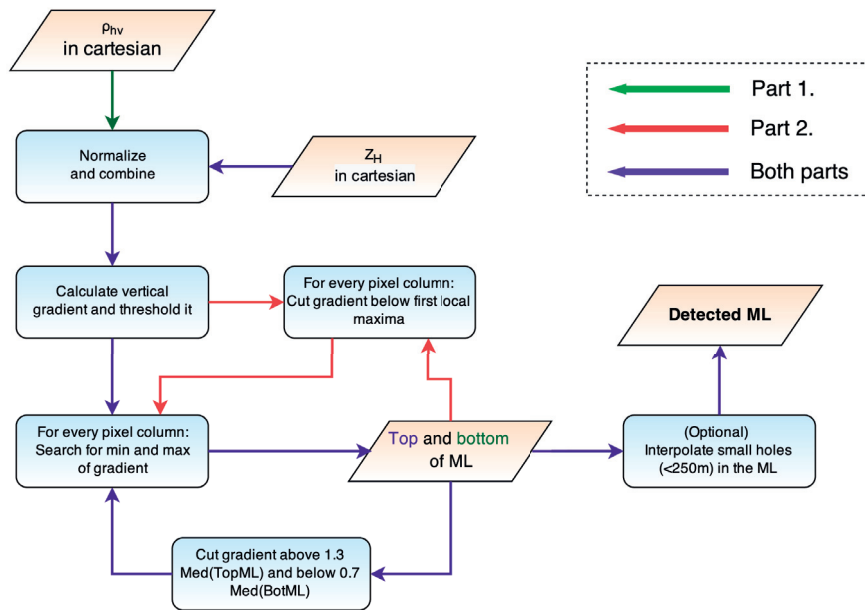


Figure 2.5 – Flow diagram of the ML detection algorithm.

### 2.4.2 Outputs

Two examples of ML detection during stratiform situations of different intensities are shown in Figure 2.6. The bottom of the detected ML matches well the sharp transition to smaller values of  $\rho_{hv}$  inside the ML, and the top of the ML corresponds well with the top of the BB. The second case shows that the algorithm also has a good sensitivity because even a weak ML can be detected. Small-scale fluctuations of the ML are also accurately detected.

Thanks to the algorithm, it is possible to estimate the distribution of polarimetric variables in the liquid phase (below the ML) and the solid phase (above). The distribution of  $\rho_{hv}$  over all datasets (Figure 2.7) shows that  $\rho_{hv}$  within the detected ML is much lower than within the liquid and solid phases, which indicates that the detected ML corresponds to a region of much larger hydrometeor variability, consistent with the presence of melting. A more quantitative analysis and evaluation of the algorithm is provided in section 2.6.

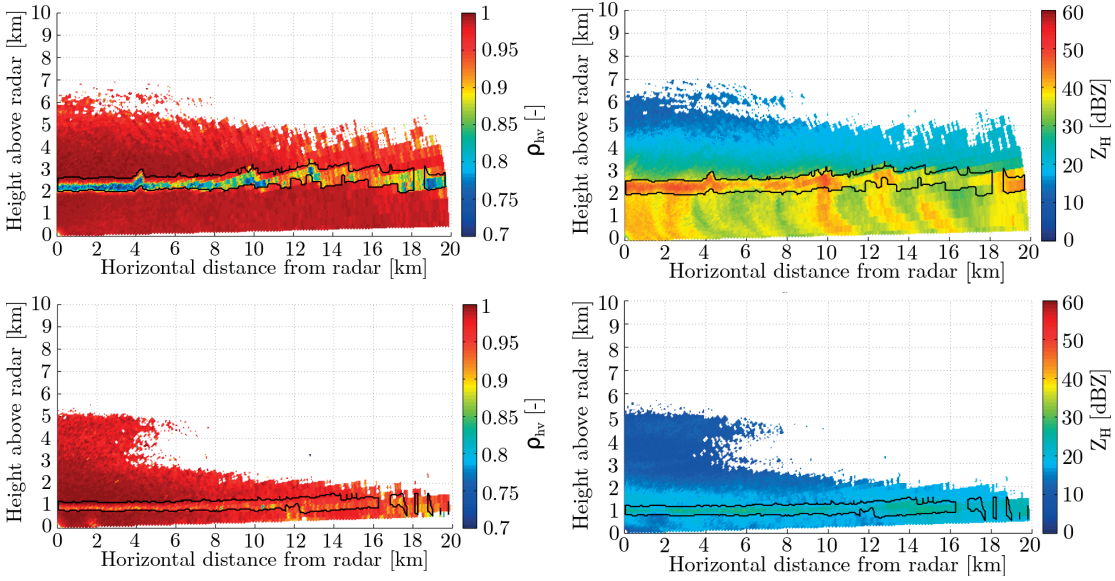


Figure 2.6 – Two examples of ML detection overlaid on  $\rho_{hv}$  (left) and  $Z_H$  (right).

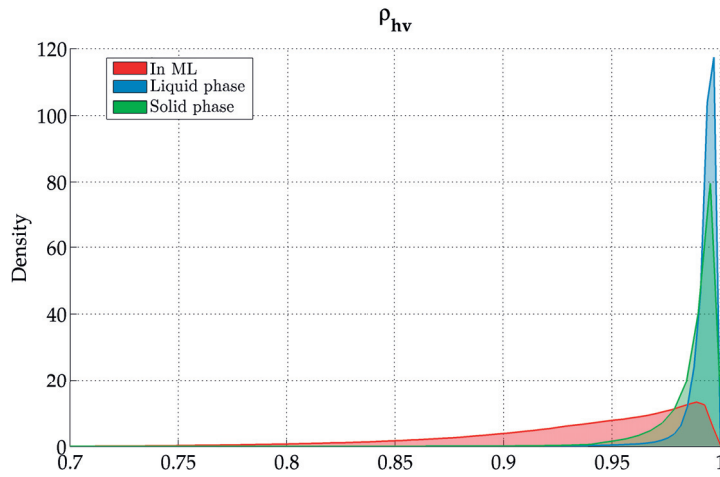


Figure 2.7 – Distributions of  $\rho_{hv}$  in the liquid and solid phases as well as in the identified ML.

### 2.4.3 Algorithm parameters

The algorithm relies on four independent parameters which are given in Table 2.3. The recommended values were first chosen empirically and then verified based on sensitivity and statistical analysis, in order to assess the potential associated uncertainty.

The first parameter of importance is  $T_{grad, min}$ , the threshold on gradient magnitude. The value of 0.02 was chosen by visual inspection as it was found that values of this magnitude are very rarely observed in situations without a ML. It is meant to avoid considering edges of too low intensity. It was observed that this constraint does not negatively affect the detection, even for relatively weak ML situations. Increasing the threshold will lead to fewer pixels being detected

Parameter	Meaning	Value	Unit
$L_{\text{filt, grad}}$	Size of moving average filter for gradient smoothing	75	m
$T_{\text{grad, min}}$	Threshold on gradient magnitude	0.02	-
$f_{\text{ML,height}}$	Maximum allowable relative fluctuation of ML top and bottom	0.3	-
$L_{\text{gaps, max}}$	Max length of gaps in the ML to be interpolated	250	m

Table 2.3 – Algorithm parameters and recommended values

and to gaps in the detected ML, but reduces the risk of erroneous detection. However, the output of the algorithm is not very sensitive to small variations of this parameter because gradients caused by the ML are many orders of magnitude larger than gradients below or above the ML. To verify this, the algorithm was run on all RHI scans (from all datasets) using values of  $T_{\text{grad, min}}$  ranging from 0.005 to 0.035. For every threshold value, an agreement score with the reference ( $T_{\text{grad, min}} = 0.02$ ) was calculated:

$$\text{Score}(k) = 2 \frac{\sum_{i=0}^N \sum_{j=0}^M \left( ML_{T_{\text{grad, min}}=k}^{i,j} \times ML_{T_{\text{grad, min}}=0.02}^{i,j} \right)}{\sum_{i=0}^N \sum_{j=0}^M \left( ML_{T_{\text{grad, min}}=k}^{i,j} + ML_{T_{\text{grad, min}}=0.02}^{i,j} \right)}$$

where  $N$  and  $M$  are the dimensions of the Cartesian radar scan grid and  $ML^{i,j}$  is the binary ML image:

$$ML^{i,j} = \begin{cases} 1 & \text{if pixel } i, j \in \text{melting layer} \\ 0 & \text{else} \end{cases}$$

In other words, the agreement score is twice the number of pixels that are classified as the ML for both gradient values, divided by the sum of the number of ML pixels detected for every single threshold value. A value of 1 implies a perfect agreement and 0 a total disagreement (the two MLs do not overlap at all). Figure 2.8 shows the agreement for every chosen threshold value. Generally the agreement is quite good (more than 90%), which shows that the detected MLs do not differ much.

The second parameter is the constraint on the relative height of the bottom and the top of the ML. In the algorithm, it is assumed that the bottom of the ML does not fluctuate below  $(1 - f_{\text{ML,height}}) \cdot \text{Med}_{\text{ML,bottom}}$ , and the top of the ML not above  $(1 + f_{\text{ML,height}}) \cdot \text{Med}_{\text{ML,top}}$ . The chosen value of  $f_{\text{ML,height}} = 0.3$  was first determined by visual inspection. To test its relevance,

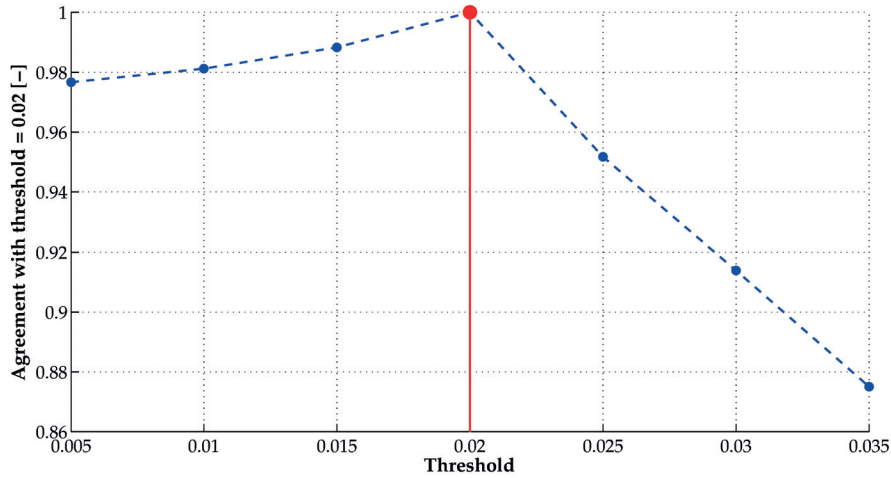


Figure 2.8 – Sensitivity of the algorithm output to variations of  $T_{\text{grad, min}}$  (gradient threshold) with respect to reference threshold (0.02), shown with a red marker.

the top and bottom relative heights of the ML were computed on all available RHI scans for a maximum distance from the radar going up to 35 km (the radar maximum range). The relative heights are defined by:

$$ML_{\text{top, rel}} = \frac{ML_{\text{top}}}{\text{Med}_{ML, \text{top}}} \quad \text{and} \quad ML_{\text{bottom, rel}} = \frac{ML_{\text{bottom}}}{\text{Med}_{ML, \text{bottom}}}$$

The distributions of the relative heights are shown in Figure 2.9. The cutting limits of 0.7 and 1.3 are displayed as red lines. The histograms are symmetrical and do not seem to be truncated near the cutting limits. The fluctuations stay generally well below the red limits, even though at 35 km range the beam broadening effect is quite important. The recommended value of 0.3 can thus be considered as appropriate and robust.

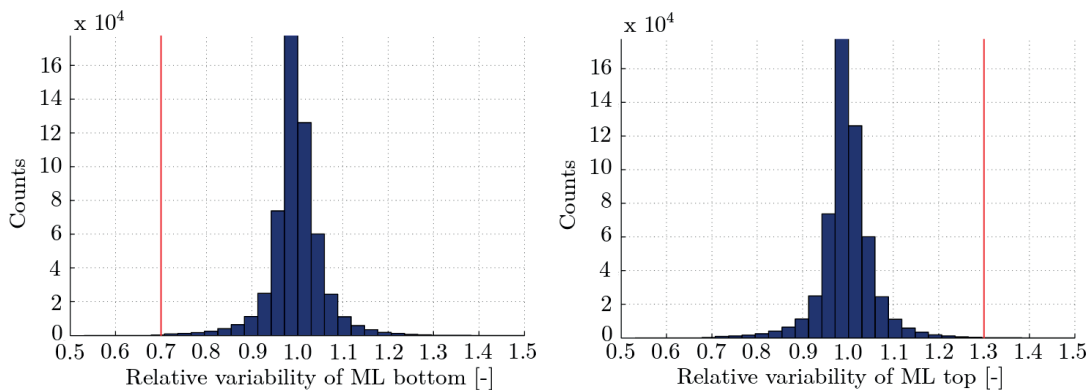


Figure 2.9 – Histogram of relative heights of the top and the bottom of the ML.

The third parameter is the maximum size of gaps that can be interpolated,  $L_{\text{gaps, max}}$ . It often happens that, on the whole scan, a couple of pixels are not detected which leads to small holes

in the detected ML. In those cases, interpolating small gaps could be considered as a valid option. In order to set a limit to the maximum size of gaps that should be interpolated, the distribution of gap sizes within the ML was computed.

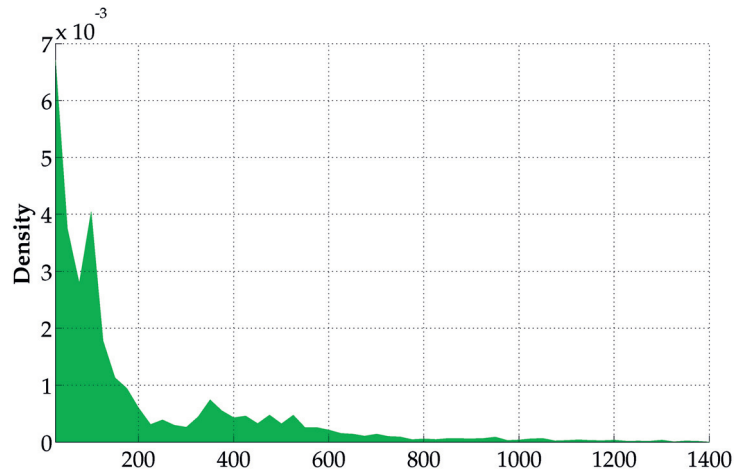


Figure 2.10 – Normalized histogram of the distribution of gap sizes in the detected MLs

It can be seen on Figure 2.10, that the vast majority of gaps are rather small ( $< 300$  m) and can thus be safely interpolated. Accordingly, the recommended value of  $L_{\text{gaps, max}}$  is 250 m.

Interpolation can be useful if the liquid and solid phases have to be discriminated, for example prior to performing a hydrometeor classification. In the context of this work, interpolation was only used in order to get an estimation as complete as possible of the freezing-level height for the hydrometeor classification, but was not used in the characterization of the ML (Section 2.6).

Finally the last parameter  $L_{\text{filt, grad}}$  is the length of the moving average filter used to smooth the gradient image, in order to compensate part of the intrinsic noisiness of the gradient. A length of 75 m is used in practice, which gives a moving window of size  $75 \times 75 \text{ m}^2$ . The size was chosen in order to average the gradient approximatively over one radar bin. The sensitivity of the algorithm to this parameter was tested in a way similar to the gradient threshold. It was observed that doubling the size of the window changes only slightly the output of the algorithm (85% of average agreement) and the distributions of the ML thickness (increase of 20 m in median), while polarimetric signatures stay largely unchanged (variations of less than 1%). This window size is hence not very critical.

## 2.5 Validation

### 2.5.1 Vertical hydrometeor fall velocities

A first assessment of the performance of the algorithm can be conducted by verifying the consistency of its output. The ML is characterized by a change in the hydrometeor fall velocity,

## Chapter 2. Detection and characterization of the melting layer of precipitation

with a transition from low velocities in the solid phase to higher velocities in the liquid phase White et al. (2002). The liquid and solid phases identified by the algorithm should confirm this behaviour.

The empirical probability density functions of hydrometeor vertical fall velocity in the liquid and solid phases, estimated by the radial velocity at 90° elevation, are shown in Figure 2.11. The overlapping coefficient, which is a measure of agreement between two distributions and corresponds to the area of overlap (Inman and Bradley, 1989) is respectively 0.06, 0.07, 0.06 and 0.11 for the Payerne, Davos, Iowa and Ardèche datasets, which shows that the distributions within the liquid and solid phases for all datasets are strongly dissimilar. Since hydrometeor fall velocities are almost<sup>2</sup> independent from the radar variables used as input to the algorithm, this result tends to indicate that the algorithm discriminates well the liquid from the solid phase.

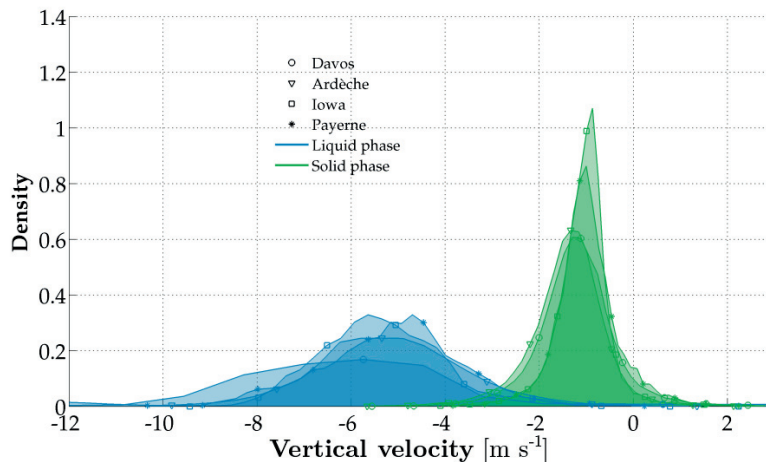


Figure 2.11 – Distributions of the hydrometeor vertical fall velocities in the liquid and solid phases. The different symbols denote the different datasets.

### 2.5.2 Comparison with Payerne radiosoundings

The Payerne dataset offers a good opportunity to assess the agreement between the output of the algorithm and the freezing-level height measured by the radio soundings, assuming that the top of the ML can be associated with the 0°C isotherm. To obtain a freezing-level estimation, the algorithm was run with a maximum range of 5 km and the detected ML top was averaged over the entire RHI. One difficulty in the comparison is that the distance and the time interval between the sounding and the radar scan can be significant. The geographical distance should not be a major issue since, for the range of isotherm 0 ° heights encountered during this campaign (1500-3000 m), the horizontal advection of the radiosonde is reasonably small, from 3 to 10 km. The time interval is more problematic since soundings are performed

<sup>2</sup>Due to reflectivity weighting, large hydrometeors, which have a strong reflectivity contribute more to the overall radial velocity.

only twice daily (at 0000 and 1200 UTC). To deal with this issue, errors were compared when all data were used (interpolating sounding heights linearly through time) and when only radar scans with a maximum time interval of 30 min to the closest sounding were used. Figure 2.12 shows that the correspondence is generally good and follows well the 1:1 line with errors rarely exceeding 200 m. This remains true when considering larger time intervals. The average errors are given in Table 2.4.

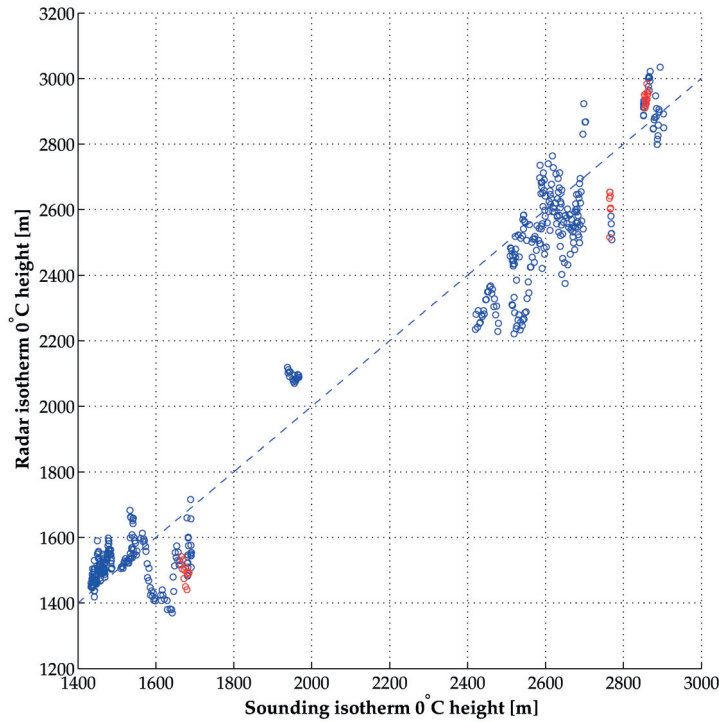


Figure 2.12 – 0°C isotherm heights, radar vs soundings in Payerne. The 1:1 line is shown in dashed blue. Red dots denote radar scans that are separated by at most 30 min from the closest sounding.

	Bias [m]	MAE [m]
All scans	-55.06	94.15
Scan with $\Delta_T < 30$ min	-80.85	130.5

Table 2.4 – Bias and mean absolute error in the radar freezing level estimation for all scans and for scans with a time interval to the radio sounding of maximum 30 min only. The bias is defined as the difference between the height of the ML top and the sounding freezing level height.

The freezing-level height estimated by the algorithm is slightly underestimated but this is still a good agreement considering the radial resolution of the radar (75 m) and the imperfect matching in time and space. It is worth noticing that the error is larger for small time intervals (red), which can be due to a sampling effect, the number of considered scans being small. Additionally, this also tends to indicate that the effect of the time interpolation is not too large and that freezing-level heights evolve regularly during the day.

A possible explanation for this bias is that the extrema of the gradient, which are assumed to correspond to the ML edges, might be within the “flank” of the peak of the normalized value and not at its base (for maxima) or top (for minima), when the gradient starts to raise from low values in the liquid/solid phase to high values in the ML. As such, the algorithm would tend to slightly underestimate the height of the ML top. This can be seen on Figure 2.4, as the top of the red area corresponding to the ML is below the first inflexion (starting from above) of  $Z_H$ .

### 2.5.3 Comparison with an algorithm adapted from PPI scans

Most ML detection algorithm are designed for PPI scans of operational radars at C- or S-band (e.g., Brandes et al., 2007; Giangrande et al., 2008). In order to compare the performance of our algorithm with a more simple approach, we adapted the algorithm of Giangrande et al. (2008) to RHI scans. The adapted algorithm works directly on polar RHI scans and classifies a pixel as belonging to the ML if:

- $\rho_{hv} > \rho_{hv,min}$  and  $\rho_{hv} < \rho_{hv,max}$
- The maximum of  $Z_H$  within a vertical window of 500 m below and above the pixel is  $> 30$  and  $< 47$  dBZ
- The maximum of  $Z_{DR}$  within a vertical window of 500 m above the pixel is  $> 0.5$  and  $< 2.5$  dB

The vertical window of 500 m corresponds to an equivalent range of  $500/\sin\theta$ , where  $\theta$  is the elevation angle. Once the ML has been identified in polar coordinates, it is converted to Cartesian coordinates as in Section 2.3.3.1.

Giangrande et al. (2008) recommend to use  $\rho_{hv,min} = 0.9$  and  $\rho_{hv,max} = 0.97$ , but we chose to use  $\rho_{hv,min} = 0.85$  instead since it is closer to the lower bound of  $\rho_{hv}$  values inside the ML (cf. Figure 2.7).

Table 2.5 shows the performance of the modified Giangrande et al. (2008) algorithm on the Payerne dataset from Section 2.5.2. It clearly appears that both the bias and the errors are much larger. The large bias shows that the algorithm underestimates the height of the freezing level because it does not sufficiently take into account the fact that the top of the BB can be significantly higher than the layer of low  $\rho_{hv}$ . The performance on the scans with  $\Delta_T < 30$  min is slightly better but still much worse than for the proposed algorithm (Table 2.4). Note that setting  $\rho_{hv,min} = 0.9$  instead of 0.85 increases slightly the bias and the error (-292 m bias and 316 m MAE for all scans).

Overall, the designed algorithm accurately detects the freezing level height and separates well the liquid and solid phases. It also performs much better than a simpler algorithm originally designed for operational PPI scans and adapted to RHI scans. A benefit of detecting the ML on



	Bias [m]	MAE [m]
All scans	-274.68	301.79
Scan with $\Delta_T < 30$ min	-226.02	229.9

Table 2.5 – Bias and mean absolute error in the radar freezing level estimation with the modified Giangrande et al. (2008) algorithm for all scans, and for scans with a time interval to the radio sounding of maximum 30 min.

RHI scans is that the height of its boundaries can be detected all along the radar profile, which allows to get more information about the geometry and the small-scale variability in shape of the ML.

This new algorithm is a very useful tool in the rest of this work which will focus on the characterization of the melting layer. It can also be used for other purposes, e.g. for comparison with numerical weather models or as a constraint for hydrometeor classification methods.

## 2.6 Characterization of the ML

All scans from all four available datasets were preprocessed and fed into the ML detection algorithm. Based on the output of the ML detection algorithm, various ML descriptors were computed, as illustrated in Figure 2.13. They can be grouped into four categories (Table 2.6). The hydrometeor classification algorithm (Section 2.3.3.3) was used to classify every pixel in the solid phase into one of three classes: aggregates, rimed particles and crystals. The fraction of hydrometeors is simply the fraction of the pixels of one class over all pixels in the solid phase.

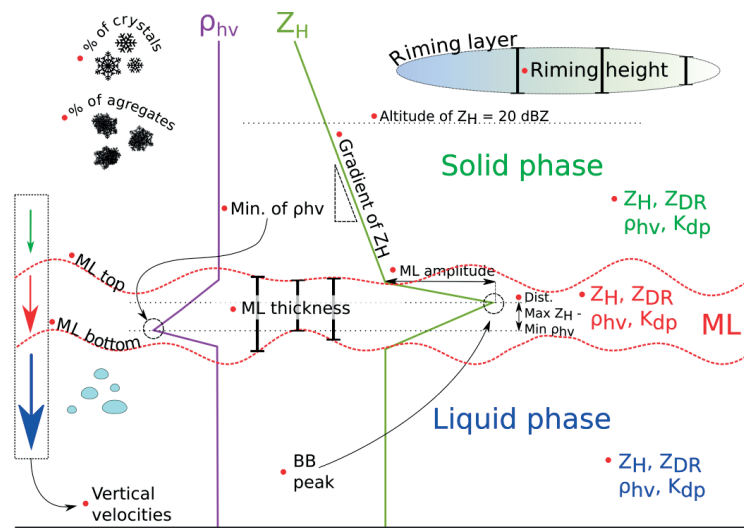


Figure 2.13 – Schematic representation of the computed ML descriptors on a RHI scan. Computed descriptors are highlighted with a red dot. Limits of the ML are shown as red dashed lines.

## Chapter 2. Detection and characterization of the melting layer of precipitation

<i>Geometry</i>	<ul style="list-style-type: none"> <li>- Thickness of ML [m]</li> <li>- Altitudes of top and bottom of ML [m]</li> </ul>
<i>Polarimetry</i>	<ul style="list-style-type: none"> <li>- Polarimetric variables (<math>Z_H</math>, <math>Z_{DR}</math>, <math>\rho_{hv}</math>, <math>K_{dp}</math>) in ML, solid phase and liquid phase</li> <li>- Bright-band intensity [dBZ]</li> <li>- Altitude of the 20 dBZ isoline [m]</li> <li>- Distance between the maximum of <math>Z_H</math> and the minimum of <math>\rho_{hv}</math> [m]</li> <li>- Gradient of <math>Z_H</math> just above the ML [dBZ m<sup>-1</sup>]</li> <li>- Amplitude (with respect to solid phase) of the bright-band peak [dBZ]</li> </ul>
<i>Doppler</i>	<ul style="list-style-type: none"> <li>- Vertical fall speeds in ML, solid and liquid phases [m s<sup>-1</sup>]</li> </ul>
<i>Hydrometeors</i>	<ul style="list-style-type: none"> <li>- Fractions of aggregates, ice crystals [-]</li> <li>- Thickness of the riming layer [m]</li> </ul>

Table 2.6 – List of melting layer descriptors by category. For polarimetric variables, the average over the whole scan are taken, without consideration for the elevation angle. For  $Z_{DR}$ , the elevation angles (45° – 90°) are discarded (Section 2.3.3.1).

### 2.6.1 The ML attenuation effect

Before focusing on the ML descriptors, the potential error due to the attenuation in the ML was investigated. Attenuation in the ML is a poorly known phenomenon, mainly because its quantification poses many instrumental and methodological problems. Bellon et al. (1997) estimated the attenuation in the ML in the vertical by comparing UHF and X-band radar reflectivity measurements in the solid phase near the echo top assuming that solid hydrometeors at this altitude behave as Rayleigh scatterers. The authors observed an increase in the attenuation effect with the intensity of the BB and estimated the total attenuation over the entire ML to be up to 1.7 dBZ for an intensity of 36.5 dBZ. At lower elevation angles, the attenuation effect could be even stronger, especially for low melting layers. Klaassen (1990) estimated the attenuation effect in the ML using a new scheme for the calculation of the dielectric properties of melting ice. They observed a variable specific attenuation through the ML with maximum values of around 1.5 dB km<sup>-1</sup> at a frequency of 12 GHz. Simulations made by Matrosov (2008) give an average specific attenuation of around 0.3-0.5 dB km<sup>-1</sup> for rain rates around 2-3 mm h<sup>-1</sup>. Pujol et al. (2012) relied on the simulation of airborne X-band measurements and found much smaller values of attenuation, with a maximum specific attenuation of around 0.2 dB km<sup>-1</sup>. For an average ML thickness of 300 m, this would be 30 times less than Bellon et al. (1997). Additionally, to the author's knowledge, no study has been conducted about the differential attenuation on  $Z_{DR}$  caused by the ML. This effect could also be quite high but is even more difficult to quantify because  $Z_{DR}$  cannot be measured at vertical incidence.

To investigate the bias caused by neglecting the melting-layer attenuation effect, a statistical analysis of the  $Z_H$  and  $Z_{DR}$  shift across the melting layer was performed. If the attenuation effect is significant, there should be on average a decrease in  $Z_H$  and  $Z_{DR}$  between the point where the beam enters the melting layer (at the bottom) and the point where it leaves the melting layer (at the top). To simplify the notation, we will denote by MLD the distance travelled by the radar beam through the ML. The decrease in  $Z_H$  and  $Z_{DR}$  should become more and more important as the MLD increases. For a given radar radial, the MLD depends on both the height of the melting layer and the elevation angle. It is maximal for low elevation angles and low melting layers. It is possible to have a rough idea of the ML attenuation effect by assuming homogeneity of the ML and by computing the shift in the differences of  $Z_H$  and  $Z_{DR}$  across the ML with increasing MLD. The validity of this approach is restricted by the assumption of homogeneity, but the very large amount of available data should alleviate the sampling effect. For  $Z_{DR}$ , the assumption of homogeneity is more difficult to justify due to the high heterogeneity of particle shapes in the solid phase which can result in a potentially large local variability of the intrinsic (non-attenuated)  $Z_{DR}$ . As such, this estimation of the differential attenuation of  $Z_{DR}$  might be biased.

To be consistent with the rest of this work, only the first 5 km from the radar were considered (Section 2.3.3.1). Results of this analysis are shown as a series of boxplots in Figure 2.14. A clear, almost linear shift in the distributions of  $Z_{DR}$  differences is visible, whereas in  $Z_H$  the shift is less evident and does not vary linearly with the distance. At a MLD of 2300 m, the shift is around 1 dB in  $Z_H$  and 0.6 dB in  $Z_{DR}$ , which corresponds to approximately 16 and 27% of the local variability, estimated for every distance bin by the  $Q_{90}$ - $Q_{10}$  interquantile. This observation could give a rough estimation of the ML specific attenuation by dividing the shift by the distance:  $0.5 \text{ dBZ km}^{-1}$  for  $Z_H$  and  $0.37 \text{ dB km}^{-1}$  for  $Z_{DR}$ .

Matrosov (2008) give a power law that estimated the ML attenuation normalized to the vertical as a function of the rain rate:  $A(\text{dB}) = 0.048R^{1.05}$ . Using this power law and the classical  $Z$ - $R$  relation  $Z = 200R^{1.6}$  (Marshall et al., 1955) separately along every radar beam crossing the ML, one can obtain the theoretical total attenuation. Dividing this attenuation for every beam by the sinus of the corresponding elevation angle and by the MLD, and averaging over all profiles gives an average specific attenuation in  $Z_H$  of around  $0.2 \text{ dB km}^{-1}$ , which is smaller than the observed value.

The measured specific BB attenuation in  $Z_H$  can also be compared with observations by Bellon et al. (1997) who measured the total BB attenuation at the vertical for some values of  $Z_H$  in rain. Interpolating between these measurements and using the same method as previously on every radar beam crossing the ML, one obtains an average specific attenuation of around  $2 \text{ dB km}^{-1}$  which is much larger than our estimation and the one of Matrosov (2008). However, one should keep in mind the strong variability from event to event.<sup>3</sup>, as well as the possibility of non-negligible attenuation in solid precipitation in the case of large aggregates.

<sup>3</sup>Bellon et al. (1997) measured for example 3 dB for an event with a BB peak of 40 dBZ and then only 0.5 dB for a nearly identical event two days later.

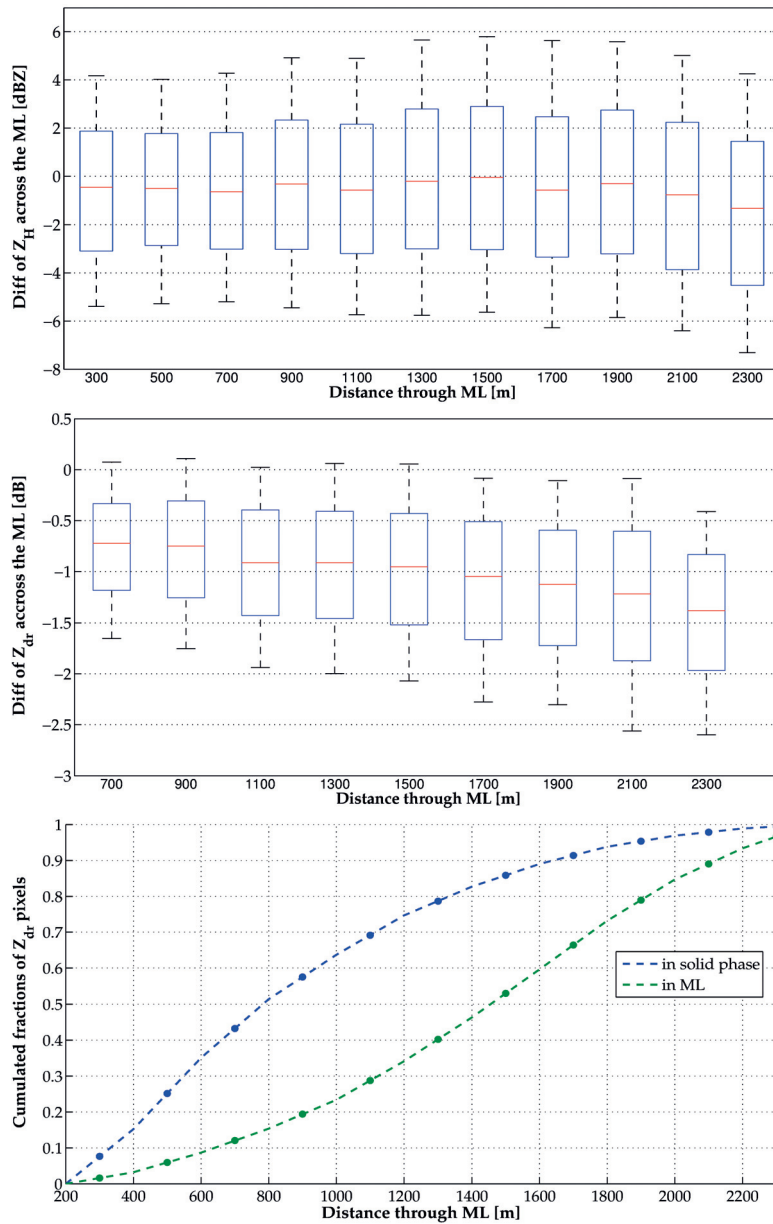


Figure 2.14 – Boxplots of the distributions of the differences in  $Z_H$  (top) and  $Z_{DR}$  (middle) across the melting layer as well as the cumulated fraction of  $Z_{DR}$  pixels for a range of MLDs. Since  $Z_{DR}$  is not reliable at high elevation angles, distributions at short distances are not available. The represented values in the boxplots are the quantiles 10 (lower whisker), 25, 50, 75 and 90 (upper whisker). The last plot gives the fraction of pixels measured in the ML and the solid phase which, in the beam of the radar, have a MLD smaller than the corresponding value in abscissa.

Another possible reason for this large difference comes from the uncertainty of extrapolating the vertical measurements of Bellon et al. (1997) to lower elevation angles.

This shift is small for  $Z_H$  compared with the typical values in stratiform rain or in the ML (20-40 dBZ). It is even smaller than the usual calibration error on  $Z_H$  which is around 1 dBZ. As such,

the output of the ML detection algorithm should not be influenced by the ML attenuation effect. Additionally, considering the high values of  $Z_H$  in the ML, the effect on the overall distribution of reflectivity in the ML should be limited.

However, the differential attenuation on  $Z_{DR}$  seems to be quite important compared with the usual range of  $Z_{DR}$  values (0-3 dB). However one should keep in mind that in the solid phase most pixels will have a low MLD and will not be affected very much by attenuation. The third plot of Figure 2.14 shows that 80% of all pixels in the solid phase have a MLD smaller than 1300 m. Since correction of this differential attenuation effect is currently not possible, values of  $Z_{DR}$  inside, and to a lesser extent above, the ML should be considered carefully, as they are certainly negatively biased.

### 2.6.2 Polarimetric signature of the ML

The distributions of  $Z_H$ ,  $Z_{DR}$ ,  $K_{dp}$  and  $\rho_{hv}$  for the four datasets are shown in Figure 2.15. The two derived variables, amplitude of the BB and distance between peak of  $Z_H$  and minimum in  $\rho_{hv}$ , are represented as well. In addition, a summary of these distributions as quantiles is given in Table 2.7. The shapes of the distributions in  $\rho_{hv}$  agree relatively well, but the Iowa and Davos datasets are characterized by the presence of a larger number of smaller values of  $\rho_{hv}$ . The shapes of the distributions in  $K_{dp}$  are quite similar for the Davos, Ardèche and Payerne datasets, but the Davos distribution is shifted towards larger  $K_{dp}$ . The Iowa dataset differs from the others as its distribution is much more symmetrical with fewer smaller  $K_{dp}$  values. Distributions in  $Z_H$  show some discrepancies between datasets. The Ardèche dataset has much stronger  $Z_H$  values, whereas the Iowa (IFloodS) dataset has much lower values. The Iowa dataset is quite small and was recorded during a limited period of time (April/May 2014). It is dominated by situations with relatively weak rain rates. In contrast, the Ardèche dataset was recorded in autumn, a season during which very heavy precipitation often occurs over the south east of France, so part of this discrepancy could be due to this sampling effect.  $Z_{DR}$  distributions generally agree quite well with the exception of the Davos dataset which has stronger values (by around 1 dB). Part of this bias could come from the fact that the radar was equipped with flexible wave-guides during that campaign, which were later replaced by a rotary joint. This could also explain the shift in  $K_{dp}$  in the Davos dataset.

Giangrande et al. (2008) detected the ML on S-band PPI scans and computed the distributions of  $Z_H$ ,  $Z_{DR}$  and  $\rho_{hv}$  in wet snow over 29 h of observation. The distribution of measured  $Z_H$  values shows a relatively symmetrical distribution with a mode around 30 dBZ whereas the distribution of  $Z_{DR}$  shows a right-skewed distribution with a mode around 1 dB, which is in close agreement with what we observe when merging all datasets. However there is some difference in the distribution of  $\rho_{hv}$  which has a smaller spread and a more symmetrical distribution, with a smaller mode (0.96), but a similar mean. Since the size of their dataset is much smaller than ours, this could be due to a sampling issue.

## Chapter 2. Detection and characterization of the melting layer of precipitation

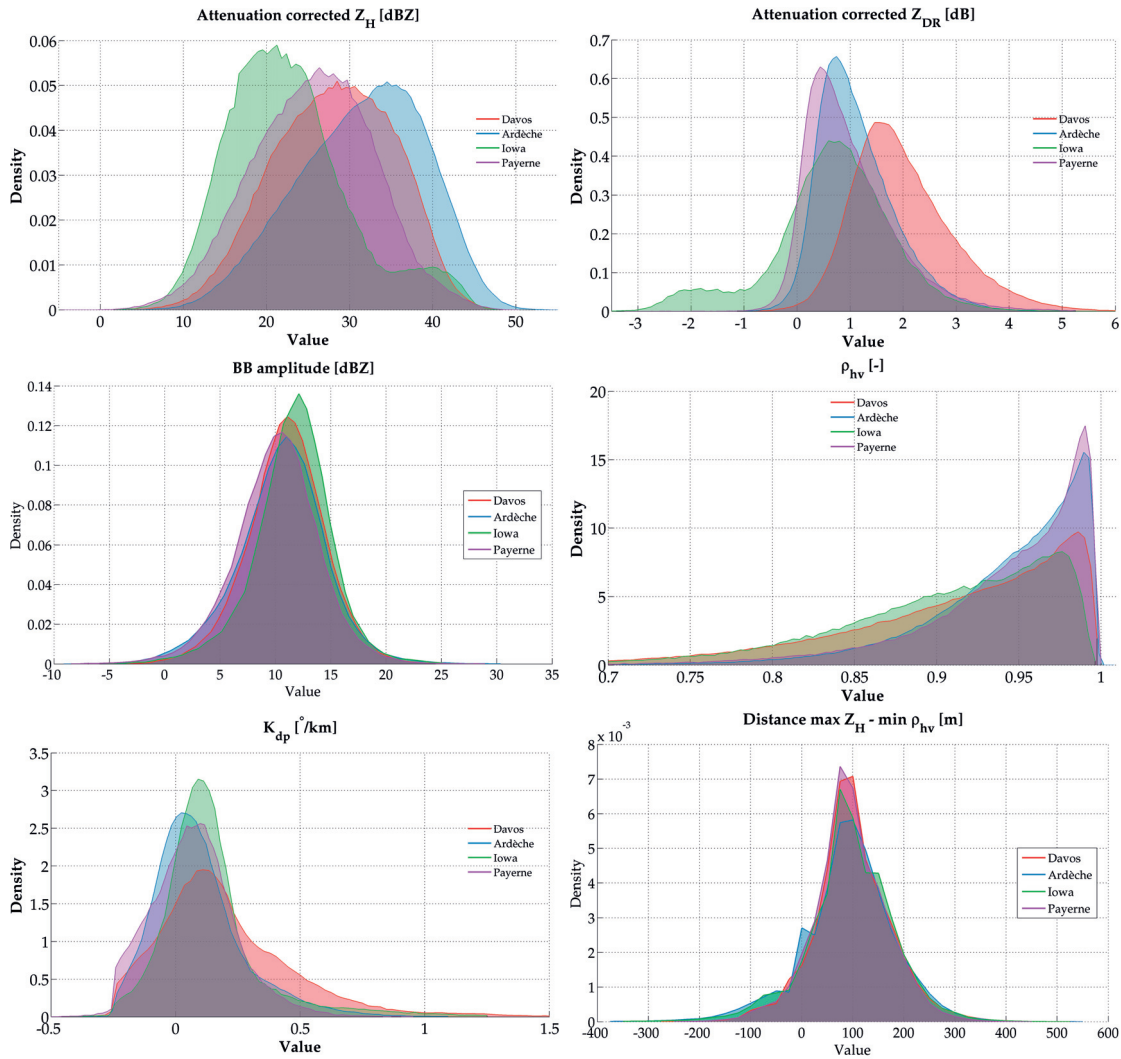


Figure 2.15 – Polarimetric signatures within the ML. From top-left to bottom-right:  $Z_H$ ,  $Z_{DR}$ , amplitude of  $Z_H$  (between solid phase and ML),  $\rho_{hv}$ ,  $K_{dp}$  and Dist. between peak in  $Z_H$  and minimum in  $\rho_{hv}$

Additionally, the two derived variables (the BB amplitude and the distance between the peak of  $Z_H$  and the minimum in  $\rho_{hv}$ ) have a very similar distribution on all datasets, which tends to show that on average concentration effects and increase of reflectivity due to the BB effect are similar. Durden et al. (1997) computed empirical moments of some ML descriptors over the tropical Pacific region. In terms of BB intensity (maximum of  $Z_H$ ) and amplitude, our overall statistics are in good agreement with their observations as well as the model profiles given by Brandes et al. (2007), with only a few dBZ of difference (31.75 in our case versus 35.4 (Durden et al., 1997) and 35 (Brandes et al., 2007)). Note also that the average minimal value of  $\rho_{hv}$  (0.86) in the ML is equal to the one found by Durden et al. (1997). The distance between the peak of  $Z_H$  and the minimum of  $\rho_{hv}$  has an average of 96 m and a standard deviation of 84 m which are quite close to those of Durden et al. (1997): 121 and 92 m respectively.

## 2.6. Characterization of the ML

The average vertical velocity in the ML is also very similar (1.22 here versus 1.4 m s<sup>-1</sup> for Durden et al. (1997)). The good agreement of our observations with those of Durden et al. (1997) indicates again that the ML has very consistent features globally.

In summary, the polarimetric signature of the ML appears to be quite consistent over all datasets, with the exception of  $Z_H$  which strongly depends on the intensity of the recorded rainfall events. Additionally, the distribution of both the BB amplitude and the distance between the maximum in  $Z_H$  and the minimum in  $\rho_{hv}$ , which is related to concentration effects, are also very similar for all the considered climatological regions.

Var.	Stat.	All	Davos	Ardèche	Iowa	Payerne
$Z_H$	Mean	29.04	28.10	31.44	22.67	25.59
	Stdev.	7.97	7.14	7.62	7.45	7.24
	Q <sub>10</sub>	18.28	18.54	20.88	14.06	16.03
	Q <sub>90</sub>	39.34	37.33	40.92	32.78	34.69
BB peak	Mean	31.75	31.01	34.02	25.46	29.00
	Stdev.	7.35	6.39	7.20	6.82	6.33
	Q <sub>10</sub>	21.81	22.40	23.95	17.15	20.48
	Q <sub>90</sub>	41.43	39.38	42.99	33.51	37.00
$Z_{DR}$	Mean	1.99	1.99	1.13	0.65	0.98
	Stdev.	0.95	0.95	0.72	1.14	0.83
	Q <sub>10</sub>	0.30	0.92	0.33	-0.77	0.12
	Q <sub>90</sub>	2.55	3.26	2.11	1.95	2.09
$\rho_{hv}$	Mean	0.93	0.91	0.94	0.91	0.94
	Stdev.	0.06	0.07	0.05	0.07	0.05
	Q <sub>10</sub>	0.85	0.81	0.88	0.81	0.87
	Q <sub>90</sub>	0.99	0.98	0.99	0.98	0.99
Min. of $\rho_{hv}$	Mean	0.86	0.82	0.89	0.82	0.88
	Stdev.	0.07	0.07	0.05	0.06	0.06
	Q <sub>10</sub>	0.76	0.71	0.81	0.73	0.79
	Q <sub>90</sub>	0.94	0.90	0.94	0.89	0.94
$K_{dp}$	Mean	0.11	0.20	0.09	0.14	0.07
	Stdev.	0.21	0.28	0.18	0.21	0.17
	Q <sub>10</sub>	-0.11	-0.10	-0.11	-0.06	-0.15
	Q <sub>90</sub>	0.38	0.55	0.33	0.37	0.28

Table 2.7 – Statistics describing the distributions of the polarimetric variables within the melting layer. The bright-band (BB) intensity is simply the maximum of  $Z_H$  in every vertical column of the ML.

### 2.6.3 Vertical profiles of polarimetric variables through the ML

The polarimetric variables are not uniform within the ML and exhibit a vertical structure. Figure 2.16 shows the distributions of  $Z_H$ ,  $Z_{DR}$  and  $\rho_{hv}$  as a function of the relative height inside the ML (0 corresponds to the bottom and 1 to the top of the detected ML). Note that  $K_{dp}$  is not represented because it shows no significant dependence on height. It can be seen that the height of the peak in  $Z_H$  (maximum of the BB) is around 25% higher than the minimum in  $\rho_{hv}$ . The ML also shows a peak in  $Z_{DR}$  in the lower part of the ML at the same height as the minimum in  $\rho_{hv}$ . The lower heights of the peaks of  $Z_{DR}$  and  $\rho_{hv}$  can be explained by the fact that, unlike  $Z_H$ , these two radar variables are insensitive to concentration effects. The decrease in  $Z_{DR}$  near the bottom of the ML could be due to the break-up of large melted aggregates. However, one should keep in mind the differential attenuation effect of the ML on  $Z_{DR}$  which could also contribute to the lower height of the  $Z_{DR}$  peak.

### 2.6.4 Geometry of the ML

#### 2.6.4.1 Thickness

The detected MLs have on average a very similar geometry on all datasets. Figure 2.17(a) shows the distribution of the ML thickness; all distributions have a similar shape with a strong mode around 300 m, and a long right tail. The melting layer in Payerne is slightly thinner (purple area) but the differences are small relative to the radial resolution. Generally differences in the mean are small (maximum 35 m) and quantiles also agree well between datasets; the quantile 10% is around 250 m whereas the quantile 90% is always around 450 m. This suggests that on average the thickness of the ML is independent of the climatological conditions and the topography. It can be observed that the thickness of the ML never gets below 175 m but can reach values up to 600 m. The minimal thickness is probably linked with the minimal time snowflakes need to completely melt. The time required for complete melting can be roughly estimated for every RHI scan by dividing the thickness of the ML by the vertical velocity. This gives an average time (over all available scans) of about 2 min for particles to melt completely.

Our observations of the ML thickness agree well with other observations made in the literature. The distribution of ML thickness observed by Giangrande et al. (2008) looks very similar with a marked right tail and a mode around 300 m. Bandera et al. (1998) used a similar ML detection algorithm to process 200 RHI scans recorded over the UK and observed an average thickness of 300 m which is very close to our observed average value (320 m). (Durdin et al., 1997) found a slightly larger average thickness of 400 m, though considering the radial resolution of the radar (75 m) this difference is barely significant. One possible explanation is that their estimation of the ML is based solely on the detection of the BB whereas on the current algorithm  $\rho_{hv}$  is also considered for the detection of the base of the ML. In the case of strong precipitation, the lower part of the BB is not as well defined as the upper part and this could lead to a slightly larger thickness of the ML.



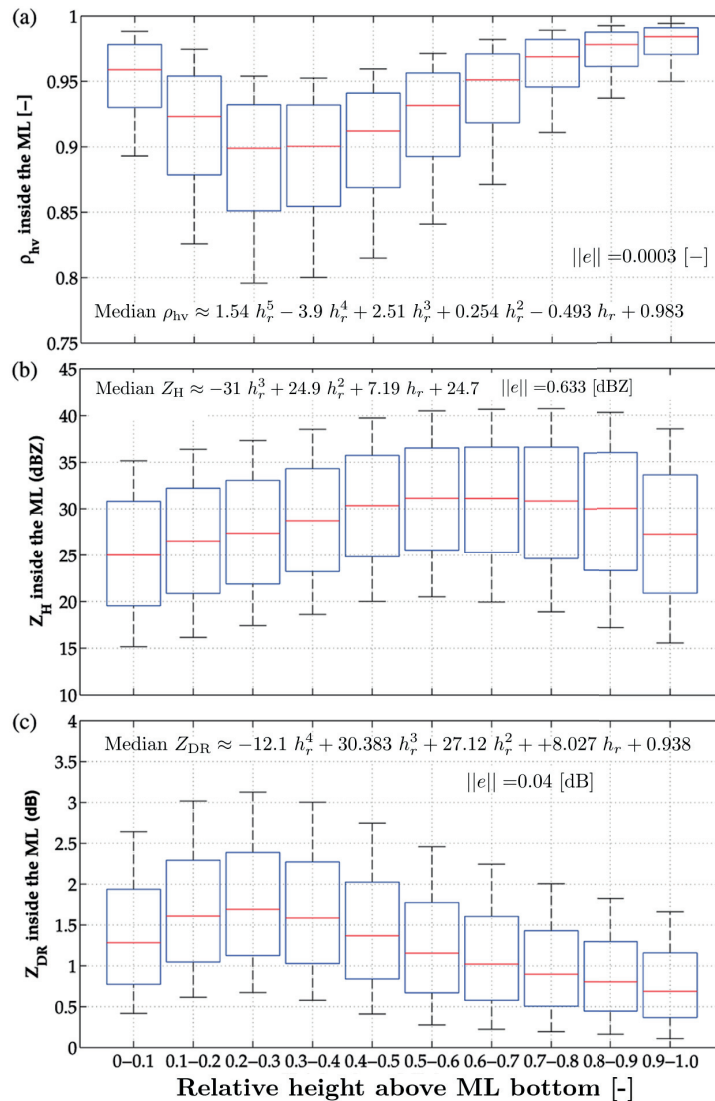


Figure 2.16 – Boxplots of the distributions of (a)  $Z_{\text{H}}$ , (b)  $\rho_{\text{hv}}$  and (c)  $Z_{\text{DR}}$  as a function of the relative height inside the ML. Least-square fitting polynomials of the medians as a function of relative height  $h_r$  are also shown, along with their associated norm of residuals  $\|e\|$ .

### 2.6.4.2 Horizontal variability

The horizontal variability of the ML can be quantified by the variograms of the ML thickness and of the heights of the top and bottom of the ML. The variogram is a function that describes the degree of spatial dependence of a spatial random field or stochastic process  $z$ . It can be defined by the empirical semivariance  $\gamma$ , which is half of the average squared difference between pairs of points separated by a given distance (Chilès and Delfiner, 1999).

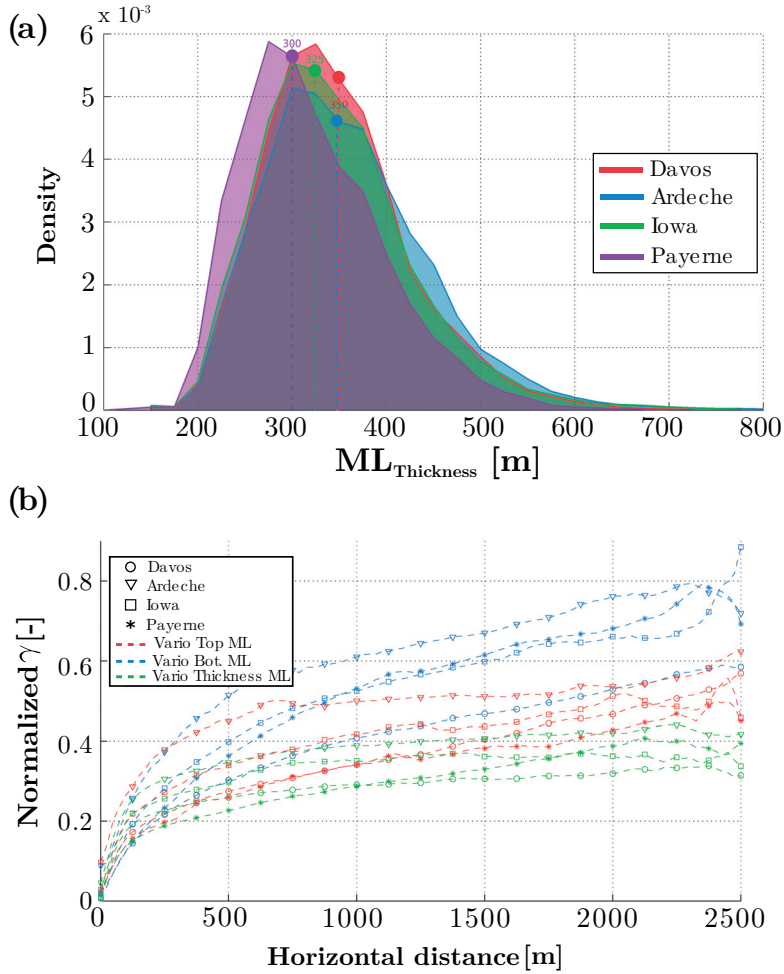


Figure 2.17 – (a) Distributions of the ML thickness for the four datasets, with medians indicated by dashed lines. (b) Normalized (by the variance) variograms of the ML thickness and top and bottom heights. The  $x$ -axis is the horizontal distance along the RHI.

$$\hat{\gamma}(h) = \frac{1}{2} \frac{1}{n(h)} \sum_{i=1}^{n(h)} [z(x_i + h) - z(x_i)]^2$$

where  $n(h)$  is the number of pair of points separated by interdistance  $h$ , and  $z(x_i)$  is the value of the spatial field at position  $x_i$ .

This gives indication about the decorrelation distance<sup>4</sup>, the sub-grid variability and the smoothness of a process. The beam-broadening effect causes an artificial trend in the thickness and boundaries of the ML with increasing distance from the radar. To alleviate this effect, the variograms were computed for every scan on linearly detrended variables. Additionally, to

<sup>4</sup>The distance at which the variogram reaches its maximum and stabilizes, also called range.

account for the fact that datasets are of different sizes, the variograms were normalized, i.e. divided by the corresponding variances (of ML thickness or top and bottom ML heights). For every dataset, the variograms were then averaged over all scans.

The normalized variograms of the ML boundaries and thickness (Figure 2.17(b)) show a similar structure between the datasets, with a similar range and a similar slope, especially at low distances where the variability is maximal. The ML top boundary reaches decorrelation at around over 1500 m, whereas the bottom of the ML seems to be smoother and does not decorrelate completely over 2500 m. Experiments show that this is mainly due to the use of only  $Z_H$  to detect the top of the ML. Indeed, unlike  $\rho_{hv}$ ,  $Z_H$  is dependent on the concentration of hydrometeors and is more strongly influenced by large hydrometeors. The variogram of the thickness has a similar trend but with an even smaller decorrelation range. This can be due to the fact that, after detrending, heights of the top and bottom of the ML are positively yet not totally correlated ( $r = 0.62$ ).

## 2.7 Correlation analysis of ML descriptors

### 2.7.1 Factors controlling the ML thickness

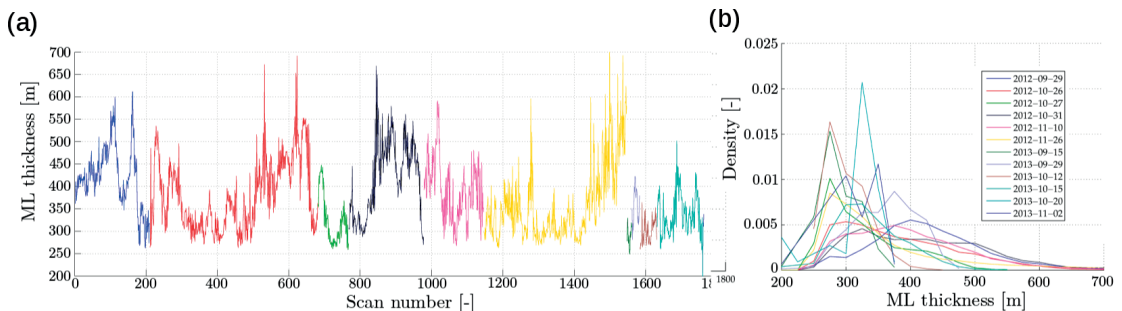


Figure 2.18 – Event by event variability of the ML thickness on the HyMeX dataset. Every coloured line corresponds to a different precipitation event. **(a)** Time series showing the mean ML thickness for every scan. Note that for visualization purposes all lines are displayed adjacently even if they are in fact temporally separated. **(b)** The distributions of the ML thickness are displayed within all precipitation events.

Although the ML has a quite consistent shape on average, variations of the ML thickness can be quite significant between and especially during precipitation events. This can be seen for example on the HyMeX dataset (Figure 2.18), where the ML thickness can easily vary from 250 to 500 m within the same precipitation event.

In order to identify the possible causes of increased thickness of the ML, a correlation analysis of all ML variables was performed. Before calculating the correlations, the ML statistics described in Table 2.6 were averaged over every single RHI scan in order to reduce them to the same dimension<sup>5</sup>.

<sup>5</sup>All ML descriptors are not defined over the same domain, for example the vertical velocity is only available at

## Chapter 2. Detection and characterization of the melting layer of precipitation

Before computing the correlations, the variables were also log-transformed to account for possible non-linearities.

First of all, it is interesting to notice that there is no correlation between the altitude of the top or bottom of the ML and the thickness of the ML ( $r = 0.08$  for the top and  $r = -0.013$  for the bottom). Consequently, the seasonal variability of the ML, characterized mostly by variations in the freezing-level height, does not seem to contribute significantly to the variability in the ML thickness.

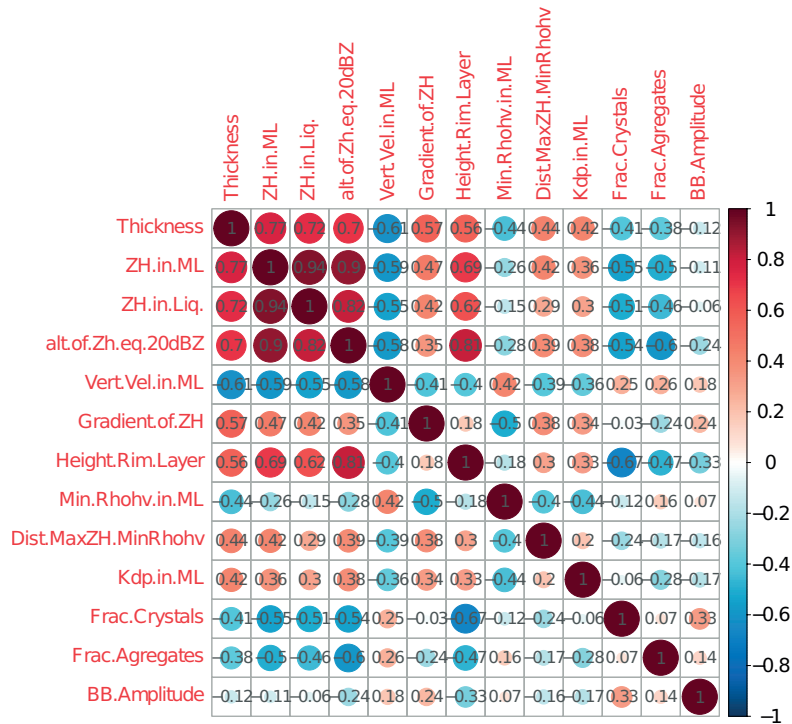


Figure 2.19 – Correlation plot of some relevant variables. Positive correlations are in red and negative correlations in blue.

However, other descriptors have quite high correlations with the ML thickness. These relations are shown in the form of a correlation plot in Figure 2.19. Unsurprisingly, the ML thickness depends strongly on the intensity of  $Z_H$  in the ML ( $r = 0.77$ ). Such a correlation was also observed by Durden et al. (1997). The clear linear trend between the two variables is shown in Figure 2.20. The ML thickness is also strongly correlated with  $Z_H$  in the liquid phase ( $r = 0.72$ ). A higher reflectivity in the liquid phase indicates a higher rain rate which corresponds to a larger mass of ice to melt, hence an increase in the ML thickness. This strong correlation also shows that by simply knowing the reflectivity in rain, one can already get some relevant information about the properties of the ML. The intensity of  $Z_H$  in the ML and the thickness are also strongly related to the vertical extension characterized by the distance of the 20 dBZ  $Z_H$  contour from the ML ( $r = 0.9$  and  $r = 0.7$  respectively). A possible explanation is the fact

the vertical whereas  $Z_{DR}$  is available only at low elevation angles.

## 2.7. Correlation analysis of ML descriptors

that intense BBs are usually associated with higher  $Z_H$  in the solid phase, due to the presence of larger hydrometeors.  $K_{dp}$  in the ML is slightly less correlated with the thickness ( $r = 0.42$ ), but considering the large amount of data this is still an important correlation. Note that  $K_{dp}$  is not redundant with  $Z_H$ , since their correlation is relatively low ( $r = 0.36$ ). Additionally, the thickness is also well correlated with the vertical fall velocity in the ML ( $r = 0.61$ ). This could be explained by two different reasons: indirectly because dense particles, which take longer to melt, have also higher terminal velocities, and directly because fast falling particles will travel further before melting and will extend the ML downwards.

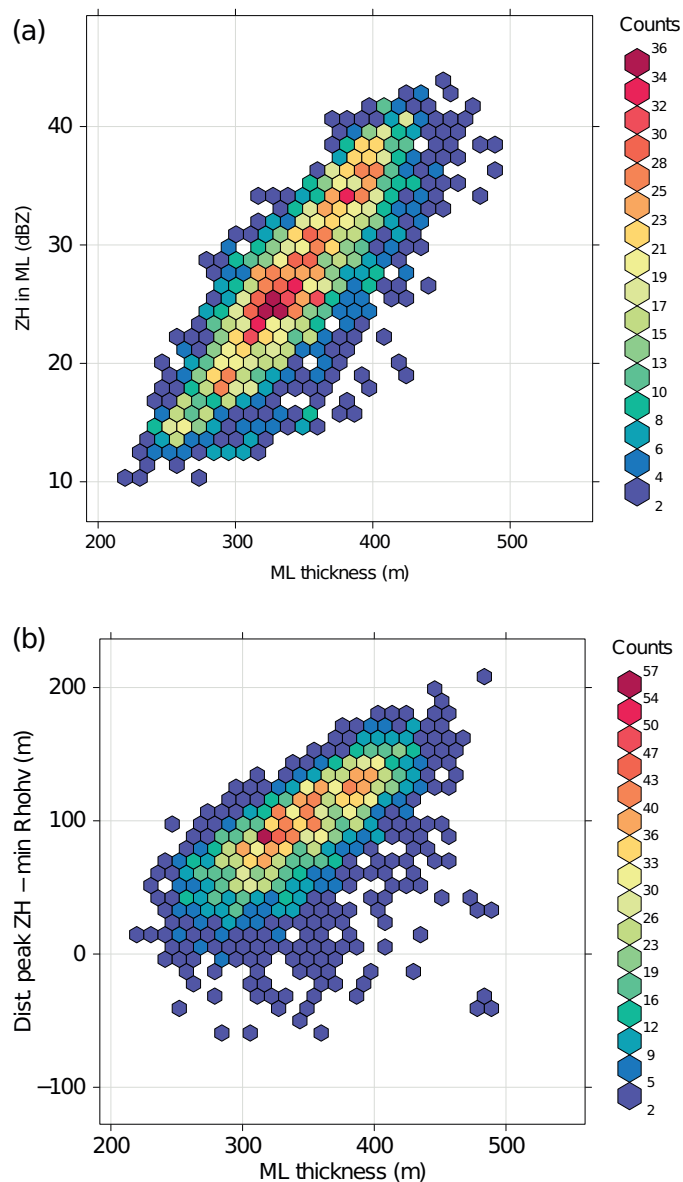


Figure 2.20 – Scatterplots of (a) thickness versus  $Z_H$  in the ML and (b) thickness versus distance between peak of  $Z_H$  and minimum of  $\rho_{hv}$ . Counts indicate the number of points in every hexagonal bin.

## Chapter 2. Detection and characterization of the melting layer of precipitation

---

Another important factor is the gradient of  $Z_H$  above the ML, which is positively correlated with the ML thickness ( $r = 0.57$ ); thicker melting layers are associated with a faster decrease in reflectivity above the melting layer. This is possibly the case when the reflectivity in the solid phase is relatively high, due to the presence of denser and larger solid particles. Fabry and Zawadzki (1995) also observed such a correlation and suggested that in the case of high rainfall rates, updrafts could be strong enough to bring considerable amounts of cloud water from below the ML into the solid phase above, resulting in “particularly wet graupel particles”, with a high reflectivity. To verify this hypothesis, the relation between the thickness of the ML and the spectral width within the ML both taken at vertical incidence was studied. However, no strong correlation was detected ( $r = 0.18$ ).

A thicker ML is quite often associated with the presence of a layer of rimed particles above the ML ( $r = 0.56$  with the thickness of the riming layer). This could be due to the higher density of these particles and hence the increasing time it takes for them to melt, as well as their larger terminal fall velocities (Pruppacher and Klett, 1997). In the same way, a thicker ML is also correlated with a smaller fraction of ice crystals, since ice crystals and rimed particles are negatively correlated ( $r = -0.67$ ). The distance between the peak in  $Z_H$  and the minimum in  $\rho_{hv}$  is also positively correlated to the thickness ( $r = 0.44$ ) which indicates that the concentration of hydrometeors also seems to play a role. The linear trend between the two variables is visible in Figure 2.20. Indeed, when the concentration of hydrometeors is higher, the shift in altitude between the peak in  $Z_H$  and the minimum in  $\rho_{hv}$  increases, since  $Z_H$  is sensitive to concentration effects but  $\rho_{hv}$  is not. An increased hydrometeor concentration could lead to an increase in the diabatic cooling of the surrounding air during the melting process. This effect can be quite important when the situation is very stable and when horizontal temperature advections are small (Kain et al., 2000). According to Durden et al. (1997), the cooling effect can increase the thickness of the ML because particles will take more time to melt. The cooling effect increases with the precipitation intensity and can significantly lower the freezing level. Note also that the minimum in  $\rho_{hv}$  in the ML is less correlated than  $Z_H$  with the ML thickness ( $r = -0.44$ ). Both variables are only weakly correlated ( $r = -0.26$ ). The differences between these two variables, computed after normalizing them by the mean, are significantly correlated with the vertical distance between the peak of reflectivity and the minimum of  $\rho_{hv}$  inside the ML ( $r = -0.59$ ), which seems to indicate that strong concentrations of solid hydrometeors above the ML can lead to a decoupling of  $Z_H$  and  $\rho_{hv}$  within the ML.

Note that all factors described above, with the exception of the BB amplitude, are statistically significantly correlated with the ML thickness (at  $\alpha = 1\%$ ).

It can seem surprising that the amplitude of the BB is not significantly correlated with the ML thickness, nor the intensity of  $Z_H$  in the ML. This can be explained by the high correlation between  $Z_H$  in the ML and  $Z_H$  in the solid phase ( $r = 0.8$ ). Small amplitudes of the ML can be caused either by a weak stratiform situation with a thin ML, where the flux is small, or by a strong stratiform situation with high reflectivity above the ML (aggregates and/or rimed particles). In fact, the relation between the amplitude of  $Z_H$  in the ML and the thickness of the

ML seems to be weakly quadratic. When considering only MLs with a thickness larger than the median ( $>350$  m), the correlation becomes negative ( $r = -0.38$ ), which shows that thick MLs tend to be associated with a smaller amplitude between the BB peak and the reflectivity in the solid phase. The correlation becomes positive ( $r = 0.25$ ) when considering only MLs with a thickness smaller than the median.

Finally, unlike Durden et al. (1997), we did not identify a significant correlation between altitude of the ML and intensity of the BB ( $r = -0.06$ ). This might be due to the fact that, unlike in tropical regions, variations in the ML height in temperate climate are dominated by seasonal variations.

### 2.7.2 Principal component analysis

Principal component analysis (PCA) is a statistical procedure that tries to explain the covariance structure of data by means of a small number of orthogonal components which are linear combinations of the original variables. Transformation is done in such a way that the components are ordered by decreasing variance and the first components explain the largest part of the variability in the data.

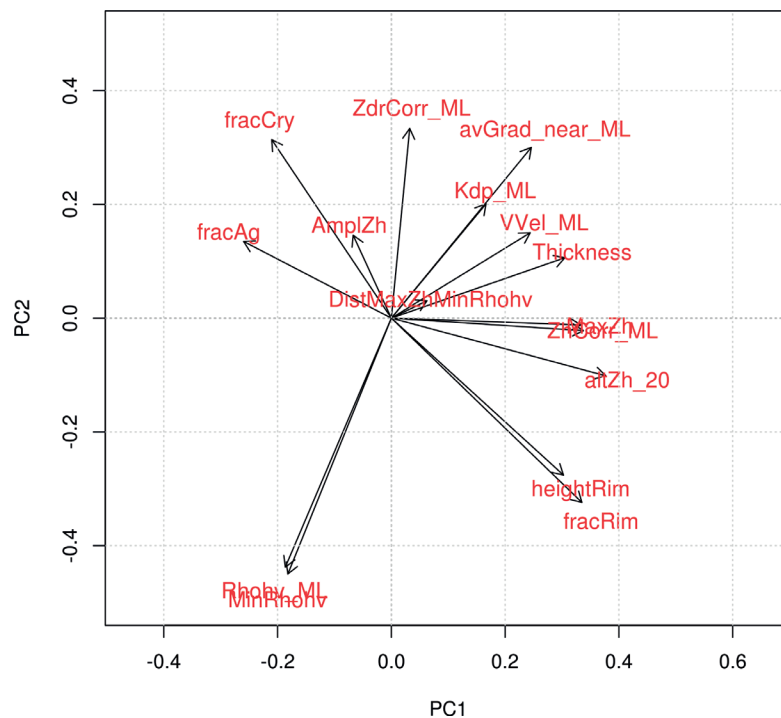


Figure 2.21 – Biplot of the ML descriptors projected onto the plane of the first two PCA components. The first two components explain 60% of the total variance. The “Corr” subscript indicates that the variable ( $Z_H$  or  $Z_{DR}$ ) has been corrected for attenuation in the liquid phase.

To gain a better understanding of the relations between the selected factors, a PCA on standardized data was performed. The PCA was performed with ROBPCA, a robust version of the

algorithm (Hubbert et al., 2005), that does not rely on the empirical covariance matrix. To simplify the analysis, only the first two components were kept. They explain respectively 52 and 24% of the total variance. The biplot representing the factors projected into the space of the two first components is shown in Figure 2.21. The arrows represent the loading which is the weight by which every standardized variable should be multiplied to get the component scores. Their length is proportional to the contribution of the variable to the two components and the angle between two arrows is an approximate measure of their correlation. Highly correlated variables point in the same direction; uncorrelated variables are at right angles to each other. It can be seen that the first component corresponds mostly to the intensity and vertical extension of the BB, the presence of riming and the thickness. The fraction of rimed particles has a similar and significant contribution to both components. The second component depends mostly on the signature in  $\rho_{hv}$  and  $Z_{DR}$  in the ML. Considering their loading and the relative weight of every component, it can be seen that the most important factors explaining the variability in the ML are (in order of importance) the fraction of riming, the gradient of  $Z_H$  in the solid phase and the signature in  $\rho_{hv}$  of the ML. The thickness of the ML depends both on the signature in  $\rho_{hv}$  and on the signature in  $Z_H$ , which correspond well to the first and second components. As such the variability in thickness is a good indicator of the overall variability of the ML. As shown in the correlation analysis, the thickness is also closely related to the vertical velocities inside and below the ML.

## 2.8 Summary and conclusions

In this work, a new algorithm was developed to automatically detect the melting layer (ML) on polarimetric RHI scans. This algorithm was then used to characterize the ML on high-resolution RHI scans collected by X-band polarimetric radars in different climatological regions.

The ML detection algorithm is based on the identification of strong vertical gradients in the reflectivity factor at horizontal polarization  $Z_H$  and the copolar cross-correlation coefficient  $\rho_{hv}$ . The algorithm takes RHI scans projected to Cartesian coordinates as input and is divided into two parts: in the first part the bottom and the top of the melting layer are detected using both  $Z_H$  and  $\rho_{hv}$ , while in the second part the estimation of the ML top is refined by using only  $Z_H$ .

The algorithm was validated by comparing the height of the top of the detected ML with freezing level measurements from collocated radio soundings. The freezing level estimation of the algorithm was shown to be accurate, with an average error close to the radial resolution of the radar and only a small negative bias. In addition, the distributions of the vertical fall velocities were compared between the liquid phase (below the detected melting layer) and the solid phase (above). The distributions are clearly separated with almost no overlap, showing that the algorithm separates well the liquid and the solid phases.

The shift in  $Z_{DR}$  and  $Z_H$  across the ML was analyzed in order to get a rough idea of the



attenuation effect of the ML. It was shown that the effect on  $Z_{DR}$  can be important and outweighs by far the attenuation effect caused by liquid stratiform rain, whereas the effect on  $Z_H$  is only small.

The ML detection algorithm was used to characterize the ML in terms of polarimetric and geometric signatures on four large datasets of radar scans from different topographical and climatological regions (south of France, Swiss Alps, Swiss plains and Iowa). Additionally, a hydrometeor classification was performed in the solid phase above the ML. The thickness of the ML was shown to be on average very similar on all datasets, with a slightly right skewed distribution and a mean between 300 and 330 m. Similarly, the horizontal variability of the thickness and the relative heights of the ML boundaries, characterized by their variograms, show very similar decorrelation ranges and slopes between datasets.

In terms of polarimetric signature, the ML has similar distributions in  $K_{dp}$ ,  $\rho_{hv}$  and  $Z_{DR}$  with the exception of the dataset from Davos in the Swiss Alps which has higher values of  $Z_{DR}$ . This could be due to the use of different radar waveguides. Differences in  $Z_H$  are more important, with variations in the mean ranging from 2 to 8 dBZ between datasets. Average values of the peak of  $Z_H$ , the minimum in  $\rho_{hv}$  and the vertical distance separating them were found to be in good agreement with observations made by Durden et al. (1997) over the Pacific tropical region.

Even though the geometrical structure of the ML is quite homogeneous on average, it is quite variable during and between precipitation events. To gain a better understanding of this variability a correlation analysis between descriptors of the ML was carried out. Results indicate that a thick ML is usually associated with a strong bright band, a higher vertical extension of precipitation, as well as a larger gradient of  $Z_H$  above the ML. A thicker ML is also associated with a higher distance between the peak in  $Z_H$  and the minimum in  $\rho_{hv}$ , a factor related to the concentration of hydrometeors. A higher concentration of particles will increase the diabatic cooling caused by the melting process, which could increase the thickness of the ML. Additionally, a significant dependency on the presence of rimed particles above the ML and the vertical velocity in the ML was found. Rimed particles are characterized by their higher density and their higher fall velocities, which leads to an increase in the distance travelled by a particle before complete melting.

Finally, a principal component analysis showed that the most important factors explaining the overall variability of the ML are (in order of importance) the fraction of riming, the gradient of  $Z_H$  in the solid phase, and values of  $\rho_{hv}$  inside the ML.

The analysis of the ML conducted during this work could be complemented with additional X-band radar datasets from other climatological regions, in order to verify the consistency of the characterization. Future work will be devoted to the extension of the algorithm to PPI and to other frequencies, in particular to the Swiss operational polarimetric C-band radar network.



# 3 Multifractal evaluation of simulated precipitation intensities

This chapter is adapted from the following article:

1. Wolfensberger, D., Gires, A., Tchiguirinskaia, I., Schertzer, D., and Berne, A.: Multifractal evaluation of simulated precipitation intensities from the COSMO NWP model, *Atmos. Chem. Phys.*, <https://doi.org/10.5194/acp-2017-73>, 2017.

This work presents a comparison of precipitation intensities simulated by the COSMO model with radar observations, over a wide range of spatial and temporal scales, using universal multifractals.

### 3.1 Summary

The framework of universal multifractals (UM) characterizes the spatio-temporal variability of geophysical data over a wide range of scales with only a limited number of scale-invariant parameters. This work aims to clarify the link between multifractals (MF) and more conventional weather descriptors and to show how they can be used to perform a multi-scale evaluation of model data.

The first part of this work focuses on a MF analysis of the climatology of precipitation intensities simulated by the COSMO numerical weather prediction model. Analysis of the spatial structure of the MF parameters and their correlations with external meteorological and topographical descriptors reveals that simulated precipitation tends to be smoother at higher altitudes, and that the mean intermittency is mostly influenced by the latitude. A hierarchical clustering was performed on the external descriptors, yielding three different classes, which correspond roughly to Alpine/continental, Mediterranean and temperate regions. Distributions of MF parameters within these three classes are shown to be statistically significantly different, indicating that the MF signature of rain is indeed geographically dependent.

The second part of this work is event-based and focuses on the smaller scales. The MF parameters of precipitation intensities at the ground are compared with those obtained from the Swiss radar composite during three events corresponding to typical synoptic conditions over Switzerland. The results of this analysis show that the COSMO simulations exhibit spatial scaling breaks that are not present in the radar data, indicating that the model is not able to simulate the observed variability at all scales. A comparison of the operational one-moment microphysical parameterization scheme of COSMO with a more advanced two-moment scheme reveals that, while no scheme systematically outperforms the other, the two-moment scheme tends to produce larger extreme values and more discontinuous precipitation fields, which agree better with the radar composite .

## 3.2 Introduction

Validation of precipitation fields simulated by a numerical weather prediction model is a delicate task as reference data (rain gauges, radar scans) are typically available at a different spatial and temporal resolution than the model. Traditional point-based verification scores are generally unable to provide sufficient information about the forecast quality, as they do not take into consideration the spatial structure and are affected by the so-called “double penalty” (Gilleland et al., 2009). Indeed, small displacements in the simulated forecast features will be penalized twice, once for missing the observation and again for giving a false alarm. The impact of this double penalty is related to the variability in the simulated fields, which tends to increase with the resolution of the model. Numerous methods have been proposed in recent years to address this issue. Some methods rely on the use of traditional scores but applied on filtered fields, estimating the forecast performance as a function of scale and precipitation intensity (e.g., Ebert, 2008; Mittermaier et al., 2013), while others detect specific features of forecast and verification fields and compare these features based on their attributes (e.g., Davis et al., 2006; Wernli et al., 2008). Yet another type of validation technique relies on the separation of scales with the use of space-frequency tools such as the 2D wavelet transform (Vasić et al., 2007).

Multifractals (MFs) offer a convenient way to analyze the variability of complex geophysical systems globally over a wide range of scales. In the context of MFs, the statistical properties of a field are related to the resolution by a power-law (Schertzer and Lovejoy, 1987). Universal Multifractals (UMs) are a framework of MFs based on the concept of multiplicative cascades, which allows for analysis and simulation of a high variability across scales with only a small number of parameters with physical meaning (e.g., Schertzer and Lovejoy, 1987; Lovejoy and Schertzer, 2007). In meteorology, UMs have been used to study a large variety of complex natural phenomena such as the distribution of rainfall intensities at the ground (e.g., Marsan et al., 1996; Gires et al., 2016, 2015), atmospheric turbulence (e.g., Parisi and Frisch, 1985a; Schertzer and Lovejoy, 2011) or climate change (e.g., Schmitt et al., 1995; Royer et al., 2008).

Gires et al. (2011) used the UM framework to compare simulations of Meso-NH, a non-hydrostatic numerical weather prediction (NWP) model developed by Météo-France and the Laboratoire d’Aérodynamique (e.g., Lafore et al., 1998; Cohard and Pinty, 2000), with composite radar images during a heavy convective rainfall event. This comparison showed that the radar quantitative precipitation estimation (QPE) and the model simulations were generally characterized by similar ranges of scaling and agreed quite well with a simple space-time scaling model.

Gires et al. (2011) focused on a rather flat area and a single event. It is therefore relevant to study the MF behavior of model simulations and radar observations over a more complex terrain and in a broader meteorological context. This work is thus divided into two parts. The first part aims to illustrate the use of MFs for characterizing regional patterns of precipitation and to relate them to meteorological and topographical features. To this end, a large-scale analysis of

## Chapter 3. Multifractal evaluation of simulated precipitation intensities

---

5 years of simulated precipitation intensities from the COSMO numerical weather prediction model is conducted. The MF properties of the corresponding climatology of precipitation intensities are then studied and related to several regional and meteorological descriptors. The second part of this paper extends the work of Gires et al. (2011) over Switzerland for three different meteorological situations (snowstorm, convective summer precipitation and stratiform rainfall) by using simulated precipitation intensities from the COSMO model run with different microphysical parameterizations.

This chapter is structured as follows: in Section 2, the COSMO model and the Swiss radar composite are briefly described. The studied events, radar datasets and model variables are then described in detail. Section 3 provides a short summary of the UM framework. In Section 4, a climatological analysis of precipitation intensities simulated by COSMO is performed with the UM framework in relation to external geographical and meteorological descriptors. In Section 5, a spatial and temporal analysis of precipitation intensities on the ground simulated by COSMO is performed during three characteristic events. The results are then compared with the UM analysis of the radar composite. Finally, Section 6 gives a summary of the main results and concludes this work.

### 3.3 Description of the data

#### 3.3.1 The COSMO model

Since an introduction to the COSMO model has been given in Section 1.2.2, only a small reminder of the key points of its microphysical parameterizations, which are of high importance in this work, will be given.

In COSMO, grid-scale clouds and precipitation are parameterized operationally with a one-moment scheme similar to Rutledge and Hobbs (1983) and Lin et al. (1983) with five hydrometeor categories: rain, snow, graupel, ice crystals and cloud droplets. The particle size distributions (PSD) are assumed to be exponential for all hydrometeors, except for rain where a gamma PSD is assumed. The only free parameter of the PSDs is the *slope* parameter  $\Lambda$  which can be obtained from the prognostic mass concentrations. The scale parameter  $\mu$  is equal to zero (exponential PSDs) for all hydrometeors except for rain where it is set to 0.5 by default. The *intercept* parameter  $N_0$  depends on the prescribed  $\mu$  for rain, but is constant during the simulation. or in the case of snow, is temperature dependent.

A more advanced two-moment scheme with a sixth hydrometeor category, hail, was developed for COSMO by Seifert and Beheng (2006). In this scheme all PSDs are assumed to be gamma distributions where the *intercept* and *slope* parameters are free parameters that can be obtained from the prognostic moment of order zero number concentration and from the prognostic mass concentration. As this scheme significantly increases the overall computation time it is currently not used operationally.

The precipitation intensity at the ground is the sum of the sedimentation fluxes of all hydrometeors at the lowest model level. Mass-diameter relations as well as velocity-diameter relations for the precipitating hydrometeors are assumed to be power-laws for both microphysical schemes, except for rain in the two-moment scheme, where a slightly more refined formula by Rogers et al. (1993) is used.

#### 3.3.2 Climatological study

In the first part of this work, a MF characterization of all precipitation intensities simulated by COSMO during 5 years is performed. The computed MF parameters are then compared with various descriptors. A total of 43115 hourly time steps of COSMO-2 simulations (at 2 km horizontal resolution) in analysis mode covering a period of 5 years (2011 to 2016) were retrieved from the MeteoSwiss archives. The first and last 100 kilometers of the COSMO-2 domain along both longitudinal and latitudinal directions were discarded from the analysis in order to avoid border effects. The remaining area is shown in Figure 3.2 (Domain 1). This area was then divided into 209 subsquares of size 64 x 64 (128 km x 128 km), with an overlap of two thirds between consecutive squares. This ratio has been chosen as a trade-off between representativity (total number of squares) and computation time.

Besides the MF parameters, which will be described later on, 11 local descriptors of the geography and meteorology were computed from the COSMO data within every square (Table 3.1). Spatial maps of all descriptors are given in Appendix A.1.

Name	Description	Unit
Average altitude	average altitude	m
Midpoint latitude	latitude of square center	degree north
Midpoint longitude	longitude of square center	degree east
Total precipitation	total precipitation during all years	mm
Standard deviation of precipitation	average standard deviation during timesteps with precip.	mm
Wet fraction	fraction of simulated precipitation amounts that exceed a threshold of 0.1 mm per hour	-
Geopotential	average geopotential height at 850 hPa	m
Wind speed	average wind speed at 850 hPa	m s <sup>-1</sup>
Wind direction	average wind direction at 850 hPa	degree
Temperature	average temperature at 850 hPa	K
Potential vorticity	average potential vorticity at 850 hPa	m <sup>2</sup> kg <sup>-1</sup> s <sup>-1</sup>

Table 3.1 – List and description of all meteorological and topographical descriptors used in the MF characterization of the climatology of precipitation intensities.

3.3.3 QPE comparison

3.3.3.1 Simulation of events

In the second part of this work, three precipitation events were simulated with COSMO and compared to the radar QPE in terms of the MF properties of their rainfall intensity fields. These events correspond to three typical meteorological situations observed over Switzerland. A brief description of the events is given in Table 3.2, and 500 hPa geopotential and pressure at mean sea level charts are shown in Figure 3.1. To simulate these events, COSMO was used with the standard “COSMO-2” set-up (COSMO, 2015). As was done in similar studies (Bohme et al., 2009), a spin-up time of 12 hours was used to account for the cold start of the model. For the initial and boundary conditions, analysis runs of the COSMO-7 model were used. This allows for forcing the model with the most accurate information available at the time of simulation. In addition, the events were also simulated using the non-operational two-moment scheme, while keeping all other namelist parameters unchanged. For all simulations, model outputs were written every 5 minutes of simulated time, which corresponds to the temporal resolution of the Swiss radar composite.

Day	Timeline	Number of time steps	Description
26 March 2010	08:00 - 18:00	144 (12 h)	Crossing of a strong cold front causing sudden drop of temperature followed by heavy graupel and snowfall as well as strong winds
08 April 2014	02:00 - 10:00	144 (12 h)	Stationary front with widespread stratiform precipitation over Switzerland
13 August 2015	12:00 - 24:00	144 (12 h)	Strong summer convection triggered by the presence of very warm and wet subtropical air over Switzerland

Table 3.2 – Short description of the three precipitation events considered.

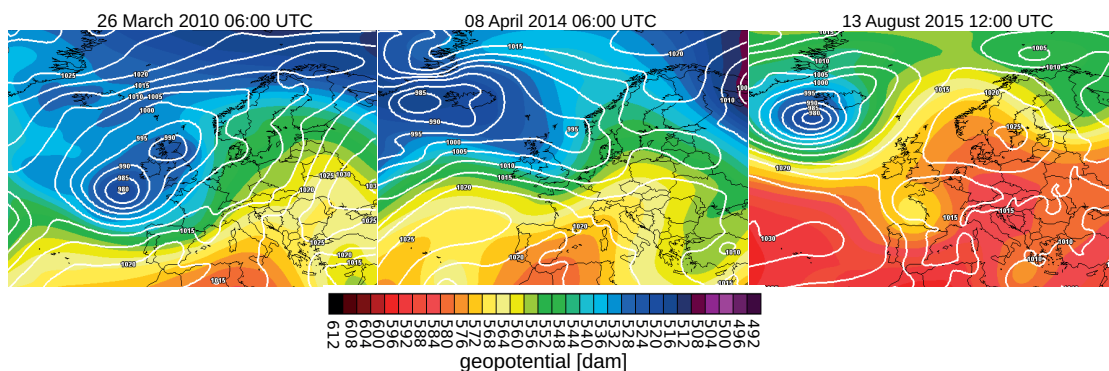


Figure 3.1 – 500 hPa geopotentials and pressure at mean sea level for the three considered events. Modified from <http://www.wetterzentrale.de/de/default.php>.



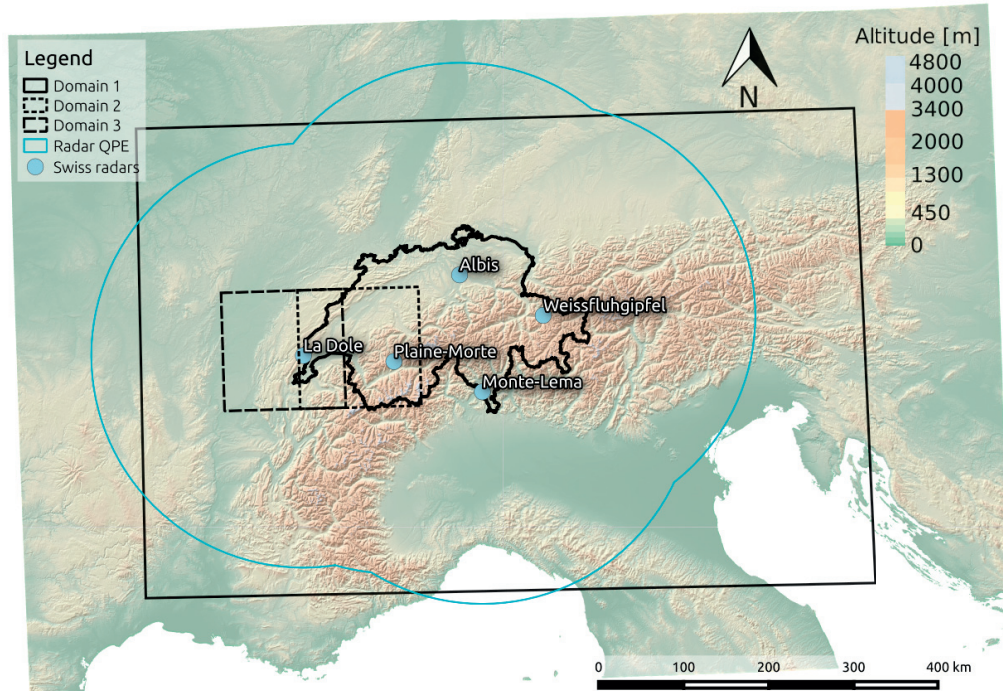


Figure 3.2 – Situation map showing the theoretical maximum extent of available QPE (light blue), the location of the Swiss operational radars (blue dots), the region used for the climatological study of COSMO precipitation intensities (domain 1), and the subregions centered over the precipitation events used in the QPE analysis (domains 2 and 3).

### 3.3.3.2 QPE data

In Section 3.6, precipitation intensities at the ground simulated by the COSMO are compared with the QPE product from the Swiss operational radar composite. The Swiss radar composite consists of PPI measurements of the four <sup>1</sup> operational polarimetric C-band radars. The QPE product of MeteoSwiss is computed in the following way: the linear equivalent radar reflectivity measurements at up to six  $1^\circ \times 1^\circ \times 83\text{m}$  clutter-free radar bins are corrected for partial beam-blocking and averaged to derive polar  $1^\circ \times 1^\circ \times 500\text{m}$  radar bins. Reflectivity measurements are then converted to equivalent precipitation intensity with a Marshall and Palmer (1948)  $Z - R$  relationship. The precipitation estimation at the ground is extrapolated from multi-radar observations aloft using a weighting function that depends on the altitude above the ground and the radar visibility. The correction for the vertical profile of reflectivity is done with an average profile based on aggregation over a few hours and over the visible part of the area located less than 70 km from the radar. More information on the MeteoSwiss QPE estimation can be found in Germann et al. (2006). Note that the Plaine-Morte radar was only installed in 2014 and was thus not available during the first event (26 March 2010). The Swiss radar composite extends radially up to 250 km from every single radar (Figure 3.2). However,

<sup>1</sup>The Weissfluhgipfel radar was not yet installed at the time of the considered events

the quality of the product improves with the proximity to the radar and in the areas where the radar scanning domains overlap. To perform a comparison of rain intensities, a smaller field of 128 km x 128 km was chosen in the center of the domain where the quality of the product is optimal (Domain 2 in Figure 3.2). For the second event (8 April 2014) the domain was moved slightly to the left in order to better follow the evolution of the precipitation event (Domain 3 in Figure 3.2).

### 3.4 The UM framework

#### 3.4.1 Multifractality

Let  $\mathcal{E}$  be a normalized (divided by its mean) conservative field, which can be one-or-two dimensional (time series or spatial map). The field  $\mathcal{E}$  also needs to have the same length in all dimensions, and this length must be a power of two.

The fractal dimension  $D_f$  of  $\mathcal{E}$  indicates how a corresponding binary field (where all values larger than a given threshold are set to 1) scales with the resolution. The resolution  $\lambda_r$  is defined by the ratio between the largest possible scale  $L$  and the considered observation scale  $l$  ( $\lambda_r = L/l$ ).

$$N_{\lambda_r} = \lambda_r^{-D_f} \quad (3.1)$$

where  $N_{\lambda_r}$  is the number of positive samples (rainy pixels for example) at a given resolution, which can be obtained with the help of box counting. An example of this box counting method is given in Appendix A.2.

It is possible to interpret this result in a probabilistic way. Indeed, consider a line or cube of size  $l$ , then  $p$  is the probability that it intersects the binary precipitation field  $\mathcal{E}$ . This probability scales with the resolution:

$$p = \frac{\lambda_r^{D_f}}{\lambda_r^D} = \lambda_r^{-c_f} \quad (3.2)$$

where  $D$  is the dimension of the field (1 for a time series, 2 for a spatial field) and  $c_f = D - D_f$  is called the fractal codimension of the field.

It is clear that the values of  $D_f$  (and  $c_f$ ) depend on the threshold that is used. Several thresholds and corresponding values of  $D_f$  are thus required to characterize the field.

In the MF framework this characterization is performed with scale-independent thresholds (Schertzer and Lovejoy, 1987), which yields a MF version of Equation 3.2.

$$p(\mathcal{E}_{\lambda_r} \leq \lambda_r^\gamma) \approx \lambda_r^{-c(\gamma)} \quad (3.3)$$

where  $c(\gamma)$  is the codimension function which is convex and increasing and  $\gamma$  is a so-called singularity, which is independent of scale.  $\lambda_r^\gamma$  can thus be seen as a scale invariant threshold. Since  $c(\gamma)$  takes several values, MFs can be understood as a hierarchy of embedded fractal sets.

It can be shown that Equation 3.3 implies that the statistical moments  $q$  of the field scale with the resolution (Schertzer and Lovejoy, 1987):

$$\langle \mathcal{E}_{\lambda_r}^q \rangle \approx \lambda_r^{K(q)} \quad (3.4)$$

where  $K(q)$  is the moment scaling function which is related to  $c(\gamma)$  by a Legendre transform (Parisi and Frisch, 1985b). For a conservative field  $\langle \mathcal{E}_{\lambda_r} \rangle = 1$ .

The quality of the scaling can be studied with the trace moment (TM) method which consists of a log-log plot of the up-scaled fields as a function of the resolution  $\lambda_r$  for each moment  $q$ , the slope being the moment scaling function.

In the UM framework (Schertzer and Lovejoy, 1987), the moment scaling function for a conservative field  $K_c(q)$  can be fully characterized with only two parameters,  $\alpha$  and  $C_1$ .

$$K_c(q) = \frac{C_1}{\alpha - 1} (q^\alpha - q) \quad (3.5)$$

$C_1$  is the mean intermittency codimension and measures the clustering of the average intensity at increasing scales.  $C_1$  is equal to zero when the field is homogeneous.  $\alpha$  is the multifractality index and measures the clustering variability with respect to the intensity level;  $\alpha \in [0, 2]$ .

The size of the sample limits the insight one can get of a statistical process. For a MF processes, if  $N_s$  samples are available this will result in a maximum singularity  $\gamma_s$  (and corresponding moment order  $q_s$ ) beyond which the values of the statistical estimates of the codimension and moment scaling function are not considered as reliable (e.g., Schertzer and Lovejoy, 1987; Lovejoy and Schertzer, 2007).

### Chapter 3. Multifractal evaluation of simulated precipitation intensities

---

It can be shown that in the MF framework,  $q_s$  and  $\gamma_s$  are equal to the following:

$$q_s = \left( \frac{D + D_s}{C_1} \right)^{\frac{1}{\alpha}} \quad \text{and} \quad \gamma_s = \alpha' C_1 \left( \frac{D + D_s}{C_1} \right)^{\frac{1}{\alpha'}} \quad (3.6)$$

where  $\frac{1}{\alpha} + \frac{1}{\alpha'} = 1$  and  $D_s$  is the sampling dimension defined by  $N_s = \lambda_r^{D_s}$ .

An example of the use of  $\gamma_s$  can be found in Royer et al. (2008) who investigated the impact of climate change on rainfall extremes with a climate model. They observed an increase in  $\gamma_s$  over time, which could result in a possible increase in the intensity of rainfall extremes over the next hundred years. Douglas and Barros (2003) and Hubert et al. (1993) also used the maximum singularity  $\gamma_s$  in the estimation of probable maximum precipitation.

In this work, the UM parameters are estimated with the double trace moment (DTM) method (Lavallée et al., 1993). This method relies on the fact that, in the context of UM, the moment scaling function  $K(q, \eta)$  of the field  $\mathcal{E}_{\lambda_r}^{(\eta)}$ , obtained by raising the field  $\mathcal{E}$  at a power  $\eta$  and up-scaled at resolution  $\lambda_r$ , can easily be expressed as a function of  $\alpha$  (Lavallée et al., 1993).

$$\langle \left( \mathcal{E}_{\lambda_r}^{(\eta)} \right)^q \rangle \approx \lambda_r^{K(q, \eta)} = \lambda_r^{\eta^\alpha K(q)} \quad (3.7)$$

$\alpha$  is thus the slope of the linear part of  $K(q, \eta)$  as a function of  $\eta$  in a log-log plot.

#### 3.4.2 Non-conservative fields

In the case of a non-conservative field  $\phi$ , we have  $\langle \phi_{\lambda_r} \rangle \neq 1$ .

One way to consider non-conservative fields within the UM framework it to assume that they can be expressed as the following:

$$\phi_{\lambda_r} = \mathcal{E}_{\lambda_r} \lambda_r^{-H} \quad (3.8)$$

where  $H$  is the non-conservation parameter ( $H = 0$  for conservative fields) and  $\mathcal{E}$  is a conservative field characterized by a moment scaling function  $K_c(q)$  with parameters  $C_1$  and  $\alpha$ .

The moment scaling function of the non-conservative field  $\phi_{\lambda_r}$  is then given by:

$$K(q) = K_c(q) - Hq \quad (3.9)$$

$H$  can be related to the spectral slope  $\beta$  by:

$$\beta = 1 + 2H - K_c(2) \quad (3.10)$$

where  $\beta$  is the exponent of the power law that characterizes the relation between power spectrum and wave numbers:

$$E(k) \propto k^{-\beta} \quad (3.11)$$

Hence the larger the value of the slope  $\beta$ , the shorter the decorrelation range. If  $\beta$  is larger than the dimension of the field, the field is non-conservative.

$\mathcal{E}_{\lambda_r}$  can be estimated from  $\phi_{\lambda_r}$  with a fractional integration (for  $H < 0$ ) or differentiation (for  $H > 0$ ) of order  $H$ , which is equivalent to a multiplication by  $k^H$  in the Fourier space. In practice however, for  $H > 0$ , particularly when  $H > 0.5$ ,  $\mathcal{E}_{\lambda_{\max}}$  (the field  $\mathcal{E}$  at the maximum resolution) is often approximated by the renormalized absolute fluctuations of the field.

$$\mathcal{E}_{\lambda_{\max}}(i) = \frac{|\phi_{\lambda_{\max}}(i+1) - \phi_{\lambda_{\max}}(i)|}{\langle |\phi_{\lambda_{\max}}(i+1) - \phi_{\lambda_{\max}}(i)| \rangle}, \quad i = 1, 2, \dots, N \quad (3.12)$$

Table 3.3 provides an overview of all MF parameters as well as their interpretation, while Appendix A.3 provides some visual examples of how varying the MF parameters affects the spatial structure of randomly generated MF fields.

### Chapter 3. Multifractal evaluation of simulated precipitation intensities

Parameter name		Interpretation
$\alpha$	multifractality index	When $\alpha = 0$ , the field is mono-fractal which means that a single fractal dimension is sufficient to fully characterize the field. The higher $\alpha$ , the larger the variability within areas with precipitation.
$C_1$	mean intermittency	Measures how concentrated the average field is, $C_1 = 0$ for a uniform field. The larger $C_1$ , the larger the intermittency of the field. High $C_1$ associated with high $\alpha$ implies strong extremes.
$\beta$	Negative of the spectral slope	The larger $\beta$ the shorter the decorrelation range of the data. If $\beta = 0$ , the power spectral density is the one of white noise, meaning there is no decorrelation. When $\beta$ is large, large-scale phenomena have a large contribution to the variability in the data, which means that the fields have a larger correlation range (smoother fields).
$H$	non-conservation parameter	Scale-independent proportionality factor relating a conservative field to the non-conservative field (a field for which the average is not scale independent). Can be seen as a smoothing factor. If $H$ is positive, the field is too smooth and one needs to differentiate it to retrieve a conservative field. If $H$ is negative, the field is too discontinuous and one needs to integrate it to retrieve a conservative field.
$\gamma_s$	maximum singularity	Maximum observable singularity (scale independent threshold) from the data. Large $\gamma_s$ implies that stronger extremes are present in the data.
$R^2$	TM coefficient of determination	Coefficient of determination of the relation between a given moment of order $q$ and the scale (Equation 3.4) on a log-log plot. If the field is MF the plot is a straight line with slope $K(q)$ . In practice, $q = 1.5$ is often used as a reference to determine $R^2$ . $R^2$ can be seen as an estimation of the quality of scaling and of the viability of the MF approach for the data.
$D_f$	Fractal dimension	Factor relating the number of rainy observations at a given scale to the corresponding scale. The larger $D_f$ , the more uniform the binary precipitation field (obtained with a threshold of zero) is.

Table 3.3 – Overview of all MF parameters

### 3.4.3 Spatio-temporal analysis

The MF analysis of time series of two-dimensional fields, such as the ones considered in this study, can be performed both in space, by considering an ensemble of two-dimensional fields (one sample for every time step), or in time, by considering an ensemble of one-dimensional time series (one sample for every coordinate in the two-dimensional field).

A simple spatio-temporal scaling model (e.g., Marsan et al., 1996; Deidda, 2000; Macor et al., 2007; Radkevich et al., 2008) is based on the hypothesis of an anisotropy coefficient between space and time:

$$K_{\text{space}}(q) = \frac{K_{\text{time}}(q)}{1 - H_t} \quad (3.13)$$

where  $H_t$  is the anisotropy coefficient between space and time, which in the theory of Kolmogorov (e.g., Kolmogorov, 1962; Marsan et al., 1996) is equal to one third. This result implies identical  $\alpha$  and proportional  $C_1$  and  $H$  parameters.

$$\frac{C_{1,\text{space}}}{C_{1,\text{time}}} = \frac{H_{\text{space}}}{H_{\text{time}}} = \frac{1}{1 - H_t} \quad (3.14)$$

## 3.5 Climatological analysis of MF parameters

Within all 209 selected squares (Section 3.3.2), the MF parameters  $\alpha$ ,  $C_1$ ,  $\beta$ ,  $H$ ,  $\gamma_s$ ,  $R^2$  and  $D_f$  were computed both in time and in space by performing an ensemble average, i.e. by taking the mean parameters over all the available realizations of the process. In space, every time step is considered as a realization of a two-dimensional geophysical process, while in time every COSMO-2 grid point is considered as a realization of a one-dimensional geophysical process (time series). For the analysis in space, this implies 43115 realizations of a 64 x 64 2D field and for the analysis in time, 4096 realizations (64 x 64) of a time series of length 32768 ( $2^{15}$  which is the closest power of 2 to 43115). Analysis of the overall temporal power spectrum (not displayed) revealed the presence of a strong peak centered around a resolution of 3 hours, which is very likely to be caused by the fact that in the assimilation scheme of COSMO, target values (references for differences) are updated only at discrete times, which for surface synoptic observations is every 3 hours. To remove the effect of the nudging in the estimation of MF parameters, only the larger timescales (from 8 hours to 5 years) were considered. Even though some areas are characterized by values of  $H > 0.5$  (non-conservative fields), it was decided to treat all areas in a consistent way, by working on the original fields instead of the fluctuations. Indeed, it was observed that using fluctuations for areas where  $H > 0.5$ , was causing important discontinuities in the spatial structure of MF parameters.

Indeed, using fluctuations is only a crude way to address the non-conservativity of the fields. A proper correction using fractional integration would allow for a much smoother correction, since it is proportional to  $H$ , but is computationally intractable because of the very large dataset that is used.

In order to test the effect of zeros on the overall analysis, the MF parameters were also estimated in space<sup>2</sup> by using only the fields where there is precipitation over at least 50% of the surface. This did, however, not impact the main conclusions in terms of correlations and spatial structure of the MF parameters. Hence the subsequent study was performed on the raw precipitation fields without any kind of filtering.

### 3.5.1 Correlation study

In the first step, the relationships between MF parameters evaluated in time and space and the descriptors detailed in Table 3.1 were analyzed by looking at the non-parametric (Spearman) correlations. Figure 3.3 displays the correlation plots for the MF parameters in space and time.

The following conclusions can be drawn from the correlation plots.  $D_f$  is strongly correlated with the latitude, indicating that the fractal dimension of rain is larger at higher latitudes (i.e. cooler climates).  $D_f$  is also quite strongly correlated to the wet fraction: the more often it rains, the higher the fractal dimension. Similarly  $C_1$  also has a strong latitudinal trend and tends to decrease in regions with a high wet fraction (less intermittency), which is typically the case in cooler climates.  $\alpha$  also seems to show a latitudinal trend, though not as strong as for  $C_1$  and  $D_f$ . The link between  $\alpha$  and the standard deviation is not obvious since the standard deviation is a second-order statistic, while the UM parameters are based on all moments.  $C_1$  and  $\gamma_s$  tend to decrease with the altitude while  $\beta$  and  $H$  tend to increase. This could be due to orographic effects, precipitation over mountains being both dominated by large-scale circulations and generally abundant.

The correlation values are roughly consistent in time and in space, although the ones in time are generally higher. In time the correlation between  $\beta$  and  $H$  is lower than in space. This can be explained by the lower values of  $\beta$  in time. Because of this and as a consequence of Equation 3.10,  $H$  becomes more correlated with  $\alpha$  and  $C_1$ .

### 3.5.2 Hierarchical clustering

A hierarchical clustering of all 209 areas was performed based on the value of their descriptors (Table 3.1), using the Ward linkage method (Ward, 1963). Investigation of the dendrogram gives an optimal number of clusters of either three or six. Figure 3.4 shows the resulting classification for three different clusters.

---

<sup>2</sup>In time, it would not be possible to filter out non rainy time steps, as it would break the continuity of the time series.



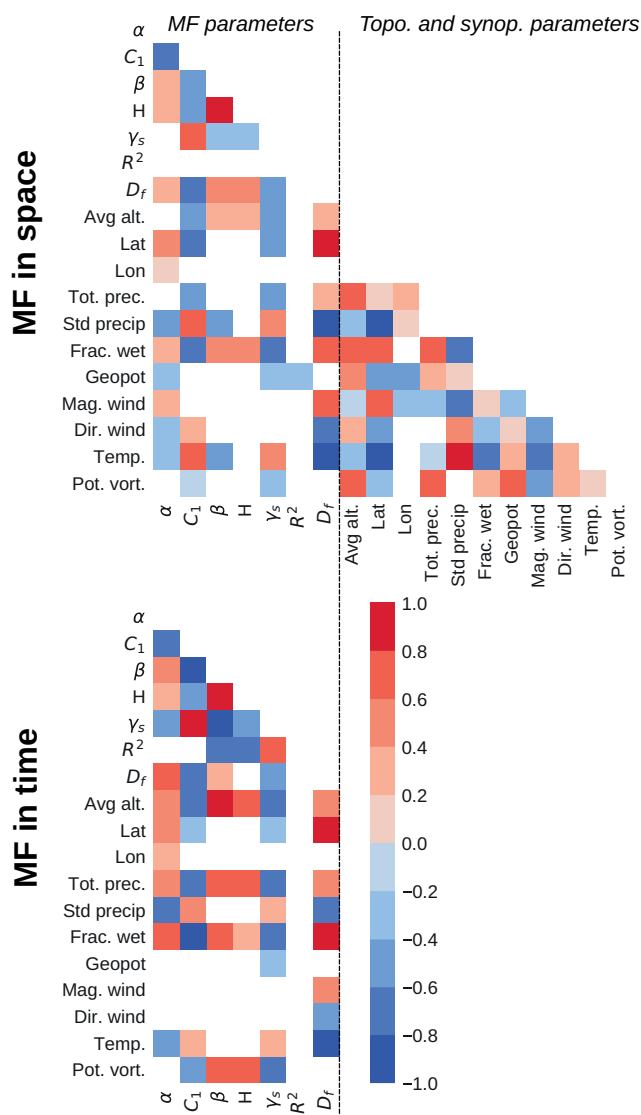


Figure 3.3 – Correlation plots showing the Spearman (rank) correlation between MF parameters and descriptors. **(a)** MF parameters estimated in space, and **(b)** with MF parameters estimated in time. Note that the part on the right of the correlation plot in time has been truncated since it is the same as on the correlation plot in space. Correlations that are not statistically significant (for a significance level of 5%) and correlations which are not consistent in sign between time and space are left in white.

As could be expected, the clustering of the meteorological and topographical descriptors results in a meaningful spatial distribution. Indeed, all clusters are spatially very coherent, with cluster 1 corresponding mostly to the Alpine regions, from the Mediterranean Sea to Austria, cluster 2 corresponding mostly to the cooler temperate regions in the east of France and south of Germany, and cluster 3 corresponding to the warmer Mediterranean regions in the south of France, in Italy and the Balkans. Note that over land areas a somewhat similar classification

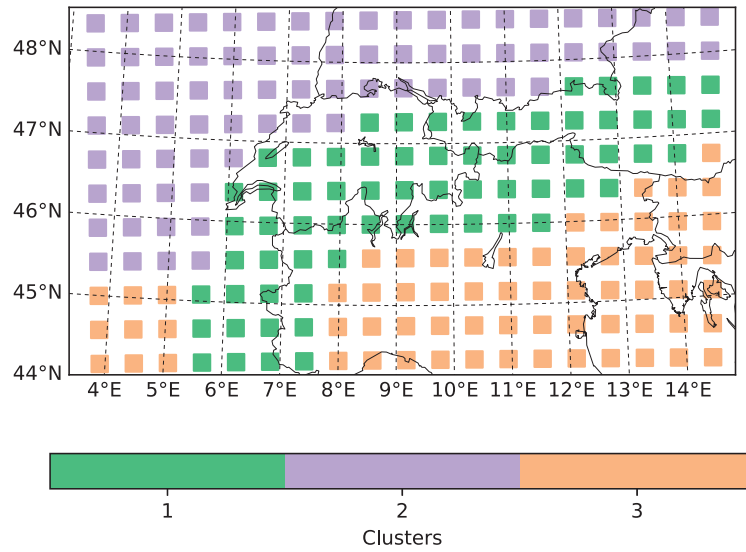


Figure 3.4 – Hierarchical clustering of the 209 regions into three clusters based on the meteorological and topographical descriptors listed in Table 3.1.

can be obtained by aggregating classes of the famous Köppen (1936) climate classification. A comparison between the meteorological clustering and the Köppen classification is performed in Appendix A.4.

The distributions of MF parameters within these clusters, as illustrated in Figure 3.5, highlight some obvious discrepancies in MF parameters between clusters. In space,  $\alpha$ ,  $H$ ,  $\beta$  and  $D_f$  seem to be lower in cluster 3 than in the others, while  $C_1$  and  $\gamma_s$  are higher. Clusters 1 and 2 do not exhibit such marked differences but differ nonetheless by stronger values of  $D_f$  and slightly larger values of  $H$ ,  $\beta$  and  $\alpha$ . In time, cluster 1 (Alpine regions) is characterized by high values of  $\alpha$  and  $\beta$  and low values of  $C_1$ , which indicates frequent rainfall and a large variability in intensities. Cluster 2 differs by its low values of  $\beta$  and  $H$ , indicating that small temporal frequencies play a bigger role in the overall variability in precipitation.

The statistical significance of these discrepancies was confirmed both with the MANOVA (multivariate analysis of variance) and the non-parametric Kruskal-Wallis statistical tests. All tests were performed with a significance level of 2.5%. The MANOVA reveals that the multivariate means of MF parameters (both in time and space) are significantly different between the three clusters, as well as between all three pairs of clusters taken separately (1 vs 2, 2 vs 3 and 1 vs 3). The non-parametric Kruskal-Wallis test, performed separately for all MF parameters, reveals that distributions of all MF parameters are significantly different between the three clusters. A pairwise comparison (1 vs. 2, 2 vs. 3 and 1 vs. 3) reveals that, in time, all MF parameters are significantly different between all pairs of clusters, except for  $H$  which is not statistically different between clusters 1 and 2. In space, the situation is similar, but this time it is  $C_1$  and  $\gamma_s$  which are not significantly different between clusters 1 and 2.

### 3.5. Climatological analysis of MF parameters

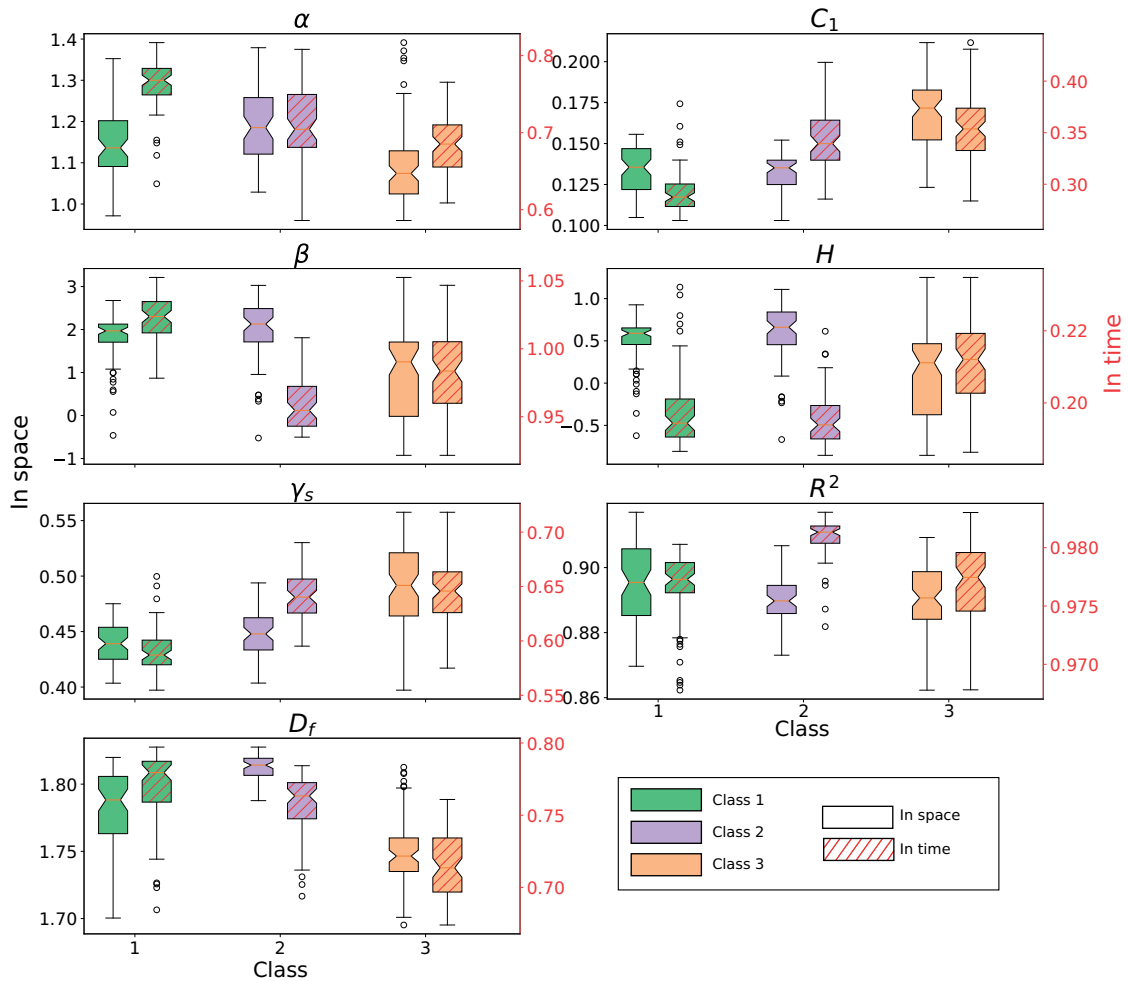


Figure 3.5 – Boxplots showing the distributions of MF parameters within the clusters. MF parameters estimated in time are shown with a dashed pattern. Note that the left y-axis applies to MF parameters in space and the right y-axis (in red) to MF parameters in time (the boxplots indicated with a red hatch).

To summarize, the statistical analysis shows that the MF parameters of precipitation intensities are significantly different within the three climatological clusters.

#### 3.5.3 Spatial structure of MF parameters

Figure 3.6 shows the spatial structure of MF parameters in space and reveals that  $\alpha$  is particularly large over Bavaria, the Piemonte region of Italy and the Champagne region of France. However these “clusters” of large values are quite difficult to relate to other trends, especially in terms of descriptors. Generally, the Swiss Alps are characterized by relatively low values of  $\alpha$ . In terms of  $C_1$ , there is a clearer trend, with a strong latitudinal and elevational negative gradient, which can be related to an increase in overall precipitation amounts. In terms of  $\beta$ , the

### Chapter 3. Multifractal evaluation of simulated precipitation intensities

---

regions over Italy show smaller values, which tend to indicate that precipitation events exhibit strong high-frequency components (such as for example short convective storms). Over the Alps and the more continental regions, where the precipitation systems are mostly frontal,  $\beta$  increases. The trend is similar for  $H$  which is related to  $\beta$ . For  $\gamma_s$ , we observe a similar trend to  $C_1$  with a decrease with altitude and elevation. This indicates that precipitation extremes are stronger in southern regions. For  $R^2$  it is difficult to identify a proper spatial structure, except that the foothill regions of the Alps generally have large  $R^2$  values. Finally for  $D_f$ , there is mostly a latitudinal trend: the value of  $D_f$  increases with the latitude, which can be related to a decrease in the number of zeros (smaller  $C_1$  and generally larger  $\alpha$ ).

In time, similar conclusions can be drawn for  $C_1$ ,  $D_f$ ,  $\gamma_s$  and  $\beta$ . For the other parameters, the latitudinal trend seems to be much more visible than in space, especially for  $H$  and  $R^2$ .  $R^2$  seems to be generally larger in time than in space. Unlike in space, for  $\alpha$  in time there is a clearer dependency on the altitude.  $\alpha$  in time tends to be larger in mountainous regions, indicating a larger temporal variability in precipitation intensities in these regions.

To summarize, the MF signature of precipitation is related both to the topography, the climate and the typical meteorological conditions. As such MFs can be used as a way to characterize precipitation fields and assess the realism of simulated atmospheric variables.

### 3.5. Climatological analysis of MF parameters

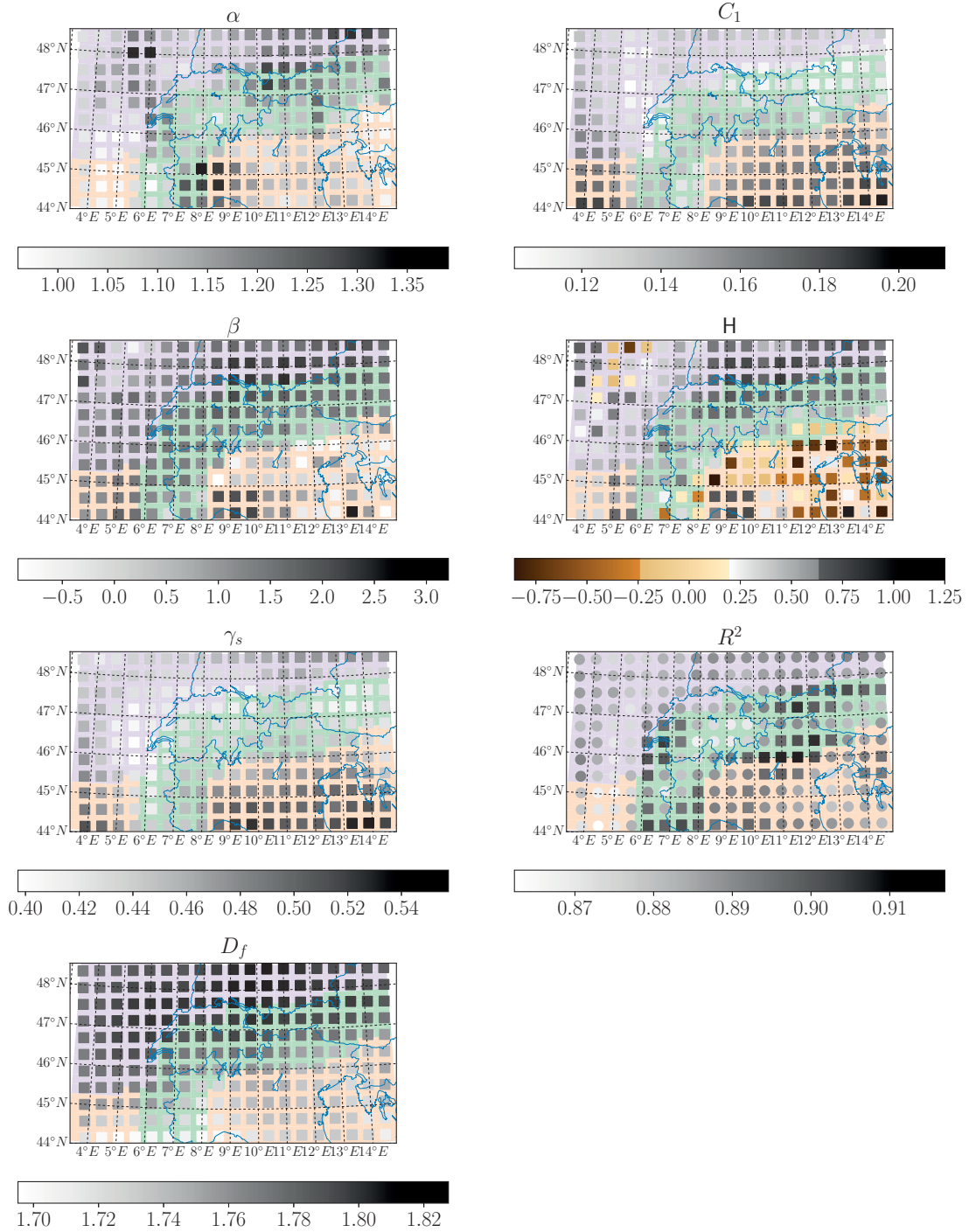


Figure 3.6 – Spatial representation of the MF parameters estimated in space for all areas. The special colormap for  $H$  has been chosen to separate positive and negative values and highlight non-conservative areas where  $|H| > 0.5$ . For  $R^2$ , circles represent all zones where  $R^2 < 0.9$ , whereas squares represent all zones with good scaling ( $R^2 \geq 0.9$ ). As previously mentioned, the size of the represented squares is not to scale. The colors in the background correspond to the hierarchical classification.

### 3.6 Comparison of simulated precipitation with radar QPE

The previous section presented the MF approach in a climatological context, which helps to link meteorology/geography and MF parameters. In the present section, we evaluate the quality of the precipitation simulated by COSMO with two different microphysical schemes, by comparing it with quantitative precipitation estimations from the Swiss radar network using the UM framework. This comparison requires the COSMO model to be run at the radar temporal resolution (5 minutes) in a very expensive setup (two-moment scheme). As such, a climatological comparison over several years is not feasible from a computational point of view. Hence, the comparison is now conducted on the event scale, which also makes the intercomparison of the microphysical parameterizations easier.

The power law  $Z - R$  relationship by Marshall and Palmer (1948), which is used by MeteoSwiss to derive the QPE, does not correspond with the  $Z - R$  relationships derived from the COSMO microphysical parameterizations. This explains part of the discrepancy between radar QPE and simulated precipitation intensities, but in general should not impact the validity of the MF comparison. Indeed, if the  $Z - R$  relationship derived from the COSMO parameterizations can be approximated by a power law, then the correction needed to account for discrepancies in  $Z - R$  relationships is itself a power law:  $R_{\text{corr}} = aR^b$ , where  $R_{\text{corr}}$  is the precipitation intensity one would obtain by first converting COSMO precipitation intensities to reflectivities and then back to precipitation intensities using the radar QPE  $Z - R$  relationship. It can be shown (Tessier et al., 1993), that in the context of UM, the corrected field will have the same value of  $\alpha$  and the same scaling properties as the original field, while  $C_1$  will be multiplied by  $b^\alpha$ . Moreover, for the one-moment scheme, it was observed that while the intercept parameter  $a$  changes significantly, the exponent parameter  $b$  is almost the same:  $R_{\text{corr}} = 0.68R^{0.98}$ . As the exponent 0.98 is close to unity, this implies an almost direct proportionality, and as such even  $C_1$  should barely be affected. Note that this power law was derived by using the T-matrix method (Mishchenko et al., 1996) to compute radar cross sections at C-band.

For the two-moment scheme, things are more complicated as no one-to-one relationship exists between rain rate and reflectivity. However, a rough estimation of the error in  $C_1$  was derived by considering a representative set of rainy time steps from all events. The estimated values of  $b$  for the two-moment scheme varies between 0.81 and 1.23, which would imply a maximum relative error in  $C_1$  of 51% on spatial fields and 23% on time series.

Overall, correcting precipitation fields for discrepancies in the  $Z - R$  relation is challenging, especially in the solid phase and for the two-moment scheme, where deriving a  $Z - R$  relation from the model parameterization is difficult. However, in the MF context, only  $C_1$  should be affected and only with significant solid precipitation or when using the two-moment scheme. This should be kept in mind when interpreting  $C_1$  values.

### 3.6.1 Scaling analysis

A MF comparison of the precipitation fields simulated by COSMO in its one-moment and two-moment schemes with the QPE product from the Swiss radar composite was performed. As a first step, a spectral analysis was performed both in time (ensemble of one-dimensional time series of precipitation intensities) and in space (ensemble of two-dimensional maps of precipitation intensities).

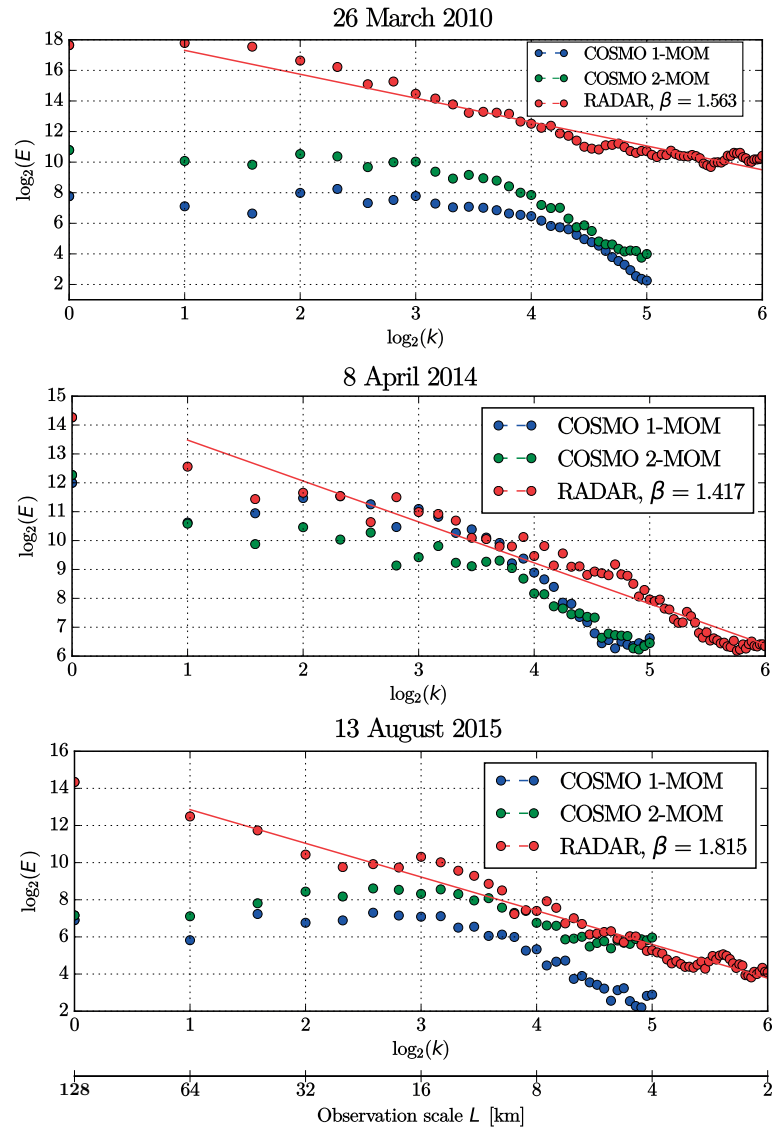


Figure 3.7 – Spectral analysis in space of the QPE products during the three events. The displayed lines are best-fit lines. The associated value of  $\beta$ , computed from the radar QPE data, is given in the legend. Note that the maximal represented observation scale, which corresponds to the Nyquist frequency, is twice the maximal resolution.

### Chapter 3. Multifractal evaluation of simulated precipitation intensities

---

Figure 3.7 shows the spectral analysis in space for all events and data. A best-fit line is shown for the radar QPE from which the value of  $\beta$  is computed.  $\beta$  is equal to  $-m$ , where  $m$  is the slope of the best-fit line.

For the 26 March 2010, we observe a single scaling regime for the radar QPE, with a good scaling both on large (16-64 km) and small scales (2-16 km), as the spread around the line is relatively small. For the model intensities, we observe strong discrepancies with the radar QPE in terms of spectral slope at smaller scales (2 – 8 km), which are not well represented. A possible explanation for this break in scaling properties of the model is the fact that large scales are dominated by the dynamics of the model (primitive equations of the atmosphere), whereas smaller scales are dominated by the parameterizations of subgrid phenomena (turbulence, convection). However, even at larger scales (8-64 km), the agreement between radar QPE and model simulations is still quite poor in terms of spectral slope. Obviously, for this rainfall event, COSMO is not able to recreate the spatial structure of precipitation observed by the radar.

For the 8 April 2014, the scaling is similar between radar and model precipitation intensities, possibly indicating that for this stratiform rain event, parameterizations and dynamics match better. Both radar and simulations show a weak scaling break at around 8 km.

For the last event, we observe again a good scaling for the radar QPE and a much worse scaling for the model precipitation intensities. However, in contrast with the first event, the larger scales ( $> 16$  km) are not well represented. Indeed, inspection of the time series of precipitation shows that COSMO is not able to locate accurately the convective cells of precipitation and generally overestimates their extent. In terms of microphysical parameterizations, we observe that the spectral slopes of the one-moment scheme are generally closer to the ones obtained from the radar QPE. This is especially visible for the last (convective) event, where the COSMO simulations show weak scaling ( $\beta$  close to zero). This implies that the simulated rainfall intensities are dominated by small-scale features, while large-scale features are underestimated. Note also that for large-scale features, the power density function of COSMO simulations corresponds to white noise, indicating that the COSMO model has a shorter decorrelation range than the radar data.

The spectral analysis in time (not displayed) generally shows similar results, but with larger values of  $\beta$  and overall better scaling (less spread).

Table 3.4 displays the non-conservation parameter  $H$  and the fractal dimension  $D_f$  evaluated for time series of precipitation intensities (analysis in time) and for spatial fields of precipitation intensities (analysis in space), for both the radar QPE (in regular font), the COSMO one-moment scheme (in bold), and the COSMO two-moment scheme (in italic) and for all events. A value of  $H$  larger than 0 indicates that the field is smoother than the observed field from a direct MF cascade process, and a value of  $H$  smaller than 0 indicates that the field is too discontinuous. The larger  $D_f$ , the more uniform the binary precipitation field is. In space  $D_f = 2$  implies that it rains everywhere, while in time  $D_f = 1$ , implies that it rains all the time.



### 3.6. Comparison of simulated precipitation with radar QPE

Taking the radar as a reference, one sees that the convective event is characterized by the largest values of  $H$ , followed by the snowfall event and the stratiform event. When comparing  $H$  between COSMO and the radar QPE, one observes that  $H$  in time is always larger with the one-moment scheme than on the radar QPE, indicating that the temporal structure of the simulated fields is likely to be too smooth. In space, the trend is not as obvious and the match between the radar QPE and the precipitation intensities simulated with the one-moment scheme seems better. In terms of fractal dimension, it can be seen that for all events, both in space and time, the radar QPE has the most discontinuous binary precipitation field due to its smaller values of  $D_f$ . COSMO simulations are characterized by larger values of  $D_f$ , indicating a wider coverage of precipitation and less convoluted precipitation fields and time series. It is interesting to notice that the two-moment scheme gives values of  $D_f$  that are closer to those of QPE, which indicates that it is better at simulating small-scale variations in the temporal and spatial occurrence of precipitation.

Overall, it is worth noticing that the two-moment scheme almost always has smaller  $H$  values than the one-moment scheme, which indicates that it is more discontinuous both in time and space.

In order to account for the fact that the fields are mostly non-conservative ( $|H| > 0.5$ ), and to treat all fields in a consistent way, all further analysis were performed on fluctuations of the original fields (Equation 3.12). Note that while this does not result in perfectly conservative fields, it still makes them more conservative since all values of  $|H|$  are smaller than 0.5 after taking the fluctuations.

	26 March 2010	8 April 2014	13 August 2015
$H_{\text{space}}$	0.411/ <b>0.432</b> /0.752	0.342/ <b>0.500</b> /0.260	0.651/ <b>0.612</b> /0.332
$H_{\text{time}}$	-0.044/ <b>0.615</b> /0.262	0.232/ <b>0.938</b> /0.238	0.696/ <b>0.818</b> /0.265
$D_{f,\text{space}}$	1.793/ <b>1.904</b> /1.825	1.836/ <b>1.921</b> /1.900	1.804/ <b>1.869</b> /1.849
$D_{f,\text{time}}$	0.893/ <b>0.960</b> /0.958	0.946/ <b>0.969</b> /0.937	0.877/ <b>0.944</b> /0.930

Table 3.4 – Values of the non-conservation parameter  $H$  and the fractal dimension  $D_f$  in time and space for all events for the radar QPE, the COSMO **one-moment scheme** and the COSMO *two-moment scheme*.

Figure 3.8 shows the TM analysis in space and time for the three events and for a value of  $q = 1.5$ . The value of  $K(q = 1.5)$  is the slope of the best-fit lines. Repeating the TM analysis for various values of  $q$  allows us to characterize  $K(q)$  and to estimate  $\alpha$  and  $C_1$ . For the first two events a scaling break can be observed at large scales for the COSMO precipitation intensities (64-128 km). These scales were excluded from the analysis due to the limited number of points in this scale range. For consistency with the observations of the spectral analysis, the scale range of 2-8 km was excluded from the analysis for the first event. This scale range does not scale well on COSMO simulations when compared with radar observation in this event. For the last event, two scaling regimes are observed for the COSMO intensities (2-16 and 16-128 km), which were studied separately. On the contrary, for the radar QPE no scaling break is

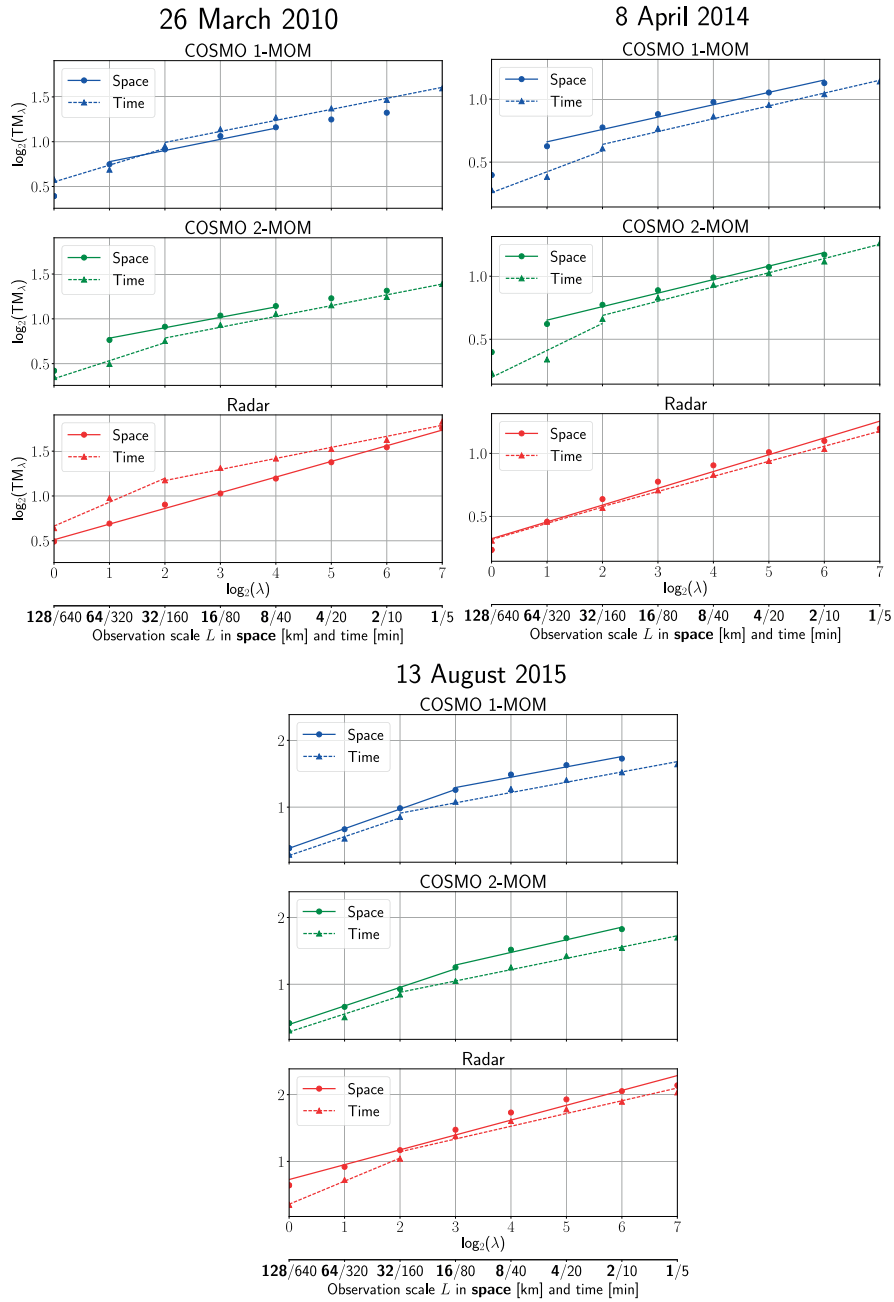


Figure 3.8 – Scaling (TM) analysis of the QPE product during the three events obtained with  $q = 1.5$ . The displayed lines are best-fit lines taking into account a possible scaling break.

observed in space. In time, a weak scaling break can be observed both for radar and COSMO intensities at a resolution of around 160 minutes. Hence, results are discussed only for the timescales between 5 and 160 min (smaller scales).

3.6.2 Spatio-temporal analysis

Values of  $\alpha$ ,  $C_1$  and  $\gamma_s$  obtained with an analysis in time and in space of the three events are given in Figure 3.9. For the first two events, all parameters are computed only on the smaller scales (up to 64 km in space and up to 160 minutes in time), in order to account for the observed scaling break. For the last event both scale ranges are considered.

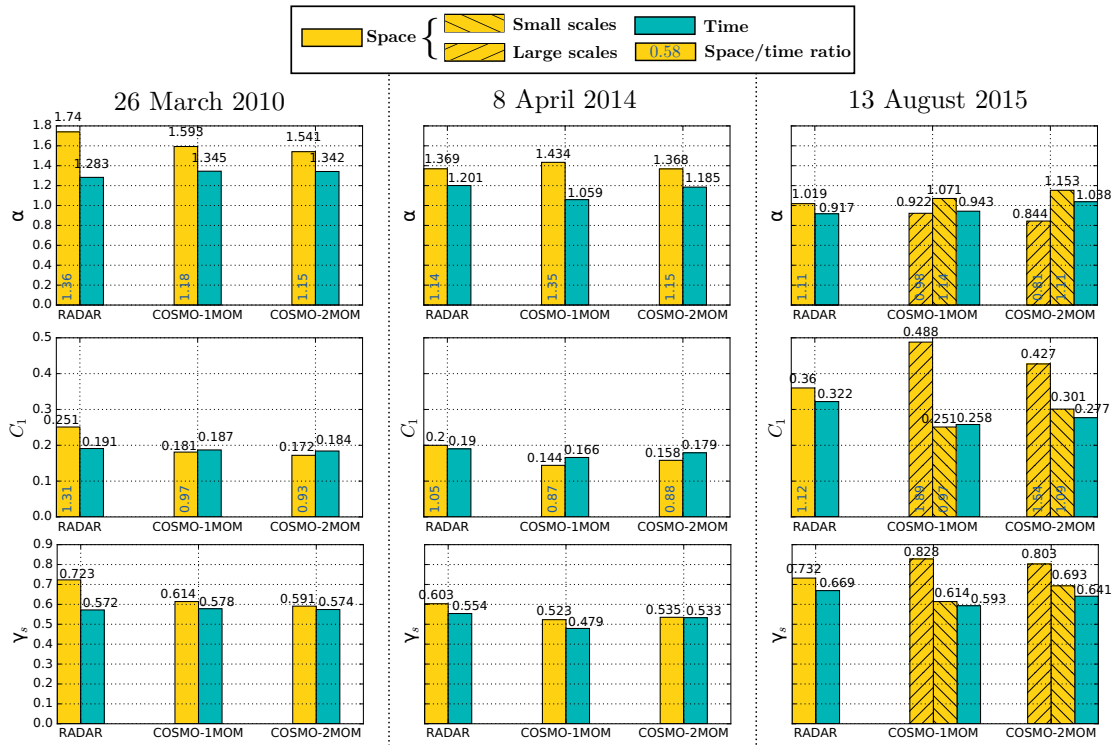


Figure 3.9 –  $\alpha$ ,  $C_1$  and  $\gamma_s$  parameter values obtained with an analysis in time and space on the fluctuations of the precipitation intensities for the three events. For the last event, both the parameters at large and small spatial scales are displayed. The numbers in blue are the space/time ratios for  $\alpha$  and  $C_1$ .

For the first event, both COSMO microphysical schemes give very similar MF parameters and the discrepancy with the radar QPE is quite important. In space, it can be observed that  $\alpha$  is slightly smaller in the COSMO simulations than on the radar QPE. It is clear as well that the simulated  $C_1$  is too small compared with the radar observations. This tends to indicate that COSMO is underestimating the spatial intermittency. Generally, the observed discrepancies in  $\alpha$  and  $C_1$  tend to indicate that the spatial structure of the simulated fields is too smooth and lacks the variability observed by the radars. In time, the agreement is better for  $C_1$ , but COSMO has clearly higher values of  $\alpha$  indicating a larger temporal variability than the radar QPE. For this event, there is a noticeable discrepancy between the maximum singularity  $\gamma_s$  in space obtained from the radar QPE (0.721) and the  $\gamma_s$  obtained from the model (around 0.6 for both schemes). This indicates that during this event COSMO had a tendency to underestimate extreme values, which might be caused by its difficulty to accurately simulate snowfall events,

### Chapter 3. Multifractal evaluation of simulated precipitation intensities

---

since COSMO does not consider partially melted snow (Frick and Wernli, 2012). Note that QPE of snow is very difficult and it is likely that the radar QPE itself is already underestimating precipitation intensities (Speirs et al., 2017), which would make this difference in  $\gamma_s$  even more noteworthy.

For the stratiform rain event, the MF parameters of the COSMO simulations are in better agreement with the radar QPE. In time, the two-moment COSMO scheme gives values that are in relatively close agreement with the radar QPE and, in this regard, outperforms the one-moment scheme. COSMO simulations show generally smaller values of  $\alpha$  and  $C_1$  than the radar QPE, which is a trend that is observed for all events.

For the last convective event, two scaling regimes are considered in space: larger scales (16-128 km) and smaller scales (2-16 km). As already observed in the spectral analysis, there is a better agreement between the radar observations and the simulations with the one-moment scheme at smaller spatial scales. In time, however, the temporal intermittency of COSMO is smaller than for the radar QPE, which can be explained by the fact that COSMO generally overestimates the extent of the convective systems. Compared with the one-moment scheme and the radar QPE, the two-moment scheme has a smaller  $\alpha$  in space but a larger  $\alpha$  in time, as well as a smaller intermittency in time and space.

In summary, the observations of the spatio-temporal analysis are consistent with the spectral and scaling analysis where (1) a strong discrepancy in scaling behavior was observed between COSMO and the radar QPE at small scales for the first event, (2) a better scaling of the model precipitation intensities was observed for the second event, (3) a discrepancy in scaling at large scales was observed between COSMO (especially for the two-moment scheme) and the radar QPE for the third event.

Overall, it can be observed that except for the first event where both schemes give similar values, the two-moment scheme is usually characterized by a larger  $C_1$  than the one-moment scheme, both in time and space, whereas in terms of  $\alpha$  there is no recurring trend. However one must keep in mind that this difference in  $C_1$  is within the expected range of uncertainty for this parameter (see second paragraph of Section 3.6). For the MF parameters  $\alpha$  and  $C_1$ , there is generally a good agreement between radar observations and simulations in the range of scales where the model exhibits a good scaling behavior. In terms of  $\alpha$  and  $C_1$ , none of the two microphysical schemes seem to perform significantly better than the other. The two-moment scheme is, however, generally characterized by a slightly larger maximum singularity  $\gamma_s$ , indicating a better capacity to simulate extreme values. This is especially visible in the last convective event. In terms of space/time ratios, the observed ratios differ significantly from the theoretical model: the  $\alpha$  space/time ratio is always larger and the  $C_1$  space/time ratio always smaller than the theoretical values (1 and 1.44 respectively).

Gires et al. (2011) found different breaks for a Cevenol event (strong precipitation events occurring in fall in the south of France): roughly 16 km in space and one hour in time, as well as a better agreement with a simple space-time model, but only for large scales which are not

the primary focus of this study. These differences could be associated with the fact that the topography of the area analyzed in this paper is more pronounced than in Gires et al. (2011). It should also be noted that, in our case, the values of UM parameters  $\alpha$  and  $C_1$  exhibit a better agreement between observations and model simulations in the relevant range of scales.

#### 3.6.3 Times series of UM parameters

To compare time series of UM parameters  $\alpha$  and  $C_1$ , the focus is put on the third (convective) event which shows the largest temporal variability. It was observed that the conclusions drawn for the third event in terms of discrepancies between radar and model MF parameters can be generalized to all events.

Figure 3.10 shows the time series of  $\alpha$  and  $C_1$  throughout the third (convective) event for the COSMO and the radar QPE precipitation intensities, as well as some illustrative precipitation fields that will be discussed.

*13 August 2015*

During the convective event, four different phases can be identified. In the first short phase (12:00-14:00 UTC), observations and simulations agree relatively well in  $\alpha$  and  $C_1$ . This period corresponds to the initial stages of the event when only a few isolated cells are present (panel (a) in Figure 3.10). In the second phase (14:00 - 17:00 UTC), a large convective system is crossing the domain on the radar observations, which causes a strong increase in  $\alpha$  and a decrease in  $C_1$ . This convective system is, however, located more in the south on the simulation and enters the domain only at around 15:30 (panel (b) in Figure 3.10). During the third phase (17:00-21:00), the large convective system is visible on the simulated field, whereas on the observed radar fields, the most intense convective cells are already out of the domain. This causes a larger  $\alpha$  in the simulations than in the observations (panel (c) in Figure 3.10). Finally, during the last phase (21:00-24:00 UTC), a new convective system is visible on the observed field but is more or less absent on the simulated fields. This causes a discrepancy, the simulated fields having a smaller  $\alpha$  and a larger  $C_1$  than the observations (panel (d) in Figure 3.10). For this event, the spatial and temporal shifts between the convective system simulated by COSMO and the real convective system observed by the radar network are the main causes of the bad scaling observed at larger scales. Note that the succession of phases detailed before is also clearly visible in the time series of wet area fraction displayed in Figure 3.11.

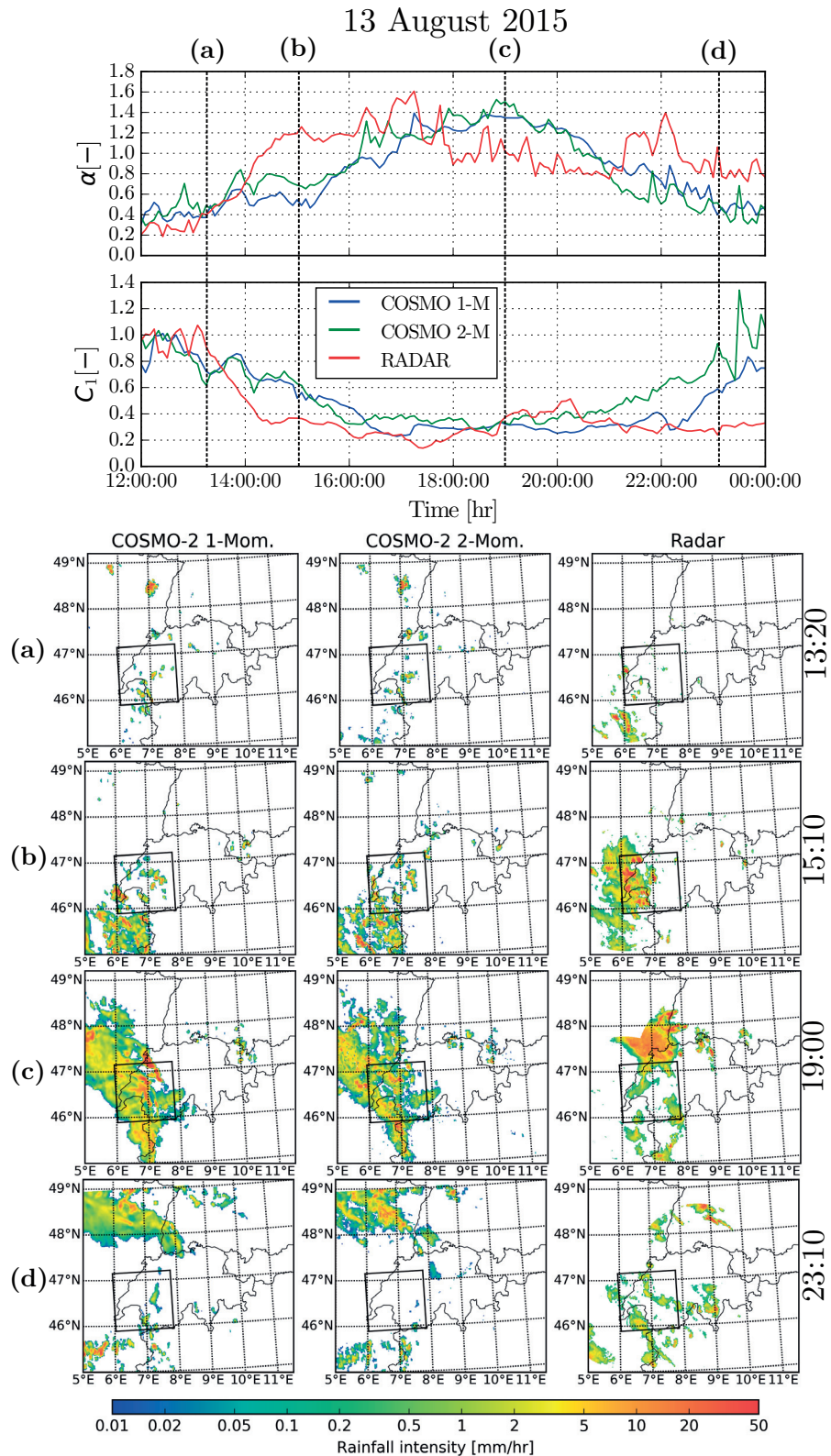


Figure 3.10 – The upper panel displays the  $\alpha$  and  $C_1$  time series during the third event. The lower panels (a), (b), (c) and (d) show the spatial structure of simulated and observed precipitation fields during four different time steps (13:20, 15:10, 19:00 and 23:10 UTC).

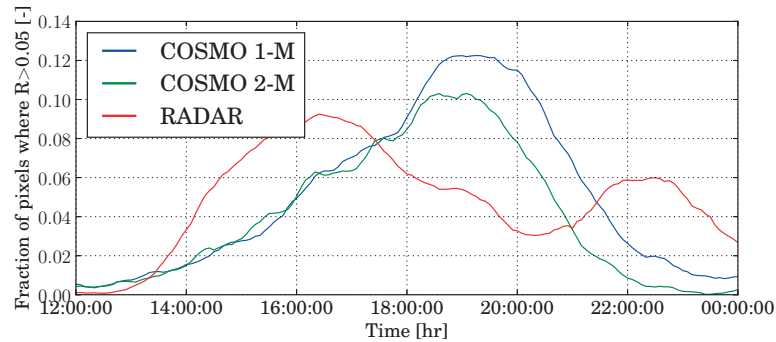


Figure 3.11 – Fraction of wet area during the event of the 13 August 2015.

For the two other events, the conclusions are similar: discrepancies in MF parameters between simulated and observed precipitation intensities, are caused primarily by temporal and spatial shifts in the simulated precipitation patterns. The effect of such shifts on the MF analysis hints at the possibility of a further analysis based not on a fixed study domain but on a study domain which follows the precipitation system, in a way similar to Nykanen and Harris (2003). Using a mobile window would make the discrepancies in MF parameters depend much more on the small-scale structures of simulated precipitation intensities, since it would strongly reduce the effect of misplacement of the simulated precipitation systems.

### 3.7 Summary and conclusions

In this work a spatial and temporal analysis of precipitation intensities simulated by the COSMO NWP model was performed using the universal multifractal (UM) framework which allows for the representation of the variability across scales with a limited number of parameters.

The first part of this work focused on a MF analysis of the climatology of precipitation intensities simulated by COSMO in its operational analysis mode. Analysis of the correlations between MF parameters and external meteorological and topographical descriptors revealed that the fractal dimension ( $D_f$ ) and the mean intermittency ( $C_1$ ) are strongly correlated to the fraction of rainy simulations. Additionally, the fractal dimension tends to increase and the mean intermittency tends to decrease with latitude, which indicates that rainfall fields are more homogeneous at higher latitudes. The effect of topography is visible in the values of  $C_1$  and the maximum singularity  $\gamma_s$  (related to extreme values) which tend to decrease with altitude, as well as in  $H$  and  $\beta$  which tend to increase with altitude. This indicates a smaller intermittency and less rainfall extremes in mountainous regions, as well as smoother rainfall intensity fields, which can be linked to the dominance of large-scale orographic effects. A hierarchical clustering was performed based on the meteorological and topographical descriptors. The resulting classification into three classes was shown to correspond well with the famous Köppen (1936) climate classification. Distributions of MF parameters within

### Chapter 3. Multifractal evaluation of simulated precipitation intensities

---

these three classes were found to be statistically significantly different, indicating that the MF signature of rain is indeed climate dependent. Finally, investigation of the spatial structure of MF fields confirmed the conclusions of the correlation analysis, namely that the values of  $\beta$  and  $H$  are mostly influenced by the altitude (simulated precipitation tends to be smoother at higher altitudes) and  $D_f$  and  $C_1$  are mostly influenced by the latitude (the intermittency decreases with latitude).

The second part of this work focused on three different events, one cold front associated with heavy snowfall, one stationary front associated with stratiform rain and a stable atmosphere, and one summer convection event with heavy rain. All events were simulated at a 2 km resolution with both the standard operational one-moment microphysical parameterization of COSMO and a more advanced two-moment microphysical scheme. A comparison of the precipitation intensities at the ground simulated by COSMO and the Swiss radar composite was performed in terms of their MF signature. Although the radar data show one single scaling regime over the studied spatial-scale ranges (1-128 km), the COSMO simulations display scaling breaks for the first and the last event. It can be observed that during the snowstorm event, COSMO is unable to properly reproduce radar observations at small scales, which might be caused by the intrinsic difficulty of simulating solid precipitation. During the last convective event, the opposite can be observed, and COSMO is struggling to reproduce the larger scales, due to its difficulty in locating accurately the convective system in time and space during this event. In the temporal scales, a scaling break is observed both for the radar data and the COSMO simulations at around 3 hours. Comparisons of the one-moment and two-moment COSMO microphysical parameterizations show that the fields simulated by the two-moment scheme tend to display a larger intermittency and variability than the one-moment scheme. This does not generally translate into a better agreement of MF parameters  $\alpha$  and  $C_1$  with the radar composite, except during the stratiform event where the two-moment scheme performs slightly better. However, the two-moment scheme gives a consistently better agreement with the radar QPE in terms of spatial and temporal fractal dimensions, which measure how convoluted the precipitation occurrence signal is.

Ultimately, the MF framework can be used to identify the scale ranges in which the model is able to simulate realistic fields of water contents, and as such this technique can be used as a diagnostic tool for model evaluation.



## **4 A forward polarimetric radar operator for the COSMO NWP model**

This chapter is adapted from the following manuscript:

1. Wolfensberger, D. and Berne, A.: From model to radar variables: a new forward polarimetric radar operator for COSMO, *Atmos. Meas. Tech. Discuss.*

This work presents a new forward polarimetric radar operator for the COSMO model, able to simulate radar observations of  $Z_H$ ,  $Z_{DR}$ ,  $K_{dp}$ , and Doppler velocity.

### 4.1 Summary

In this work, a new forward polarimetric radar operator for the COSMO numerical weather prediction (NWP) model is proposed. This operator is able to simulate measurements of radar reflectivity at horizontal polarization, differential reflectivity as well as specific differential phase shift and Doppler variables for ground based or spaceborne radar scans from atmospheric conditions simulated by COSMO. The operator includes a new Doppler scheme, which allows to estimate the full Doppler spectrum, as well a melting scheme which allows to represent the very specific polarimetric signature of melting hydrometeors. In addition, the operator is adapted to both the operational one-moment microphysical scheme of COSMO and its more advanced two-moment scheme. The parameters of the relationships between the microphysical and scattering properties of the various hydrometeors are derived either from the literature or, in the case of graupel and aggregates, from observations collected in Switzerland.

The operator is evaluated by comparing the simulated fields of radar observables with observations from the Swiss operational radar network, from a high resolution X-band research radar and from the GPM-DPR. This evaluation shows that the operator is able to simulate an accurate Doppler spectrum and accurate radial velocities as well as realistic distributions of polarimetric variables in the liquid phase. In the solid phase, the simulated reflectivities agree relatively well with radar observations, but the simulated  $Z_{DR}$  and  $K_{dp}$  tend to be underestimated. This radar operator makes it possible to compare directly radar observations from various sources with COSMO simulations and as such is a valuable tool to evaluate and test the microphysical parameterizations of the model.

## 4.2 Introduction

Weather radars deliver areal measurements of precipitation at a high temporal and spatial resolution. Most recent operational weather radar systems have dual-polarization and Doppler capabilities (called polarimetric in the following), which provide not only information about the intensity of precipitation, but also about the type of precipitation (e.g. phase, homogeneity and shape of hydrometeors). Additionally, the Doppler capability of weather radars allows to monitor the radial velocity of hydrometeors. In view of their capacities, weather radars offer great opportunities for validation of and assimilation in numerical weather prediction (NWP) models. This is unfortunately far from being a trivial task since radar observables which are derived from the backscattered power and phase from precipitation cannot be simply put into relation with the state of the atmosphere as simulated by the model. There is thus the need for a conversion tool, able to simulate synthetic radar observations from simulated model variables: a so-called *forward radar operator*.

Over the past few years, several forward radar operators have been developed. One of the first efforts was made by Pfeifer et al. (2008) who designed a polarimetric operator for the COSMO model, able to simulate horizontal reflectivity  $Z_H$ , differential reflectivity  $Z_{DR}$  and linear depolarization ratio (LDR) observations. The operator relies on the T-matrix method (Mishchenko et al., 1996) to estimate scattering properties of individual hydrometeors. Assumptions about shape, density and canting angles, which cannot be obtained from the NWP model were obtained from a sensitivity study. A limitation of this operator is that it does not perform any integration over the antenna power density pattern and thus neglects the beam broadening effect which can be quite significant at longer distances from the radar (Ryzhkov, 2007).

Cheong et al. (2008) developed a three-dimensional stochastic radar simulator able to simulate raw time series of weather radar data. Doppler characteristics are retrieved by moving discrete scatterers with the three-dimensional model wind field, which allows to produce sample-to-sample time series data, instead of theoretical moments as with conventional radar simulators. Thanks to this, the radar simulator is able to generate the full Doppler spectrum, at the expense, however, of a high computation cost and without taking attenuation into account.

Jung et al. (2008) developed a polarimetric radar operator able to simulate  $Z_H$ ,  $Z_{DR}$  and  $K_{dp}$ , and adapted it for two different microphysical schemes: one single-moment scheme and one two-moment scheme. The authors also proposed a method to simulate the effect of the melting layer with a weather model that does not explicitly simulate wet hydrometeors. They used this operator to simulate realistic polarimetric radar signatures of a supercell storm from simulations obtained with the Advanced Regional Prediction System (ARPS; Xue et al. (2000)). The validation of the operator was however limited to idealized cases at S-band only.

Ryzhkov et al. (2011) developed an advanced forward radar operator for a research cloud model with spectral microphysics able to simulate  $Z_H$ ,  $Z_{DR}$ , LDR and  $K_{dp}$ . Scattering amplitudes of smaller particles are estimated with the Rayleigh approximation whereas the T-matrix method

## Chapter 4. A forward polarimetric radar operator for the COSMO NWP model

---

is used for larger hydrometeors. Note, however, that this cloud model is computationally expensive and is not used for operational weather prediction.

Augros et al. (2016) elaborated a polarimetric forward radar operator for the French non-hydrostatic mesoscale research NWP model Meso-NH (Lafore et al., 1998), based on the forward conventional radar operator of Caumont et al. (2006), and which simulates all operational polarimetric radar observables:  $Z_H$ ,  $Z_{DR}$ ,  $\phi_{DP}$ ,  $\rho_{hv}$  and  $K_{dp}$ . The operator uses the T-matrix method for rain, snow and graupel particles and Mie scattering for pristine ice particles. Beam-broadening is taken into account by approximating the integration over the antenna normalized power density pattern with a Gauss-Hermite quadrature scheme.

Finally, Zeng et al. (2016) developed a forward radar operator for the COSMO model. The operator is designed for operational purposes (assimilation and validation) with an emphasis on performance and modularity. It simulates Doppler velocity with fall speed and reflectivity weighting as well as attenuated horizontal reflectivity, with different levels of approximation that can be specified. Note that the operator is currently not able to simulate polarimetric variables.

Most available radar operators are primarily designed to simulate operational PPI (plane position indicator) scans from operational weather radars at S, C or X bands. In research however, other types of radar data are available which can also be relevant in the evaluation of a NWP model, especially for the simulated vertical structure of precipitation. Some examples of radar data used for research include satellite swaths at higher frequencies, such as measurements from the dual-frequency precipitation radar (DPR, Furukawa et al. (2016)), on-board the GPM core satellite, as well as power weighted distributions of scatterer radial velocities (Doppler spectra), commonly recorded by many research radars.

The purpose of this work is to design a state of the art forward polarimetric radar operator for the COSMO NWP model taking into account the physical aspects of beam propagation and scattering as accurately as possible, while ensuring a reasonable computation time on a standard desktop computer. The radar operator also needs to be versatile and able to simulate a variety of radar variables at many frequencies and for different microphysical schemes, in order to be used in the future as a model evaluation tool with operational and research weather radar data. As such, this radar operator includes a number of innovative features: (1) the ability to simulate the full Doppler spectrum at a very low computational cost, (2) the ability to simulate observations from both ground and spaceborne radars (3) a probabilistic parameterization of the properties of solid hydrometeors derived from a large dataset of observations in Switzerland and (4) the inclusion of cloud hydrometeors (which contribution becomes important at higher frequencies). In addition the radar operator has been thoroughly evaluated using a large selection of radar data at different frequencies and corresponding to various synoptic conditions.

The chapter is structured as follows. In Section 2, a description of the COSMO NWP model as well as the radar data used for the evaluation of the operator is given; in Section 3; the different

steps of the polarimetric radar operator are extensively described and its assumptions are discussed in details. Section 4 focuses on the evaluation of simulated radar observables using real radar observations from both operational and research ground weather radars as well as GPM-DPR satellite data. Finally Section 5 summarizes the main results and opens perspectives for possible applications of the operator.

## 4.3 Description of the data

### 4.3.1 COSMO model

As in Chapter 3, only a reminder of the key points of the microphysical parameterizations of COSMO will be given.

In COSMO, grid-scale clouds and precipitation are parameterized operationally with a one-moment scheme with five hydrometeor categories: rain, snow, graupel, ice crystals and cloud droplets. Snow is assumed to be in the form of rimed aggregates of ice-crystals that have become large enough to have an appreciable fall velocity. Cloud ice is assumed to be in the form of small hexagonal plates with no appreciable fall velocity. The particle size distributions (PSD) of precipitating hydrometeors are assumed to be exponential for all hydrometeors, except for rain, where a gamma PSD is assumed. Ice crystals and cloud droplets do not have a spectral representation in the one-moment scheme of COSMO, but are instead treated as bulk, with the total number of particles being a function of the air temperature. In terms of terminal velocities, in the version of COSMO that is being used (5.04), neither ice crystals nor cloud droplets are sedimentating, however in more recent versions (starting from 5.1), ice crystals have a bulk non-diameter dependent terminal velocity, that depends on their mass concentration.

A more advanced two-moment scheme with a sixth hydrometeor category, hail, was developed for COSMO by Seifert and Beheng (2006). In this scheme all PSDs are assumed to be generalized gamma distributions that depend on particle mass.

In COSMO, for both microphysical schemes, mass-diameter relations as well as velocity-diameter relations for the precipitating hydrometeors are assumed to be power-laws, except for rain in the two-moments scheme, where a slightly more refined formula by Rogers et al. (1993) is used. Additionally, in contrast with the one-moment scheme, ice crystals are considered to have a diameter-dependent terminal velocity in the two-moment scheme, in the form of a power-law.

## Chapter 4. A forward polarimetric radar operator for the COSMO NWP model

For both schemes, all PSDs can be expressed as particular cases of generalized gamma PSDs.

$$N(D) = N_0 D^\mu \exp(-\Lambda \cdot D^\nu) \quad \text{m}^{-3} \text{mm}^{-1} \quad (4.1)$$

where  $N_0$  is the *intercept* parameter in units of  $\text{mm}^{-1-\mu} \text{m}^{-3}$ ,  $\mu$  is the dimensionless *shape* parameter,  $\Lambda$  is the *slope* parameter in units of  $\text{mm}^{-\nu}$  and  $\nu$  is the dimensionless *family* parameter.

In the one-moment scheme, which is used operationally, the only free parameter of the PSDs is the slope parameter  $\Lambda$  which can be obtained from the prognostic mass concentrations. The intercept parameter  $N_0$  is either assumed to be constant or in the case of snow to be temperature dependent. The shape parameter  $\mu$  is equal to zero (exponential PSDs) for all hydrometeors, except for rain where it is set to 0.5 by default and  $\nu$  is always equal to one.

In the two-moment scheme, both  $\Lambda$  and  $N_0$  are prognostic parameters, and can be obtained from the prognostic moment of order zero (number concentration  $Q_N$  in  $\text{m}^{-3}$ ) and from the mass concentration  $Q_M$  in  $\text{kg m}^{-3}$ .  $\mu$  and  $\nu$  are defined *a-priori*.

Table 4.1 gives the values of PSD parameters  $\mu$ ,  $N_0$  and  $\nu$ , *mass-diameter* power-law parameters  $a$  and  $b$  and *terminal velocity-diameter* power-law parameters  $a_\nu$  and  $b_\nu$  for all hydrometeor types and the two microphysical schemes..

	<b>Rain</b>	<b>Snow</b>	<b>Graupel</b>	<b>Hail</b>	<b>Ice crystals</b>
$N_0$	2529/free	<sup>1</sup> /free	4000/free	$\emptyset$ /free	-/free
$\mu$	0.5/2	0/1.2	0/5.37	$\emptyset$ /5	-/
$\nu$	1/1	1/1.1	1/1.06	-/1	$\emptyset$ /
$a$	5.236E-7/5.245E-7	3.8E-8/3.8E-8	8.5E-8/8.5E-8	$\emptyset$ /3.392E-7	1.300E-7/1.170E-7
$b$	3.00/3.00	2.00/2.00	3.10/3.10	$\emptyset$ /3.00	3.00/3.31
$a_\nu$	4.11/-	0.871/0.871	0.945/1.258	$\emptyset$ /3.362	-/0.966
$b_\nu$	0.50/-	0.25/0.20	0.89/0.85	$\emptyset$ /0.50	-/1.20

Table 4.1 – Parameters of the hydrometeors PSDs and power-laws for the one-moment and two-moment parameterizations (separated by a slash sign).  $\emptyset$  indicates that the hydrometeor is not simulated in this scheme, a dash indicates that this parameter is not defined in this parameterization, and “free” indicates a prognostic parameter. Note that the value of  $\mu$  for rain can be specified in the user namelists, 0.5 being the default value. The parameters  $a$  and  $b$  correspond to the power-law:  $m(D) = aD^b$ , where  $m$  is in kg and  $D$  in mm. The parameters  $a_\nu$  and  $b_\nu$  correspond to the power-law:  $v_t(D) = a_\nu D^{b_\nu}$ , with  $v_t$  being the terminal velocity in  $\text{m s}^{-1}$  and  $D$  in mm.

<sup>1</sup>for snow, a relation of  $N_0$  with the temperature is used (Field et al., 2005)

### 4.3. Description of the data

	MXPol	Swiss radar network
Location	Payerne: 46.81350°N, 6.94308°E, 495 m a.s.l	Albis: 47.28436°N, 8.51201°E, 891 m a.s.l La Dôle: 46.42561°N, 6.09995°E, 1680 m a.s.l Monte Lema: 46.04079°N, 8.83321°E, 1604 m a.s.l
Frequency $f$	9.41 GHz (X-band)	5.6 GHz (C-band)
Pulse width $\tau$	0.5 $\mu$ s	0.577 $\mu$ s
PRF	1666 Hz	500 to 1500 Hz (depends on elevation)
FFT length	128	-
3dB beamwidth	1.45°	1°
Sensitivity (SNR = 8 dB)	11 dBZ at 10 km	0 dBZ at 10 km

Table 4.2 – Specifications of the ground radars used in the evaluation of the radar operator

#### 4.3.2 Radar data

For the evaluation of the simulated polarimetric variables, the final product from the Swiss operational radar network is used. The Swiss network consists of five polarimetric C-band radars, performing PPI scans at 20 different elevation angles (Germann et al., 2006). The final quality-checked measurements are corrected for ground clutter, calibrated and aggregated at a resolution of 500 m. Starting from the data provided by MeteoSwiss, additional pre-processing steps have been undertaken. These include the correction of  $Z_{DR}$  with a daily radar-dependent calibration constant provided by MeteoSwiss, and a numerical estimation of  $K_{dp}$  from  $\Psi_{DP}$  with the ensemble Kalman filter method of Schneebeli et al. (2013). Note that two of the operational radars were installed only quite recently (2014 and 2016) and were thus not used in this study (see Figure 4.1).

For the evaluation of simulated Doppler variables (mean radial velocity and Doppler spectrum at vertical incidence), observations from a mobile X-band radar (MXPol) deployed in Payerne in Western Switzerland in Spring 2014 were used. The radar was operated in the context of the PARADISO measurement campaign (Figueras i Ventura et al., 2015). The PARADISO dataset provides a great opportunity to evaluate the simulated radial velocities, as Payerne is the location from which the operational radio soundings, which are assimilated in the model, are launched. Additionally, for the evaluation of ice crystals in the forward operator, MXPol measurements recorded during three pure snowfall events in the Eastern Swiss Alps in Davos were used. More details about these events will be given in Section 4.3.3.

An overview of the specifications of all radars used in this study is given in Table 4.2. The location of the three Swiss operational radars used in the evaluation of the radar operator (Section 4.5.3) and their maximum considered range (100 km) are shown in Figure 4.1.

Besides ground radar data, measurements from the GPM-DPR radar were used to validate the simulation of spaceborne radar swaths. The GPM-DPR radar operates at both Ku (13.6 GHz) and Ka (35.6 GHz) bands. At Ku-band, the satellite swath covers approximately 245 km in width, with an horizontal resolution approximately 5 km and a 250 m vertical (radial) resolution. At Ka-band, the satellite swath is more narrow, covering only 125 km in width.

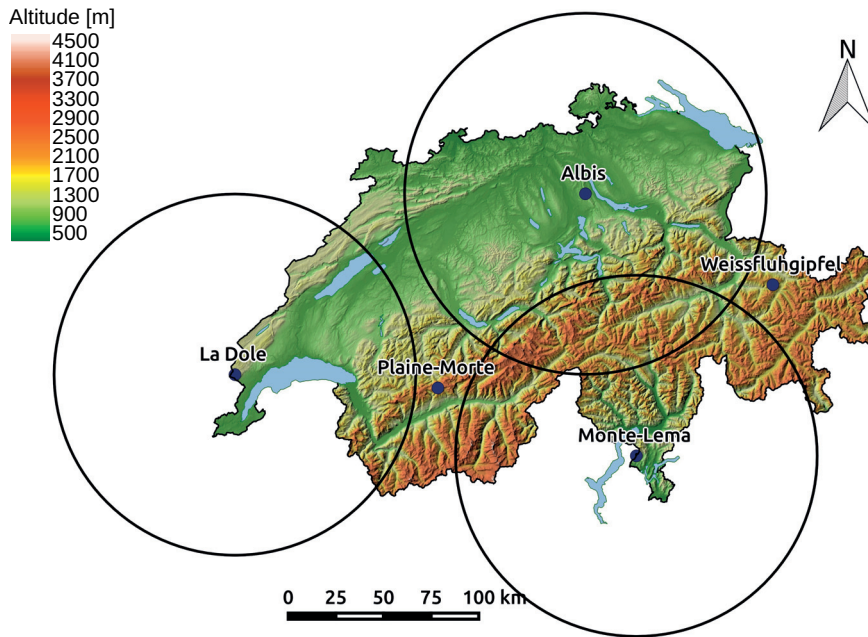


Figure 4.1 – Location of the five Swiss operational radars. The black circles indicate the maximum range of radar data (100 km) used for the evaluation of the radar operator (Section 4.5.3). Since they were installed only quite recently, no data from the Weissfluhgipfel and Plaine Morte radars were used in this study.

### 4.3.3 Precipitation events

A list and short description of all 5 events used for the evaluation of the radar operator with data from the operational C-band radars (Section 4.5.3), all 6 events from the PARADISO campaign used for the evaluation of the radar operator with data from MXPoL (Section 4.5.2), and all 3 solid precipitation events used for the evaluation of ice crystals (Section 4.5.5) is given in Table 4.3.

For the comparison of simulated GPM swaths with real observations (Section 4.5.4), the 100 overpasses with the largest precipitation fluxes recorded between March 2014 and the end of 2016 were selected. Overall, this selection is a balanced mix between widespread low-intensity precipitation and local strong convective storms.

## 4.4 Description of the polarimetric radar operator

The radar operator simulates observations of  $Z_H$ ,  $Z_{DR}$ ,  $K_{dp}$ , average Doppler (radial) velocity and of the full Doppler spectrum based on COSMO simulations and user-specified radar characteristics, such as its position, its frequency, the 3 dB antenna beamwidth  $\Delta_{3dB}$ , the pulse duration  $\tau$  and the pulse repetition frequency (PRF). Figure 4.2 summarizes the main steps of this procedure, which will be more extensively detailed in the further section.



#### 4.4. Description of the polarimetric radar operator

Event	Description	Used for
1 February 2013	Heavy snowfall event with strong westerly geostrophic winds.	A
22 March 2014	Stationary front with widespread stratiform liquid precipitation over Switzerland.	B
8 April 2014	After the crossing of a cold front, presence of mostly liquid widespread stratiform precipitation over Switzerland.	A/B
1th May 2014	Occlusion over Switzerland with mild temperatures and widespread stratiform precipitation	B
7 May 2014	Wake of a cold front with scattered stratiform precipitation	B
11 May 2014	Wake of a cold front with strong scattered stratiform and occasionally convective precipitation	B
14 May 2014	Occlusion over Switzerland with mild temperatures and widespread stratiform precipitation	B
8 November 2014	The first two weeks of november 2014 were characterized by very heavy rainfall over the Southern Alps with strong Foehn winds, due to the presence of a very strong low pressure system over the Mediterranean (Xandra).	A
9 January 2015	Crossing of a warm front over Switzerland with widespread stratiform precipitation and snowfall over the Swiss Alps.	C
26 January 2015	Snowfall event over the Swiss Alps with very similar characteristics to the 9 January 2015 event	C
23 February 2015	Crossing of a cold front over Switzerland with some widespread and medium-intensity snowfall	C
13 August 2015	Strong summer convection triggered by the presence of very warm and wet subtropical air over Switzerland.	A
7 June 2016	Presence of warm and moist air over Western Europe with a succession of thunderstorms.	A

Table 4.3 – List of all events used for the comparison of simulated radar observables with real ground radar observations. The last column indicates the context of the comparison. *A* indicates the comparison with the operational C-band radars (Section 4.5.3), *B* indicates the comparison with the X-band radar (Section 4.5.2) in Payerne and *C* indicates the evaluation of ice crystals with the X-band radar in the Swiss Alps in Davos (Section 4.5.5).

##### 4.4.1 Propagation of the radar beam

Microwaves in the atmosphere propagate along curved lines at speeds  $v < c$  as the permittivity of the atmosphere  $\epsilon$  is larger than  $\epsilon_0$ , the permittivity of vacuum. In the case of large atmospheric permittivity gradients the beam can even be refracted back to the surface, which can cause distant ground objects to appear on the radar scan. Obviously in order to simulate the propagation of the radar beam, the effect of atmospheric refraction needs to be taken into account. In the radar operator, computing the distance at the ground  $s$ , and the height above ground  $h$  for every radial distance  $r$  (see Figure 4.3), can be done in two ways.

###### *Equivalent Earth Model*

The Equivalent Earth Model is a simple yet often used model, in which the atmospheric refractive index  $n = \sqrt{\epsilon}$  is assumed to be a horizontally homogeneous linear function of height  $\frac{dn}{dh} = \text{const.}$ . This approximation is simple and often used in practice, as it does not require any knowledge about the current state of the atmosphere, and is quite accurate as long as the assumed vertical profile of  $n$  is valid in the first kilometers of the atmosphere.

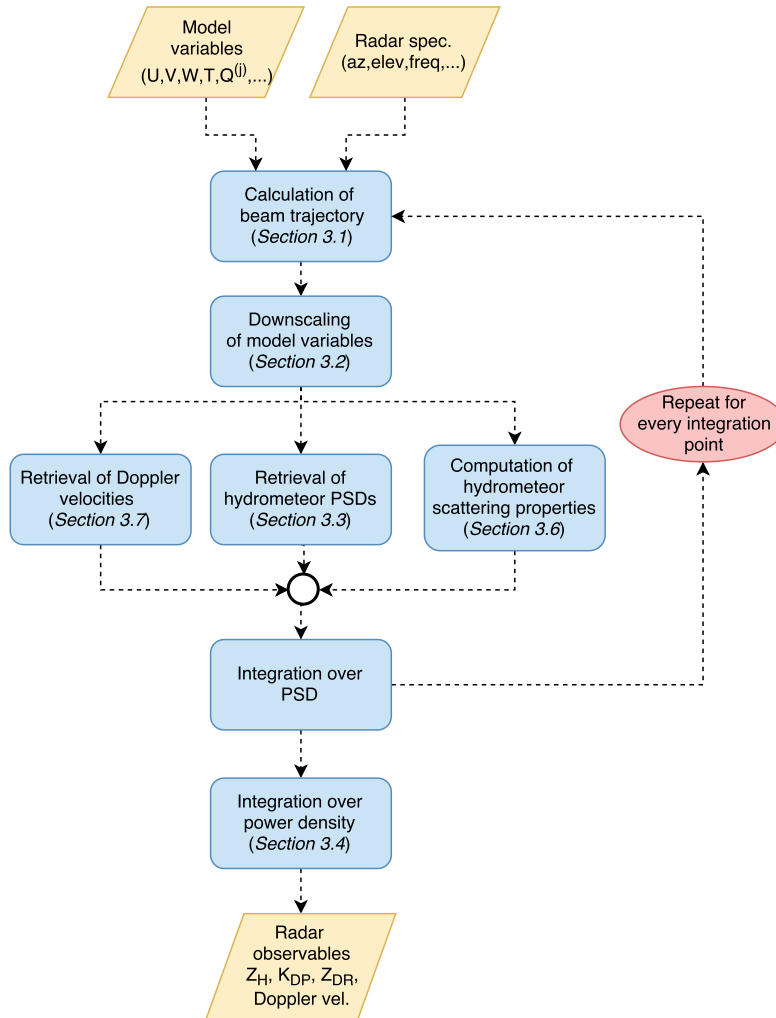


Figure 4.2 – Forward operator workflow

*Atmospheric refraction model (Zeng et al., 2014)*

In case of non-standard temperature profiles, such as a temperature inversion, the profile of  $n$  can vary significantly from the one assumed by the Equivalent Earth Model, which can lead to strong underestimation of the beam refraction. Fortunately Zeng et al. (2014) proposed a more generic and accurate model that is based on the vertical profile of atmospheric refractivity derived from the model data. This vertical profile can be approximated from the temperature  $T$ , the partial pressure of water vapor  $P_w$  and the total pressure  $P$  (Doviak and Zrnić, 2006). The height at a given range can then be estimated by solving a second order ordinary differential equation derived from Snell's law for spherically stratified layers. Again, this model assumes horizontal homogeneity of the atmospheric refractivity.

The choice of the refraction model (Earth equivalent or atmospheric refraction) is left to the user of the radar operator, noting that the computation cost for the latter is slightly larger. The

whole evaluation of the radar operator presented in Section 4.5 was performed with the more advanced model of Zeng et al. (2014).

### 4.4.2 Downscaling of model variables

Once the distance at the ground  $s$  and the height above ground  $h$ , are obtained from the refraction model for a given range, it is easy to retrieve the lat/lon/height coordinates  $(\psi^{\text{WGS}}, \lambda^{\text{WGS}}, h)$  of the corresponding radar gate, knowing the beam elevation  $\theta_g$  and azimuth  $\phi_g$  angles at the radar gate, as well as the position of the radar.

Now that the coordinates of all radar gates have been defined, the model variables must be downscaled to the location of the radar gates. The advantage of downscaling model variables before estimating radar observables, instead of doing the opposite, is twofold. At first, it is much more computationally efficient, because computing radar observables requires numerical integration over a particle size distribution at every bin, which is costly. Secondly, model variables are much less correlated than the final radar observables, which tend to be strongly correlated, with the exception of the radial velocity. This was tested by computing the non-linear Spearman rank correlations for a representative subsets of model simulations. For model variables, the correlations are generally low ( $\pm 0.2$ ), except between temperature, snow and graupel concentration where they are around 0.7. For radar observables, however, the correlations are very high (almost 1 between  $K_{\text{dp}}$  and  $Z_{\text{H}}$  and around 0.9 between  $Z_{\text{DR}}$  and  $Z_{\text{H}}$ ). Since multidimensional interpolation is difficult and expensive, it is thus preferable to aggregate the less correlated model variables.

Technical details about the trilinear downscaling procedure are given in Appendix B.1.

### 4.4.3 Retrieval of particle size distributions

In the one-moment scheme, for a given hydrometeor type ( $j$ ), the COSMO specific mass concentration  $Q_M^{(j)}$  in  $\text{kg m}^{-3}$  is proportional to a specific moment of the particle size distributions (PSD), as the COSMO parameterizations assumes simple power-laws for the mass-diameter relations:  $m^{(j)}(D) = a^{(j)} D^{b^{(j)}}$ . Because all COSMO PSDs belong to the class of generalized gamma PSDs,  $Q_M$  can be expressed as:

$$Q_M^{(j)} = a^{(j)} \int_{D_{\min}^{(j)}}^{D_{\max}^{(j)}} D^{b^{(j)}} \cdot \overbrace{N_0^{(j)} D^{\mu^{(j)}} \exp(-\Lambda^{(j)} D^{\nu^{(j)}})}^{N^{(j)}(D)} dD \quad (4.2)$$

As is done in the COSMO microphysical parameterization (see Doms et al. (2011)), the PSDs are assumed to be only weakly truncated and the integration bounds  $[D_{\min}^{(j)}, D_{\max}^{(j)}]$  are replaced by

$[0, \infty)$ , in order to get an analytical solution and avoid the cost of numerical root finding. Note that this truncation hypothesis is done only for the retrieval of  $\Lambda$  and not when computing the radar observables (Section 4.4.6.3 and Appendix B.3). For the one-moment scheme, by integrating the Equation 4.2, one gets the following expression for the free parameter  $\Lambda^{(j)}$ .

$$\Lambda^{(j)} = \left( \frac{N_0^{(j)} a^{(j)} \Gamma\left(\frac{b^{(j)} + \mu^{(j)} + 1}{v^{(j)}}\right)}{v^{(j)} Q_M^{(j)}} \right)^{v^{(j)} / (b^{(j)} + \mu^{(j)} + 1)} \quad (4.3)$$

For the two-moment scheme, the method is similar, except that both mass and number concentrations are needed to retrieve  $\Lambda$  and  $N_0$ . The corresponding mathematical formulation is given in Appendix B.2.

Equation 4.3 allows to retrieve the PSD parameters for all hydrometeors in Table 4.1<sup>2</sup> at every radar gate using the model variable  $Q_M^{(j)}$ , and, for the two-moments scheme,  $Q_N^{(j)}$  as well. Knowing the PSDs ( $N^{(j)}(D)$ ) makes it possible to perform the integration of polarimetric variables over ensemble of hydrometeors as will be described in the next steps of the operator.

The contribution of ice crystals and cloud droplets to the overall radar signature has often been neglected in other radar simulators (e.g., Augros et al., 2016; Jung et al., 2008). In our radar operator, cloud droplets are neglected because the radar operator is designed for common precipitation radar frequencies (2.7 up to 35 GHz), for which the contribution of cloud droplets is very small (Fabry, 2015). However at higher frequencies and in weak precipitation, the contribution of ice crystals can be significant, especially for  $Z_{DR}$ , as these crystals can be quite oblate (Battaglia et al., 2001). Therefore, ice crystals are considered explicitly, even though they do not have a spectral representation in the one-moment scheme of COSMO. Instead, a realistic PSD is retrieved with the double-moment normalization method of Lee et al. (2004). This formulation of the PSD requires to know two moments of the PSD as well as an appropriate normalized PSD function. Field et al. (2005) proposes best-fit relations between the moments of ice crystals PSDs as well as fits of generating functions for different pair of moments. Taking advantage of these results, the PSDs of ice crystals in the one-moment scheme can be retrieved by estimating the second moment from the third moment (the COSMO mass concentration) and by using these two moments with the corresponding generating function proposed by Field et al. (2005). Note that this method is not used in the two-moment scheme, where ice crystals have prescribed gamma PSDs like any other hydrometeor type.

---

<sup>2</sup>except for the ice crystals in the one-moment scheme, where COSMO does not consider any spectral representation and where another approach has to be considered.

#### 4.4.4 Integration over the antenna pattern

As stated previously, for a real radar antenna, part of the transmitted power is directed away from the axis of the main beam, which increases the size of the radar sampling volume with range, an effect known as beam-broadening. Depending on the antenna beamwidth this effect can be quite significant and needs to be accounted for by integrating the radar observables at every gate over the antenna power density pattern. Equation 4.4 formulates the antenna integration for an arbitrary radar observable  $y$  and a normalized power density pattern of the antenna represented by  $f^2$ , as in Doviak and Zrnić (2006).

$$I[y](r_g, \theta_g, \phi_g) = \int_{r_g - \Delta_r/2}^{r_g + \Delta_r/2} \int_{\theta_g - \pi/2}^{\theta_g + \pi/2} \int_{\phi_g - \pi}^{\phi_g + \pi} y(r, \theta, \phi) f^4(\theta_g - \theta, \phi_g - \phi) |W(r_g - r)|^2 \cos\theta dr d\theta d\phi \quad (4.4)$$

In our operator, similarly to Caumont et al. (2006) and Zeng et al. (2016), we set  $W(r_g - r) = 1$  if  $r \in [r_g - \frac{c\tau}{4}, r_g + \frac{c\tau}{4}]$  and  $W(r_g - r) = 0$  otherwise. Indeed since the model resolution (1-2 km) is about one order of magnitude larger than the typical gate length of a modern radar (80-250 m), effects related to the finite receiver bandwidth can be neglected. Integration over  $r$  can still be done *a posteriori* by using a higher radial resolution and aggregating the simulated radar observables afterwards.

Another often used simplification is to neglect side lobes in the power density pattern and to approximate  $f^2$  by a circularly symmetric Gaussian. These simplifications reduce the integration to Equation 4.5.

$$I[y](r_g, \theta_g, \phi_g) = \int_{\theta_g - \pi/2}^{\theta_g + \pi/2} \int_{\phi_g - \pi}^{\phi_g + \pi} y(r_g, \theta, \phi) \exp\left(-8 \ln 2 \frac{(\theta_g - \theta)^2}{\Delta_{3\text{dB}}} - 8 \ln 2 \frac{(\phi_g - \phi)^2}{\Delta_{3\text{dB}}}\right) \cos\theta d\theta d\phi \quad (4.5)$$

This integration can be accurately approximated with a Gauss-Hermite quadrature (Caumont et al., 2006):

$$I[y](r_g, \theta_g, \phi_g) \approx \sum_{j=1, k=1}^{J, K} w'_j w'_k y(r_g, \theta_g + z'_j, \phi_g + z'_k) \cos(\theta_g + z'_k) \quad (4.6)$$

where  $w' = \sigma w, z' = \sigma z$  with  $\sigma = \frac{\Delta_{3\text{dB}}}{2\sqrt{2\log 2}}$ , where  $\Delta_{3\text{dB}}$  is the 3 dB beamwidth of the antenna in

## Chapter 4. A forward polarimetric radar operator for the COSMO NWP model

degrees, and  $w$  and  $z$  are respectively the weights and the roots of the Hermite polynomial of order  $J$  (for azimuthal integration) or  $K$  (for elevational integration). For the integration in the radar operator, default values of  $J = 5$  and  $K = 7$  are used according to Zeng et al. (2016). The quadrature points thus correspond to separate sub-beams with different azimuth and elevation angles that are resolved independently. A schematic example of this quadrature scheme is shown in Figure 4.3 for  $J, K = 3$ .

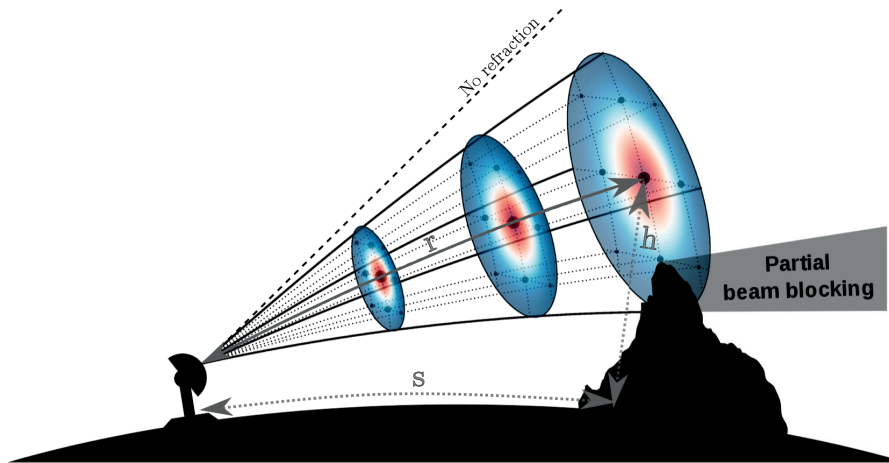


Figure 4.3 – Beam broadening increases the sampling volume with increasing range and is caused by the fact that the normalized power density pattern of the antenna (shown in red/blue tones) is not completely concentrated on the beam axis. The blue dots correspond to the integration points used in the quadrature scheme (in this case with  $J, K = 3$  for illustration purposes) and their size depends on their corresponding weights. The effect of atmospheric refraction on the propagation of the radar beam is also illustrated:  $r$  is the radial distance (radar range) and  $s$  and  $h$  are the distance at ground and above ground which need to be estimated accurately.

Another advantage of using a quadrature scheme is that it makes it easy to consider partial beam-blocking (greyed out area in Figure 4.3). Note that in our operator, the blocked sub-beams are simply lost (i.e. are not considered in the integration) and no modelling of ground echoes is performed. However, as was done in the evaluation of the operator (Section 4.5), these beams can easily be identified and removed when comparing simulated radar observables with real measurements.

The choice of this simple Gaussian quadrature was validated by comparison with an exhaustive integration scheme during three precipitation events (two stratiform and one convective). The exhaustive integration consists in the decomposition of the real MXPOL antenna pattern (obtained from laboratory measurements) into a regular grid of  $200 \times 200$  sub-beams. Such an integration is obviously extremely computationally expensive and cannot be considered as a reasonable method for integration in practice. Four other quadrature schemes were tested, (1) a sparse Gauss-Hermite quadrature scheme (Smolyak, 1963), (2) a custom hybrid Gauss-Hermite/Legendre quadrature scheme based on the decomposition of the real antenna diagram in radial direction with a sum of Gaussian functions (3) a Gauss-Legendre quadrature

#### 4.4. Description of the polarimetric radar operator

scheme weighted by the real antenna pattern and (4) a recursive Gauss-Lobatto scheme (Gautschi, 2006) based on the real MXPoI antenna pattern. All schemes were tested in terms of bias and root mean square error (RMSE) in horizontal reflectivity  $Z_H$  and differential reflectivity  $Z_{DR}$  as a function of beam elevation (from 0 to 90°), taking the exhaustive integration scheme as a reference.

Figure 4.4 shows an example for one of the two stratiform events. It can be observed that the simple Gauss-Hermite scheme is the one which performs the best on average (lowest bias and RMSE for both  $Z_H$  and  $Z_{DR}$ ), with schemes (1) and (3) performing almost systematically worse. Schemes (2) and (4) tend to perform slightly better at low elevation angles in particular situations where strong vertical gradients are present, generated for instance by a melting layer or by strong convection. This is due to the fact that, in these situations, the contribution of the side lobes can become quite important, for example when the main beam is located in the solid precipitation above the melting layer but the first side lobe shoots through the melting layer or the rain underneath. However, considering that these schemes are more computationally expensive and tend to perform worse at elevations  $> 3^\circ$ , it was decided to choose the simple Gauss-Hermite scheme, which seems to offer the best trade-off. As an improvement to the operator, it could be conceivable to design an adaptive scheme that depends on the specific state of the atmosphere and the beam elevation.

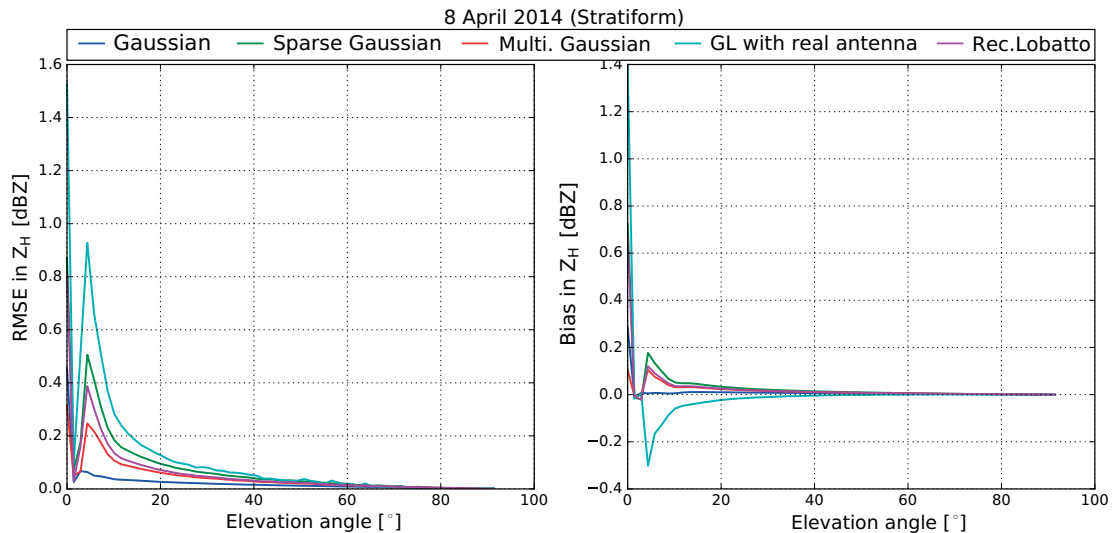


Figure 4.4 – Bias and RMSE in terms of  $Z_H$  during one day of stratiform of precipitation (around 120 RHI scans), for the five considered quadrature schemes. The exhaustive quadrature scheme is used as a reference. The other two events show similar results.

#### 4.4.5 Derivation of polarimetric variables

All radar observables for a simultaneous transmitting radar can be defined in terms of the backscattering covariance matrix  $C^b$  and the forward scattering vector  $S^f$ , which are the following for a given hydrometeor of type ( $j$ ) and diameter  $D$ :

$$C^{b,(j)}(D) = \begin{bmatrix} |s_{hh}^{b,(j)}|^2 & s_{vv}^{b,(j)} \left( s_{hh}^{b,(j)} \right)^* \\ s_{hh}^{b,(j)} \left( s_{vv}^{b,(j)} \right)^* & |s_{vv}^{b,(j)}|^2 \end{bmatrix} \in \mathbb{R}^{2 \times 2} \quad (4.7)$$

and

$$S^{f,(j)}(D) = \begin{bmatrix} s_{hh}^{f,(j)} \\ s_{vv}^{f,(j)} \end{bmatrix} \in \mathbb{C}^{2 \times 1} \quad (4.8)$$

where the superscripts  $b$  and  $f$  indicate backward, respectively forward scattering directions and  $s$  are elements of the scattering matrix that relates the scattered electric field to the incident electric field for a given particle of diameter  $D$ .

The radar backscattering cross sections  $\sigma^b$  are easily obtained from  $C^b$ :

$$\begin{aligned} \sigma_h^{b,(j)}(D) &= 4\pi C_{1,1}^{b,(j)}(D) \\ \sigma_v^{b,(j)}(D) &= 4\pi C_{2,2}^{b,(j)}(D) \end{aligned} \quad (4.9)$$

All polarimetric variables at the radar gate polar coordinates  $(r_g, \theta_g, \phi_g)$  are function of  $C^b$  and  $S^f$  and can be obtained by first integrating these scattering properties over the particle size distributions, summing them over all hydrometeor types and finally integrating them over the antenna power density. The exhaustive mathematical formulation of all simulated radar observables is given in Appendix B.3. Additionally, real radar observations of  $Z_H$  and  $Z_{DR}$  are affected by attenuation, which needs to be accounted for to simulate realistic radar measurements. The specific differential phase shift on propagation  $K_{dp}$  also needs to be modified in order to account for the specific phase shift on backscattering (see Appendix B.3).

#### 4.4.6 Scattering properties of individual hydrometeors

Estimation of  $C^{b,(j)}$  and  $S^{f,(j)}$  for individual hydrometeors is performed with the transition-matrix (T-matrix) method. The T-matrix method is an efficient and exact generalization of Mie scattering by randomly oriented nonspherical particles (Mishchenko et al., 1996). Since the



---

#### 4.4. Description of the polarimetric radar operator

shape of raindrops is widely accepted to be well approximated by spheroids (e.g., Andsager et al., 1999; Beard and Chuang, 1987; Thurai et al., 2007), the T-matrix method provides a well suited method for the computation of the scattering properties of rain. This method is also used for the solid hydrometeors (snow, graupel and hail), at the expense of some adjustments, that will be described later on.

The T-matrix method requires knowledge about the permittivity, the shape, and the canting angle of particles. Since particles are assumed to be spheroids, the aspect-ratio  $a_r$ , defined in the context of this radar operator as the ratio between the smallest dimension and the largest dimension of a particle, is sufficient to characterize their shapes. The canting angle  $\alpha$  is defined as the angle formed between the horizontal and the major axis ( $\in [-90,90]$ ) and is related to the Euler angle  $\beta$  (pitch).

In order to make the overall computation time reasonable, the scattering properties for the individual hydrometeors are pre-computed for various common radar frequencies and stored in three-dimensional lookup tables: *diameter*, *elevation* and *temperature* for standard hydrometeors and *diameter*, *elevation* and *wet fraction* for wet hydrometeors (Section 4.4.7). On run time, these scattering properties are then simply queried from the lookup tables, for a given elevation angle and temperature or wet fraction.

##### 4.4.6.1 Aspect-ratios and canting angles

###### *Rain*

For liquid precipitation (raindrops), the aspect-ratio model of Thurai et al. (2007) is used and the drop canting angle is assumed to be normally distributed with a zero mean and a standard deviation of  $7^\circ$  according to Bringi and Chandrasekar (2001).

###### *Snow and graupel*

For solid precipitation, estimation of these parameters is a much more arduous task, since solid particles have a very wide variability in shape. Few aspect-ratio models have been reported in the literature and even less is known about the canting angles of solid hydrometeors.

In terms of aspect ratio, Straka et al. (2000) report values ranging between 0.6 and 0.8 for dry aggregates and between 0.6 and 0.9 for graupels while Garrett et al. (2015) report a median aspect ratio of 0.6 for aggregates and a strong mode in graupel aspect ratios around 0.9.

In terms of canting angle distributions, both Ryzhkov et al. (2011) and Augros et al. (2016) consider a Gaussian distribution with zero mean and a standard deviation of  $40^\circ$  for aggregates and graupels in their simulations.

Given the large uncertainty associated with the geometry of solid hydrometeors, a parameterization of aspect ratios and canting angles for graupel and aggregates was derived using observations from a multi-angle snowflake camera (MASC). A detailed description of the

## Chapter 4. A forward polarimetric radar operator for the COSMO NWP model

---

MASC can be found in Garrett et al. (2012). MASC observations recorded during one year in the Eastern Swiss Alps were classified with the method of Praz et al. (2017), giving a total of around 30'000 particles for both hydrometeor types. The particles were grouped into 50 diameter classes and inside every class a probability distribution was fitted for the aspect ratio and the canting angles. For sake of numerical stability, the fit was done on the inverse of the aspect-ratio (large dimension over small dimension). In accordance with the microphysical parameterization of the model, the considered reference for solid hydrometeor diameter is the maximum diameter (largest dimension of a solid hydrometeor).

The inverse of aspect ratio,  $1/a_r$ , is assumed to follow a gamma distribution, whereas the canting angle  $o$  is assumed to be normally distributed with zero mean, and the parameters of these distributions depend on the considered diameter  $D$ .

$$o : f(o, D) = \mathcal{N}(0, \sigma_o^D) \quad (4.10)$$

$$\frac{1}{a_r} : f\left(\frac{1}{a_r}, D\right) = \frac{\left(\frac{1}{a_r} - 1\right)^{\Lambda_{a_r}(D)-1} \exp\left(-\frac{\frac{1}{a_r}-1}{M(D)}\right)}{(M(D))^{\Lambda_{a_r}(D)} \Gamma(\Lambda_{a_r}(D))} \quad (4.11)$$

where  $\Lambda_{a_r}$  and  $M$  are the *shape* and *scale* parameters of the gamma aspect-ratio probability density function and  $\sigma_o$  is the *standard deviation* of the Gaussian canting angle distribution. Technically  $\Lambda$ ,  $M$  and  $\sigma_o$  have been fitted at fixed diameter bins, then the dependence of these parameters to  $D$  has been fitted by power-laws for each parameter:

$$\begin{aligned} \sigma_o(D) &= 58.07 D^{-0.11} \\ \Lambda_{a_r}(D) &= 6.33 D^{-0.4} \\ M(D) &= 0.06 D^{-0.71} \end{aligned} \quad (4.12)$$

Note that the gamma distribution is rescaled with a constant shift of 1, to account for the fact that the smallest possible inverse of aspect-ratio is 1 and not 0. The relationship of all parameters  $\Lambda_{a_r}$ ,  $M$ , and  $\sigma_o$  to the diameter bins  $[D]$ , was fitted with a power law, which allows to estimate them for any arbitrary maximum diameter  $D$ . This also allows integration over the canting angle and aspect-ratio distributions for all particle sizes.

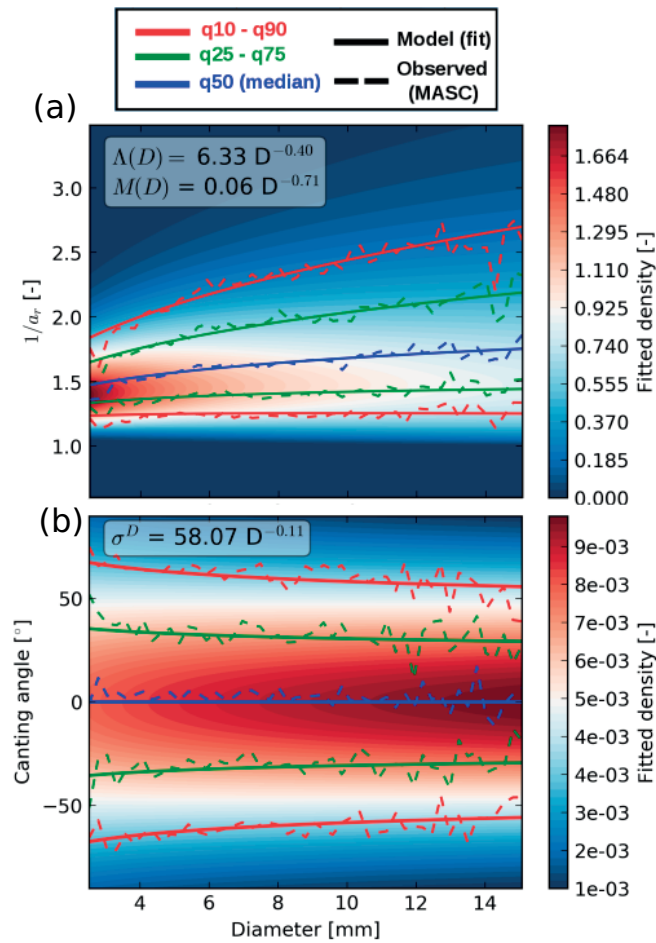


Figure 4.5 – Fitted probability density functions for the inverse of the aspect-ratio (a) and the canting angle (b). The power-laws relating the particle density function parameters to the diameter are displayed in the grey boxes on the top-left. Note that the fit was performed on the inverse of the aspect-ratio (major axis over minor axis).

Figure 4.5 shows the fitted densities for every diameter and every value of inverse aspect-ratio and canting angle. Overlaid are the empirical quantiles (dashed lines) and the quantiles of the fitted distributions (solid lines). Generally the match is quite good. The fitted models are able to take into account the increase in aspect-ratio spread and decrease in canting angle spread with particle size, which are the two dominant trends that can be identified in the observations.

Figure 4.6 shows the effect of using this MASC-based parameterization instead of the values from the literature (Ryzhkov et al., 2011) on the resulting polarimetric variables. Whereas only a small increase is observed for the horizontal reflectivity  $Z_H$ , the difference is quite important for  $Z_{DR}$  and  $K_{dp}$ , especially for graupel. The MASC parameterization tends to produce a stronger polarimetric signature. It is interesting to notice that  $Z_{DR}$  tends to decrease with the concentration, which is rather counter-intuitive as  $Z_{DR}$  is thought to be independent

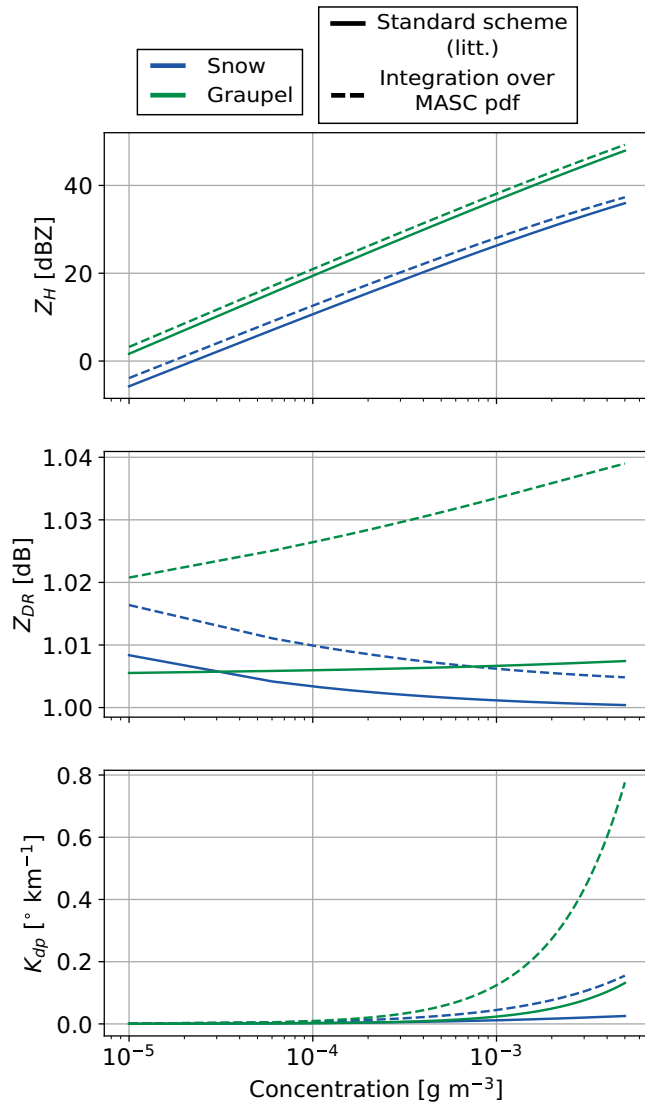


Figure 4.6 – Polarimetric variables as a function of the mass concentration for snow and graupel when using canting angle and aspect ratio parameterizations from the literature (Ryzhkov et al., 2011) (solid line) and when using the parameterization based on MASC data (dashed line).

of concentration effects. This can be explained by the fact that, in COSMO, the density of snowflakes decreases with their size (they become less compact) and therefore the permittivity computed with the mixture model (Equation 4.14) decreases as well. When the concentration increases, the proportion of larger (and more oblate) snowflakes increases but given their smaller permittivity, the overall trend is a slight decrease in  $Z_{DR}$ .

Note that even if this increase in the polarimetric signature of aggregates and graupel seems particularly drastic, comparisons with real radar measurements indicate that the operator is still underestimating the polarimetric variables in snow (Section 4.5.3).

##### *Hail*

A similar analysis could not be performed for hail, as no MASC observations of hail were available. Hence, the canting angle distribution is assumed to be Gaussian with zero mean and a standard deviation of  $40^\circ$ , whereas the aspect ratio model is taken from (Ryzhkov et al., 2011).

$$a_r^{\text{hail}} = \begin{cases} 1 - 0.02D, & \text{if } D < 10 \text{ mm} \\ 0.8, & \text{if } D \geq 10 \text{ mm} \end{cases} \quad (4.13)$$

##### *Ice crystals*

For ice-crystals, the aspect ratio model is taken from Auer and Veal (1970) for hexagonal columns, whereas the canting angle distribution is assumed to be Gaussian with zero mean and a standard deviation of  $5^\circ$ , which corresponds to the upper range of the canting angle standard deviations observed by Noel and Sassen (2005) in cirrus and midlevel clouds.

#### 4.4.6.2 Permittivities

##### *Rain*

For the permittivity of rain  $\epsilon^r$ , the well known model of Liebe et al. (1991) for the permittivity of water at microwave frequencies is used. Note that recently, a new model for water permittivity has been proposed by Turner et al. (2016), which appears to provide a better agreement with field observations at high frequencies. However, for common precipitation radar frequencies ( $< 30$  GHz) and temperatures ( $> -20^\circ$ ) both models agree very well.

##### *Snow, graupel, hail and ice crystals*

Dry solid hydrometeors consist of a mixture of air and solid ice. The permittivity of such mixtures can be estimated with a special case of the Maxwell-Garnett mixing formula (e.g., Ryzhkov et al., 2011).

$$\epsilon^{(j)} = \frac{1 + 2V_f^{\text{ice}} \frac{\epsilon^{\text{ice}} - 1}{\epsilon^{\text{ice}} + 2}}{1 - V_f^{\text{ice}} \frac{\epsilon^{\text{ice}} - 1}{\epsilon^{\text{ice}} + 2}} \quad (4.14)$$

where  $V_f^{\text{ice}}$  is the volume fraction of ice within the given hydrometeor (snow, graupel or hail) and  $\epsilon^{\text{ice}}$  is the complex permittivity of ice, which can be estimated with Hufford (1991)'s formula. Note that this is a special case of the more general Maxwell-Garnett formula (the

## Chapter 4. A forward polarimetric radar operator for the COSMO NWP model

---

general form is given in (Bohren and Huffman, 1983)), and is valid only for two-component mixtures where one component (the matrix) is air.

The volume fraction of ice  $V_f^{\text{ice}}$  can be estimated with the COSMO mass-diameter relations:

$$V_f^{\text{ice}} \approx \frac{\rho^{(j)}}{\rho^{\text{ice}}} \approx \frac{6a^{(j)}D^{b^{(j)}}}{\pi D^3 a_r^{(j)}(D)\rho^{\text{ice}}} \quad (4.15)$$

where the density of ice is assumed to be constant  $\rho^{\text{ice}} = 916 \text{ kg m}^{-3}$ . The aspect-ratio  $a_r^{(j)}$  has to be taken into account in the computation of the particle volume because the reference diameter for snowflakes and graupels is the maximum diameter and not the equivolume diameter.

### 4.4.6.3 Integration of scattering properties

The matrices  $C^{b,(j)}(D)$  (Equation 4.7) and  $S^{f,(j)}(D)$  (Equation 4.8) are obtained by integration over distributions of canting angles and, for snow and graupel, aspect-ratios.

For  $C^{b,(j)}$  this gives for snow and graupel:

$$C^{b,(j)}(D) = \frac{1}{2\pi} \int_0^{2\pi} \int_0^{\pi} \int_0^1 c^{b,(j)}(D, a_r, \alpha, \beta) \cdot \sin(\beta) p(\beta) p(a_r) d\alpha d\beta da_r \quad (4.16)$$

And for rain and hail, where  $a_r$  is constant for a given diameter:

$$C^{b,(j)}(D) = \frac{1}{2\pi} \int_0^{2\pi} \int_0^{\pi} c^{b,(j)}(D, \alpha, \beta) d\alpha d\beta \quad (4.17)$$

where  $c^{b,(j)}(D, \alpha, \beta)$  are the scattering properties for a fixed diameter and  $\alpha$  and  $\beta$  (the canting angle) are the yaw (azimuthal orientation) and pitch Euler angles. The only difference between  $\alpha$  and  $\beta$  is that  $\beta \in [0, \pi]$  and  $\alpha \in [-\pi/2, \pi/2]$ .  $p(\beta)$  and  $p(a_r)$  are the probabilities of  $\beta$  and  $a_r$  for a given diameter  $D$  as obtained from Equations 4.11 and 4.10. Note that the final scattering properties are averaged over all azimuthal angles  $\alpha$ , which are all considered to be equiprobable. The  $\sin(\beta)$  in the equation is the *surface element* which arises from the fact that the integration over  $\alpha$  and  $\beta$  is a surface integration in spherical coordinates. The procedure for  $S^f$  is exactly the same.

Since the computation of the T-matrix for a large number of canting angles and aspect-ratios can be quite expensive, two different quadrature schemes were used, one Gauss-Hermite scheme for the integration over the Gaussian distributions of canting angles, and one recursive Gauss-Lobatto scheme (Gander and Gautschi, 2000) for the integration over aspect-ratios.

### 4.4.6.4 Taking into account the radar sensitivity

The received power at the radar antenna decreases with the square of the range, which leads to a decrease of signal-to-noise ratio (SNR) with the distance. To take into account this effect, all simulated radar variables at range  $r_g$  are censored if:

$$Z_H(r_g) < S + G + \text{SNR}_{\text{thr}} + 20 \cdot \log_{10} \left( \frac{r_g}{r_0} \right) \quad (4.18)$$

where  $G$  is the overall radar gain in dB,  $S$  is the radar antenna sensitivity in dBm,  $Z_H$  is the horizontal reflectivity factor in dBZ, and  $\text{SNR}_{\text{thr}}$  corresponds to the desired signal-to-noise threshold in dB (typically 8 dB in the following).  $r_0$  is a distance used to normalize the argument of the logarithm.  $r_0$  has the same units as the distances defined in Equation 1.40. If all units are consistent then  $r_0 = 1$ .

### 4.4.7 Simulation of the melting layer effect

Stratiform rain situations are generally associated with the presence of a melting layer (ML), characterized by a strong signature in polarimetric radar variables (e.g., Szyrmer and Zawadzki, 1999; Fabry and Zawadzki, 1995; Matrosov, 2008; Wolfensberger et al., 2016). In order to simulate realistic radar observables, this effect needs to be taken into account by the radar operator. Unfortunately COSMO does not operationally simulate wet hydrometeors, even though a non-operational parameterization was developed by Frick et al. (2013). Jung et al. (2008) proposed a method to retrieve the concentration of wet snow aggregates by considering co-existence of rain and dry hydrometeors as an indicator of melting. A certain fraction of rain and dry snow is then converted to wet snow which shows intermediate properties between rain and dry snow, depending on the fraction of water within (wet fraction). Initially, the method of Jung et al. (2008) has been implemented and adapted to also consider wet graupel. However, two issues with this method have been observed. First of all the co-existence of liquid water and wet hydrometeors causes a secondary mode in the Doppler spectrum within the melting layer, due to the different terminal velocities, a mode that was never observed in the corresponding radar measurements. Secondly, the splitting of the total mass into separate hydrometeor classes (rain and wet hydrometeors) causes a localized but unrealistic decrease in reflectivity just underneath the melting layer. It was thus decided to use an alternative parameterization in which only wet aggregates and wet graupel exist within the melting layer. At the bottom of the melting layer, where the wet fraction is usually almost equal to unity, these particles behave almost like rain and at the top of the melting layer, where the wet fraction is usually very small, these particles behave like their dry counterparts. Note that, in contrary to Frick et al. (2013) which explicitly consider separate prognostic variables for the meltwater on snowflakes, our scheme is purely diagnostic and is meant to be used in post-processing, when the COSMO model has been run without a parameterization for melting snow.

Note that the described melting layer scheme is valid only for the operational one-moment

scheme. Adapting it to the two-moments would be quite complex as it requires to also estimate the number concentrations of melting hydrometeors.

#### 4.4.7.1 Mass concentrations of wet hydrometeors

The fraction of wet hydrometeor mass is obtained by converting the total mass of rain and dry hydrometeors within the melting layer into melting aggregates and melting graupel.

$$Q^{ms} = Q^s + \left( Q^r \frac{Q^s}{Q^s + Q^g} \right) \quad (4.19)$$

$$Q^{mg} = Q^g + \left( Q^r \frac{Q^g}{Q^s + Q^g} \right) \quad (4.20)$$

where the superscripts  $s$ ,  $g$  and  $r$  indicate dry snow, dry graupel and rain, and  $ms$  and  $mg$  indicate wet snow and graupel.  $D$  is the maximal diameter of the melting particle (along its major dimension). Note that the mass of rainwater is added to the mass of wet hydrometeors proportionally to their relative fractions.

The wet fraction within melting hydrometeors can be estimated by the fraction of mass coming from rainwater over the total mass:

$$f_{\text{wet}}^{ms} = \frac{Q^r Q^s}{Q^s (Q^s + Q^g) + Q^r Q^s} \quad (4.21)$$

$$f_{\text{wet}}^{mg} = \frac{Q^r Q^g}{Q^g (Q^s + Q^g) + Q^r Q^g} \quad (4.22)$$

#### 4.4.7.2 Diameter dependent properties

*Mass*

For the mass of wet hydrometeors, the quadratic relation proposed by Jung et al. (2008) is used:

$$m^m(D) = (f_{\text{wet}}^m)^2 m^r(D) + \left[ 1 - (f_{\text{wet}}^m)^2 \right] m^d(D) \quad (4.23)$$

where the superscript  $d$  indicates the corresponding dry hydrometeor and the superscript  $m$  indicates the melting hydrometeor.



##### *Terminal velocity*

For the terminal velocity  $v_t^m$  of melting hydrometeors, the equation is computed from the terminal velocities of rain and dry hydrometeors, using a best-fit obtained from wind tunnel observations by Mitra et al. (1990).

$$v_t^m(D) = \phi v_t^r(D) + (1 - \phi) v_t^d(D) \quad (4.24)$$

where  $\phi = 0.246 f_{\text{wet}}^m + (1 - 0.246) (f_{\text{wet}}^m)^7$

This relation is also used by Frick et al. (2013) and Szyrmer and Zawadzki (1999).

##### *Canting angle distributions*

For the canting angle distributions, a linear shift of  $\sigma_o$  (the standard deviation of the Gaussian distribution of canting angle) with  $f_{\text{wet}}^m$  is considered:

$$\sigma_o^m(D) = f_{\text{wet}}^m \sigma_o^r(D) + (1 - f_{\text{wet}}^m) \sigma_o^d(D) \quad (4.25)$$

##### *Aspect-ratio*

For a given diameter, the distribution of aspect-ratio for melting hydrometeors is the renormalized sum of the gamma distribution of dry aspect-ratios obtained from the MASC observations (Equation 4.11) and the aspect-ratio distribution of rain, linearly weighted by the melting fraction  $f_{\text{wet}}^m$ . Since for rain the aspect-ratio is considered to be constant for a given diameter, the distribution would be a Dirac. Instead, in order to perform the weighted sum, the distributions of aspect-ratios in rain are represented by a very narrow Gaussian distribution ( $\sigma_{\text{a-r}}^r = 0.001$ ) centered around the corresponding aspect-ratio.

##### *Permittivity*

To estimate the permittivity of these mixtures, the two-component Maxwell-Garnett mixture model, as given in Equation 4.14 is used again. However, melting hydrometeors are a mixture of three components: water, ice, and air, which requires to use the two-component model recursively, first to derive the permittivity of dry snow, and then the permittivity of the dry snow and water mixture. The volume fractions of all components  $V_f$  can again be estimated with the mass-diameter model:

$$V_f^{\text{water}} = f_{\text{wet}}^m \frac{\rho^m}{\rho^{\text{water}}} \quad (4.26)$$

$$V_f^{\text{ice}} = \frac{\rho^m - V_f^{\text{water}} \rho^{\text{water}}}{\rho^{\text{ice}}} \quad (4.27)$$

$$V_f^{\text{air}} = 1 - V_f^{\text{water}} - V_f^{\text{ice}} \quad (4.28)$$

$$(4.29)$$

where  $\rho^m$  is the density of the melting particle, which can be obtained by:

$$\rho^m(D) = \frac{m^m(D)}{V^m(D)} \approx \frac{6m^m(D)}{\pi D^3 a_r^m} \quad (4.30)$$

where  $m^m(D)$  is given by Equation 4.23 and  $a_r^m$  is the aspect-ratio of the melting hydrometeor.

Unfortunately the estimated permittivity will depend on whether water is treated as the matrix and dry snow as the inclusions, or the opposite, giving two different possible outcomes. To overcome this issue, a formulation proposed by Meneghini and Liao (1996) is used, where the final permittivity is a weighted sum of both permittivities and where the weights are function of the wet fraction. This method is also used by Ryzhkov et al. (2011).

#### 4.4.7.3 Particle size distribution for melting hydrometeors

Once the mass concentrations and the wet fractions are known, it is possible to retrieve a particle size distribution for melting hydrometeors. Szyrmer and Zawadzki (1999) suggest to match the flux of rainwater at every diameter:

$$N^r(D) v_t^r(D) = N^m(D) v_t^m(D) \implies N^m(D) = N^r(D) \frac{v_t^r(D)}{v_t^m(D)} \quad (4.31)$$

where  $v_t$  is the hydrometeor terminal velocity.

#### 4.4. Description of the polarimetric radar operator

---

In our model, this PSD is adjusted by multiplying it with a mass conservation factor  $\kappa$  to ensure that the integral of the PSD weighted by the particle mass matches the concentrations of wet hydrometeors  $Q^m$ . Hence

$$N^{m,\text{corr}}(D) = \kappa N^m(D) \quad (4.32)$$

with

$$\kappa = \frac{Q^m}{\int_{D_{\min}}^{D_{\max}} m^m(D) N^r(D) dD} \quad (4.33)$$

where  $m^m(D)$  is the mass of a melting particle of diameter  $D$  (Equation 4.23).

##### 4.4.7.4 Integration scheme

Due to the sharp transition it causes in the simulated polarimetric variables, the melting layer effect causes major difficulties when integrating radar variables over the antenna power density. Indeed, the Gauss-Hermite quadrature scheme is appropriate only for continuous functions and will work well with a small number of quadrature points only for a relatively smooth function. Using a small number of quadrature points in the case of a melting layer was found to create unrealistic artefacts with the presence of several shifted melting layers of decreasing intensities. Globally increasing the number of quadrature points by a significant amount is not a viable solution as it increases linearly the computation time. Instead, the best compromise was found by increasing the number of quadrature points only at the edges of the melting layer, where the transitions are the strongest. In practice this is done by using ten times more quadrature points in the vertical than normally, but taking into account only the 10% of quadrature points with the highest weights for the computation of radar variables, except near the melting layer edges where all points are used.

In practice, the number of quadrature points used near the ML edge (which corresponds to the lowest/highest occurrence of snow/graupel and rain coexistence), decreases with the distance to the edge, according to a Gaussian function with a standard deviation equal to twice the radial resolution of the radar. This Gaussian function reaches its maximum (100% = all points) at the location of the ML edges and quickly reaches its minimum of 10% at a certain distance from the edge.

#### 4.4.8 Retrieval of Doppler velocities

##### 4.4.8.1 Average radial velocity

As illustrated in Figure 4.7, the average radial velocity  $v_{\text{rad}}$  is the power-weighted sum of the projections of  $U$  (eastward wind component),  $V$  (northward wind component),  $W$  (vertical wind component), and  $v_t$ , the hydrometeor terminal velocity, onto the axis of the radar beam defined by elevation  $\theta_g$  and azimuth  $\phi_g$ .

Estimating  $v_{\text{rad}}$  requires to know the terminal velocity of precipitating hydrometeors. In this work, the power-law relations prescribed by COSMO's microphysical parameterizations are used, with parameters as given in Table 4.1.

It can be shown (e.g., Bringi and Chandrasekar, 2001) that, in the hypothesis of radial homogeneity inside a radar resolution volume, the average radial velocity at a given radar gate characterized by coordinates  $r_g$  (range),  $\phi_g$  (azimuth) and  $\theta_g$  (elevation) is given by Equation 4.34.

$$v_{\text{rad}}(r_g, \phi_g, \theta_g) = \frac{I \left[ \sum_{j=1}^H \int_{D_{\min}^{(j)}}^{D_{\max}^{(j)}} v_{\text{rad}}^{(j)}(D, r_g, \phi_g, \theta_g) \sigma_h^{(j)}(D) N^{(j)}(D) dD \right]}{I \left[ \underbrace{\sum_{j=1}^H \int_{D_{\min}^{(j)}}^{D_{\max}^{(j)}} \sigma_h^{(j)}(D) N^{(j)}(D) dD}_{\eta(r_g, \phi_g, \theta_g)} \right]}$$

where

$$v_{\text{rad}}^{(j)}(D, r, \phi, \theta) = [U(r_g, \phi_g, \theta_g) \sin \phi_g + V(r_g, \phi_g, \theta_g) \cos \phi_g] \cos \theta_g + [W(r_g, \phi_g, \theta_g) - v_t^{(j)}(D)] \sin \theta_g \quad (4.34)$$

where  $I$  is the quadrature antenna integration operator defined in Equation 4.6 and  $\sigma_h^{b,(j)}(D)$  is the backscattering radar cross-section at horizontal polarizations for an hydrometeor of type  $j$  and diameter  $D$ ,

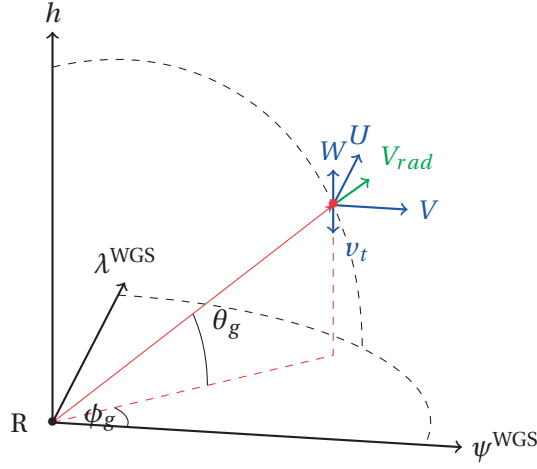


Figure 4.7 – Trigonometric expression of the radial velocity as the sum of the projection into the beam axis of the 3-dimensional wind field ( $U, V, W$ ) and the hydrometeor terminal velocity  $v_t$ .

#### 4.4.9 Doppler spectrum

In this section a simple scheme is proposed that is able to compute the Doppler spectrum at any incidence at a very small computational cost (less than 10% of the total cost). Unlike Cheong et al. (2008), this approach is not based on sampling and is thus deterministic, but the computational cost is much smaller.

Using the specified hydrometeor terminal velocity relations, it is possible to not only compute the average radial velocity, but also the Doppler spectrum: the power weighted distribution of scatterer radial velocities within the radar resolution volume.

First, the resolved velocity classes of the Doppler spectrum  $v_{r,\text{bins}}[i]$  are computed for every bin  $i$ , based on the specified radar FFT window length  $N_{\text{FFT}}$  and Nyquist velocity  $v_{\text{Nyq}}$ .

$$v_{\text{rad,bins}}[i] = \left(i - \frac{N_{\text{FFT}}}{2}\right) \frac{v_{\text{nyq}}}{N_{\text{FFT}}} \quad \forall i = -\frac{N}{2}, \dots, \frac{N}{2} \quad (4.35)$$

where  $v_{\text{Nyq}}$  is the Nyquist velocity, in  $\text{m s}^{-1}$ , given by

$$v_{\text{Nyq}} = 100 \frac{\text{PRF} \cdot \lambda}{2} \quad (4.36)$$

where  $\lambda$  is the radar wavelength in cm and PRF is the pulse repetition frequency of the radar (number of pulses transmitted per second).

## Chapter 4. A forward polarimetric radar operator for the COSMO NWP model

For every hydrometeor  $j$  and every velocity bin  $i$ , given the three-dimensional wind components  $(U, V, W)$ , one can estimate the hydrometeor terminal velocity  $v_t$  that would be needed to yield the radial velocity  $v_{\text{rad,edges}}[i]$ :

$$v_t^{(j)}(r, \phi', \theta')[i] = W(r, \phi', \theta') + \frac{U(r, \phi', \theta') \sin \phi' + V(r, \phi', \theta') \cos \phi'}{\tan \theta'} - \frac{v_{\text{rad,bins}}[i]}{\sin \theta'} \quad (4.37)$$

Once this is done, the corresponding diameters  $D^{(j)}[i]$  can be retrieved by inverting the diameter-velocity power-laws (see Table 4.1). Finally, for a given radar gate defined by coordinates  $(r_g, \phi_g, \theta_g)$  the Doppler spectrum  $S$  in linear  $Z_e$  units ( $\text{mm}^6 \text{m}^{-3}$ ), for a given velocity bin  $i$  is

$$S(r_g, \phi_g, \theta_g)[i] = \frac{\lambda^4}{\pi^5 |K_w|^2} I \left[ \sum_{j=1}^H \int_{D^{(j)}[i+1]}^{D^{(j)}[i]} \sigma_h^{b,(j)}(D) N^{(j)}(D) dD \right] \quad (4.38)$$

Any statistical moment can then be computed from this spectrum. The average radial velocity, for example is simply the first moment of the Doppler spectrum:

$$v_{\text{rad}}(r_g, \phi_g, \theta_g) = \frac{\sum_{i=0}^N v_{\text{rad,bins}}[i] S(r, \phi, \theta)[i]}{\sum_{i=0}^N S(r_g, \phi_g, \theta_g)[i]} \quad (4.39)$$

### 4.4.10 Turbulence and antenna motion correction

The standard deviation of the Doppler spectrum, often referred to as the spectral width, is a function of both radar system parameters and meteorological parameters that describe the distribution of hydrometeor density and velocity within the sampling volume (Doviak and Zrnić, 2006). Assuming independence of the spectral broadening mechanisms, the square of the velocity spectrum width  $\sigma_v^2$  (i.e. standard deviation of the spectrum) can be considered as the sum of all contributions (Doviak and Zrnić, 2006).

$$\sigma_v^2 = \sigma_s^2 + \sigma_\alpha^2 + \sigma_d^2 + \sigma_o^2 + \sigma_t^2 \quad (4.40)$$

where  $\sigma_s^2$  is due to the wind shear,  $\sigma_\alpha^2$  to the rotation of the radar antenna,  $\sigma_d^2$  to variations in hydrometeor terminal velocities,  $\sigma_o^2$  to changes in orientations or vibration of hydrometeors and  $\sigma_t^2$  to turbulence.

#### 4.4. Description of the polarimetric radar operator

In the forward radar operator,  $\sigma_s^2$  is already taken into account by the integration scheme,  $\sigma_d^2$  by the use of the diameter-velocity relations and  $\sigma_o^2$  by the integration of the scattering properties over distributions of canting angles. Thus, the spectrum computed in Equation 4.4.9 needs to be corrected only for turbulence and antenna motion. Doviak and Zrnić (2006) gives the following estimation for  $\sigma_\alpha$ .

$$\sigma_\alpha = \left( \frac{\omega \lambda \cos \theta_g}{2\pi \Delta_{3\text{dB}}} \right) \sqrt{\ln 2} \quad (4.41)$$

where  $\omega$  is the angular velocity (in  $\text{rad s}^{-1}$ ). Note that  $\sigma_\alpha$  is equal to zero at vertical incidence, which is the most common configuration for Doppler spectrum retrievals.

For  $\sigma_t$ , Doviak and Zrnić (2006) gives the following estimation, originally derived by Labitt (1981), which is based on the hypothesis of isotropic and homogeneous turbulence, with all contributions to turbulence coming from the inertial subrange.

$$\sigma_t = \begin{cases} \left[ \frac{\epsilon_t r_g (1.35B)^{3/2}}{0.72} \right]^{1/3} & \text{if } \sigma_r \ll r\sigma_\theta \\ \left[ \frac{\epsilon_t \sigma_r (1.35B)^{3/2}}{\left[ \frac{11}{15} + \frac{4}{15} (r^2 \sigma_{\theta_g}^2 \sigma_r^{-2}) \right]^{-3/2}} \right]^{1/3} & \text{else} \end{cases} \quad (4.42)$$

where  $B$  is a constant between 1.53 and 1.68<sup>3</sup> and  $\epsilon_t$  is the eddy dissipation rate (EDR) expressed in units of  $\text{m}^2 \text{s}^{-3}$ .  $\epsilon_t$  is the rate at which turbulent kinetic energy is converted into thermal internal energy. It is a model variable, simulated by the turbulence parameterization and can be obtained as any other variable used in the radar operator, by downscaling to the radar gates. Finally  $\sigma_r$  and  $\sigma_\theta$  depend on the radar specifications:  $\sigma_r = 0.35c\tau/2$  ( $\tau$  is the pulse duration in s) and  $\sigma_\theta = \Delta_{3\text{dB}}/4\sqrt{\ln(2)}$ .

This makes it possible to estimate both  $\sigma_o$  and  $\sigma_t$  using the specified radar system parameters and simulated turbulence variables. If one assumes the spectral broadening caused by the antenna motion and turbulence to be Gaussian with zero mean (e.g., Babb et al., 2000; Kang, 2008), the corrected spectrum can be obtained by convolution with the corresponding Gaussian kernel.

<sup>3</sup>A constant value of 1.6 is used in the radar operator.

$$S^{\text{corr}}[i] = \sum_{j=0}^{N_{\text{FFT}}} S[i-j] \frac{1}{\sqrt{2\pi\sigma_{t+\alpha}^2}} \exp\left[-\frac{v_{\text{rad,bins}}[j]}{2\sigma_{t+\alpha}^2}\right] \quad (4.43)$$

where  $\sigma_{t+\alpha} = \sigma_t + \sigma_\alpha$

#### 4.4.11 Attenuation correction in the Doppler spectrum

In reality, attenuation will cause a decrease in observed radar reflectivities at all velocity bins within the spectrum. To take into account this effect, the path integrated attenuation in linear units at a given radar gate ( $k_h$  in Equations B.6) is distributed uniformly throughout the spectrum.

$$S(r_g, \phi_g, \theta_g)^{\text{att}}[i] = S(r_g, \phi_g, \theta_g)[i] \cdot \exp\left(-2 \int_{r=0}^{r_g} k_h(r, \theta_g, \phi_g) dr\right) \quad (4.44)$$

#### 4.4.12 Simulation of satellite swaths

The radar operator was adapted to be able to simulate swaths from spaceborne radar systems such as the GPM-DPR (Iguchi et al., 2003) at both Ku and Ka bands. The main modifications to the standard routine concern the beam tracing, which is estimated from the GPM data files (in HDF5 format) by using the WGS84 coordinates at the ground and the satellite position in Earth-centered Earth-fixed coordinates to retrieve the coordinates of every radar gate. Currently, the atmospheric refraction is neglected which leads to an average positioning error of 55 m, the error being minimal at the center of the swath (where the incidence angle is nearly vertical) and maximal at the edges of the swath. The integration scheme remains unchanged and a fixed beamwidth of  $0.5^\circ$  is used according to GPM specifications. An important advantage of simulating satellite radar measurements over simply comparing the precipitation intensities at the ground, is that it allows a three-dimensional evaluation of the model data.

#### 4.4.13 Computation time

Though being mostly written in Python, the forward radar operator was optimized for speed as all computations are parallelized and its most time consuming routines are implemented in C. In addition, the scattering properties of individual hydrometeors are pre-computed and stored in lookup tables. Table 4.4 gives some indication of the computation times encountered for different types of simulated scans. The RHI scan consists of 150 different elevation angles in the main direction of the precipitation system, with a maximal range of 20 km and a radial resolution of 75 m. The RHI scan is also computed with the full Doppler scheme (Section 4.4.9),



and the melting layer is simulated with the quadrature oversampling scheme described in Section 4.4.7.4. The PPI scan consists of 360 different azimuth angles at  $1^\circ$  elevation at C-band, with a maximal range of 150 km and a radial resolution of 500 m. All scans are performed in a stratiform rain situation (8 April 2014 for ground radars and 4 April 2014 for GPM), with a wide precipitation coverage. The advanced refraction scheme by Zeng et al. (2014) is used for all scans except the GPM swath. To integrate over the antenna density pattern, 3 quadrature points in the horizontal and 5 in the vertical are used for all scans (with an oversampling factor of 10 at the ML edges).

It can be seen from Table 4.4 that the computation times are usually reasonable even on a standard desktop computer, except when simulating the melting layer effect on a PPI scan at low elevation. However, it can be seen that the forward radar operator scales very well with increasing number of computation power and nodes, as the computation time decreases more or less linearly with increasing computer performance.

	RHI, with ML and spectrum	PPI, no ML	PPI, with ML	GPM Ku band, no ML
Desktop	2.1 min	5.3 min.	11.1 min.	8.9 min.
Server	1 min.	2.1 min.	6.16 min.	5.3 min.

Table 4.4 – Observed computation times for three types of scans and two computers. The desktop has an 8 cores i7-4770S CPU with 3.1 GHz (30.5 GFlops/s) and 32 GB of RAM, the server has a 12 cores i7-3930K with 3.20GHz (59 GFlops/s) and 32 GB of RAM

## 4.5 Evaluation of the operator

In this section, a comparison of simulated radar fields with radar observations is performed. It is important to realize that discrepancies between measured and simulated radar variables can be caused both by:

1. The inherent inexactitude of the model which manifests itself by differences in magnitude as well as temporal and spatial shifts in the simulated state of the atmosphere, compared with the real state of the atmosphere.
2. Limitations of the forward radar operator, e.g. imperfect assumptions on hydrometeor shapes, density and permittivity, inaccuracies due to numerical integration, non-consideration of multiple scattering effects.

When validating the radar operator, only the second factor is of interest but as the discrepancies are often dominated by the first factor, validation becomes a difficult task.

Hence, for evaluation purposes, it is important to run the model in its best configuration, in order to limit as much as possible its inaccuracy. This is why the model was run in analysis mode, with a 12 hours spin-up time, using analysis runs of the coarser COSMO-7 (7 km resolution) as input and boundary condition. Note that even though COSMO has recently become operational at a resolution of 1 km over Switzerland, the simulations performed in this work were still done at a 2 km resolution. Note that the present evaluation was done with the standard one-moment scheme, for sake of simplicity, but Appendix B.2 gives some additional indications and results for the two-moments scheme.

Evaluation of the radar operator was first done by visual inspection on a time step basis and was followed by a more quantitative evaluation over the course of the whole precipitation events.

### 4.5.1 Qualitative comparisons

#### 4.5.1.1 PPI scans at C-band

Figures 4.8 and 4.9 show two examples of simulated and observed PPI scans from the La Dôle radar in western Switzerland at  $1^\circ$  elevation during one mostly convective event (13 August 2015) and one mostly stratiform event (8 April 2014). The displayed radar reflectivities are raw uncorrected ones, and the attenuation effect is taken into account for simulated reflectivities. It can be seen that in both cases, the model is able to locate the center of the precipitation event quite accurately but tends to overestimate its extent, especially in the convective case. Generally, the simulated  $Z_H$ ,  $Z_{DR}$  and  $K_{dp}$  are of the same order of magnitude as the observed ones, with the exception of the stratiform case, where the simulated  $K_{dp}$  is underestimated on the edges of the precipitating system. The simulated radial velocities seem very realistic and agree well with observations both in terms of amplitude and spatial structure.

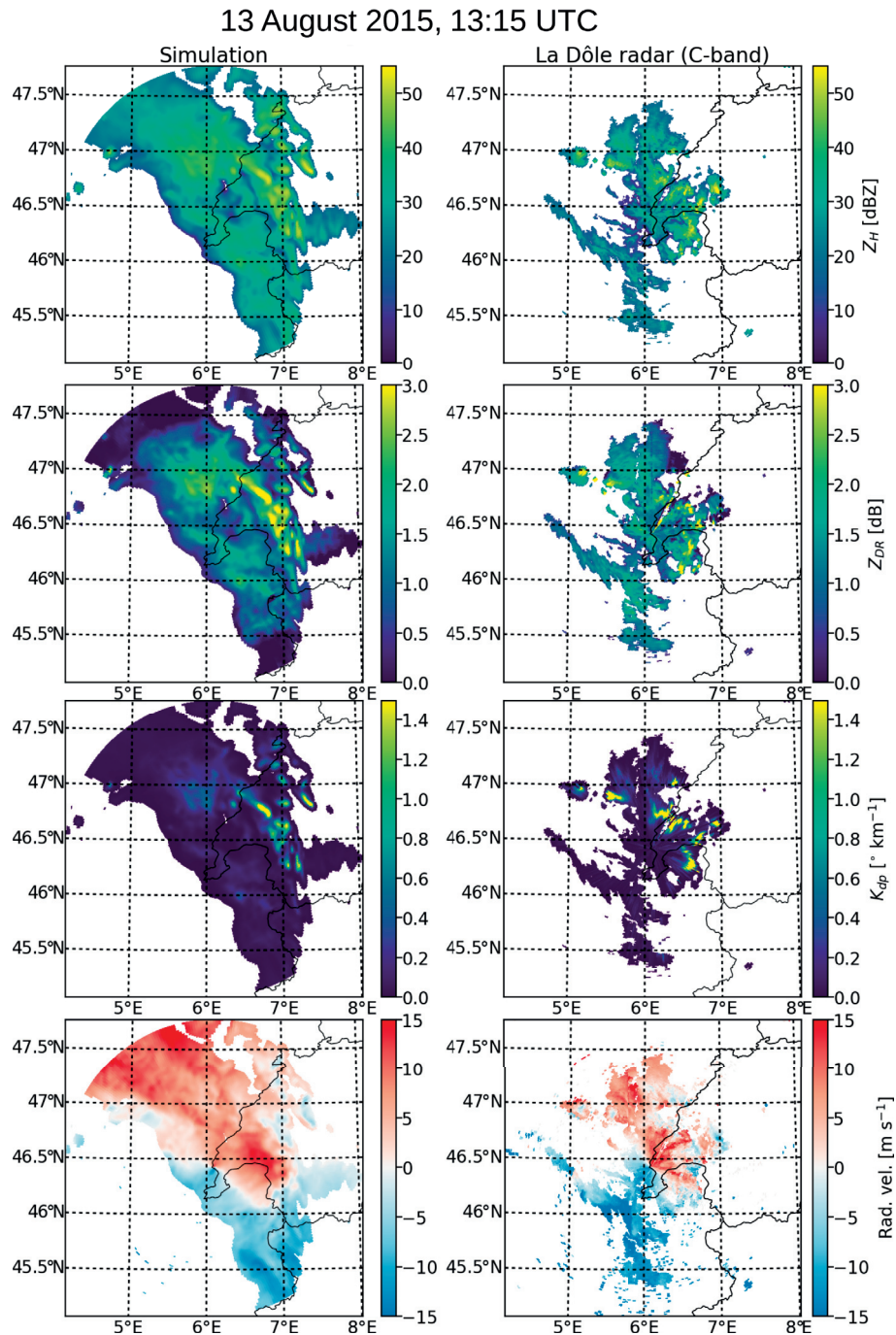


Figure 4.8 – Example of simulated and observed (with the Swiss La Dôle C-band radar) PPI at  $1^\circ$  elevation during the 13 August 2015 convective event (Table 4.3). The left side panel corresponds to the simulated radar observables and the right side to the observed ones. The displayed variables are, from top to bottom, the horizontal reflectivity factor (in dBZ), the differential reflectivity (in dB), the specific differential phase shift upon propagation (in  $^\circ \text{km}^{-1}$ ), and the radial velocity (in  $\text{m s}^{-1}$ ).

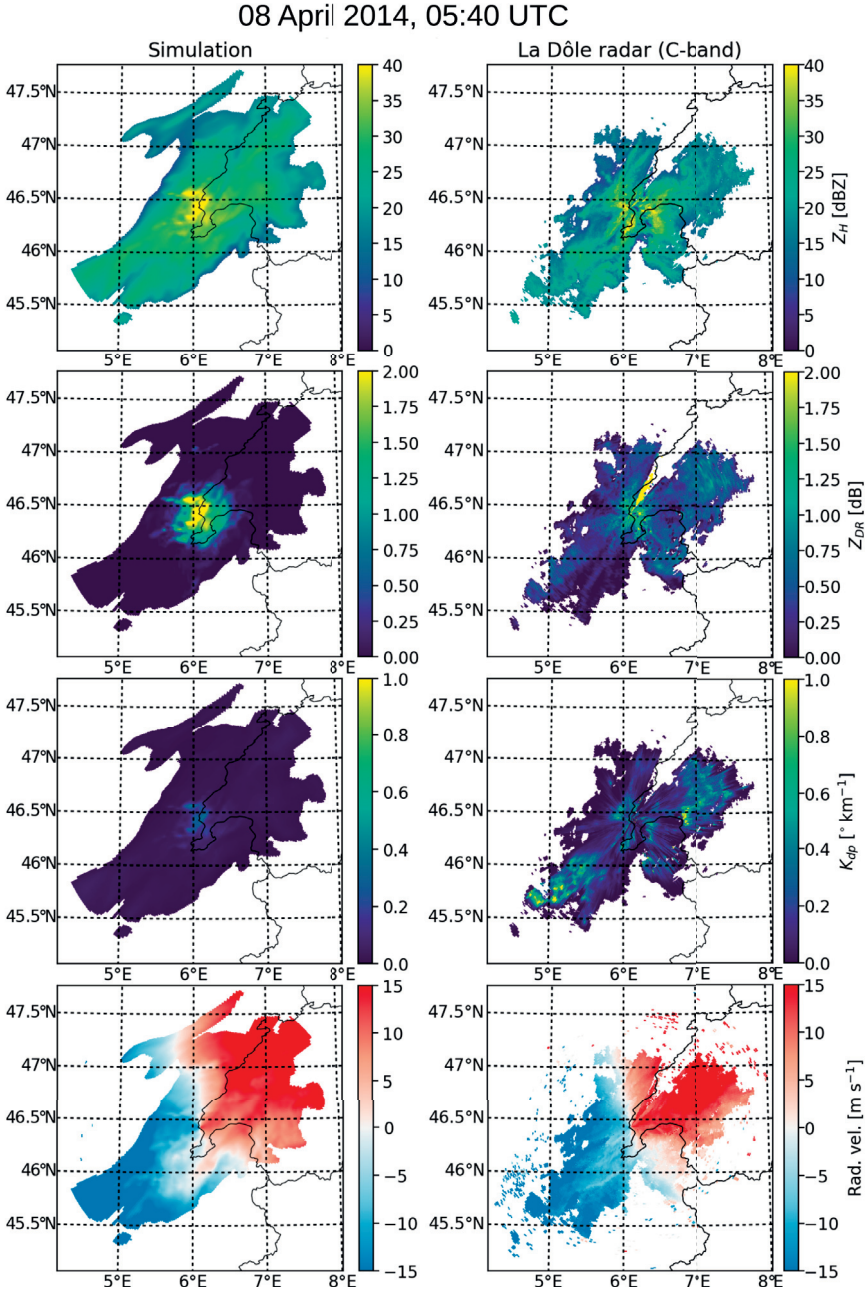


Figure 4.9 – Same as Figure 4.8 but for the stratiform event on the 8 April 2014 (Table 4.3).

## 4.5.1.2 RHI with melting layer at X-band

Figure 4.10 shows one example of simulated and observed RHI scan in a stratiform situation (22 March 2014) with a clearly visible melting layer at low altitude. It can be seen that the forward radar operator is indeed able to simulate a realistic polarimetric signature within the melting layer with a clearly visible bright-band in  $Z_H$ , an increase in  $Z_{DR}$  followed by a sharp decrease in the solid phase above and higher values of  $K_{dp}$ . The extent of the melting layer seems also to be quite accurate when compared with radar measurements. Note that, in this case, the model slightly overestimates the signature in  $Z_{DR}$  and  $Z_H$  below the melting layer, but this is related to the fact that COSMO tends to overestimate the rain intensity during this particular event. In terms of radial velocities, again the model simulates some very realistic patterns that agree well with the observations, with two shear transitions at around 1 and 3.5 km altitude followed by a strong increase in velocities at higher altitudes.

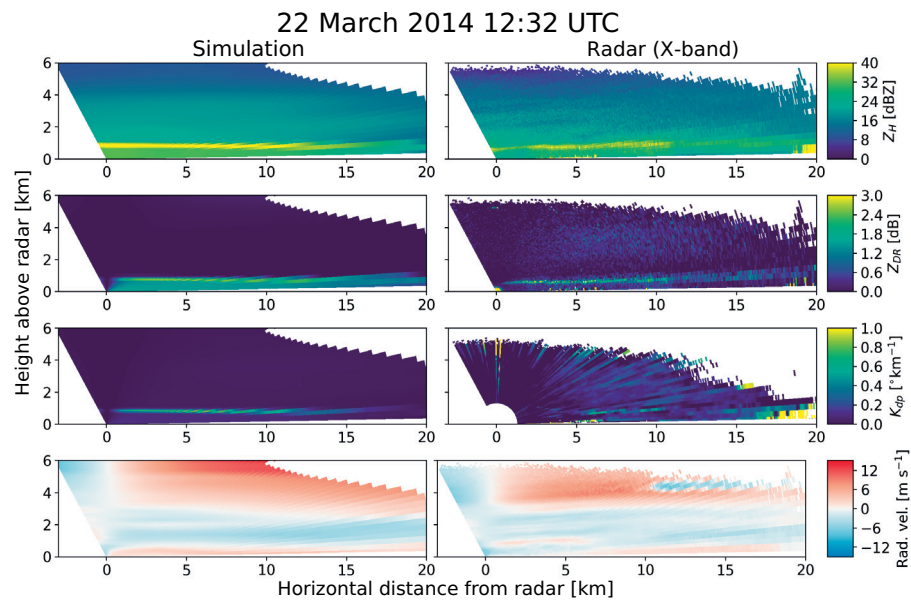


Figure 4.10 – Example of RHI showing the observed and simulated melting layer during the PARADISO campaign in Spring 2014 (Table 4.3). The left panel corresponds to the simulated radar observables, the right panel to the observed values at X-band.

### 4.5.1.3 GPM swath

Figure 4.11 shows an example of simulated and measured GPM swath at Ku band at different altitudes. Again the forward radar operator produces a realistic horizontal and vertical structure as well as plausible values of reflectivities, given the fact that in this case the simulated average rain rate is lower than the GPM estimated average rain rate ( $0.38 \text{ mm s}^{-1}$  vs  $0.46 \text{ mm s}^{-1}$ ).

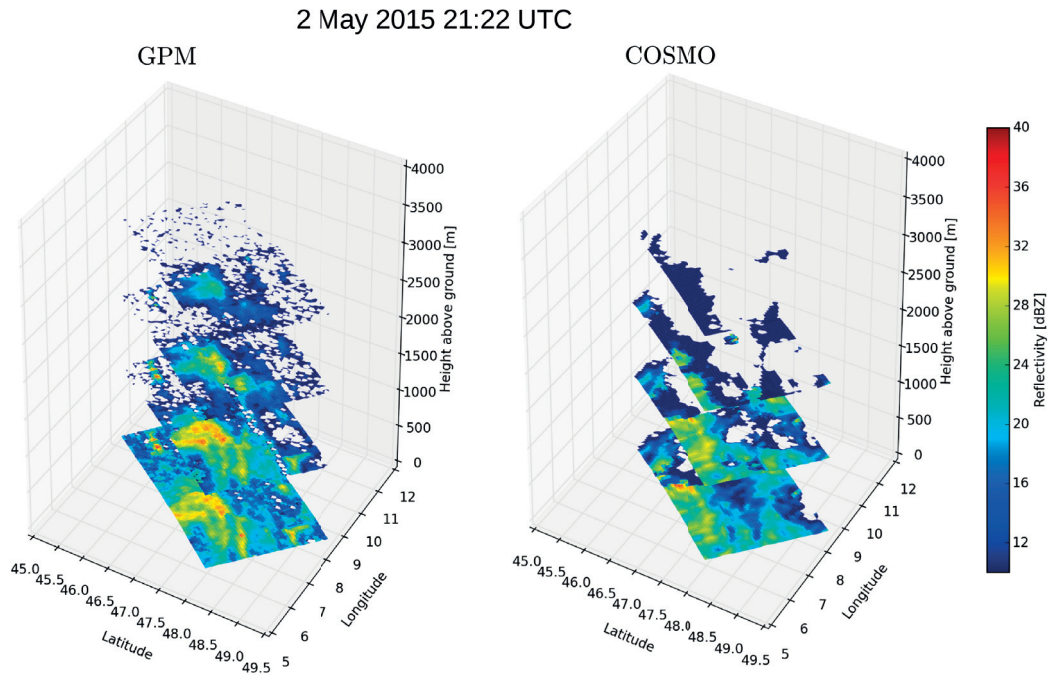


Figure 4.11 – One example of comparison at several altitude levels between GPM radar observations at Ka band (left) and the corresponding radar operator simulation from the COSMO model (right) for one GPM overpass. Note that there is an area with velocity folding (blue area in the middle of a larger red area) around 5 km altitude and 10-15 km horizontal distance on the radar RHI scan.

### 4.5.2 Doppler variables

Evaluation of the simulated average radial velocities was performed by comparison of simulated velocities with observations from the MXPoL X-band radar deployed in Payerne in Western Switzerland in Spring 2014 in the context of the PARADISO measurement campaign.

A total of 720 RHI scans (from 0 to  $180^\circ$  elevation) were simulated over six days of mostly stratiform precipitation (c.f. Table 4.3). Figure 4.12 shows a comparison of the distributions of radial velocities between the simulation and the radar observations. The scatter-plot in Figure 4.13 shows the excellent overall agreement when considering all events and scans. Simulations match very well observations, both in terms of distributions and in terms of one-to-one relations, which shows that the radar operator is indeed able to simulate accurate

radial velocities. Since wind observations from the radio soundings performed in Payerne are assimilated into the model, one can expect it to perform well in this regard. These results indeed confirm these expectations.

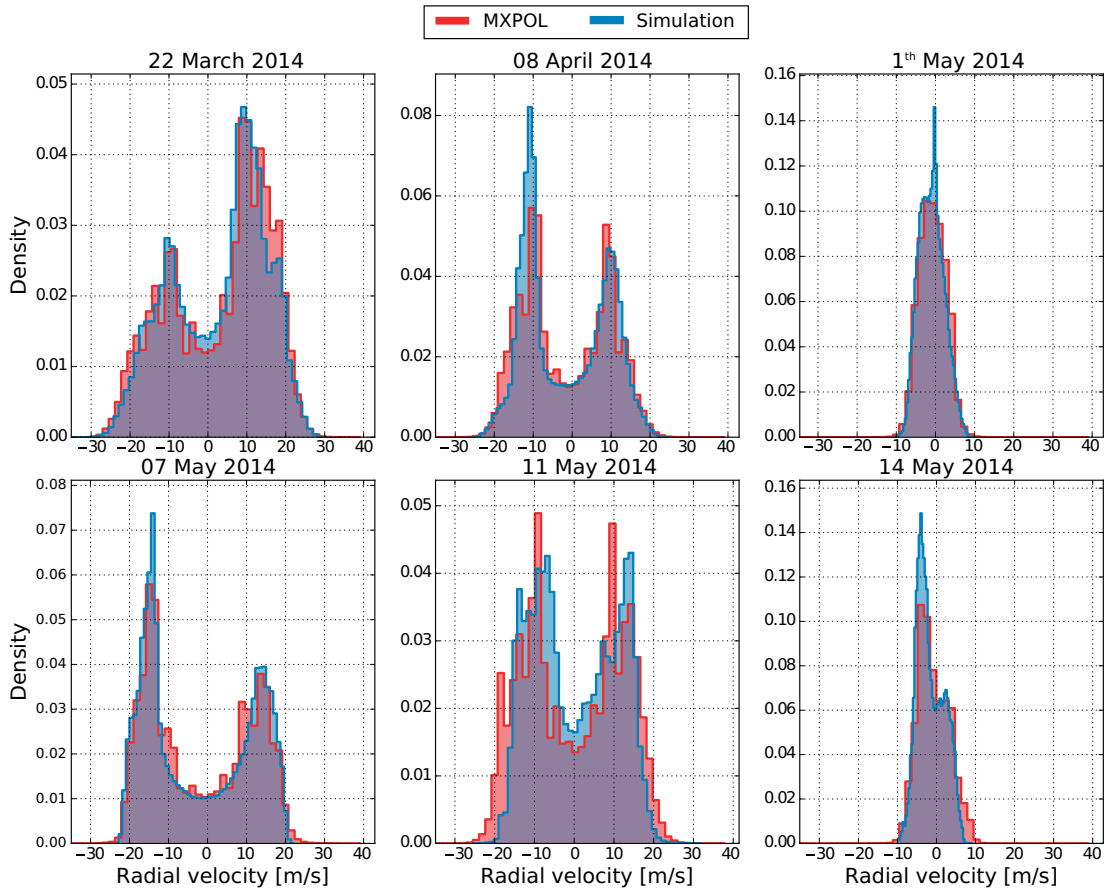


Figure 4.12 – Distributions of simulated (blue) and observed (red) radial velocities during six days of precipitation in Western Switzerland.

During the PARADISO campaign, MXPol was also retrieving the Doppler spectrum at vertical incidence, which allows to compare simulated spectra with real measurements. Figure 4.14 shows the daily averaged simulated and measured Doppler spectra during the same six days of precipitation. Generally, the simulated spectrum is able to reproduce the transition from high velocities near the ground (in liquid precipitation) to smaller velocities in altitude (solid precipitation). The height of this transition, which corresponds roughly to the isotherm  $0^{\circ}$ , as well as the simulated velocities above and below the isotherm  $0^{\circ}$  agree quite well with the observations. Thanks to the melting layer scheme, the operator is able to produce a quite realistic transition between solid and liquid phase. Indeed, when the melting scheme is disabled, the simulated Doppler spectra show a very abrupt and unrealistic transition in velocities. In terms of reflectivity, the bright-band effect is clearly visible on the simulated spectra and its magnitude relative to the reflectivities below and above the melting layer agrees well with observations. In absolute terms however, some events show a good agreement (22

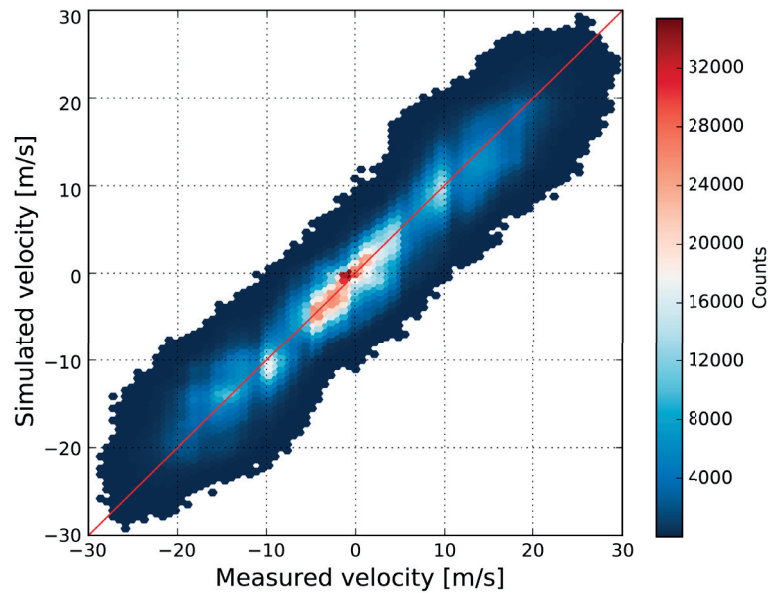


Figure 4.13 – Scatter-plot of overall agreement between measured and simulated radial velocities (for all events). The red line shows the 1:1 relation. The coefficient of determination ( $R^2$ ) is 0.9.

March 2014, 7 May 2014), while in others, the simulated reflectivities tend to be overestimated over the whole spectrum (8 April 2014, 14 May 2014, 1st May 2014). It is likely however, that these discrepancies are mostly caused by the larger precipitation intensities simulated by the model during these days.

Precipitation measurements with a rain gauge collocated with the radar tend to confirm this hypothesis. For the two events with the strongest discrepancies (1st May and 14 May), the gauge measured in total 1.9 and 1.2 mm of precipitation, whereas the model simulated 16.9 and 2.1 mm of precipitation in the closest grid cell.

### 4.5.3 Polarimetric variables

Evaluation of polarimetric variables ( $Z_H$ ,  $Z_{DR}$  and  $K_{dp}$ ) is difficult, because their agreement with radar observations depends heavily on the temporal and spatial accuracy of simulated precipitation fields. However, when averaging over a sufficiently large number of samples, the radar operator should at least be able to simulate realistic distributions of polarimetric variables, as well as realistic relations between these polarimetric variable. Augros et al. (2016) for example, validated their operator, inter alia, by comparing simulated and observed membership functions between the polarimetric functions.

In order to test the quality of the simulated polarimetric variables, five events corresponding to different synoptic situations with widespread precipitation over Switzerland were selected (Table 4.3). The simulated polarimetric variables were compared with observations from three



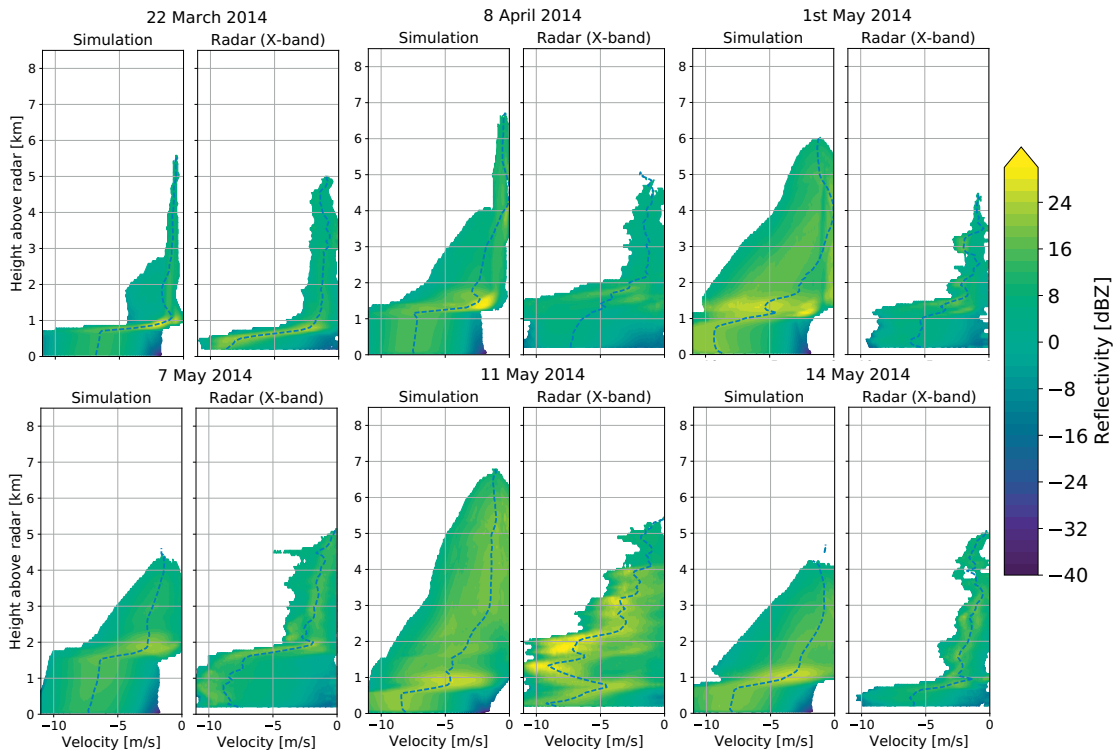


Figure 4.14 – Simulated and measured average (over the event) Doppler spectra at vertical incidence during six days of precipitation in Western Switzerland. The dashed line represents the radial velocity calculated from the spectrum (Equation 4.39)

operational C-band radars (La Dôle, Albis and Monte Lema).

The duration of all events ranges between 12 and 24 hours with a resolution in time of 5 minutes (which corresponds to the temporal resolution of the available radar data). A total of 1017 PPI scans were simulated at  $1^\circ$  elevation with a maximum range of 100 km (in order to limit the effect of beam-broadening). Both observed and simulated radar data were censored with an  $SNR_{thr}$  value of 8 dB (Equation 4.18).

The *shape* parameter of the gamma DSD used in COSMO for rain has a strong influence on the outcome of the radar operator. Indeed, the skewness of the gamma distribution is inversely proportional to  $\mu^{rain}$ , so DSDs with small values of  $\mu^{rain}$  will have longer right tails. This is of particular importance when simulating polarimetric variables that are related to statistical moments of a high order, such as  $Z_{DR}$ . Two values of  $\mu^{rain}$  have been tested,  $\mu^{rain} = 0.5$ , which is the default value in the model and  $\mu^{rain} = 2$  which corresponds to the upper range of recommended values in the model.

The comparison between simulated and observed radar variables was performed separately in the liquid and solid phases. Indeed, the uncertainty in the liquid phase is expected to be lower than in the ice phase because the scattering properties of raindrops are more reliable than in

snowfall. The simulated model temperatures were taken as a criterion to separate the phases; the liquid phase corresponds to  $T > 5^\circ$  and the solid phase to  $T < -5^\circ$  as in Augros et al. (2016). Areas with temperatures in between have been ignored in order to limit the contribution of wet snow which is not directly simulated by COSMO. It was observed that increasing the temperature margin between liquid and solid phases did not change significantly the main results and conclusions. Decreasing it, however, would affect quite significantly the observed radar signatures due to the inclusion of measurements from the melting layer, which have a much stronger polarimetric signature than dry snow.

Figure 4.15 shows the corresponding histograms of observed and simulated polarimetric variables and precipitation intensities at the ground in the liquid phase, for  $\mu^{\text{rain}} = 2$ . The histograms for  $\mu^{\text{rain}} = 0.5$  (not displayed) show only minor differences. The simulated distributions agree well with the observed ones in terms of broad features, which confirms the fact that the operator is able to simulate realistic radar observables at least in liquid phase. One can observe that the radar operator is not able to simulate negative  $Z_{\text{DR}}$ , which can be explained by the assumptions about the drop shapes and canting angles, which make it almost impossible for a drop to have a vertical dimension larger than its horizontal dimension. In addition, the radar operator seems to produce slightly smaller values of  $Z_{\text{H}}$  than observed, but this can be attributed to the fact that COSMO tends to simulate smaller precipitation intensities than the ones estimated from the radar reflectivities (bottom-right of Figure 4.15). Indeed, the discrepancies in  $Z_{\text{H}}$  agree well with the discrepancies in precipitation intensities.

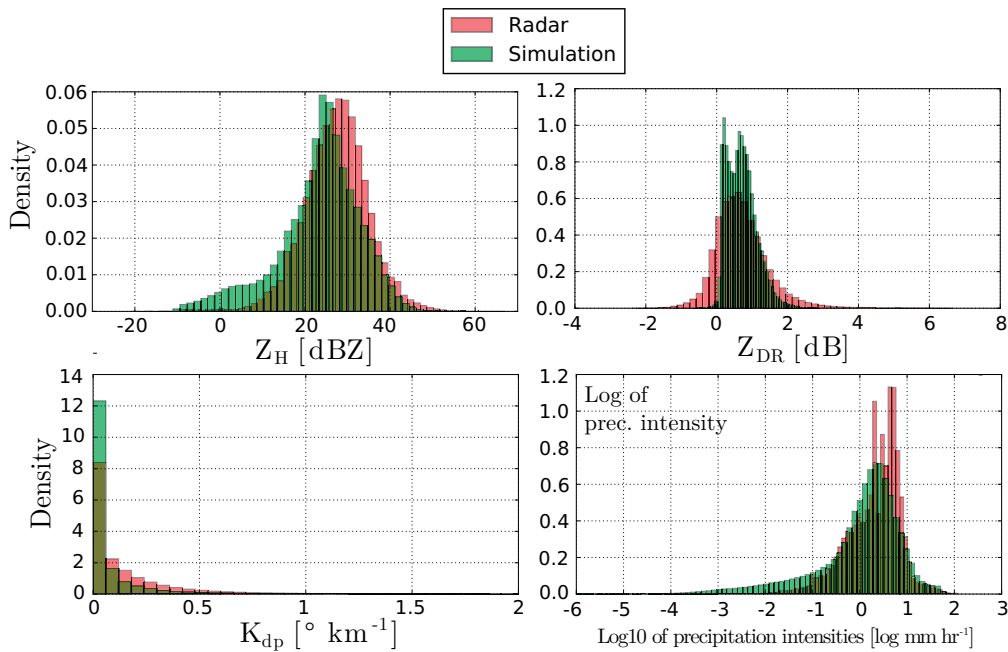


Figure 4.15 – Observed (red) and simulated (green) distributions of polarimetric variables ( $Z_{\text{H}}$ ,  $Z_{\text{DR}}$  and  $K_{\text{dp}}$ ) as well as the precipitation intensities on the ground (in log scale) for the one-moment scheme with  $\mu^{\text{rain}} = 2$  in the liquid phase.

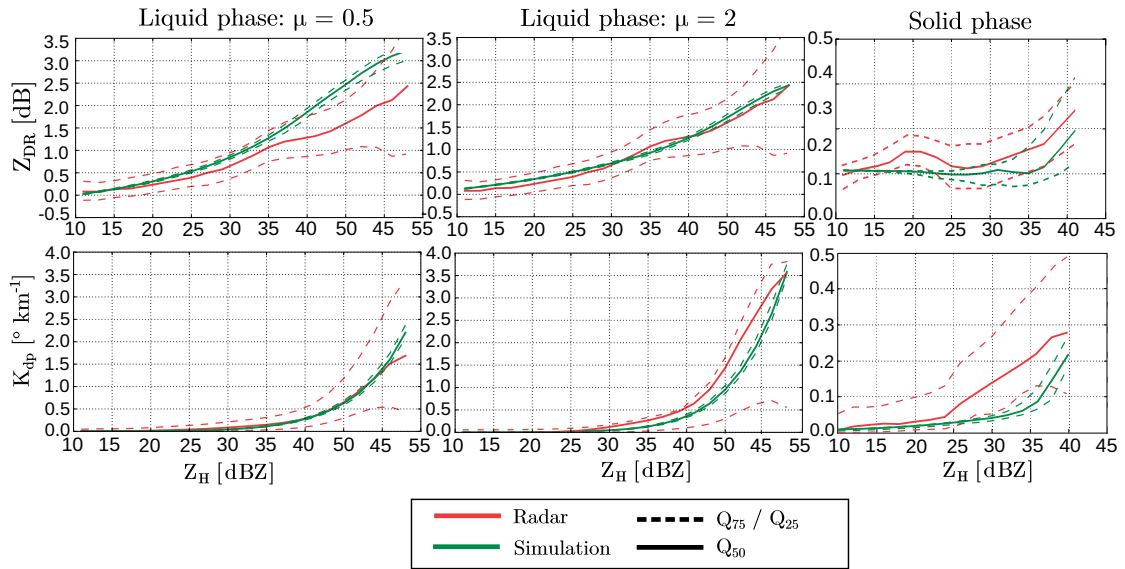


Figure 4.16 – Observed (red) and simulated (green)  $Z_H - Z_{DR}$  and  $Z_H - K_{dp}$  relationships for the COSMO one-moment scheme in liquid and solid phases. These membership functions are computed by dividing all simulated values in bins of reflectivity of 1 dBZ of width, and computing the quantiles of the dependent variable (on the  $y$ -axis) within every bin.

Figure 4.16 shows the observed (from MeteoSwiss radars) and the simulated  $Z_H - Z_{DR}$  and  $Z_H - K_{dp}$  relations averaged over all radars and all events in the liquid and solid phases. It appears that the radar operator is able to simulate realistic relations between polarimetric variables at least in the liquid phase. In terms of  $Z_{DR}$ , a value of  $\mu^{\text{rain}} = 2$  seems more appropriate than a value of 0.5, which tends to overestimate the differential reflectivity for a given horizontal reflectivity. For  $K_{dp}$  the trend is reversed. A possible explanation is that  $Z_{DR}$  is independent of the concentration and highly dependent on the length of the DSD tail, i.e. small differences in the numbers of large and oblate drops can cause large differences in differential reflectivity.  $K_{dp}$  however, depends on both the total concentration and the tail of the DSD, and is quite sensitive to the mode of the DSD. However, one must also keep in mind that the “observed”  $K_{dp}$  values are in fact estimated from noisy  $\Psi_{dp}$  measurements and as such are likely to be underestimated (Grazioli et al., 2014a). This dependency of simulated polarimetric variables on small changes in the DSD shape illustrates quite well the difficulty to parameterize the DSDs to match both the lower order moments used in weather prediction (number and mass concentration) and the higher order moments, to which the radar observables are related.

In the solid phase, the radar operator tends to underestimate  $Z_{DR}$  and  $K_{dp}$ , which is a trend also observed by Augros et al. (2016). This is likely due to the combination of the imperfect parameterization of snow PSD in the model, the crude assumptions about the permittivity of snow and graupel (mixture model derived from the COSMO density parameterizations), and the estimation of the scattering properties (T-matrix is likely not correct for ice-phase hydrometeors).

#### 4.5.4 GPM swaths

In order to evaluate the simulation of GPM swaths, the distributions of simulated and observed reflectivities at both Ku and Ka band were compared for 100 GPM overpasses over Switzerland, corresponding to the overpasses with the largest precipitation fluxes (c.f. Section 4.3.3).

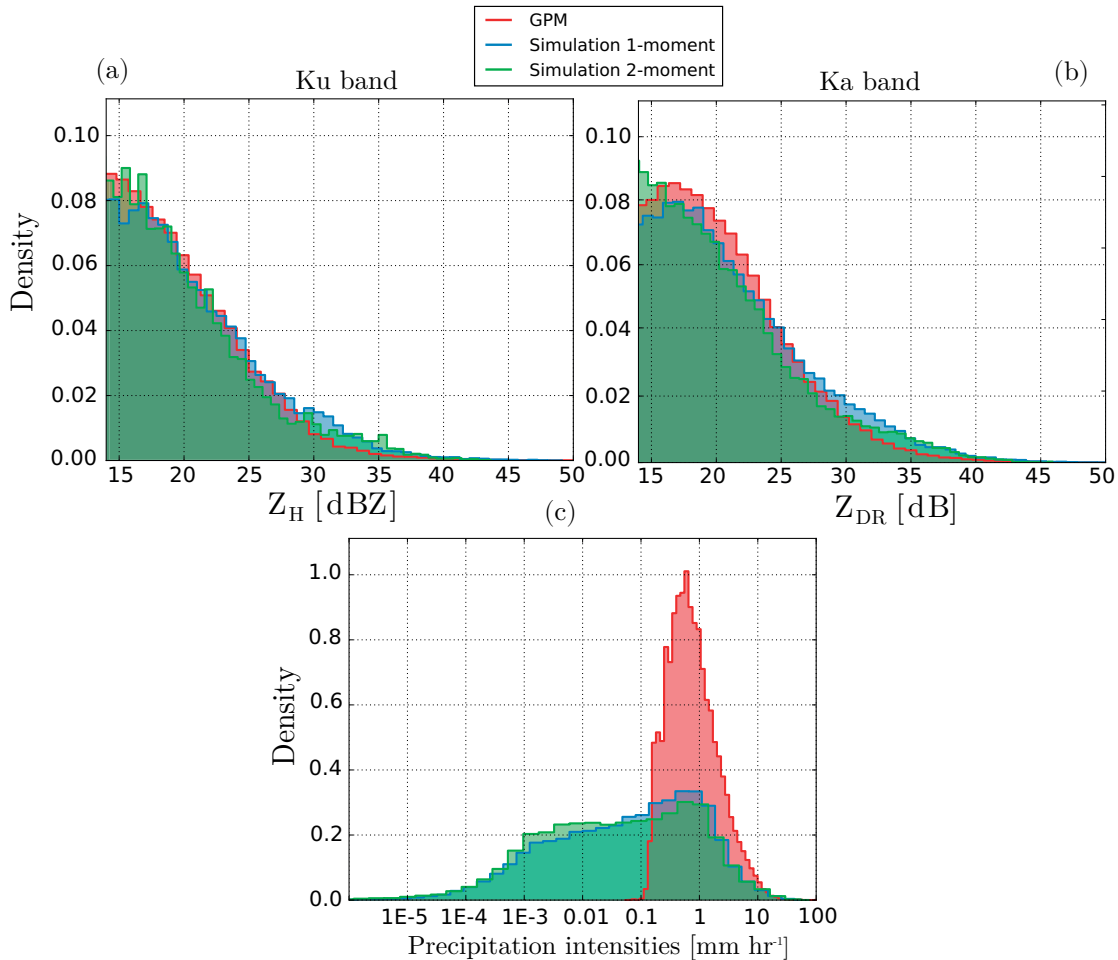


Figure 4.17 – Observed (red) and simulated (blue = one-moment, green = two-moments) reflectivities at Ku band (a) and Ka band (b), as well as the precipitation intensities (in log-scale) at the ground (c) estimated by GPM and simulated by COSMO

Figure 4.17 shows the overall distributions of reflectivity at both frequency bands as well as the distributions of estimated GPM precipitation intensities and COSMO simulated intensities. Note that all reflectivities below 14 dBZ have been discarded as this corresponds roughly to the radar sensitivities at Ka and Ku band (Toyoshima et al., 2015). Although the distributions are very consistent, some minor discrepancies are present, mostly for low reflectivities (at Ka band only) and high reflectivities which appear more frequently in the simulations than in the measurements from the GPM-DPR. Again, this is consistent with the differences in simulated precipitation intensities (in panel c). COSMO tends to produce a larger number of precipitation intensities  $\geq 30$  mm hr<sup>-1</sup> as well as a larger number of precipitation intensities

below  $0.15 \text{ mm hr}^{-1}$  which corresponds roughly to 14 dBZ. In addition, comparison of GPM measurements with ground radar observations confirms that GPM tends to underestimate larger reflectivities Speirs et al. (2017). Overall, the simulated distributions of reflectivity at both frequency bands are realistic and agree quite well with the observations for both microphysical scheme. Note that when neglecting ice crystals the match is much poorer (see Section 4.5.5).

#### 4.5.5 Effect of ice crystals

In order to evaluate the addition of ice crystals to the forward operator, a two-fold analysis was performed. First, the simulated polarimetric variables obtained with and without considering ice crystals were compared with real observations by MXPoL during three pure snowfall events in the Swiss Alps in Davos (Table 4.3). Since no liquid precipitation or melting layer was present during these events, the attenuation effect is expected to be negligible. Note that the analysis focused on the one-moment scheme but the effect on the two-moment scheme is expected to be quite similar.

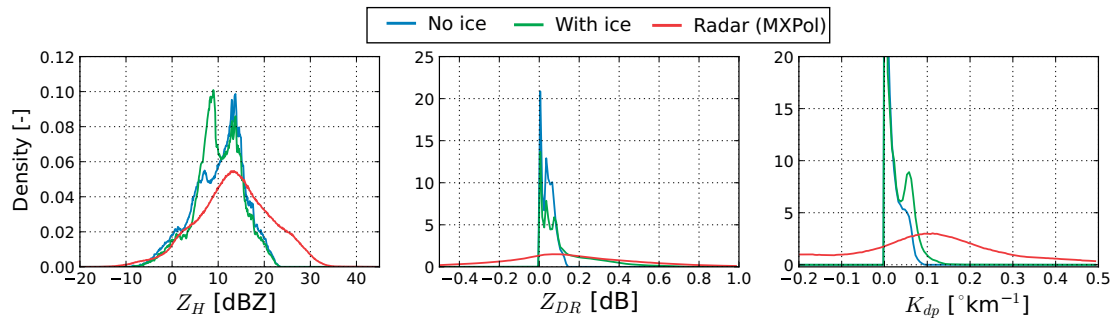


Figure 4.18 – Observed and simulated (with and without ice crystals) distributions of polarimetric variables during three pure snowfall events for the one-moment microphysical scheme.

Figure 4.18 shows a comparison of the distributions of polarimetric variables in the solid phase averaged over all three events for the one-moment microphysical scheme. On  $Z_H$ , the effect of adding ice crystals is characterized by an additional mode around 8 dBZ, which is not present on radar observations. This mode is caused by the large homogeneity in the simulated ice crystals, which, according to the microphysical parameterization, are all assumed to be hexagonal plates. In reality, ice crystals can have a large variability of shapes (e.g., Magono and Lee, 1966; Bailey and Hallett, 2009), and their backscattering coefficients can be quite different (Liu, 2008), which would result in a much more spread out reflectivity signature of ice crystals. On  $Z_{DR}$ , one can see that, when neglecting ice crystals, one completely removes the right tail of the distribution (values above 0.2 dBZ) that is clearly visible on the observed values. When considering ice crystals, which have a quite strong signature in differential reflectivity, this right tail gets accurately reproduced and matches well with the observations. However, even when adding ice crystals, the radar operator is not able to reproduce the negative  $Z_{DR}$  values

that are quite frequent in the observations. On  $K_{dp}$ , a similar effect can be observed, though not as clear. Still, the addition of ice crystals creates an additional mode in the distribution of simulated values which slightly better matches with the observed one (longer tail and good agreement of the additional mode with the mode of the observed distribution). Just as with  $Z_{DR}$ , the radar operator is not really able to simulate negative values of  $K_{dp}$ , which are also frequent in the observations. These discrepancies could however also be due in part to uncertainties in the radar observations, coming from possible miscalibration (for  $Z_{DR}$ ) and inaccuracies in the retrieved  $K_{dp}$  values. Still, overall at X-band, the addition of ice crystals leads to a much better representation of  $Z_{DR}$  in solid precipitation, a slightly better representation of  $K_{dp}$  and no significant improvement in  $Z_H$ .

Due to their smaller sizes, the effect of ice crystals on  $Z_H$  should increase with the frequency. To investigate this effect, a second comparison was performed on the simulation of GPM swaths, with and without ice crystals. The resulting distributions of  $Z_H$  at Ku and Ka band were compared with means of QQ-plots of observed versus simulated quantiles. Figure 4.19 shows these QQ-plots at Ka band for both the one-moment and the two-moments scheme. The red line is the 1:1 which implies a perfect match with the observed quantiles. The results at Ku band are not displayed as they are visually very similar to the results at Ka band. For the one-moment scheme, a much better agreement with observations is observed for small quantiles (up to 20 dBZ) when adding ice crystals. Without ice crystals, small quantiles tend to be underestimated. Large simulated quantiles tend to be overestimated when compared with GPM observations. For very large quantiles, this overestimation is slightly stronger when adding ice crystals but this might be a sampling effect as large quantiles are very sensitive to outliers. For the two-moments scheme, adding ice crystals does not seem to significantly improve the agreement with observed quantiles.

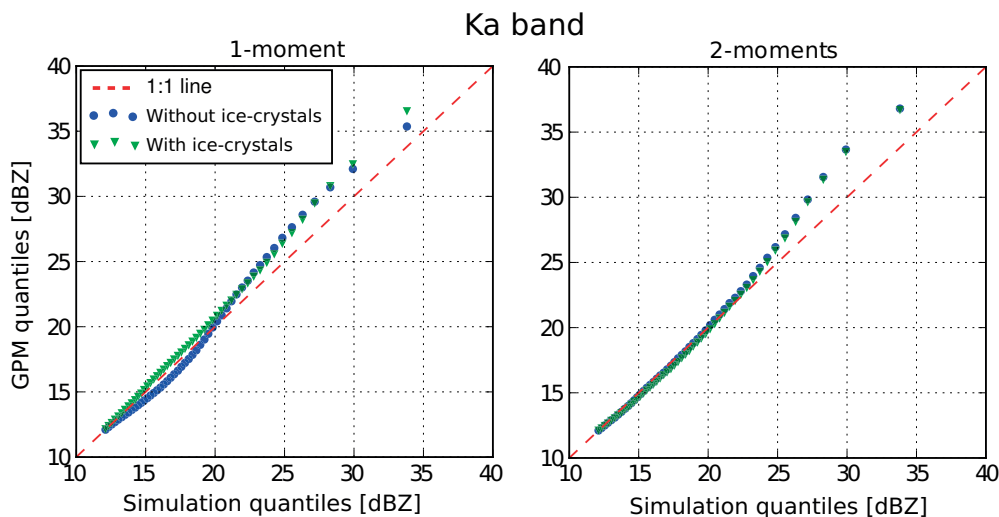


Figure 4.19 – QQ-plots of the quantiles of simulated  $Z_H$  values versus the quantiles of observed GPM  $Z_H$  values at Ku band. The red line corresponds to the 1:1 line indicating a perfect match with observed quantiles.

As a conclusion, adding ice crystals improves the quality of the simulated  $Z_{DR}$  and  $K_{dp}$  in pure solid precipitation at X-band and when simulating horizontal reflectivities at K band.

### 4.6 Summary and conclusions

In this chapter we proposed a new polarimetric radar forward operator for the COSMO NWP model which is able to simulate measurements of reflectivity at horizontal polarization, differential reflectivity and specific differential phase shift on propagation for ground based or spaceborne (e.g. GPM) radar scans, while taking into account most physical effects affecting the propagation of the radar beam (atmospheric refractivity, beam-broadening, partial beam-blocking and attenuation). Integration over the antenna pattern is done with a simple Gauss-Hermite quadrature scheme. This scheme was compared with more advanced schemes that also take into account antenna side lobes, but was shown to offer on average the best trade-off, due to its better representation of the main lobe and lower computational cost. The operator was extended with a new Doppler scheme, which allows to efficiently estimate the full Doppler spectrum, by taking into account all factors affecting the spectral width (antenna rotation, turbulence, wind shear and attenuation), as well as a melting layer scheme able to reproduce the very specific polarimetric signature of melting hydrometeors, even though the COSMO model does not explicitly simulate them. Finally, the operator was adapted both to the operational one-moment microphysical scheme of COSMO and to its more advanced two-moment scheme. Performance tests showed that the operator is sufficiently fast and efficient to be run on a simple desktop computer.

The scattering properties of individual hydrometeors are pre-computed with the T-matrix method and stored into lookup tables for various frequencies. The permittivities for the complex hydrometeors (snowflakes, hail and graupel) are obtained with a mixture model by using the mass-diameter relations of COSMO to estimate their densities. The other required parameters for the T-matrix method (canting angle distributions and aspect-ratios) are obtained from the literature (for rain, hail and ice crystals) and from measurements performed in the Swiss Alps with a multi-angle snowflake camera (MASC), for snow and graupel. A large number of MASC pictures are used to estimate realistic parameterizations of the distributions of aspect-ratio and canting angle of graupels and aggregates, leading to a good agreement with measured quantiles. Integration of the hydrometeors scattering properties over these distributions was shown to increase the polarimetric signature of solid hydrometeors, which tends to be often underestimated in simulations.

The operator was evaluated by a comparison of the simulated fields of radar observables with observations from the operational Swiss radar network, from a high resolution X-band research radar and from GPM swaths. Visual comparisons between simulated and measured polarimetric variables show that the operator is indeed able to simulate realistic looking fields of radar observables both in terms of spatial structure and intensity, and to simulate a realistic melting layer both in terms of thickness and polarimetric signature. Comparisons of the radial

## **Chapter 4. A forward polarimetric radar operator for the COSMO NWP model**

---

velocities measured by the X-band radar and simulated by the radar operator, in the vicinity of the Payerne radiosounding site show an excellent agreement with a high determination coefficient. The operator is also able to simulate realistic Doppler spectra at vertical incidence, with realistic fall velocities and reflectivities below and above the melting layer, as well as within the melting layer, thanks to the melting scheme. A comparison of the distributions of polarimetric variables as well as the relations between these variables with measurements from the Swiss operational C-band radar network was performed. In the liquid phase, the radar operator is generally able to simulate realistic distributions of polarimetric variables and realistic relations between them.

In the solid phase, however, the polarimetric variables tend to be underestimated when using the T-matrix method to simulate hydrometeor scattering properties, even with the local MASC parameterization. Finally the effect of considering or not ice crystals in the simulation was investigated and it was observed that at X-band the agreement with observed differential reflectivity and differential phase shift improves significantly, whereas at GPM frequencies, the simulated distributions of reflectivity are more realistic, especially for smaller reflectivities.

Ultimately, this operator provides a convenient way to relate outputs of a NWP model (state of the atmosphere, precipitation) to polarimetric radar measurements. The evaluation of the operator has shown that this tool is a promising way to test the validity of some of the hypothesis of the microphysical parameterization of COSMO. In the next chapter, a detailed sensitivity analysis of the main parameters and assumptions of the radar operator will be performed, taking again a large dataset of radar observations as reference. In the liquid phase, the analysis will focus on the geometry of raindrops as well as the parameterization of the DSD. In the solid phase, the polarimetric variables simulated with the T-matrix method will be compared with more sophisticated scattering models, such as the discrete dipole approximation or the generalized multi-Mie method (Lu et al., 2016).



# 5 Sensitivity study of the polarimetric radar operator

## 5.1 Summary

In this chapter, the sensitivity of the radar variables simulated by the radar operator described in details in Chapter 4 to some of its main assumptions is tested. The study is separated between the liquid phase, where the geometrical parameters of raindrops and the effect of the drop size distribution parameterization are tested, and the solid phase, where several methods for the estimation of scattering by solid hydrometeors are compared. In the liquid phase, the results indicate that  $Z_{DR}$  and to a lesser extent  $K_{dp}$  are very sensitive to the considered DSD model. In addition  $Z_{DR}$  depends strongly on the aspect-ratio model and the canting angle distribution. It is shown also that a simple generalized gamma DSD model could be optimized to provide a much better agreement between observed and simulated radar quantities, while providing the same concentration and rainrate as the original COSMO DSD. This alternative models also shows a better agreement with Parsivel observations in terms of median DSD.

In the solid phase, it is shown that T-matrix based methods tend to underestimate strongly the signature in  $Z_{DR}$  and  $K_{dp}$  even when integrating over realistic geometries derived from MASC observations. It reveals that the T-matrix method tends to underestimate strongly the polarimetric signature in snow, and to underestimate the reflectivity factors at higher frequencies. In this regard, the more advanced discrete dipole approximation and generalized multi-Mie scattering methods give promising results that could lead to a significant improvement in the simulated radar variables.

### 5.2 Introduction

In Chapter 4, a polarimetric forward radar operator for the COSMO NWP model has been presented. This operator has been evaluated with radar data from the Swiss operational radar network, from an X-band polarimetric research radar and with swaths from the spaceborne GPM-DPR. The evaluation showed that the radar operator is able to simulate realistic Doppler information, both in terms of average velocity and spectrum as well as realistic values of horizontal reflectivity ( $Z_H$ ), differential reflectivity ( $Z_{DR}$ ) and specific differential phase shift ( $K_{dp}$ ) in the liquid phase. It was also hinted that some assumptions of the COSMO model and the radar operator could have a strong impact on the observed discrepancies. For example when changing the *shape* parameter  $\mu$  of the gamma DSD of rain, the polarimetric signature in rain changes significantly with a better agreement in the  $Z_H - Z_{DR}$  relationship at the expense of a poorer match in the  $Z_H - K_{dp}$  relation.

In the solid phase the agreement is generally much worse than in the liquid phase and the radar operator is strongly underestimating the polarimetric signature in  $K_{dp}$  and  $Z_{DR}$ . A large part of this discrepancy could be explained by the crude assumptions used by the radar operator to determine the scattering properties of solid hydrometeors: all particles are assumed to be spheroids with a diameter-dependent homogeneous permittivity, a quite unrealistic model when compared for example with the intricate structure of a dendrite aggregate.

In this work we will investigate in more details the relation between the polarimetric signature simulated by the radar operator and some of the relevant parameters and assumptions that are used. Here again the radar data will be used as a reference. In the liquid phase, the effect of drop geometry and DSD model will be tested, while in the solid phase, the simple T-matrix model will be compared with two more sophisticated scattering estimation methods. The first alternative method is still based on the T-matrix method but uses MASC measurements to estimate more realistic particle geometries, while the second method uses the polarimetric scattering database of Lu et al. (2016). Real radar observations from both ground radars (operational Swiss radar network at C-band, and MXPol at X-band), and from the GPM-DPR satellite radars (Ku and Ka bands) will be used again as a reference.

This chapter is structured as follows: in Section 2, a description of the various parameters, data and methods used in this sensitivity analysis will be described, in Section 3, the main results of this sensitivity analysis will be presented, first in the liquid phase and then in the solid phase. Finally, Section 4 gives a summary of the main results and concludes this work.

### 5.3 Methods and data

A sensitivity analysis is performed in order to quantify the influence of the main assumptions and parameterizations on which the radar operator is based. The analysis is conducted separately in the liquid and solid phase because the main sources of uncertainty are different. In the liquid phase, the T-matrix scattering method is exact as long as the particles are spheroids

(Mishchenko et al., 1996), and the permittivity of water can be estimated with great precision (Liebe et al., 1991). As such, for rain, the T-matrix model is well suited, and the analysis focuses on the assumptions about the *shape* of raindrops used in the T-matrix computations. In the solid phase, the T-matrix method is only a crude approximation, as solid hydrometeors have complex shapes and their permittivities cannot be known with precision. Hence, in the solid phase, the analysis focuses on an intercomparison of different scattering methods.

### 5.3.1 Scattering in the liquid phase

The T-matrix method is a reasonable choice for raindrops whose shape can be well approximated by spheroids. However the simulated scattering properties depend quite strongly on three parameters, on which the sensitivity analysis will focus:

#### Canting angle distributions

A Gaussian distribution with zero mean is a reasonable choice to estimate the probability density function of canting angles for raindrops (Bringi and Chandrasekar, 2001). However, the standard deviation  $\sigma_o^{\text{rain}}$  of this distribution is variable and there is no agreement on the best value to be used. In this study, values of  $\sigma_o^{\text{rain}}$  ranging from 2.5 to 17.5 ° with a step of 2 ° are used.

#### Aspect-ratio models

The aspect-ratio model prescribes the oblateness of a raindrop spheroid as a function of its diameter. Several models have been proposed in the literature. Four different aspect-ratio models are tested: Andsager et al. (1999), Thurai and Bringi (2005), Brandes et al. (2002) and Thurai et al. (2007)

#### Shape parameter of the rain drop size distribution

Another crucial parameter is the  $\mu^{\text{rain}}$  *shape* parameter in the rain drop size distribution, which can be chosen *a-priori* in the COSMO set-up. An example of the effect of  $\mu^{\text{rain}}$  for a constant rain concentration is given in Figure 5.1. The gamma DSD varies between an exponential distribution (for  $\mu^{\text{rain}} \rightarrow 0$ ) and a Gaussian distribution (for  $\mu^{\text{rain}} \rightarrow \infty$ ). The length of the right tail is inversely proportional to  $\mu^{\text{rain}}$  and affects strongly the resulting polarimetric variables, as they are very sensitive to large particles. In this study values of  $\mu^{\text{rain}}$  ranging from 0.5 to 5 with a step of 0.5 are used.

### 5.3.2 Scattering in the ice phase

In the ice phase, most of the uncertainty comes from the estimation of the permittivity and the validity of the considered scattering estimation method. Initially, the same study as in

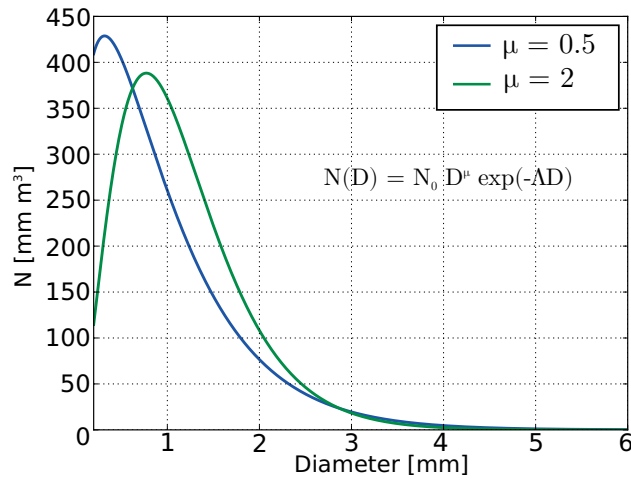


Figure 5.1 – Effect of the *shape* parameter  $\mu$  on the raindrop size distribution for a constant mass concentration of  $1 \text{ g m}^{-3}$  of rain

the liquid phase was repeated in the solid phase<sup>1</sup>, using the same radar observations and simulated events, but with the canting angle standard deviation and aspect ratios of snow and graupel as parameters. It appeared that the match with the radar observations was poor regardless of the values used.

Hence, instead of focusing on the parameters of the T-matrix method, the analysis compares three different scattering methods to estimate the scattering properties of aggregates, graupel and ice crystals.

### Simple T-matrix

In this method, the permittivities of snow aggregates, graupel and ice crystals are estimated with the Maxwell-Garnett mixing formula as described in Formula 4.14 using again the COSMO mass-diameter relations to estimate the particle densities. For the aspect-ratio, a constant value of 0.6 for aggregates and 0.9 for graupel is considered, which correspond to the median values observed by Garrett et al. (2015) on MASC data. The canting angle distributions of both aggregates and graupels are assumed to be Gaussians with a zero mean and a standard deviation of  $40^\circ$  as in Augros et al. (2016) and Ryzhkov et al. (2011). For ice-crystals the aspect ratio model is taken from Auer and Veal (1970) for hexagonal columns and the canting angle distribution is assumed to be Gaussian with zero mean and a standard deviation of  $5^\circ$ , which corresponds to the upper range of the values observed by Noel and Sassen (2005) in cirrus and midlevel clouds. Ice crystals, aggregates and graupel particles are all approximated as spheroids and their polarimetric scattering properties are estimated with the T-matrix method. (Mishchenko et al., 1996).

<sup>1</sup>Defined in this case by all radar gates where the simulated COSMO temperature is lower than  $-5^\circ$

### MASC T-matrix

This set-up corresponds to the default scattering method used by the radar operator described in Chapter 4. It is very similar to the previous one, with the sole difference that the scattering properties estimated with the T-matrix method for snow aggregates and graupels are integrated over realistic distributions of aspect-ratios and canting-angles obtained from MASC observations in the Swiss Alps (Section 4.4.6.1). This allows to better take into account the effect of very oblate particles, which, even though they are rare, can strongly affect the overall polarimetric signature, especially in  $Z_{DR}$ .

### DDA/GMM

This method is based on the polarimetric scattering database ICEPART developed by Lu et al. (2016), which contains polarimetric scattering property information for plates, columns, branched planar crystals, aggregates and conical graupel computed with either the discrete dipole approximation (DDA) or the generalized multi-particle Mie method (GMM). In the current version of the database, the scattering properties are available for X, Ku, Ka and W frequency bands.

The DDA method is based on the discretization of an ice particle into a cluster of polarizable points. The method takes into account both the induction of dipoles by the incident electric field and the interaction between all the dipoles. The GMM method gives an analytical solution of Maxwell's equations for a particle approximated as a cluster of non-overlapping small spheres with fixed size and permittivity (Xu, 1995). Lu et al. (2016) use the GMM method for aggregates because the DDA method is numerically efficient only for relatively compact particles. For all other particle types, the DDA method is used. The database focuses on isolated particles (and not populations of particles), for which the scattering properties are computed for a large number of azimuthal and elevational incidence angles.

Note that other scattering databases exist that use similar methods (e.g., Tyynelä and Chandrasekar, 2014; Kuo et al., 2016) but they can not currently be used in the context of this radar operator, as they do not give any information about forward scattering (Kuo et al., 2016), or consider only an ensemble of particles with various sizes (Tyynelä and Chandrasekar, 2014). Indeed in order to use these databases in the context of the radar operator, the backscattering covariance matrix  $C^{b,(j)}$  and the forward scattering vector  $S^{f,(j)}$  for every hydrometeor type  $j$  need to be estimated for a large number of different diameters in order to allow integration of these properties over the particle size distributions (PSD). Using Lu et al. (2016)'s database it is possible to retrieve this information with the following pre-processing steps:

1. For every incident elevation angle and particle, the individual scattering properties ( $S^f$  and  $C^b$ ) are averaged for all incident azimuths.

2. Using the COSMO mass-diameter relations, the mass of every individual particle (as provided in the database) is related to an equivalent maximum diameter. Particles are then sorted by increasing diameter.
3. For every hydrometeor type, a set of 25 diameter bins are determined, linearly increasing from the minimal to the maximal diameter. The scattering properties are then averaged within every diameter bin.
4. The resulting scattering properties are then interpolated over 1024 bins covering the same range. This is done in order to be generic with the T-matrix method, where the scattering properties are weighted by the PSD and integrated over 1024 diameter bins (by default).

As a final step, for aggregates and graupels only, a Gaussian filter with a diameter-dependent standard deviation  $\sigma_o(D)$  is applied in the elevational direction in order to account for the variability in canting angle. As in the *MASC T-matrix* method, the values of  $\sigma_o(D)$  are obtained from MASC observations (see Equation 4.10 and Figure 4.5).

### 5.3.3 Data

### 5.3.4 Radar data

For the study in the liquid phase, all PPI scans used in the inter-comparison with the Swiss radar network (Section 4.5.3) were simulated and compared with the radar observations of three Swiss C-band radars (index A in Table 4.3). For computational reasons, it is not possible to do an exhaustive sensitivity study, where all possible combinations of all parameters are tested. Instead, all parameters are varied independently of each other. This study was performed on pure liquid phase areas only, defined in this case by all radar gates where the simulated COSMO temperature is larger than  $5^\circ$ . A maximal range of 100 km is considered in the analysis.

The sensitivity analysis in the solid phase is divided in two separate studies. In the first study, the simulated radar variables were evaluated with observations from MXPoI, an X-band radar (see Table 4.2), recorded during two field campaigns performed in Davos in the Eastern Swiss Alps in 2010 and in 2014 (index C in Table 4.3). The radar was located at a high altitude and recorded several events with pure solid phase precipitation. The study focuses on five events (four from 2014 and one from 2010). All events can be considered as pure solid phase as the temperature at the radar was negative and all retrieved data is located above the radar. This allows to rule out the contribution of liquid and partly melted precipitation, and hence attenuation can be neglected. A maximal range of 30 km is considered in the analysis.

In the second study, the simulated reflectivities were compared with measurements from the GPM-DPR radar satellite at both Ka (35.6 GHz) and Ku (13.6 GHz) bands. The comparison is based on the same 100 overpasses, with the largest precipitation fluxes, used in 4.5.4. As the

study focuses on the solid phase, only GPM measurements classified as such were retained (see Iguchi et al. (2010) for details about GPM phase classification).

To simulate the studied events, the standard operational MeteoSwiss set-up of COSMO was used. As in Section 4.5, operational analysis of COSMO-7 are used as initial and boundary conditions.

To simulate radar observables from COSMO outputs, the radar operator described in Chapter 4 was run in its “standard” configuration, using the Gaussian quadrature scheme with 3 quadrature points in the azimuthal direction and 5 in the elevational direction ( $J, K$  in Equation 4.6). For the computation of the atmospheric refraction, the ordinary differential equation method of Zeng et al. (2014) was used. The melting scheme was not used, because the sensitivity study considers only pure liquid and solid phases.

### 5.3.5 Parsivel data

In order to compare the COSMO drop size distribution parameterizations with real observations, data from three Parsivel-1 (Particle size and velocity) optical disdrometers were used. These instruments were deployed at short distance from each other, near the Payerne MeteoSwiss station. Like the X-band radar presented above, these instruments were deployed in the context of the PARADISO measurement campaign. The same six events used for the validation of Doppler variables were also used for this comparison (Index C in Table 4.3). The measured drop size distributions were corrected with measurements from a 2-dimensional video disdrometer (2DVD) using the method of Raupach and Berne (2015). For more details regarding these instruments, see Raupach and Berne (2015). All disdrometers were located within the same COSMO grid cell, so the measured DSDs were simply averaged before comparing them with the COSMO parameterizations.

## 5.4 Results

### 5.4.1 Sensitivity in rain

#### 5.4.1.1 Polarimetric distributions and relations

One cannot expect a 1:1 match between simulated and observed radar variables, because the COSMO model is never perfectly accurate both in terms of spatial and temporal structure of the atmospheric fields. However over a sufficiently large sample (several events), one can expect a good agreement between simulated and observed probability density functions of radar observables as well as similar relationships between them. This requires however that the parameterization of hydrometeors within the model is realistic (e.g. PSD, mass/velocity-diameter relations).

## Chapter 5. Sensivity study of the polarimetric radar operator

Figure 5.2 shows the relations between polarimetric variables obtained using radar observations and simulated with different values of the three considered parameters of raindrops. It appears that the  $Z_H$ - $Z_{DR}$  relation seems to be more affected than the  $Z_H$ - $K_{dp}$  relation. The most sensitive factor seems to be  $\mu^{\text{rain}}$  which is the only parameter to significantly affect the  $Z_H$ - $K_{dp}$  relation. In terms of  $\mu^{\text{rain}}$ , higher values around 3 give a better  $Z_H$ - $Z_{DR}$  relation but increase the overestimation in the  $Z_H$ - $K_{dp}$  relation. This highlights the fact that the one-moment COSMO DSD, being a quite simple model, is not really able to accurately represent all observed moments. In terms of aspect-ratio model, no model seems to be consistently better than the other and they all tend to overestimate low  $Z_{DR}$  values at small reflectivities. In terms of canting angle distributions, larger values around 10-15 ° seem preferable as they reduce the overestimation in both polarimetric relations.

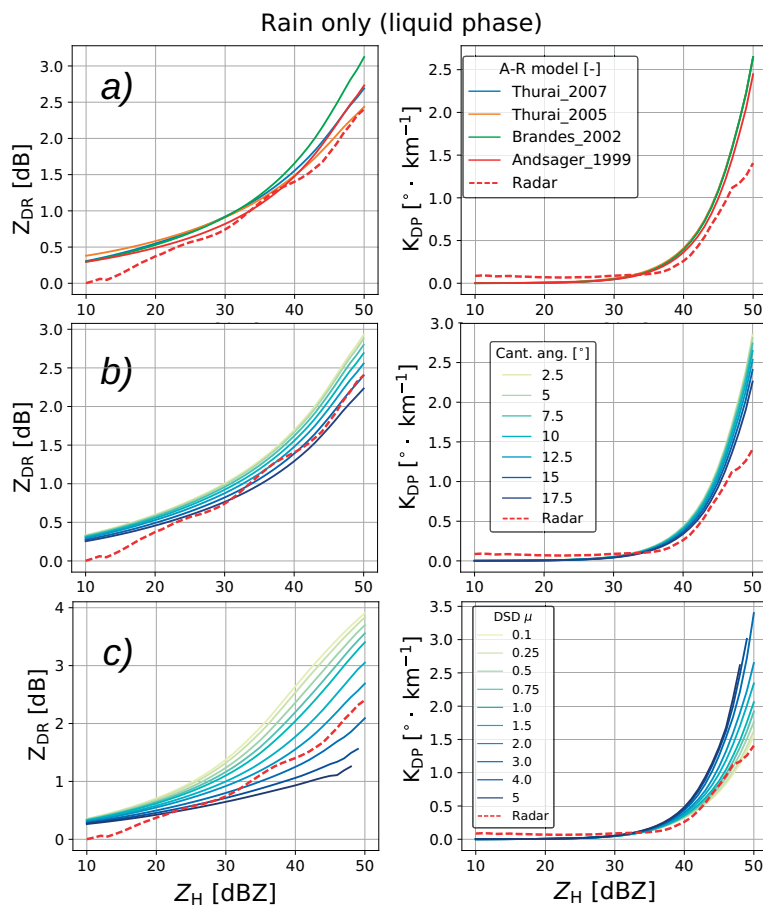


Figure 5.2 – Observed and simulated relations between polarimetric variables obtained for various aspect-ratio models (a), canting angle standard deviations (b) and  $\mu^{\text{rain}}$  (c)

Figure 5.3 shows how varying  $\mu^{\text{rain}}$  affects the distributions of simulated polarimetric variables. It appears that  $Z_{DR}$  is the radar variable that is the most sensitive to variations of  $\mu^{\text{rain}}$ , whereas  $K_{dp}$  and the radial velocity seem to be barely affected. The distribution of  $Z_{DR}$  tends to become more and more heavy tailed when  $\mu^{\text{rain}}$  decreases. A similar effect can be observed for  $Z_H$ , although to a much smaller extent. Compared with radar observations, using a low value of



$\mu^{\text{rain}}$  tends to yield a more realistic location of the mode but a tail that is too short, whereas using a high value of  $\mu^{\text{rain}}$  will cause the opposite effect.

Histograms of radar variables for different aspect-ratio models and canting angle standard deviations (not displayed) show that only  $Z_{\text{DR}}$  seems to be significantly affected. The general conclusion which is valid for all parameters is that no perfect match with radar observations can be found for  $Z_{\text{DR}}$ : either the tail of the simulated distributions are too short (for example with the Andsager et al. (1999) aspect-ratio model or with  $\sigma_o^{\text{rain}} > 10^\circ$ ), either the mode is located too much on the right (for example with the Thurai et al. (2007) aspect-ratio model or with  $\sigma_o^{\text{rain}} < 5^\circ$ ).

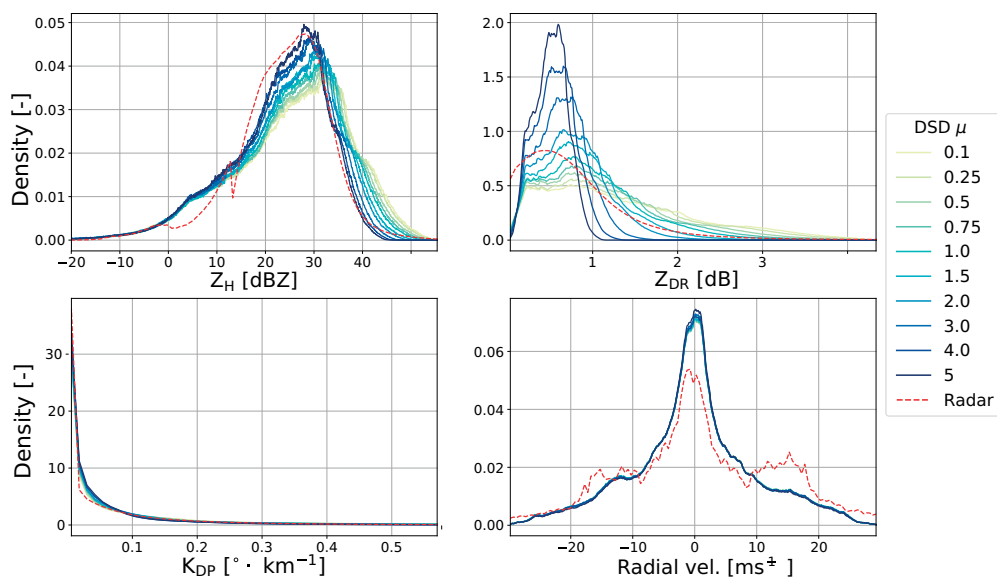


Figure 5.3 – Observed and simulated distributions of radar variables in rain for different values of  $\mu^{\text{rain}}$

#### 5.4.1.2 Alternative DSD model

Since  $\mu^{\text{rain}}$  seems to be the main contributing factor in the polarimetric signature of rain, an optimization procedure was performed to try to find an alternative model with similar properties but a better match with radar observables. The model that was adjusted is a generalized gamma distribution (Auf der Maur, 2001):

$$N(D) = N_0 D^\mu \exp(-\Lambda D^\nu) \quad \text{m}^{-3} \text{mm}^{-1} \quad (5.1)$$

where  $N_0$  is the *intercept* parameter in  $\text{mm}^{-1} \mu \text{m}^{-3} \text{m}^{-3}$ ,  $\Lambda$  is the *slope* parameter in  $\text{mm}^{-\nu}$ ,  $\mu$  is the dimensionless *shape* parameter and  $\nu$  is the dimensionless *family* parameter.

The generalized gamma distribution is a versatile model, whose moments have an analytical

## Chapter 5. Sensivity study of the polarimetric radar operator

solution. The considered DSD is also constrained to give the same mass concentration and rain rate as the original COSMO one-moment Gamma DSD with  $\mu = 0.5$  (see Table 4.1). which ultimately leaves two free parameters ( $\mu, \nu$ ) to optimize. The cost (objective) function for optimization is computed in the following way: For every polarimetric variable, the overlap coefficient between simulated and observed histograms is computed (the area shared by both histograms  $\in [0, 1]$ ). For every polarimetric relation ( $Z_H$  vs  $Z_{DR}$  and  $Z_H$  vs  $K_{dp}$ ), the sum of all absolute differences between radar and model (for every  $Z_H$  bin) is computed and divided by the total area under the radar relation (the integral of the polarimetric relation). The sum of these individual scores is then divided by five, which gives a normalized score. The best set of parameters ( $\mu, \nu$ ) was found with the particle swarm optimization, an efficient metaheuristic method for global minimization (Kennedy and Eberhart, 1995).

The best match was found with ( $\mu = 9.91662053$ ,  $\nu = 0.66075762$ ) giving a cost of 0.354, corresponding to an improvement of 31% with respect to the reference DSD (cost = 0.512). Note that the value of  $\mu = 0.108$  is much lower than the value around 3.5 found for Parsivel DSDs (Figure 5.5), but these values can not be compared directly, because the considered distribution models are quite different (the generalized gamma DSD includes an exponent of  $\nu = 1.2$  on the diameter on the exponential). The two constrained parameters  $\Lambda$  and  $N_0$  can be obtained by:

$$\begin{aligned} \lambda &= \left[ \frac{R\Gamma\left(\frac{\mu+b+1}{\nu}\right)}{a_\nu Q\Gamma\left(\frac{\mu+b+b_\nu+1}{\nu}\right)} \right]^{-\frac{\nu}{b_\nu}} \\ N_0 &= \frac{\nu Q\lambda^{\frac{\mu+b+1}{\nu}}}{a\Gamma\left(\frac{\mu+b+1}{\nu}\right)} \end{aligned} \quad (5.2)$$

where  $R$  is the rain rate and  $Q_M$  is the mass concentration of raindrops,  $a$  and  $b$  are the intercept and slope parameters of the mass-diameter relation and  $a_\nu$  and  $b_\nu$  the intercept and slope parameters of the velocity-diameter relation of raindrops.

Figure 5.4 shows the observed and simulated histograms of polarimetric variables as well as the polarimetric relations obtained with the reference COSMO DSD and the optimized model. It can be clearly seen that the optimized DSD gives a better representation of the mode of the polarimetric distributions, as well as a better agreement in the  $Z_H$ - $Z_{DR}$  relation. The agreement in the  $Z_H$ - $K_{dp}$  relation also seems better for  $Z_H < 45$  dBZ. The resulting DSDs are shown in the bottom right. The optimized model produces much less small drops, but more larger drops which have a strong influence on polarimetric radar variables.

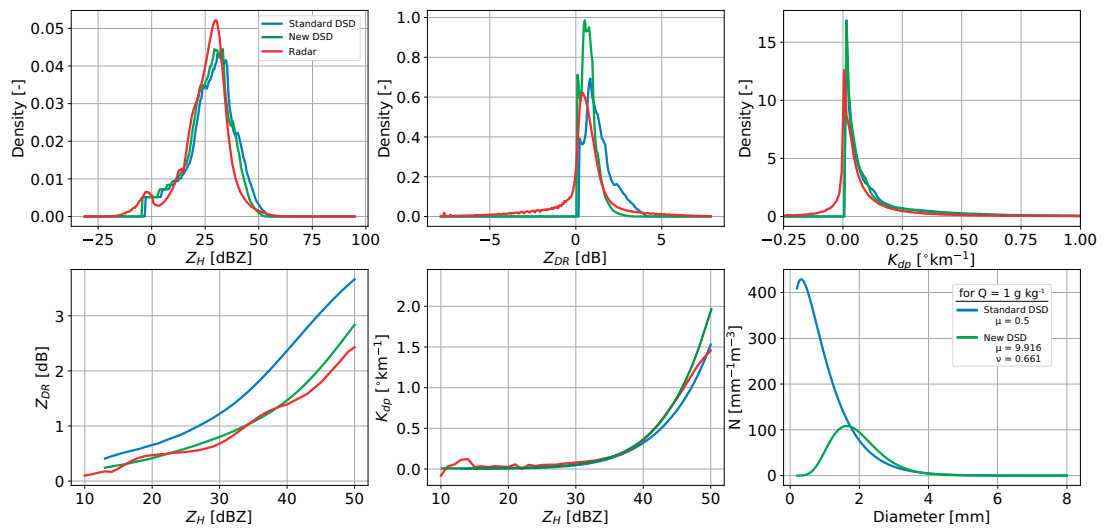


Figure 5.4 – Observed and simulated histograms of polarimetric variables as well as polarimetric relations obtained with the reference COSMO DSD and the optimized DSD for a rain concentration of  $1 \text{ g m}^{-3}$ . The corresponding DSDs are shown at the bottom-right.

#### 5.4.1.3 Comparison of the COSMO DSDs with ground measurements

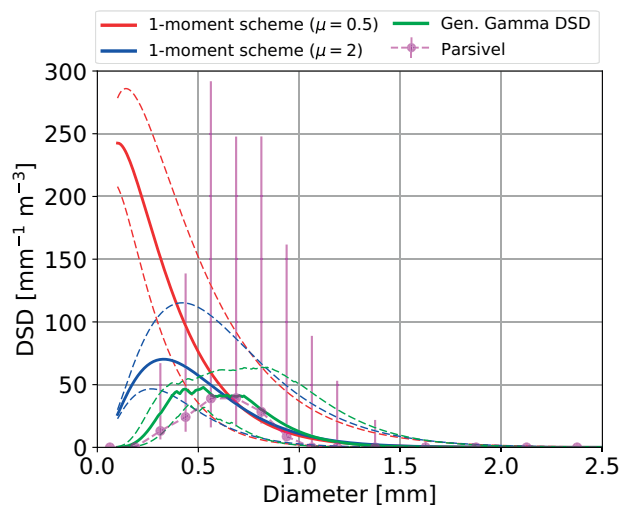


Figure 5.5 – Median measured (pink dots) and COSMO parameterized rain DSDs (blue, red and green lines) at the ground in Payerne over six stratiform precipitation events. The dashed lines correspond to the interquartile of parameterized DSDs, whereas the pink bars correspond to the interquartile of measured DSDs.

Figure 5.5 shows a comparison of the average median rain DSD observed by Parsivels, the operational gamma COSMO DSDs (with  $\mu = 0.5$  and  $\mu = 2$ ), and the alternative generalized gamma DSD over the six days of precipitation during the PARADISO campaign (Section 5.3.5 and Table 4.3). It is obvious that the gamma COSMOS DSD with  $\mu^{\text{rain}} = 0.5$  tends to produce

too many small drops when compared with the Parsivel data. However one must keep in mind that due to the instrument's limitations, the Parsivel, as most disdrometers, has difficulty to measure very small drops and might underestimate their numbers (Thurai et al., 2017). However, one can still observe with certitude that the mode of the COSMO parameterized DSDs is located too much on the left, especially for  $\mu^{\text{rain}} = 0.5$ . The generalized gamma DSD gives a much better agreement with the median Parsivel DSD, with a much better position in the mode. Note that all COSMO DSDs tend to underestimate by far the observed variability, which can be explained mostly by the limited resolution of the model and the deterministic nature of the radar operator.

These results tend to confirm that the alternative DSD model is more realistic and could be useful to reduce the intrinsic bias in simulated radar quantities caused by discrepancies between the real drop size distributions and its operational parameterization.

### 5.4.2 Sensitivity in the solid phase

#### 5.4.2.1 Polarimetric variables at X-band

Figure 5.6 (a) compares observed histograms of polarimetric variables and simulated histograms with the three different scattering methods. It can be seen that the DDA/GMM method tends to overestimate  $Z_{\text{DR}}$  and  $K_{\text{dp}}$ , whereas the T-matrix methods tend to underestimate it. The MASC T-matrix method brings only very minor improvement. The DDA/GMM method has a better agreement in terms of  $Z_{\text{H}}$ , and is at least able to simulate larger values of  $Z_{\text{DR}}$  and  $K_{\text{dp}}$ , which are totally absent with the T-matrix methods. The two peaks in  $Z_{\text{DR}}$  caused by the DDA/GMM method correspond to aggregates and ice crystals whose modelled shapes are quite asymmetric. In terms of polarimetric relations (Figure 5.6 (b)), the DDA/GMM method is the only one able to simulate a significant dependence of  $Z_{\text{DR}}$  on  $Z_{\text{H}}$ . Though  $Z_{\text{DR}}$  seems largely overestimated, if one ignores the almost constant bias, the shape of the relation seems to agree roughly with the radar observations. The DDA/GMM method also overestimates  $K_{\text{dp}}$  at higher reflectivity values, but, considering the fact that the T-matrix methods barely give any response in  $K_{\text{dp}}$ , still seems the better choice. Overall, it can be seen that the DDA/GMM method seems promising as it is able to simulate larger polarimetric variables in the solid phase. It should be noted that, in our opinion, the existing databases are not yet mature enough to be used in the context of a polarimetric forward radar operator, as they are either non-polarimetric or do not include any dependency on the canting angle distributions. This will likely change in the near-future though, given the current effort of the community.

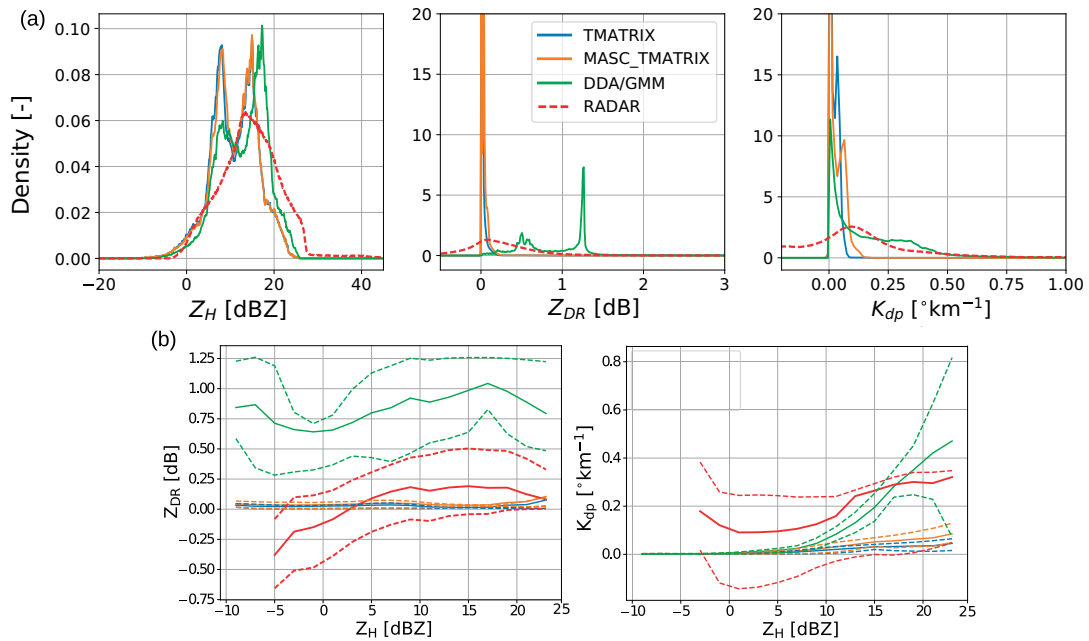


Figure 5.6 – (a) Observed and simulated histograms of polarimetric variables. (b) Observed and simulated relations between polarimetric variables in the solid phase using three different scattering methods

#### 5.4.2.2 Reflectivities at Ka and Ku bands

In its matched scan configuration, the GPM-DPR radar provides collocated measurements of reflectivity factors at both Ka and Ku band. When the Rayleigh conditions are not satisfied at least at one frequency, which is typically the case at both GPM-DPR frequencies, the measured reflectivity factors at both frequencies differ (Matrosov et al., 2005). The logarithmic difference of reflectivity is defined as the dual frequency ratio (DFR) and yields information about the characteristic particle size. Unfortunately, in liquid precipitation, the DFR is often dominated by variations in attenuation rates between both frequencies (Le et al., 2016), which limits its applications for ground based radars.

For airborne or spaceborne radar, however, which provide top-down observations, the differential attenuation effect is expected to be quite small in solid precipitation (Matrosov et al., 2005). Therefore, comparison of simulated reflectivity factors at both Ka and Ku bands with GPM-DPR observations in solid precipitation (Figure 5.7), can be used as a way to evaluate the accuracy of the considered scattering model.

Figure 5.7 shows that all scattering methods yield a much smaller variability than what is observed on GPM data. This can be explained by the intrinsic smoothness of the COSMO model and its limited resolution. Indeed, in reality, precipitation is far from being homogeneous within a COSMO grid cell (Raupach and Berne, 2016). Moreover, even though a radar

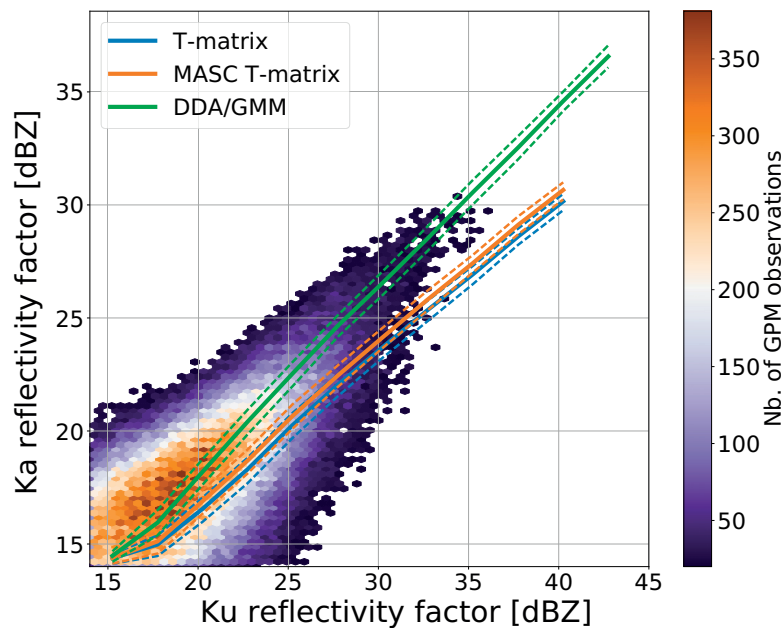


Figure 5.7 – Observed and simulated reflectivities at Ku and Ka bands. The hexagonal density plot corresponds to the bivariate distribution of Ka and Ku reflectivities observed on the GPM DPR data. The bold line correspond to the average trend observed for the simulated reflectivities using the three scattering methods. The dashed lines correspond to the quantiles 25 and 75.

emits many pulses in the same direction. the sampling within its resolution volume is never exhaustive and two radar measurements performed by the same radar at the same time and place could yield different outcomes. This is especially true for airborne radars, such as GPM, which tend to have large resolution volumes close to the surface. In terms of average trend, however, the DDA method clearly outperforms the T-matrix based approaches, as it follows closely the trend observed in the bivariate GPM density, especially for smaller reflectivities. The T-matrix methods seems to underestimate reflectivity at Ka band, resulting in a larger DFR. Here as well, using the MASC parameterization in the T-matrix method provides only a very minor improvement. It is interesting to notice that the discrepancy between DDA and T-matrix increases for larger reflectivities, where one can expect larger hydrometeor diameters and, thus, more deviation from the Rayleigh regime. This agrees well with Ka band simulations by Tynnelä et al. (2011), who observed a clear underestimation of horizontal backscattering cross-sections with the T-matrix method, for aggregates larger than 6 mm, that tends to increase with the diameter.

Overall, when compared with the T-matrix methods, the DDA method yields more accurate reflectivities for larger frequencies and larger diameters, where the Rayleigh approximation is no longer valid.

## 5.5 Summary and conclusions

A sensitivity analysis of some of the main parameters of the radar operator presented in Chapter 4 has been performed, both in the liquid and the solid phases. In the liquid phase, the analysis focused on the comparison of C-band measurements with simulated radar observables, using different aspect-ratio models, raindrop canting angle distributions and DSD *shape* parameters. In the solid phase, the analysis focused on the comparison of X-band measurements in pure solid precipitation with radar observables simulated using different scattering estimation methods for snowflakes, graupel and ice crystals.

In the liquid phase, the sensitivity study reveals that the agreement between simulated and observed polarimetric variables depends strongly on the assumptions about the geometry of raindrops. It was shown that using different aspect-ratio models affects significantly the simulated differential reflectivities, with no model performing distinctly better than the others. However, the most important parameter seems to be the *shape* parameter  $\mu$  in the drop size distributions formulation in COSMO, which has a strong influence on the asymmetry of the DSD. Using a larger  $\mu$  tends to underestimate the  $Z_H$ - $K_{dp}$  relation but overestimate the  $Z_H$ - $Z_{DR}$  relation, and inversely for a smaller  $\mu$ . Nonetheless, it was shown that is possible to use a generalized gamma distribution with optimized parameters, to significantly improve the match with radar observations while preserving the same mass concentration and rain rate. A comparison with measurements from Parsivel disdrometers reveals that this alternative DSD model gives a better agreement with the median Parsivel observed DSD than the original COSMO gamma DSD, which tends to locate the mode too much on the left, especially for  $\mu = 0.5$ . These results suggest that this DSD model could be useful for assimilation purposes, to reduce the intrinsic bias between simulated and observed radar variables, caused by the assumptions of the COSMO microphysical parameterizations.

In the solid phase, the polarimetric variables tend to be underestimated when using the T-matrix method to simulate hydrometeor scattering properties, even when using MASC observations to derive realistic aspect-ratios and canting angles. However when using discrete dipole and generalized multi-particle Mie scattering databases instead of the T-matrix method, the situation is reversed and the polarimetric signature in the solid phase are too strong, which can be explained by the crude assumptions used to adapt the databases to the radar operator. Moreover, with these databases, the trend between simulated reflectivity factors at Ku and at Ka bands agrees much better with the trend observed on the real GPM observations. Ultimately, this study reveals that the T-matrix method is not able to simulate realistic polarimetric quantities in snow and points out the potential benefit of using more exhaustive DDA scattering databases, that should be available in the near-future .





## 6 Conclusions and further perspectives

### 6.1 Summary

This thesis work was devoted to investigating the potential use of polarimetric radar data in NWP, with a focus on precipitation, at several scales and in mountainous terrain. Three main topics have been covered, the detection and characterization of the melting layer of precipitation, the evaluation of simulated precipitation intensities with a multi-scale approach, and the design and evaluation of a polarimetric forward radar operator. The techniques developed and the results drawn are relevant for the parameterization of sub-grid processes, the validation of model simulations and parameterizations, and, on a longer term, for assimilation purposes.

The density, the terminal velocity and the electromagnetic properties of precipitation depend strongly on its phase, and for melting hydrometeors, on their liquid water content. As such, when validating NWP models, it is crucial to be able to distinguish the phases of precipitation in radar data. In Chapter 2, a new algorithm able to detect the extent of the melting layer (ML) on polarimetric RHI scan was proposed. Validation of the algorithm with radio sounding showed that it is able to estimate the height of the isotherm  $0^{\circ}\text{C}$  with good precision and accuracy, and outperforms by far a simple alternative method adapted from PPI scans. Thanks to this new algorithm, a detailed characterization of the geometrical and polarimetric properties of the melting layer was performed, at various locations in the world. The thickness of the ML was shown to be on average very similar on all datasets, with a slightly right skewed distribution and an average between 300 and 330 m. Riming was identified as the most important factor explaining the overall variability of the ML. The algorithm was also used to obtain a rough estimation of the total attenuation within the melting layer. It was shown that the values of  $Z_{\text{DR}}$  within and above the melting layer could be significantly affected by attenuation. Overall, this algorithm can be used as a way to validate the simulated freezing level height, and the results of the characterization can be relevant to evaluate a parameterization scheme for melting hydrometeors.

Validation of simulated precipitation intensities is difficult, because the outcome of traditional performance scores depends very much on the considered scale. To try to alleviate this

## Chapter 6. Conclusions and further perspectives

---

difficulty, the potential of multifractals (MF) for model evaluation was investigated in Chapter 3. Indeed, MFs offer obvious benefits, because they allow to characterize the spatio-temporal variability of geophysical data over a wide range of scales with only a limited number of scale-invariant parameter. To try to clarify the physical meaning of MF parameters a climatological study over several years of simulated precipitation fields was performed. It was observed that the MF signature of specific areas was indeed related to their topographical and meteorological properties, though this relation is not always simple to determine. The study then focused on three different events, corresponding to synoptical conditions over Switzerland, for which the MF parameters of simulated precipitation fields was compared with the MF parameters of the operational radar QPE. It was observed that the radar QPE generally displays a better and more uniform scaling over all considered ranges (1-128 km), than the model simulations. In particular, the simulated precipitation fields show a poor scaling at small scales during the snowstorm event (too smooth) and at large scales during the convective event (mislocation of the convective system). When comparing the one and two-moment microphysical schemes, it was observed that the two-moment scheme gives a larger variability of precipitation and a consistently better agreement with the radar QPE in terms of spatial and temporal fractal dimensions, which measure how convoluted the precipitation occurrence signal is. Overall, it was shown that MFs can be used to easily identify at which spatial and temporal scales the model deviates from the observations, even though this is not easy to relate to specific aspects of the model parameterizations.

Another way to validate NWP simulations is to convert them to variables that can be directly compared to radar observations. To this end, a new forward polarimetric radar operator for COSMO model has been proposed. This operator is able to simulate measurements of radar reflectivity at horizontal polarization, differential reflectivity as well as specific differential phase shift and Doppler variables for ground based or spaceborne radar scans, from atmospheric conditions simulated by COSMO. The operator includes a new Doppler scheme, which allows to estimate the full Doppler spectrum, as well a melting scheme which allows to represent the very specific polarimetric signature of melting hydrometeors. The operator was evaluated by comparing the simulated fields of radar observables with observations from the Swiss operational radar network, from a high resolution X-band research radar and from the GPM-DPR. This evaluation showed that the operator is able to simulate an accurate Doppler spectrum and accurate radial velocities as well as realistic distributions of polarimetric variables in the liquid phase.

In Chapter 5, a sensitivity analysis of the radar operator showed that the agreement between simulated and observed polarimetric variables depends strongly on the assumptions about the geometry of raindrops and the considered DSD model. It was observed that using a larger DSD *shape* parameter  $\mu$  tends to underestimate the  $Z_H-K_{dp}$  relation but overestimate the  $Z_H-Z_{DR}$  relation, and inversely for a smaller  $\mu$ . Similar conclusions are reached in terms of aspect-ratio models and standard deviations of canting angle distributions. Nonetheless, it was shown that is possible to replace the standard DSD with a generalized gamma distribution with optimized parameters to significantly improve the match with radar observations, while preserving the

same mass concentration and rain rate. In the solid phase, the polarimetric variables tend to be strongly underestimated when using the T-matrix method, even when MASC observations are used to parameterize the geometry of snowflakes and graupels. With the use of more advanced scattering databases (based on the DDA and GMM methods), the situation is reversed and the polarimetric signature in the solid phase tends to be too strong. These methods, however, provide much more realistic values of reflectivity at higher frequencies (Ka band). Ultimately, the expected publication of more exhaustive DDA scattering databases in the near-future seems promising to simulate realistic radar observables in solid precipitation.

## 6.2 Important contributions of this thesis

The most important contributions of this thesis can be summarized as follows:

1. A melting layer detection algorithm able to detect the lower and upper boundaries of the melting layer with good accuracy has been proposed and described in details.
2. A quite exhaustive characterization of the geometrical and radar properties of the melting layer has been performed. The results indicate that many properties of the melting layer seem to be climate independent.
3. The potential of MFs for model evaluation has been investigated. The relationship between MF parameters and more classical meteorological and topographical descriptors has been studied. Additionally, the presence of scaling breaks in simulated precipitation field was highlighted.
4. A new polarimetric forward operator for the COSMO model has been developed. Its main novelties are the use of a parameterization based on MASC observations for the geometrical properties of snow aggregates and graupels, as well as a very computationally efficient scheme to compute the full Doppler spectrum. The code for the radar operator is open-source and available online<sup>1</sup>.
5. The effect of uncertainties in the geometry of raindrops on the simulated radar observables has been investigated. For solid hydrometeors, the T-matrix method has been compared with more advanced scattering methods (DDA and GMM) in terms of agreement with observed radar variables. Although this comparison had already been done for isolated particles, it had never been performed in the context of a full-fledged radar operator.
6. Two python libraries potentially useful for the COSMO community have been shared online. The first one *pycosmo*<sup>2</sup> allows to read, write, plot and process COSMO GRIB files. It also allows to create profiles of model data, at fixed geographical coordinates, or at the

---

<sup>1</sup>[https://github.com/wolfidan/cosmo\\_pol](https://github.com/wolfidan/cosmo_pol)

<sup>2</sup><https://github.com/wolfidan/pycosmo>

location of PPI or RHI radar scans. The second one *cosmo\_query*<sup>3</sup> allows to automatically retrieve COSMO data from the central CSCS (Swiss National Supercomputing Centre) archives, for fixed days, locations, subset of variables, etc.

### 6.3 Perspectives

Various aspects of the research presented in this thesis could benefit from further attention. In terms of melting layer detection, the presented algorithm could be adapted to operational PPI scans, which represent by far the most common type of radar scan. The main difficulty would be to account for the fact that in PPI scans, the edges of the melting layer are much less clear and well-defined. Preliminary tests showed that the algorithm can still deliver satisfying results, provided that some of the constants parameters (thresholds) are adjusted accordingly. Moreover, part of the uncertainty related to the use of PPI scans could be lifted by also including  $Z_{DR}$  in the ML detection algorithm on PPI scans. The crude estimation of the attenuation effect through the ML performed in Section 2.6.1 could be greatly improved by using two or more radars, located relatively close to each other. These radars should perform quasi-simultaneous sampling of the same volume, but with different incidence angles, and thus different distances through the melting layer (MLD as in Section 2.6.1. The PARADISO campaign set-up could have been appropriate, because there were two X-band radars operating at the same time, not far away from each other. Unfortunately, one of the two radars was performing a vertical profile, while the other radar was performing a RHI scan in the direction of the first radar, making it impossible to compare  $Z_{DR}$  values (as it is always 0 at vertical incidence).

In the multifractal study, at the end of Chapter 3 it was suggested that using a mobile domain moving with the precipitation system, instead of a fixed domain, could have been more relevant. Indeed, it was observed that the discrepancies in multifractal properties seem to be somewhat dominated by temporal and spatial shifts of the simulated precipitation systems, which tend to become more important over the course of the event. Using a mobile window could help to focus more on the simulated structure of precipitation fields rather than simply on its spatial and temporal occurrence.

The polarimetric forward operator developed in Chapter 4 is already quite sophisticated, but in Chapter 5 two potential axes of improvement have been identified. The prescribed DSD model in COSMO could be adapted to a model providing a better agreement with radar observables. This would require to carefully evaluate this new DSD model and assess that it doesn't affect negatively the simulated precipitation fields. Moreover, it was observed that more advanced scattering methods (DDA and GMM) could help to simulate more realistic polarimetric variables in solid precipitation. Following a workshop in June 2017, several scientists active in the study of solid precipitation agreed to publish a new common database of solid hydrometeor scattering properties in the near future. This database could provide great opportunities for improvements, as the current ones tend to be too incomplete or

---

<sup>3</sup>[https://github.com/wolfidan/cosmo\\_query](https://github.com/wolfidan/cosmo_query)

too focused. In terms of melting hydrometeors, it would be interesting to adapt the radar operator to the mixed phase scheme of Frick and Wernli (2012) and see how well the simulated radar observables in the ML agree with the simple diagnostic melting scheme proposed in Section 4.4.7.

Once it is guaranteed that the radar operator is able to simulate realistic radar observables in solid, mixed and liquid phases, it would be interesting to merge the polarimetric radar operator with the operational and much more polished single polarization radar operator of Zeng et al. (2016). The radar operator could then be used to assess several parameters of the COSMO microphysical parameterizations, such as, for example, the mass-diameter relations and velocity-diameter relations, which are often based on quite dated empirical fits. It would also be possible to adapt the radar operator to higher frequencies such as the W band (60-100 GHz), a frequency band often used by cloud radars<sup>4</sup>. This would require to take into account small non-precipitating cloud droplets and to parameterize the multiple scattering effect, which becomes significant at high frequencies (Battaglia et al., 2007). On the longer term, this radar operator could be used for data assimilation, in the context of a Local Ensemble Kalman Filter (LEKF), as was done already by Zeng (2013) for Doppler velocity. A major difficulty in assimilating polarimetric variables, however, is that their measurement noises are both large and strongly correlated, and are very much instrument-dependent. Moreover, the relation between simulated polarimetric variables and model variables is very non-linear and prone to large uncertainties, especially for solid phase hydrometeors.

---

<sup>4</sup>A Doppler cloud radar profiler at W-band has recently been purchased by the LTE lab



# **A Appendix of Chapter 2**

## **A.1 Spatial representation of all descriptors**

Figure A.1 shows the spatial representation of all areas used in the climatological study of MF parameters as well as the corresponding local descriptors.

## Appendix A. Appendix of Chapter 2

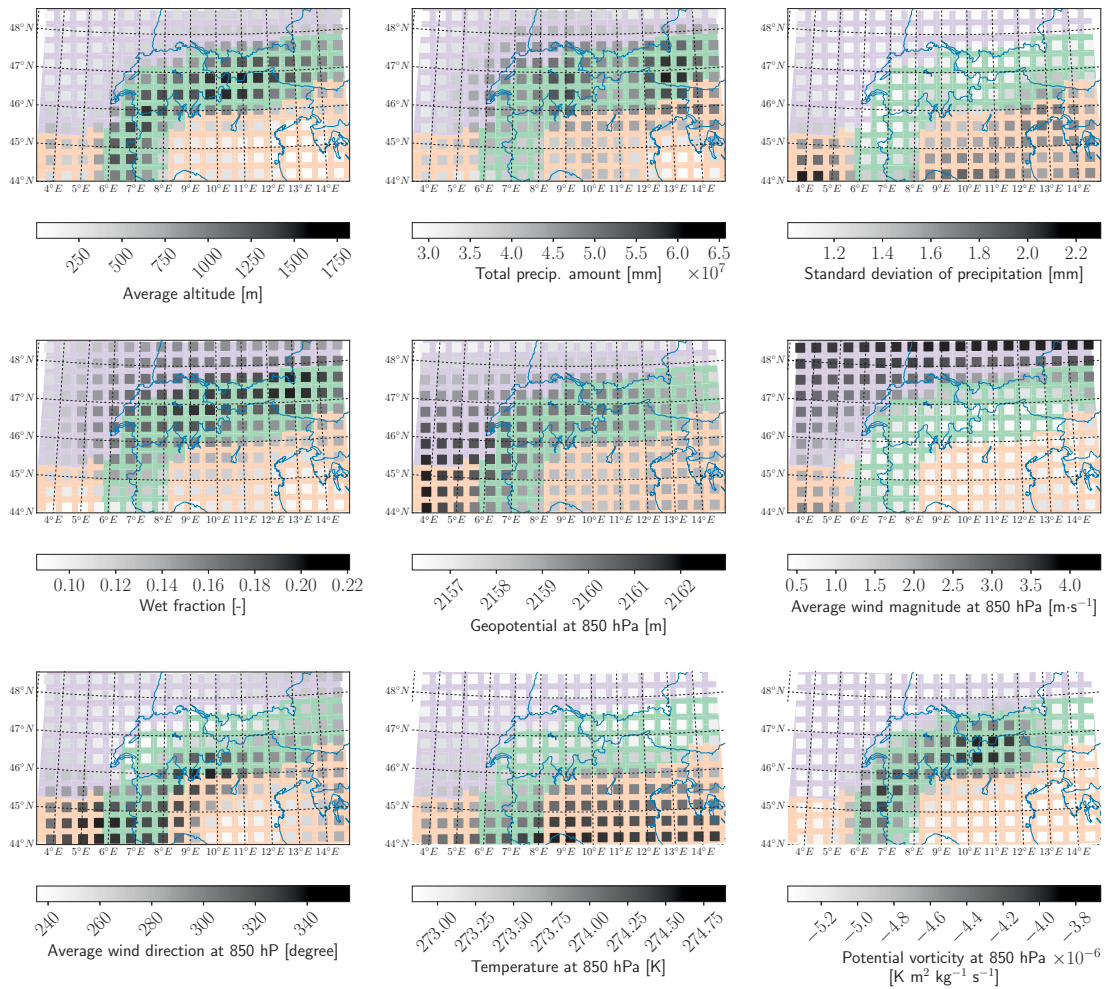


Figure A.1 – Spatial representation of all areas used in the climatological study and the corresponding local descriptors. The squares are indicators of the location of the center of all areas and are not drawn to scale. The colors drawn below the squares correspond to the classification obtained in Section 3.5.2.



## A.2 A visual example of box counting

Figure A.2 illustrates an example of box counting on a binary field of precipitation. For every consecutive resolution, the data is average in  $2 \times 2$  boxes, and if at least one grid cell is rainy, the aggregated grid cell will be rainy as well. Finally, the fractal dimension  $D_f$  is obtain with a best-fit of the logarithm of the number of rainy grid cells as a function of the logarithm of the scale. Obviously, in practice the value of  $D_f$  will depend on the threshold that is used to binarize the precipitation field, which is the main idea behind multifractals.

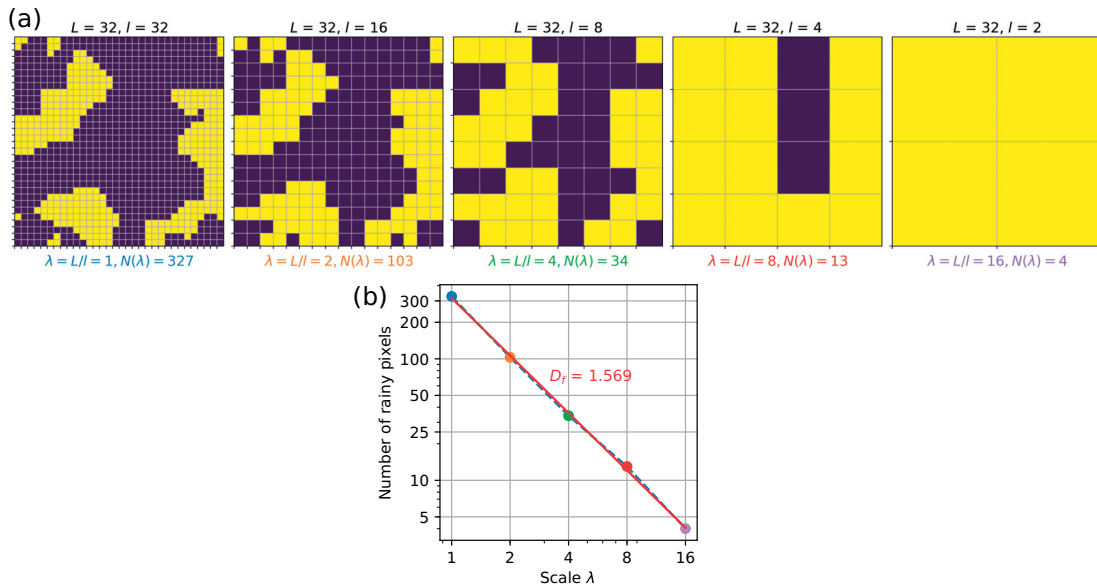


Figure A.2 – A visual example of box counting. Yellow grid cells correspond to rainy cells, purple grid cells to non-rainy cells. The panel of images in row (a) correspond to the binary field aggregated at increasing resolution  $\lambda$ .  $\lambda = 1$  corresponds to the original binary field which has an outer (maximum) scale of 32 pixels. (b) corresponds to the log-log plot of scale  $\lambda$  versus number of rainy cells  $N$ .

### A.3 Visual example of the effect of multifractals on the structure of a field

Figure A.3 illustrates the effect of varying  $\alpha$  and  $C_1$  on randomly generated isotropic conservative MF fields. One can see how increasing  $\alpha$  increases the variability within non-zero intensity regions, whereas increasing  $C_1$  decreases the intermittency and makes the field look more spatially homogeneous.

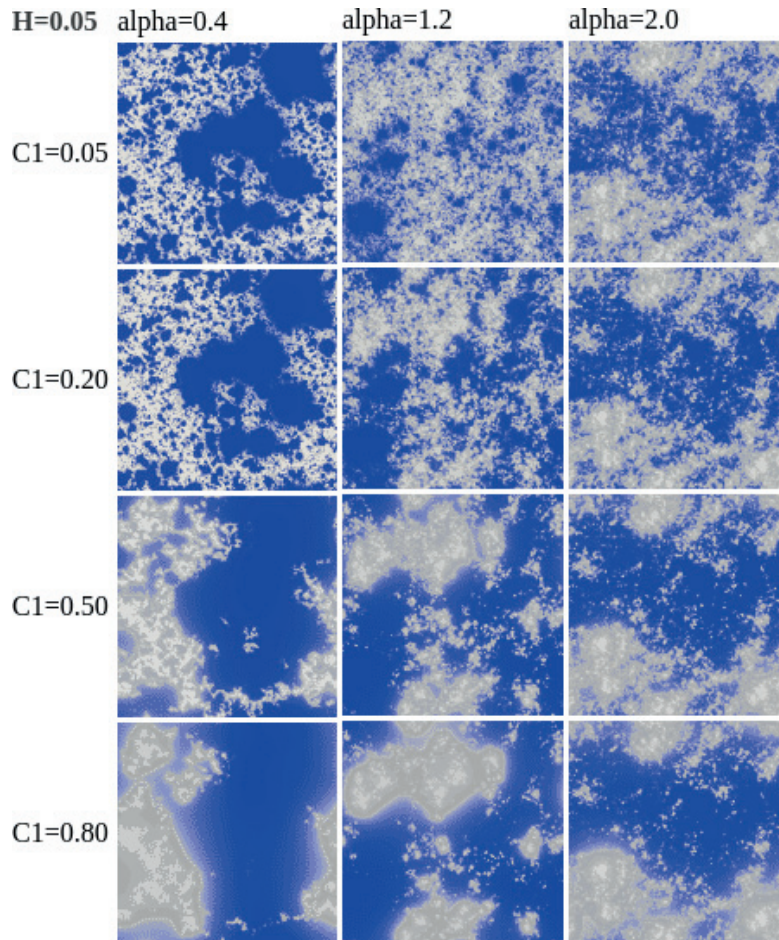


Figure A.3 – Illustration of the effect of  $\alpha$  and  $C_1$  on randomly generated fields. Blue pixels correspond to zero intensity, whereas pixels with non-zero intensity are shown with a greyscale colormap. Taken from Lovejoy (2017)

Figure A.4 illustrates the effect of  $H$  on isotropic MF fields, with constant  $\alpha$  and  $C_1$ .  $H$  can be considered as a kind of smoothness parameter that denotes the order of integration ( $H < 0$ ) or differentiation ( $H > 0$ ) needed to obtain the observed field from a direct MF cascade process.

### A.3. Visual example of the effect of multifractals on the structure of a field

---

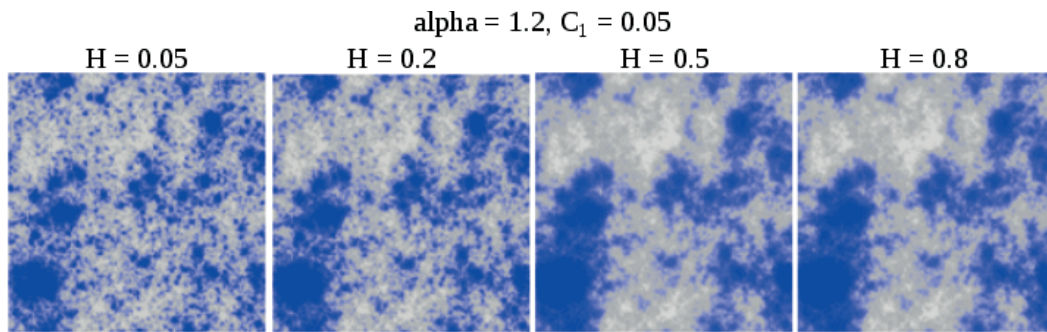


Figure A.4 – Illustration of the effect of  $H$  on randomly generated fields for  $\alpha = 1.2$  and  $C_1 = 0.05$ . Blue pixels correspond to zero intensity, whereas pixels with non-zero intensity are shown with a greyscale colormap. Taken from Lovejoy (2017)

### A.4 Comparison with the Köppen classification

Figure A.5 shows the Köppen classification of the 209 subsquares used in Section 3.5. Indeed, the classification is quite close to the one obtained in Section 3.5.2 with topographical and meteorological descriptors. The main differences are the fact that class 3 gets smaller and class 2 larger, especially in the southwest, that some areas in the north of Italy are in class 2, and that sea regions are absent, since the Köppen classification does consider only land areas.

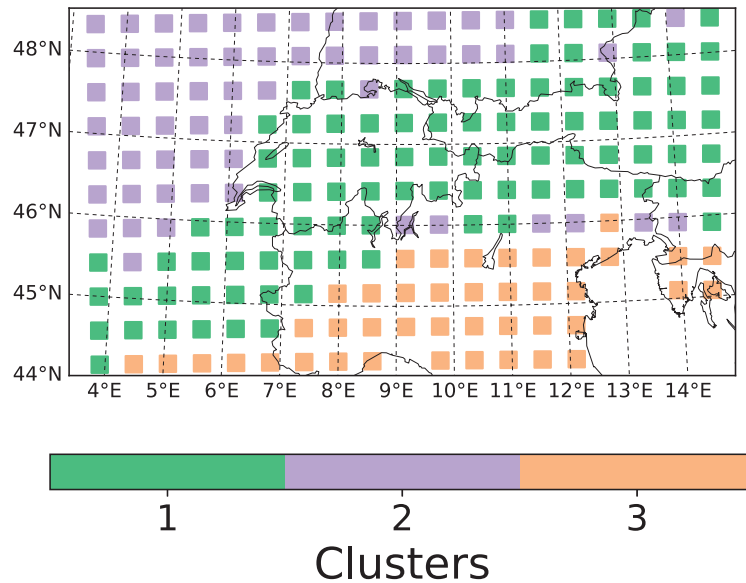


Figure A.5 – Aggregated Köppen climate classification within all 209 subsquares used in Section 3.5.2. class 1 corresponds to Köppen classes Dwa, Dwb and Dfc (Cold climates), class 2 to Köppen class Cfb (temperate with warm summer) and class 3 to Köppen classes Cfa and Csa (temperate with hot summer).

Distribution of MF parameters within Köppen areas (not displayed) show only minor deviations from those obtained with the meteorological classification (Figure 3.5). However, some differences are visible in space for the distributions of  $\alpha$  and  $C_1$ , which tend to be less distinguishable between classes 1 and 2 than on the original meteorological classification. As a consequence, in the Köppen classification, differences in the distributions of  $\alpha$  in space are not statistically significant according to the Kruskal-Wallis test. All other statistical tests, however, give similar outcomes than with the original classification, but often with a larger  $p$  value.

## B Appendix of Chapter 3

### B.1 Trilinear downscaling

Downscaling is computationally faster if the radar gate coordinates are first converted from the World Geodetic System 1984 (WGS) lat/lon coordinates to the local pole-rotated model coordinates, where the model variables are defined on a regular grid. To this end, the spherical WGS coordinates of the radar gate ( $\psi^{\text{WGS}} = \text{lon}$ ,  $\lambda^{\text{WGS}} = \text{lat}$ ) are first projected to Earth-centered, earth-fixed (ECEF) coordinates  $(x, y, z)$  and then rotated to the pole-rotated system using two rotations matrices, one for the longitudinal rotation of the pole  $\Delta_{\lambda^{\text{WGS}}}$ , and one for the latitudinal rotation of the pole  $\Delta_{\psi^{\text{WGS}}}$ , to yield  $(x^{\text{rot}}, y^{\text{rot}}, z^{\text{rot}})$ .

$$\begin{pmatrix} x_m \\ y_m \\ z_m \end{pmatrix} = \begin{pmatrix} \cos \Delta_{\lambda^{\text{WGS}}} & \sin \Delta_{\lambda^{\text{WGS}}} & 0 \\ -\cos \Delta_{\lambda^{\text{WGS}}} & \cos \Delta_{\lambda^{\text{WGS}}} & 0 \\ 0 & 0 & 1 \end{pmatrix} \begin{pmatrix} \cos \Delta_{\psi^{\text{WGS}}} & 0 & \sin \Delta_{\psi^{\text{WGS}}} \\ 0 & 1 & 0 \\ -\sin \Delta_{\psi^{\text{WGS}}} & 0 & 1 \end{pmatrix} \begin{pmatrix} x \\ y \\ z \end{pmatrix} \quad (\text{B.1})$$

Finally, the Cartesian coordinates  $(x_m, y_m, z_m)$  in the model pole-rotated system, are projected back to spherical coordinates to yield  $(\psi^{\text{rot}}, \lambda^{\text{rot}})$ , the spherical coordinates of radar gates in the model pole-rotated system.

For every radar gate, the eight neighbor model nodes can efficiently be identified by direct mapping of the  $(\psi^{\text{rot}}, \lambda^{\text{rot}})$  coordinates (which as stated are on a regular grid) and by binary search through all vertical model levels. Once the neighbors have been identified (Figure B.1), downscaling is done by first linearly interpolating all neighbors with identical  $(\psi^{\text{rot}}, \lambda^{\text{rot}})$  to the height  $z$  of the radar gate:  $(A_u, A_l) \rightarrow A^*$ ,  $(B_u, B_l) \rightarrow B^*$ ,  $(C_u, C_l) \rightarrow C^*$ ,  $(D_u, D_l) \rightarrow D^*$ . The resulting points  $(A_*, B_*, C_*, D_*)$  are then bilinearly interpolated to the horizontal location of the radar gate.

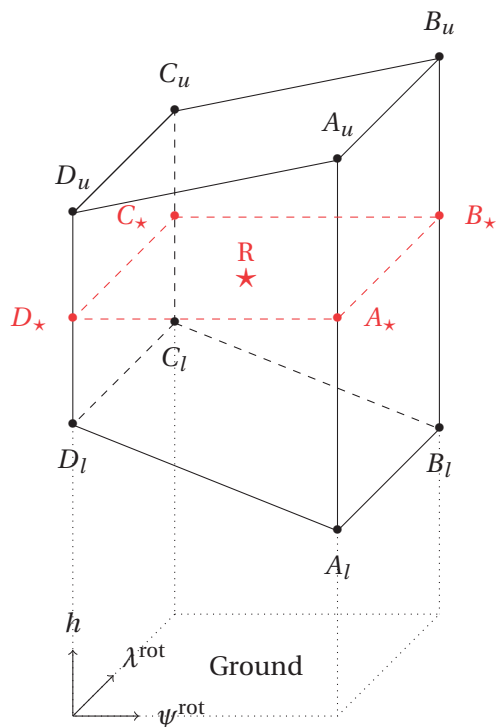


Figure B.1 – Location of the eight neighbours of a radar gate  $R$ . The position of the radar gate is shown by a red star.

## B.2 Specificities of the two-moments scheme

In the two-moment scheme all prescribed PSDs are initially defined as a function of particle mass.

$$N_m(x) = N_{0,m} x^{\mu_m} \exp(-\Lambda_m x^{\nu_m}) \quad (\text{B.2})$$

where the subscript  $m$  denotes that the quantity is mass-based and  $N_m(x)$  is in units of  $\text{kg}^{-1}\text{m}^{-3}$ .

However in the context of this radar operator, it is much more convenient to work with diameter-based PSDs. This conversion can be done by using the prescribed mass-diameter relations which are part of the microphysical scheme:  $D(x) = a_m x^{b_m} \Rightarrow x = \frac{D}{a_m}^{\frac{1}{b_m}}$  and by considering that  $N_m(D) = N_d(x) \cdot \frac{dD}{dx} = a_m (b_m - 1) x^{b_m - 1} N_d(x)$ , where the subscript  $d$  denotes that the quantity is diameter-based and  $N_d(x)$  is in units of  $\text{mm}^{-1}\text{m}^{-3}$ . Replacing this in

Equation B.2 yields:

$$N_d(x) = N_{0,d} D^{\mu_d} \exp(-\Lambda_d D^{\nu_d}) \quad (\text{B.3})$$

with

$$\begin{aligned} N_{0,d} &= \frac{N_{0,m}}{b_m} \left( \frac{1}{a_m} \right)^{\frac{\mu_m+1}{b_m}} \\ \mu_d &= \frac{\mu_m+1}{b_m} - 1 \\ \Lambda_d &= \frac{\Lambda_m}{a_m^{\nu_m/b_m}} \\ \nu_d &= \frac{\nu_m}{b_m} \end{aligned} \quad (\text{B.4})$$

By equating  $\mathcal{M}_0$  with the number concentration  $Q_N$  and  $a_d \mathcal{M}_{b_d}$  with the mass concentration  $Q_M$ , where  $a_d = a_m^{-1/b_m}$  and  $b_d = 1/b_m$ , one is able to retrieve the  $N_{0,d}$  and  $\Lambda_d$  from the prognostic parameters of the PSDs.

$$N_{0,d} = \frac{\nu_d Q_N}{\Gamma\left(\frac{\mu_d+1}{\nu_d}\right)} \Lambda_d^{\frac{\mu_d+1}{\nu_d}} \quad \text{and} \quad \Lambda_d = \left[ \frac{1}{a_d} \frac{\Gamma\left(\frac{\mu_d+1}{\nu_d}\right)}{\Gamma\left(\frac{\mu_d+b_d+1}{\nu_d}\right)} \bar{x} \right]^{-\nu_d/b_d} \quad (\text{B.5})$$

where  $\bar{x} = Q_M/Q_N$  is the average particle mass.

Note that besides these differences in PSD retrieval, the two-moment scheme also yields slightly different hydrometeor scattering properties, since the mass-diameter relations differ from the one-moment scheme.

### B.3 Polarimetric equations

Equations B.6 give the basic polarimetric equations integrated over ensembles of hydrometeors for every radar gate defined by a given set of spherical coordinates  $x_g = (r_g, \theta_g, \phi_g)$ , where  $r_g$  is the range,  $\theta_g$  is the elevation angle  $\theta_g$  and  $\phi_g$  is the azimuth angle. The backscattering covariance matrix  $C^b$ , forward scattering vector  $S^f$ , and backscattering cross-sections  $\sigma^b$  for a given hydrometeor ( $j$ ), are defined as in Equations 4.7, 4.8 and 4.9.  $\lambda$  is the wavelength in cm.

$$\begin{aligned}
 Z_h(x_g) &= \frac{\lambda^4}{\pi^5 |K_w|^2} \sum_{j=0}^H \int_{D_{\min}^{(j)}}^{D_{\max}^{(j)}} N^{(j)}(D, x_g) \cdot \sigma_h^{b,(j)}(D, x_g) dD \quad [\text{mm}^6 \text{m}^{-3}] \\
 Z_v(x_g) &= \frac{\lambda^4}{\pi^5 |K_w|^2} \sum_{j=0}^H \int_{D_{\min}^{(j)}}^{D_{\max}^{(j)}} N^{(j)}(D, x_g) \cdot \sigma_v^{b,(j)}(D, x_g) dD \quad [\text{mm}^6 \text{m}^{-3}] \\
 K_{\text{dp}}(x_g) &= \frac{0.18}{\pi} \lambda \sum_{j=0}^H \int_{D_{\min}^{(j)}}^{D_{\max}^{(j)}} N^{(j)}(D, x_g) \cdot \Re \left( S_1^{f,(j)}(D, x_g) - S_2^{f,(j)}(D, x_g) \right) dD \quad [^\circ \text{km}^{-1}] \\
 \delta_{\text{hv}}(x_g) &= \frac{180}{\pi} \lambda \arg \left( \sum_{j=0}^H \int_{D_{\min}^{(j)}}^{D_{\max}^{(j)}} N^{(j)}(D, x_g) C_{2,1}^{b,(j)}(D, x_g) dD \right) \quad [^\circ] \\
 k_h(x_g) &= \lambda \sum_{j=0}^H \int_{D_{\min}^{(j)}}^{D_{\max}^{(j)}} N^{(j)}(D, x_g) \Im \left( S_1^{f,(j)}(D, x_g) \right) dD \quad [\text{km}^{-1}] \\
 k_v(x_g) &= \lambda \sum_{j=0}^H \int_{D_{\min}^{(j)}}^{D_{\max}^{(j)}} N^{(j)}(D, x_g) \Im \left( S_2^{f,(j)}(D, x_g) \right) dD \quad [\text{km}^{-1}]
 \end{aligned} \tag{B.6}$$

where  $Z_h$  and  $Z_v$  are the linear reflectivity factors at horizontal and vertical polarizations,  $K_{\text{dp}}$ , is the specific differential phase shift upon propagation,  $\delta_{\text{hv}}$  is the total differential phase shift upon backscattering, and  $k_h$  and  $k_v$  are the attenuation coefficients in linear scale.

The phase shift upon backscattering  $\delta_{\text{hv}}$  is not taken into account in  $K_{\text{dp}}$ , because the radar  $K_{\text{dp}}$  retrieval method that is being used (Schneebeil et al., 2013) is able to remove the contribution of  $\delta_{\text{hv}}$ . However besides  $K_{\text{dp}}$ , the total phase shift  $\Psi_{\text{dp}}$  is also simulated<sup>1</sup>, which combines the phase shift due to backscattering and propagation. Additionally, the effect of two-way attenuation is taken into account for  $Z_h$  and  $Z_v$ . This yields the following polarimetric products at every radar gate and for every sub-beam (Equations B.8).

---

<sup>1</sup>Despite being simulated, this quantity was not used in the context of this thesis as it cumulative and thus cannot be related in an easy way to other radar observables. Besides, it is often very noisy on real radar data. In fact its derivative  $K_{\text{dp}}$ , estimated from radar observations with robust differentiation techniques, is much more useful and widely used.



$$\begin{aligned}
 Z_{\text{h}}^{\text{att}}(x_g) &= Z_{\text{h}}(x_g) \cdot \exp\left(-2 \int_{r=0}^{r_g} k_{\text{h}}(r, \theta_o, \phi_o) dr\right) & [\text{mm}^6 \text{m}^{-3}] \\
 Z_{\text{v}}^{\text{att}}(x_g) &= Z_{\text{v}}(x_g) \cdot \exp\left(-2 \int_{r=0}^{r_g} k_{\text{v}}(r, \theta_o, \phi_o) dr\right) & [\text{mm}^6 \text{m}^{-3}] \\
 \Psi_{\text{dp}}(x_g) &= 2 \int_{r=0}^{r_g} K_{\text{dp}}(r, \theta_g, \phi_g) + \delta_{\text{hv}}(x_g) & [^\circ]
 \end{aligned} \tag{B.7}$$

The final volume-integrated polarimetric estimates  $\overline{Z_{\text{H}}^{\text{att}}}$ ,  $\overline{Z_{\text{DR}}^{\text{att}}}$ ,  $\overline{K_{\text{dp}}}$  and  $\overline{\Psi_{\text{dp}}}$  are obtained by integrating the necessary quantities over all sub-beams with the quadrature antenna integration operator  $I$  defined in Equation 4.6. The linear reflectivity factors are also converted to logarithmic scale.

$$\begin{aligned}
 \overline{Z_{\text{H}}^{\text{att}}}(x_g) &= 10 \log_{10}(I[Z_{\text{h}}^{\text{att}}(x_g)]) \\
 \overline{Z_{\text{V}}^{\text{att}}}(x_g) &= 10 \log_{10}(I[Z_{\text{v}}^{\text{att}}(x_g)]) \\
 \overline{Z_{\text{DR}}^{\text{att}}}(x_g) &= \overline{Z_{\text{H}}^{\text{att}}}(x_g) - \overline{Z_{\text{V}}^{\text{att}}}(x_g) \\
 \overline{K_{\text{dp}}}(x_g) &= (I[K_{\text{dp}}(x_g)]) \\
 \overline{\Psi_{\text{dp}}}(x_g) &= (I[\Psi_{\text{dp}}(x_g)])
 \end{aligned} \tag{B.8}$$



## Bibliography

- Andsager, K., Beard, K. V., and Laird, N. F.: Laboratory measurements of axis ratios for large rain drops, *J. Atmos. Sci.*, 56, 2673–2683, doi:10.1175/1520-0469(1999)056<2673:LMOARF>2.0.CO;2, 1999.
- Auer, A. H. and Veal, D. L.: The dimensions of ice crystals in natural clouds, *J. Atmos. Sci.*, 27, 919–926, doi:10.1175/1520-0469(1970)027<0919:TDOICI>2.0.CO;2, 1970.
- Auf der Maur, A. N.: Statistical Tools for Drop Size Distributions: Moments and Generalized Gamma, *J. Atmos. Sci.*, 58, 407–418, doi:10.1175/1520-0469(2001)058<0407:STFDSD>2.0.CO;2, 2001.
- Augros, C., Caumont, O., Ducrocq, V., Gaussiat, N., and Tabary, P.: Comparisons between S-, C- and X-band polarimetric radar observations and convective-scale simulations of the HyMeX first special observing period, *Q. J. R. Meteorol. Soc.*, 142, 347–362, doi:10.1002/qj.2572, URL <http://dx.doi.org/10.1002/qj.2572>, 2016.
- Babb, D. M., Verlinde, J., and Rust, B. W.: The Removal of Turbulent Broadening in Radar Doppler Spectra Using Linear Inversion with Double-Sided Constraints, *J. Atmos. Oceanic Technol.*, 17, 1583–1595, doi:10.1175/1520-0426(2000)017<1583:TROTBI>2.0.CO;2, 2000.
- Bailey, M. P. and Hallett, J.: A comprehensive habit diagram for atmospheric ice crystals: conformation from the laboratory, AIRS II, and other field studies, *J. Atmos. Sci.*, 66, 2888–2899, doi:10.1175/2009JAS2883.1, 2009.
- Bandera, J., Papatsoris, A. D., Watson, P. A., Tan, J., and Goddard, J. W.: Method for detecting the extend of the melting layer, *IET Elec. Letters*, 11, 2104–2105, doi:10.1049/el:19981462, 1998.
- Battaglia, A., Sturniolo, O., and Prodi, F.: Analysis of polarization radar returns from ice clouds, *Atmos. Res.*, 59-60, 231 – 250, doi:[https://doi.org/10.1016/S0169-8095\(01\)00118-1](https://doi.org/10.1016/S0169-8095(01)00118-1), URL <http://www.sciencedirect.com/science/article/pii/S0169809501001181>, 13th International Conference on Clouds and Precipitation, 2001.
- Battaglia, A., Ajewole, M. O., and Simmer, C.: Evaluation of radar multiple scattering effects in Cloudsat configuration, *Atmos. Chem. Phys.*, 7, 1719–1730, 2007.

## Bibliography

---

- Bauer, H.-S., Schwitalla, T., Wulfmeyer, V., Bakhshaii, A., Ehrer, U., Neuper, M., and Caumont, O.: Quantitative precipitation estimation based on high-resolution numerical weather prediction and data assimilation with WRF – a performance test, *Tellus A: Dynamic Meteorology and Oceanography*, 67, 25 047, doi:10.3402/tellusa.v67.25047, URL <http://dx.doi.org/10.3402/tellusa.v67.25047>, 2015.
- Beard, K. V.: Terminal velocity adjustment for cloud and precipitation drops aloft, *J. Atmos. Sci.*, 34, 1293–1298, 1977.
- Beard, K. V. and Chuang, C.: A new model for the equilibrium shape of raindrops, *J. Atmos. Sci.*, 44, 1509–1524, 1987.
- Bellon, A., Zawadzki, I., and Fabry, F.: Measurements of melting layer attenuation at X-band frequencies, *Radio Sci.*, 32, 943–955, 1997.
- Berenguer, M., Sempere-Torres, D., Corral, C., and Sánchez-Diezma, R.: A fuzzy logic technique for identifying nonprecipitating echoes in radar scans, *J. Atmos. Oceanic Technol.*, 23, 1157–1180, doi:10.1175/JTECH1914.1, 2006.
- Besic, N., Figueras i Ventura, J., Grazioli, J., Gabella, M., Germann, U., and Berne, A.: Hydrometeor classification through statistical clustering of polarimetric radar measurements: a semi-supervised approach, *Atmos. Meas. Tech.*, 9, 4425–4445, doi:10.5194/amt-9-4425-2016, URL <https://www.atmos-meas-tech.net/9/4425/2016/>, 2016.
- Blahak, U.: Towards a better representation of high density ice particles in a state-of-the-art two-moment bulk microphysical scheme, in: 15th International Conf. on Clouds and Precipitation, Cancun, Mexico, [https://www.researchgate.net/publication/228387376\\_Towards\\_a\\_better\\_representation\\_of\\_high\\_density\\_ice\\_particles\\_in\\_a\\_state-of-the-art\\_two-moment\\_bulk\\_microphysical\\_scheme](https://www.researchgate.net/publication/228387376_Towards_a_better_representation_of_high_density_ice_particles_in_a_state-of-the-art_two-moment_bulk_microphysical_scheme), 2008.
- Bohme, T., Van Lipzig, N., Delobbe, L., and Seifert, A.: Precipitation patterns above Belgium using weather radar and COSMO model reflectivity data, in: Proceedings of the 8th International Symposium on Tropospheric Profiling, Delft, The Netherlands, URL <http://www.ch2011.ch/pdf/CH2011reportHIGH.pdf>, 2009.
- Bohren, F. C. and Huffman, R. D.: *In Absorption and Scattering of Light by Small Particles*, vol. 25, 1983.
- Brandes, E., Zhang, G., and Vivekanandan, J.: Experiments in rainfall estimation with a polarimetric radar in a subtropical environment, *J. Appl. Meteorol.*, 41, 674–685, 2002.
- Brandes, E. A., Ikeda, K., Zhang, G., Schonhuber, M., and M., R. R.: A statistical and physical description of hydrometeor distributions in Colorado snowstorms using a video disdrometer, *J. Appl. Meteor. Clim.*, 46, 634–650, doi:10.1175/JAM2489.1, 2007.
- Bringi, V. N. and Chandrasekar, V.: *Polarimetric doppler weather radar*, Cambridge University Press, 2001.

- Caumont, O., Ducrocq, V., Delrieu, G., Gosset, M., Pinty, J.-P., Parent du Châtelet, J., Andrieu, H., Lemaître, Y., and Scialom, G.: A radar simulator for high-resolution nonhydrostatic models, *J. Atmos. Oceanic Technol.*, 23, 1049–1067, doi:10.1175/JTECH1905.1, 2006.
- Chahine, M. T.: The hydrological cycle and its influence on climate, *Nature*, 359, 373–380, 1992.
- Chang, S. W. and Holt, T. R.: Impact of Assimilating SSM/I Rainfall Rates on Numerical Prediction of Winter Cyclones, *Mon. Weather Rev.*, 122, 151–164, doi:10.1175/1520-0493(1994)122<0151:IOASRR>2.0.CO;2, URL [https://doi.org/10.1175/1520-0493\(1994\)122<0151:IOASRR>2.0.CO;2](https://doi.org/10.1175/1520-0493(1994)122<0151:IOASRR>2.0.CO;2), 1994.
- Chen, S.-G. and Sun, W.-Y.: A One-dimensional Time Dependent Cloud Model., *J. Meteorol. Soc. Jpn*, 80, 99–118, doi:10.2151/jmsj.80.99, 2002.
- Cheong, B. L., Palmer, R. D., and Xue, M.: A Time Series Weather Radar Simulator Based on High-Resolution Atmospheric Models, *J. Atmos. Oceanic Technol.*, 25, 230–243, doi:10.1175/2007JTECHA923.1, 2008.
- Chilès, J.-P. and Delfiner, P.: *Geostatistics: Modeling spatial uncertainty*, Probability and statistics, Wiley, 1999.
- Cohard, J.-M. and Pinty, J.-P.: A comprehensive two-moment warm microphysical bulk scheme. I: Description and tests, *Q. J. R. Meteorol. Soc.*, 126, 1815–1842, doi:10.1002/qj.49712656613, URL <http://dx.doi.org/10.1002/qj.49712656613>, 2000.
- COSMO: COSMO namelists and variables, <http://www.cosmo-model.org/content/tasks/operational/nmlDoc/cosmoDefault.htm?ver=3&mode=printerFriendly>, 2015.
- Das, S., Maitra, A., and Shukla, A. K.: Melting layer characteristics at different climatic conditions in the Indian region: Ground based measurements and satellite observations, *Atmos. Res.*, 101, 78–83, doi:10.1016/j.atmosres.2011.01.013, 1993.
- Davies, H. C.: A lateral boundary formulation for multi-level prediction models, *Q. J. R. Meteorol. Soc.*, 102, 405–418, doi:10.1002/qj.49710243210, 1976.
- Davis, C., Brown, B., and Bullock, R.: Object-based verification of precipitation forecasts. part i: methodology and application to mesoscale rain areas, *Mon. Weather Rev.*, 134, 1772–1784, doi:10.1175/MWR3145.1, 2006.
- Davolio, S. and Buzzi, A.: A Nudging Scheme for the Assimilation of Precipitation Data into a Mesoscale Model, *Weather Forecast.*, 19, 855–871, doi:10.1175/1520-0434(2004)019<0855:ANSFTA>2.0.CO;2, URL [https://doi.org/10.1175/1520-0434\(2004\)019<0855:ANSFTA>2.0.CO;2](https://doi.org/10.1175/1520-0434(2004)019<0855:ANSFTA>2.0.CO;2), 2004.
- De Michele, C. and Ignaccolo, M.: New perspectives on rainfall from a discrete view, *Hydrol. Processes*, 27, 2379–2382, doi:10.1002/hyp.9782, 2013.

## Bibliography

---

- Deidda, R.: Rainfall downscaling in a space-time multifractal framework, *Water Resour. Res.*, 36, 1779–1794, doi:10.1029/2000WR900038, 2000.
- Dolan, B. and Rutledge, S. A.: A theory-based hydrometeor identification algorithm for X-band polarimetric radars, *J. Atmos. Oceanic Technol.*, 26, 2071–2088, doi:10.1175/2009JTECHA1208.1, 2009.
- Domaszczyński, P.: Performance evaluation of a network of polarimetric X-Band radars used for rainfall estimation, Ph.D. thesis, University of Iowa, 2012.
- Doms, G. and Baldauf, M.: A description of the nonhydrostatic regional COSMO model, Part I: Dynamics and Numerics, <http://www.cosmo-model.org/content/model/documentation/core/cosmoDynNumcs.pdf>, 2015.
- Doms, G., Förstner, J., Heise, E., Herzog, H.-J., Mironov, D., Raschendorfer, M., Reinhardt, T., Ritter, B., Schrodin, R., Schulz, J.-P., et al.: A description of the nonhydrostatic regional COSMO model, Part II: Physical Parameterization, <http://www.cosmo-model.org/content/model/documentation/core/cosmoPhysParamtr.pdf>, 2011.
- Douglas, E. M. and Barros, A. P.: Probable maximum precipitation estimation using multifractals: application in the eastern United States, *J. Hydrometeorol.*, 4, 1012–1024, doi:10.1175/1525-7541(2003)004<1012:PMPEUM>2.0.CO;2, 2003.
- Doviak, R. and Zrnić, D.: Doppler radar and weather observations, second edition, Dover Publications, 2006.
- Drobinski, P., Ducrocq, V., Alpert, P., Anagnostou, E., Béranger, K., Borga, M., Braud, I., Chanzy, A., Davolio, S., Delrieu, G., Estournel, C., Filali Boubrahmi, N., Font, J., Grubisic, V., Gualdi, S., Homar, V., Ivancan-Picek, B., Kottmeier, C., Kotroni, V., Lagouvardos, K., Lionello, P., Llasat, M. C., Ludwig, W., Lutoff, C., Mariotti, A., Richard, E., Romero, R., Rotunno, R., Roussot, O., Ruin, I., Somot, S., Taupier-Letage, I., Tintore, J., Uijlenhoet, R., and Wernli, H.: HyMeX, a 10-year multidisciplinary program on the Mediterranean water cycle, *Bull. Amer. Meteor. Soc.*, doi:10.1175/BAMS-D-12-00242.1, 2013.
- Ducrocq, V., Braud, I., Davolio, S., Ferretti, R., Flamant, C., Jansà, A., Kalthoff, N., Richard, E., Taupier-Letage, I., Ayrat, P.-A., Belamari, S., Berne, A., Borga, M., Boudevillain, B., Bock, O., Boichard, J.-L., Bouin, M.-N., Bousquet, O., Bouvier, C., Chiggiato, J., Cimini, D., Corsmeier, U., Coppola, L., Cocquerez, P., Defer, E., Delanoë, J., Di Girolamo, P., Doerenbecher, A., Drobinski, P., Dufournet, Y., Fourrié, N., Gourley, J. J., Labatut, L., Lambert, D., Le Coz, J., Marzano, F. S., Molinié, G., Montani, A., Nord, G., Nuret, M., Ramage, K., Rison, B., Roussot, O., Said, F., Schwarzenboeck, A., Testor, P., Van-Baelen, J., Vincendon, B., Aran, M., and Tamayo, J.: HyMeX-SOP1, the field campaign dedicated to heavy precipitation and flash flooding in the northwestern Mediterranean, *Bulletin of the American Meteorological Society*, 95, 1083–1100, doi:10.1175/BAMS-D-12-00244.1, 2014.

- Durden, S. L., Kitiyakara, A., Eastwood, I., Tanner, A. B., Haddad, Z. S., Li, F. K., and Wilson, W. J.: ARMAR Observations of the Melting Layer During TOGA COARE, *IEEE T. Geosci. Remote Sens.*, 35, 1453–1456, doi:10.1109/36.649800, 1997.
- Dutton, J. A. and Fichtl, G. H.: Approximate Equations of Motion for Gases and Liquids, *J. Atmos. Sci.*, 26, 241–254, doi:10.1175/1520-0469(1969)026<0241:AEOMFG>2.0.CO;2, 1969.
- Ebert, E. E.: Fuzzy verification of high-resolution gridded forecasts: a review and proposed framework, *Met. Apps*, 15, 51–64, doi:10.1002/met.25, 2008.
- Fabry, F.: On the determination of scale ranges for precipitation fields, *J. Geophys. Res.*, 101, 12 819–12 826, doi:10.1029/96JD00718, 1996.
- Fabry, F.: *Radar Meteorology, Principles and Practice*, Cambridge University Press, 2015.
- Fabry, F. and Zawadzki, I.: Long Term Observations of the Melting Layer of Precipitation and Their Interpretation, *J. Atmos. Sci.*, 52, 838–851, doi:10.1175/1520-0469(1995)052<0838:LTROOT>2.0.CO;2, 1995.
- Field, P. R., Hogan, R. J., Brown, P. R. A., Illingworth, A. J., Choullarton, T. W., and Cotton, R. J.: Parametrization of ice-particle size distributions for mid-latitude stratiform cloud, *Q. J. R. Meteorol. Soc.*, 131, 1997–2017, doi:10.1256/qj.04.134, URL <http://dx.doi.org/10.1256/qj.04.134>, 2005.
- Figueras i Ventura, J., Schneebeli, M., Leuenberger, A., Gabella, M., Grazioli, J., Raupach, T. H., Wolfensberger, D., Graf, P., Wernli, H., Berne, A., and Germann, U.: The PARADISO campaign, description and first results, in: 37th Conference on Radar Meteorology, Norman, USA, 2015.
- Frei, C., Scholl, R., Fukutome, S., Schmidli, R., and Vidale, P. L.: Future change of precipitation extremes in Europe: Intercomparison of scenarios from regional climate models, *J. Geophys. Res.*, 111, doi:10.1029/2005JD005965, 2006.
- Frick, C. and Wernli, H.: A Case Study of High-Impact Wet Snowfall in Northwest Germany (25-27 November 2005): Observations, Dynamics, and Forecast Performance, *Weather Forecast.*, 27, 1217–1234, doi:10.1175/WAF-D-11-00084.1, 2012.
- Frick, C., Seifert, A., and Wernli, H.: A bulk parametrization of melting snowflakes with explicit liquid water fraction for the COSMO model, *Geosci. Model Dev.*, 6, 1925–1939, doi:10.5194/gmd-6-1925-2013, URL <https://www.geosci-model-dev.net/6/1925/2013/>, 2013.
- Furukawa, K., Nio, T., Konishi, T., Masaki, T., Kubota, R., Oki, T., and Iguchi, T.: Current status of the dual-frequency precipitation radar on the global precipitation measurement core spacecraft and the new version of GPM standard products, vol. 10000, pp. 10 000 – 10 000 – 6, doi:10.1117/12.2240907, URL <http://dx.doi.org/10.1117/12.2240907>, 2016.
- Gal-Chen, T. and Somerville, R. C. J.: On the use of a coordinate transformation for the solution of the Navier-Stokes equations, *J. Comput. Phys.*, 17, 209–228, 1975.

## Bibliography

---

- Gander, W. and Gautschi, W.: Adaptive Quadrature—Revisited, *BIT Numerical Mathematics*, 40, 84–101, doi:10.1023/A:1022318402393, URL <http://dx.doi.org/10.1023/A:1022318402393>, 2000.
- Garrett, T. J., Fallgatter, C., Shkurko, K., and Howlett, D.: Fall speed measurement and high-resolution multi-angle photography of hydrometeors in free fall, *Atmos. Meas. Tech.*, 5, 2625–2633, doi:10.5194/amt-5-2625-2012, 2012.
- Garrett, T. J., Yuter, S. E., Fallgatter, C., Shkurko, K., Rhodes, S. R., and Endries, J. L.: Orientations and aspect ratios of falling snow, *Geophys. Res. Lett.*, 42, 4617–4622, doi:10.1002/2015GL064040, URL <http://dx.doi.org/10.1002/2015GL064040>, 2015GL064040, 2015.
- Gautschi, W.: Orthogonal Polynomials, Quadrature, and Approximation: Computational Methods and Software (in Matlab), pp. 1–77, Springer Berlin Heidelberg, Berlin, Heidelberg, doi:10.1007/978-3-540-36716-1\_1, URL [http://dx.doi.org/10.1007/978-3-540-36716-1\\_1](http://dx.doi.org/10.1007/978-3-540-36716-1_1), 2006.
- Germann, U., Galli, G., Boscacci, M., and Bolliger, M.: Radar precipitation measurement in a mountainous region, *Q. J. R. Meteorol. Soc.*, 132, 1669–1692, doi:10.1256/qj.05.190, 2006.
- Giangrande, S. E., Krause, J. M., and Ryzhkov, A. V.: Automatic designation of the melting layer with a polarimetric prototype of the WSR-88D radar, *J. Appl. Meteor. Clim.*, 47, 1354–1364, doi:10.1175/2007JAMC1634.1, 2008.
- Gilleland, E., Ahijevych, D., Brown, B. G., Casati, B., and Ebert, E. E.: Intercomparison of spatial forecast verification methods, *Weather Forecast.*, 24, 1416–1430, doi:10.1175/2009WAF2222269.1, 2009.
- Gires, A., Tchiguirinskaia, I., Schertzer, D., and Lovejoy, S.: Multifractal and spatio-temporal analysis of the rainfall output of the Meso-NH model and radar data, *Hydrol. Sci. J.*, 55, 2011.
- Gires, A., Tchiguirinskaia, I., Schertzer, D., and Berne, A.: 2DVD Data Revisited: Multifractal Insights into Cuts of the Spatiotemporal Rainfall Process, *J. Hydrometeorol.*, 16, 548–562, doi:10.1175/JHM-D-14-0127.1, 2015.
- Gires, A., Tchiguirinskaia, I., and Schertzer, D.: Multifractal comparison of the outputs of two optical disdrometers, *Hydrol. Sci. J.*, 61, 2016.
- Grazioli, J., Schneebeli, M., and Berne, A.: Accuracy of Phase-Based Algorithms for the Estimation of the Specific Differential Phase Shift Using Simulated Polarimetric Weather Radar Data, *IEEE Geosci. Remote Sens. Lett.*, 11, 763–767, doi:10.1109/LGRS.2013.2278620, 2014a.
- Grazioli, J., Tuia, D., Monhart, S., Schneebeli, M., Raupach, T., and Berne, A.: Hydrometeor classification from two-dimensional video disdrometer data, *Atmos. Meas. Tech.*, 7, 2869–2882, doi:10.5194/amt-7-2869-2014, URL <http://www.atmos-meas-tech.net/7/2869/2014/>, 2014b.



- Grazioli, J., Tuia, D., and Berne, A.: Hydrometeor classification from polarimetric radar measurements: a clustering approach, *Atmos. Meas. Tech.*, 8, 149–170, doi:10.5194/amt-8-149-2015, URL <http://www.atmos-meas-tech.net/8/149/2015/>, 2015.
- Heymsfield, A.: Ice crystal terminal velocities, *J. Atmos. Sci.*, 29, 1348–1357, doi:10.1175/1520-0469(2000)057<0916:CCTV>2.0.CO;2, 1972.
- Heymsfield, A. J., Schmitt, C. G., Bansemer, A., Baumgardner, D., Weinstock, E. M., Smith, J. T., and Sayres, D.: Effective ice particle densities for cold anvil cirrus, *Geophys. Res. Lett.*, 31, n/a–n/a, doi:10.1029/2003GL018311, 2004.
- Hubbert, M., Rousseeuw, P. J., and Branden, K. V.: ROBPCA: A New Approach to Robust Principal Component Analysis, *Technometrics*, 47, 64–79, doi:10.1198/004017004000000563, 2005.
- Hubert, P., Tessier, Y., Lovejoy, S., Schertzer, D., Schmitt, F., Ladoy, P., Carbonnel, J., Violette, S., and Desurosne, I.: Multifractals and extreme rainfall events, *Geophys. Res. Lett.*, 20, 931–934, doi:10.1029/93GL01245, 1993.
- Hufford, G. A.: A model for the complex permittivity of ice at frequencies below 1 THz, *Int. J. Infrared Milli.*, 12, 677–682, doi:10.1007/BF01008898, 1991.
- Iguchi, T., Hanado, H., Takahashi, N., Kobayashi, S., and Satoh, S.: The dual-frequency precipitation radar for the GPM core satellite, in: *Geoscience and Remote Sensing Symposium, 2003. IGARSS'03. Proceedings. 2003 IEEE International*, vol. 3, pp. 1698–1700, IEEE, doi:10.1109/IGARSS.2003.1294221, 2003.
- Iguchi, T. S., Seto, S., Meneghini, R., Yoshida, N., Awaka, J., Le, M., Chandrasekar, V., and Kubota, T.: GPM/DPR Level-2 Algorithm Theoretical Basis Document. Tech. Rep., Tech. rep., NASA/JAXA, URL [https://pmm.nasa.gov/sites/default/files/document\\_files/ATBD\\_GPM\\_DPR\\_n3\\_dec15.pdf](https://pmm.nasa.gov/sites/default/files/document_files/ATBD_GPM_DPR_n3_dec15.pdf), 2010.
- Inman, H. F. and Bradley, E. L. J.: The overlapping coefficient as a measure of agreement between probability distributions and point estimation of the overlap of two normal densities, *Commun. Stat.-Theor. M.*, 18, 3851–3874, doi:10.1080/03610928908830127, 1989.
- Jackson, R. B., Carpenter, S. R., Dahm, C. N., McKnight, D. M., Naiman, R. J., Postel, S. L., and Running, S. W.: Water in a changing world, *Ecol. Appl.*, 11, 1027–1045, doi:10.2307/3061010, 2001.
- Jaffrain, J. and Berne, A.: Experimental quantification of the sampling uncertainty associated with measurements from Parsivel disdrometers, *J. Hydrometeorol.*, 12, doi:10.1175/2010JHM1244.1, 2011.
- Jameson, A. R.: Microphysical interpretation of multi-parameter radar measurements in rain: Part I: interpretation of polarization measurements and estimation of raindrop shapes, *J. Atmos. Sci.*, 40, 1792 – 1802, 1983.

## Bibliography

---

- Jones, R. C.: A New Calculus for the Treatment of Optical SystemsI. Description and Discussion of the Calculus, *J. Opt. Soc. Am.*, 31, 488–493, doi:10.1364/JOSA.31.000488, URL <http://www.osapublishing.org/abstract.cfm?URI=josa-31-7-488>, 1941.
- Joss, J. and Gori, E.: Shapes of raindrop size distributions, *J. Appl. Meteorol.*, 17, 1054–1061, doi:10.1175/1520-0450(1978)017<1054:SORSDD>2.0.CO;2, 1978.
- Jung, Y., Ming, X., and Zhang, G.: Assimilation of Simulated Polarimetric Radar Data for a Convective Storm Using the Ensemble Kalman Filter. Part I: Observation Operators for Reflectivity and Polarimetric Variables, *Mon. Weather Rev.*, 136, 2228–2245, doi:10.1175/2007MWR2083.1, 2008.
- Kain, J. S., Goss, S., and Baldwin, E.: The Melting Effect as a Factor in Precipitation-Type Forecasting, *Weather Forecast.*, 15, 700–714, doi:10.1175/1520-0434(2000)015<0700:TMEAAF>2.0.CO;2, 2000.
- Kalogiros, J., Anagnostou, M. N., Anagnostou, E., Montopoli, M., Picciotti, E., and Marzano, F. S.: Correction of Polarimetric Radar Reflectivity Measurements and Rainfall Estimates for Apparent Vertical Profile in Stratiform Rain, *J. Appl. Meteor. Clim.*, 52, 1170–1186, doi:10.1175/JAMC-D-12-0140.1, 2013.
- Kang, E.: *Radar System Analysis, Design, and Simulation*, Artech House radar library, Artech House, URL <https://books.google.ch/books?id=tjMfAQAAIAAJ>, 2008.
- Kennedy, J. and Eberhart, R. C.: Particle swarm optimization, in: *Proceedings of the 1995 IEEE International Conference on Neural Networks*, vol. 4, pp. 1942–1948, Perth, Australia, IEEE Service Center, Piscataway, NJ, 1995.
- Klaassen, W.: Attenuation and reflection of radio waves by a melting layer of precipitation, *IEEE T. Antenn. Propag.*, 137, 39–44, doi:10.1049/ip-h-2.1990.0007, 1990.
- Kolmogorov, A. N.: A refinement of previous hypotheses concerning the local structure of turbulence in viscous incompressible fluid at high Reynolds number, *J. Fluid. Mech.*, 13, 82–85, doi:10.1017/S0022112062000518, 1962.
- Köppen, W.: *Das geographische System der Klimate*, Allgemeine Klimalehre, Borntraeger, URL <https://books.google.ch/books?id=hM2uugAACAAJ>, 1936.
- Kumjian, M. R., Khain, A. P., Benmoshe, N., Iltoviz, E., Ryzhkov, A. V., and Phillips, V. T. J.: The Anatomy and Physics of ZDR Columns: Investigating a Polarimetric Radar Signature with a Spectral Bin Microphysical Model, *J. Appl. Meteor. Clim.*, 53, 1820–1843, doi:10.1175/JAMC-D-13-0354.1, URL <https://doi.org/10.1175/JAMC-D-13-0354.1>, 2014.
- Kunkel, K. E., Pielke, R. A., and Changnon, S. A.: Temporal fluctuations in weather and climate extremes that cause economic and human health impacts: A review, *Bull. Amer. Meteor. Soc.*, 80, 1077–1098, doi:10.1175/1520-0477(1999)080<1077:TFIWAC>2.0.CO;2, 1999.

- Kuo, K.-S., Olson, W. S., Johnson, B. T., Grecu, M., Tian, L., Clune, T. L., van Aartsen, B. H., Heymsfield, A. J., Liao, L., and Meneghini: The Microwave Radiative Properties of Falling Snow Derived from Nonspherical Ice Particle Models. Part I: An Extensive Database of Simulated Pristine Crystals and Aggregate Particles, and Their Scattering Properties, *J. Appl. Meteor. Clim.*, 55, 691–708, doi:10.1175/JAMC-D-15-0130.1, 2016.
- Labitt, M.: Coordinated radar and aircraft Observations of turbulence, Proj. Rep. ATC 108 1468, Massachusetts Institute of Technology, Lincoln Lab., Cambridge, URL [https://www.ll.mit.edu/mission/aviation/publications/publication-files/atc-reports/Labitt\\_1981\\_ATC-108\\_WW-15318.pdf](https://www.ll.mit.edu/mission/aviation/publications/publication-files/atc-reports/Labitt_1981_ATC-108_WW-15318.pdf), 1981.
- Lafore, J. P., Stein, J., Asencio, N., Bougeault, P., Ducrocq, V., Duron, J., Fischer, C., Hérel, P., Mascart, P., Masson, V., Pinty, J. P., Redelsperger, J. L., Richard, E., and Vilà-Guerau de Arellano, J.: The Meso-NH Atmospheric Simulation System. Part I: adiabatic formulation and control simulations, *Annales Geophysicae*, 16, 90–109, doi:10.1007/s00585-997-0090-6, URL <http://www.ann-geophys.net/16/90/1998/>, 1998.
- Langleben, M. P.: The terminal velocity of snowflakes, *Q. J. R. Meteorol. Soc.*, 80, 174–181, doi:10.1002/qj.49708034404, URL <http://dx.doi.org/10.1002/qj.49708034404>, 1954.
- Lavallée, D., Lovejoy, S., and Ladoy, P.: Nonlinear variability and landscape topography: analysis and simulation, in: *Fractals in geography*, edited by de Cola, L. and Lam, N., pp. 171–205, Prentice-Hall, 1993.
- Le, M., Chandrasekar, V., and Biswas, S.: Evaluation and Validation of GPM Dual-Frequency Classification Module after Launch, *J. Atmos. Oceanic Technol.*, 33, 2699–2716, doi:10.1175/JTECH-D-15-0253.1, URL <https://doi.org/10.1175/JTECH-D-15-0253.1>, 2016.
- Lee, G., Zawadzki, I., Szyrmer, W., Sempere-Torres, D., and Uijlenhoet, R.: A general approach to double-moment normalization of drop size distributions, *J. Appl. Meteorol.*, 43, 264–281, doi:10.1175/1520-0450(2004)043<0264:AGATDN>2.0.CO;2, 2004.
- Liebe, H., Hufford, G., and Manabe, T.: A Model for the Complex Permittivity of Water at Frequencies Below 1 THZ, *Int. J. Infrared Milli.*, 12, 659–675, doi:10.1007/BF01008897, 1991.
- Lin, Y.-L., Farley, R. D., and Orville, H. D.: Bulk Parameterization of the Snow Field in a Cloud Model, *J. Climate Appl. Meteorol.*, 22, 1065–1092, doi:10.1175/1520-0450(1983)022<1065:BPOTSF>2.0.CO;2, 1983.
- Liu, G.: A DATABASE OF MICROWAVE SINGLE-SCATTERING PROPERTIES FOR NONSPHERICAL ICE PARTICLES, *Bull. Amer. Meteor. Soc.*, 89, 1563–1570, doi:10.1175/2008BAMS2486.1, 2008.
- Locatelli, J. and Hobbs, P.: Fall Speeds and Masses of Solid Precipitation Particles, *J. Geophys. Res.*, 79, 2185–2197, doi:10.1029/JC079i015p02185, 1974.

## Bibliography

---

- Löffler-Mang, M. and Joss, J.: An optical disdrometer for measuring size and velocity of hydrometeors, *J. Atmos. Oceanic Technol.*, 17, 130–139, doi:10.1175/1520-0426(2000)017<0130:AODFMS>2.0.CO;2, 2000.
- Lovejoy, S.: Multifractal Explorer, <http://www.physics.mcgill.ca/~gang/multifrac/multifractals/isotropic.htm>, 2017.
- Lovejoy, S. and Schertzer, D.: Scaling and multifractal fields in the solid earth and topography, *Nonlinear Proc. Geoph.*, 14, 465–502, doi:10.5194/npg-14-465-2007, 2007.
- Lovejoy, S., Schertzer, D., and Allaire, V. C.: The remarkable wide range spatial scaling of TRMM precipitation, *Atmos. Res.*, 90, 10–32, doi:10.1016/j.atmosres.2008.02.016, 2008.
- Lu, Y., Jiang, Z., Aydin, K., Verlinde, J., Clothiaux, E. E., and Botta, G.: A polarimetric scattering database for non-spherical ice particles at microwave wavelengths, *Atmos. Meas. Tech.*, 9, 5119–5134, doi:10.5194/amt-9-5119-2016, URL <https://www.atmos-meas-tech.net/9/5119/2016/>, 2016.
- Macor, J., Schertzer, D., and Lovejoy, S.: Multifractal methods applied to rain forecast using radar data, *La Houille Blanche - Revue internationale de l'eau*, pp. 92–98, doi:10.1051/lhb:2007052, 2007.
- Magono, C. and Lee, C. W.: Meteorological classification of natural snow crystals, *J. Fac. Sci., Hokkaido Univ., Series VII*, 2, 321–335, doi:10.5331/seppyo.24.33, 1966.
- Marsan, D., Schertzer, D., and Lovejoy, S.: Causal space-time multifractal processes: Predictability and forecasting of rain fields, *J. Geophys. Res.*, 101, 26 333–26 346, doi:10.1029/96JD01840, 1996.
- Marshall, J. S. and Palmer, W. M.: The distribution of raindrops with size, *J. Meteor.*, 5, 165–166, 1948.
- Marshall, J. S., Langille, R. C., and Palmer, W. M.: Measurement of rainfall by radar, *J. Meteor.*, 4, 186–192, doi:10.1175/1520-0469(1947)004<0186:MORBR>2.0.CO;2, 1947.
- Marshall, J. S., Hitschfeld, W., and Gunn, K. L. S.: Advances in radar weather, *Adv. Geophys.*, 2, 1–56, doi:10.1016/S0065-2687(08)60310-6, 1955.
- Matrosov, S. Y.: Assessment of radar signal attenuation caused by the melting hydrometeor layer, *IEEE T. Geosci. Remote Sens.*, 46, 1039–1047, doi:10.1109/TGRS.2008.915757, 2008.
- Matrosov, S. Y., Heymsfield, A. J., and Wang, Z.: Dual-frequency radar ratio of nonspherical atmospheric hydrometeors, *Geophys. Res. Lett.*, 32, n/a–n/a, doi:10.1029/2005GL023210, URL <http://dx.doi.org/10.1029/2005GL023210>, 113816, 2005.
- Matrosov, S. Y., Clark, K. A., and Kingsmill, D. E.: A polarimetric radar approach to identify rain, melting-layer, and snow regions for applying corrections to vertical profiles of reflectivity, *J. Appl. Meteor. Clim.*, 46, 154–166, doi:10.1175/JAM2508.1, 2007.

- Mellor, G. L. and Yamada, T.: Development of a turbulence closure model for geophysical fluid problems., *Rev. Geophys. Space Phys.*, 20, 851–875, doi:10.1029/RG020i004p00851, 1982.
- Meneghini, R. and Liao, L.: Comparisons of Cross Sections for Melting Hydrometeors as Derived from Dielectric Mixing Formulas and a Numerical Method, *J. Appl. Meteorol.*, 35, 1658–1670, doi:10.1175/1520-0450(1996)035<1658:COCSFM>2.0.CO;2, 1996.
- Mishchenko, M., Travis, L., and Lacis, A.: *Scattering, Absorption, and Emission of Light by Small Particles*, Cambridge University Press, 2002.
- Mishchenko, M. I., Travis, L. D., and Mackowski, D. W.: T-matrix computations of light scattering by nonspherical particles: A review, *J. Quant. Spectrosc. Radiat. Transfer*, 55, 535–575, doi:10.1016/0022-4073(96)00002-7, 1996.
- Mitra, S. K., Wohl, O., Ahr, M., and Pruppacher, H. R.: A Wind Tunnel and Theoretical Study of the Melting Behavior of Atmospheric Ice Particles. IV: Experiment and Theory for Snow Flakes, *J. Atmos. Sci.*, 47, 584–591, doi:10.1175/1520-0469(1990)047<0584:AWTATS>2.0.CO;2, 1990.
- Mittermaier, M., Roberts, N., and Thompson, S. A.: A long-term assessment of precipitation forecast skill using the Fractions Skill Score, *Met. Apps*, 20, 176–186, doi:10.1002/met.296, 2013.
- Noel, V. and Sassen, K.: Study of Planar Ice Crystal Orientations in Ice Clouds from Scanning Polarization Lidar Observations, *J. Appl. Meteorol.*, 44, 653–664, doi:10.1175/JAM2223.1, 2005.
- Noppel, H., Blahak, U., Seifert, A., and Beheng, K. D.: Simulations of a hailstorm and the impact of CCN using an advanced two-moment cloud microphysical scheme, *Atmos. Res.*, 96, 286–301, doi:10.1016/j.atmosres.2009.09.008, 2010.
- Nykanen, D. K. and Harris, D.: Orographic influences on the multiscale statistical properties of precipitation, *J. Geophys. Res. Atmos.*, 108, doi:10.1029/2001JD001518, 8381, 2003.
- Parisi, G. and Frisch, U.: On the singularity structure of fully developed turbulence, in: *Turbulence and Predictability in Geophysical Fluid Dynamics and Climate Dynamics*, pp. 84–88, North-Holland, 1<sup>st</sup> edn., 1985a.
- Parisi, G. and Frisch, U.: A multifractal model of intermittency, in: *Turbulence and Predictability in Geophysical Fluid Dynamics and Climate Dynamics*, pp. 111–114, North-Holland, 1<sup>st</sup> edn., 1985b.
- Peel, M. C., Finlayson, B. L., and McMahon, T. A.: Updated world map of the Koeppen-Geiger climate classification, *Hydrology and Earth System Sciences*, 11, 1633–1644, doi: 10.5194/hess-11-1633-2007, URL <https://www.hydrol-earth-syst-sci.net/11/1633/2007/>, 2007.

## Bibliography

---

- Pfeifer, M., Craig, G. C., Hagen, M., and Keil, C.: A polarimetric radar forward operator for model evaluation, *J. Appl. Meteor. Clim.*, 47, 3202–3220, doi:10.1175/2008JAMC1793.1, 2008.
- Praz, C., Roulet, Y.-A., and Berne, A.: Solid hydrometeor classification and riming degree estimation from pictures collected with a Multi-Angle Snowflake Camera, *Atmos. Meas. Tech.*, 10, 1335–1357, doi:10.5194/amt-10-1335-2017, URL <https://www.atmos-meas-tech.net/10/1335/2017/>, 2017.
- Probert-Jones, J. R.: The radar equation in meteorology, *Q. J. R. Meteorol. Soc.*, 88, 485–495, doi:10.1002/qj.49708837810, 1962.
- Pruppacher, H. R. and Klett, R. L.: Microphysics of clouds and precipitation, no. 18 in *Atmospheric and Oceanographic Sciences Library*, Kluwer Academic Press, 2<sup>nd</sup> edn., 1997.
- Pujol, O., Mesnard, F., and Sauvageot, H.: Effects of Melting Layer in Airborne Meteorological X-Band Radar Observations, *IEEE T. Geosci. Remote Sens.*, 50, 2318–2324, 2012.
- Rabier, F.: Overview of global data assimilation developments in numerical weather-prediction centres, *Q. J. R. Meteorol. Soc.*, 131, 3215–3233, doi:10.1256/qj.05.129, URL <http://dx.doi.org/10.1256/qj.05.129>, 2005.
- Radkevich, A., Lovejoy, S., Strawbridge, K. B., Schertzer, D., and Lilley, M.: Scaling turbulent atmospheric stratification. III: Space–time stratification of passive scalars from lidar data, *Q. J. R. Meteorol. Soc.*, 134, 317–335, doi:10.1002/qj.203, 2008.
- Raupach, T. H. and Berne, A.: Correction of raindrop size distributions measured by Parsivel disdrometers, using a two-dimensional video disdrometer as a reference, *Atmos. Meas. Tech.*, 8, 343–365, doi:10.5194/amt-8-343-2015, URL <http://www.atmos-meas-tech.net/8/343/2015/>, 2015.
- Raupach, T. H. and Berne, A.: Small-Scale Variability of the Raindrop Size Distribution and Its Effect on Areal Rainfall Retrieval, *J. Hydrol.*, 17, 2077–2104, doi:10.1175/JHM-D-15-0214.1, 2016.
- Reinhardt, T. and Seifert, A.: A Three-Category Ice Scheme for LMK, URL [http://www.cosmo-model.org/content/model/documentation/newsLetters/newsLetter06/cnl6\\_reinhardt.pdf](http://www.cosmo-model.org/content/model/documentation/newsLetters/newsLetter06/cnl6_reinhardt.pdf), 2006.
- Rico-Ramirez, M. A. and Cluckie, I.: Classification of ground clutter and anomalous propagation using dual-polarization weather radar, *IEEE T. Geosci. Remote Sens.*, 46, 1892–1904, doi:10.1109/TGRS.2008.916979, 2008.
- Ritter, B. and Geleyn, J.-F.: A Comprehensive Radiation Scheme for Numerical Weather Prediction Models with Potential Applications in Climate Simulations, *Mon. Weather Rev.*, 120, 303–325, doi:10.1175/1520-0493(1992)120<0303:ACRSFN>2.0.CO;2, 1992.

- Rogers, R. R., Baumgardner, D., Ethier, S. A., Carter, D. A., and Ecklund, W. L.: Comparison of Raindrop Size Distributions Measured by Radar Wind Profiler and by Airplane, *J. Appl. Meteorol.*, 32, 694–699, doi:10.1175/1520-0450(1993)032<0694:CORSDM>2.0.CO;2, 1993.
- Royer, J.-F., Biaou, A., Chauvin, F., Schertzer, D., and Lovejoy, D.: Multifractal analysis of the evolution of simulated precipitation over France in a climate scenario, *Comptes Rendus Geoscience*, 340, 431 – 440, doi:10.1016/j.crte.2008.05.002, 2008.
- Rutledge, S. A. and Hobbs, P.: The Mesoscale and Microscale Structure and Organization of Clouds and Precipitation in Midlatitude Cyclones. VIII: A Model for the “Seeder-Feeder” Process in Warm-Frontal Rainbands, *J. Atmos. Sci.*, 40, 1185–1206, doi:10.1175/1520-0469(1983)040<1185:TMAMSA>2.0.CO;2, 1983.
- Ryzhkov, A. V.: The Impact of Beam Broadening on the Quality of Radar Polarimetric Data, *J. Atmos. Oceanic Technol.*, 24, 729–744, doi:10.1175/JTECH2003.1, 2007.
- Ryzhkov, A. V., Schuur, T. J., Burgess, D. W., Heinselman, P. L., Giangrande, S. E., and Zrnica, D. S.: The joint polarization experiment, polarimetric rainfall measurements and hydrometeor classification, *Bull. Amer. Meteor. Soc.*, 86, 809–824, doi:10.1175/BAMS-86-6-809, 2005.
- Ryzhkov, A. V., Pinsky, M., Pokrovsky, A., and Khain, A.: Polarimetric Radar Observation Operator for a Cloud Model with Spectral Microphysics, *J. Appl. Meteor. Clim.*, 50, 873–894, doi:10.1175/2010JAMC2363.1, 2011.
- Salonen, K., Järvinen, H., Järvenoja, S., Niemelä, S., and Eresmaa, R.: Doppler radar radial wind data in NWP model validation, *Meteorol. Appl.*, 15, 97 – 102, doi:10.1002/met.47, 2008.
- Sánchez-Diezma, R., Zawadzki, I., and Sempere-Torres, D.: Identification of the bright band through the analysis of volumetric radar data, *J. Geophys. Res.*, 105, 2225–2236, doi:10.1029/1999JD900310, 2000.
- Schertzer, D. and Lovejoy, S.: Physical modeling and analysis of rain and clouds by anisotropic scaling multiplicative processes, *J. Geophys. Res.*, 92, 9693–9714, doi:10.1029/JD092iD08p09693, 1987.
- Schertzer, D. and Lovejoy, S.: Multifractals, generalized scale invariance and complexity in geophysics, *Int. J. Bifurcat. Chaos*, 21, 3417–3456, doi:10.1142/S0218127411030647, 2011.
- Schleiss, M., Jaffrain, J., and Berne, A.: Stochastic simulation of intermittent DSD fields in time, *J. Hydrometeorol.*, 13, 621–637, doi:10.1175/JHM-D-11-018.1, 2012.
- Schmitt, F., Lovejoy, S., and Schertzer, D.: Multifractal analysis of the Greenland ice-core project climate data, *Geophys. Res. Lett.*, 22, 1689–1692, doi:10.1029/95GL015221, 1995.
- Schneebeli, M. and Berne, A.: An extended Kalman filter framework for polarimetric X-band weather radar data processing, *J. Atmos. Oceanic Technol.*, 29, 711–730, doi:10.1175/JTECH-D-10-05053.1, 2012.

## Bibliography

---

- Schneebeili, M., Sakuragi, J., Biscaro, T., Carvalho da Costa, I., Angelis, C. F., Morales, C., and Machado, L. A. T.: Polarimetric X-band weather radar measurements in the tropics: radome and rain attenuation correction, *Atmos. Meas. Tech.*, 5, 2183–2199, doi:10.5194/amt-5-2183-2012, 2013.
- Schneebeili, M., Grazioli, J., and Berne, A.: Improved estimation of the specific differential phase shift using a compilation of Kalman filter ensembles, *IEEE T. Geosci. Remote Sens.*, 52, 5137–5149, doi:10.1109/TGRS.2013.2287017, 2014.
- Schönhuber, M., Lammer, G., and Randeu, W. L.: The 2D-video-distrometer, in: *Precipitation: Advances in measurement, estimation and prediction*, pp. 3–31, Springer, 2008.
- Schrodin, R. and Heise, E.: The MultiLayer Version of the DWD Soil Model TERRA\_LM, Tech. Rep. 2, Consortium for Small Scale Modelling, Offenbach, Germany, URL <http://www.cosmo-model.org/content/model/documentation/techReports/docs/techReport02.pdf>, 2002.
- Schär, C., Leuenberger, D., Fuhrer, O., Lüthi, D., and Girard, C.: A New Terrain-Following Vertical Coordinate Formulation for Atmospheric Prediction Models, *Mon. Weather Rev.*, 130, 2459–2480, doi:10.1175/1520-0493(2002)130<2459:ANTFVC>2.0.CO;2, 2002.
- Seifert, A. and Beheng, K. D.: A two-moment cloud microphysics parameterization for mixed-phase clouds. Part 1: Model description, *Meteorol. Atmos. Phys.*, 92, 45–56, doi:10.1007/s00703-005-0112-4, 2006.
- Sheppard, B. E.: Measurement of raindrop size distributions using a small Doppler radar, *J. Atmos. Oceanic Technol.*, 7, 255–268, doi:10.1175/1520-0426(1990)007<0255:MORSDU>2.0.CO;2, 1990.
- Smolyak, S. A.: Quadrature and interpolation formulas for tensor products of certain class of functions, *Dokl. Akad. Nauk SSSR*, 148, 1042–1053, transl.: *Soviet Math. Dokl.* 4:240-243, 1963, 1963.
- Sommeria, G. and Deardorff, J. W.: Subgrid-Scale Condensation in Models of Nonprecipitating Clouds, *J. Atmos. Sci.*, 34, 344–355, doi:10.1175/1520-0469(1977)034<0344:SSCIMO>2.0.CO;2, 1977.
- Speirs, P., Gabella, M., and Berne, A.: A comparison between the GPM dual-frequency precipitation radar and ground-based radar precipitation rate estimates in the Swiss Alps and Plateau, *J. Hydrometeorol.*, 18, doi:10.1175/JHM-D-16-0085.1, 2017.
- Straka, J. M., Zrnic, D. S., and Ryzhkov, A. V.: Bulk hydrometeor classification and quantification using polarimetric radar data: synthesis of relations, *J. Appl. Meteorol.*, 39, 1341–1372, doi:10.1175/1520-0450(2000)039<1341:BHCAQU>2.0.CO;2, 2000.
- Szyrmer, W. and Zawadzki, I.: Modeling of the Melting Layer. Part I: Dynamics and Microphysics, *J. Atmos. Sci.*, 56, 3573–3592, doi:10.1175/1520-0469(1999)056<3573:MOTMLP>2.0.CO;2, 1999.



- Tessier, Y., Lovejoy, S., and Schertzer, D.: Universal multifractals: theory and observations for rain and clouds, *J. Appl. Meteorol.*, 32, 223–250, doi:10.1175/1520-0450(1993)032<0223:UMTAOF>2.0.CO;2, 1993.
- Testud, J., Le Bouar, E., Obligis, E., and Ali-Mehenni, M.: The rain profiling algorithm applied to polarimetric weather radar, *J. Atmos. Oceanic Technol.*, 17, 332–356, doi:10.1175/1520-0426(2000)017<0332:TRPAAT>2.0.CO;2, 2000.
- Thurai, M. and Bringi, V. N.: Drop axis ratios from a 2D video disdrometer, *J. Atmos. Oceanic Technol.*, 22, 966–978, doi:10.1175/JTECH1767.1, 2005.
- Thurai, M., Huang, G., Bringi, V., Randeu, W., and Schönhuber, M.: Drop shapes, model comparisons, and calculations of polarimetric radar parameters in rain, *J. Atmos. Oceanic Technol.*, 24, 1019–1032, 2007.
- Thurai, M., Bringi, V. N., and Petersen, W. A.: Rain microstructure retrievals using 2-D video disdrometer and C-band polarimetric radar, *Adv. Geosci.*, 20, 13–18, doi:10.5194/adgeo-20-13-2009, URL <https://www.adv-geosci.net/20/13/2009/>, 2009.
- Thurai, M., Gatlin, P., Bringi, V. N., Petersen, W., Kennedy, P., Notaroš, B., and Carey, L.: Toward Completing the Raindrop Size Spectrum: Case Studies Involving 2D-Video Disdrometer, Droplet Spectrometer, and Polarimetric Radar Measurements, *J. Appl. Meteor. Clim.*, 56, 877–896, doi:10.1175/JAMC-D-16-0304.1, 2017.
- Tiedtke, M.: A Comprehensive Mass Flux Scheme for Cumulus Parameterization in Large-Scale Models, *Mon. Weather Rev.*, 117, 1779–1800, doi:10.1175/1520-0493(1989)117<1779:ACMFSF>2.0.CO;2, 1989.
- Toyoshima, K., Masunaga, H., and Furuzawa, F. A.: Early Evaluation of Ku- and Ka-Band Sensitivities for the Global Precipitation Measurement (GPM) Dual-Frequency Precipitation Radar (DPR), vol. 11 of *Scientific Online Letters on the Atmosphere (SOLA)*, Meteorological Society of Japan, 2015.
- Trömel, S., Kumjian, M. R., Ryzhkov, A. V., Simmer, C., and Diederich, M.: Backscatter Differential Phase—Estimation and Variability, *J. Appl. Meteor. Clim.*, 52, 2529–2548, doi:10.1175/JAMC-D-13-0124.1, URL <https://doi.org/10.1175/JAMC-D-13-0124.1>, 2013.
- Turner, D. D., Kneifel, S., and Cadeddu, M. P.: An Improved Liquid Water Absorption Model at Microwave Frequencies for Supercooled Liquid Water Clouds, *J. Atmos. Oceanic Technol.*, 33, 33–44, doi:10.1175/JTECH-D-15-0074.1, URL <https://doi.org/10.1175/JTECH-D-15-0074.1>, 2016.
- Tyynelä, J. and Chandrasekar, V.: Characterizing falling snow using multifrequency dual-polarization measurements, *J. Geophys. Res.-Atmos.*, 119, 8268–8283, doi:10.1002/2013JD021369, URL <http://dx.doi.org/10.1002/2013JD021369>, 2014.

## Bibliography

---

- Tyynelä, J., Leinonen, J., Moisseev, D., and Nousiainen, T.: Radar Backscattering from Snowflakes: Comparison of Fractal, Aggregate, and Soft Spheroid Models, *J. Atmos. Oceanic Technol.*, 28, 1365–1372, doi:10.1175/JTECH-D-11-00004.1, 2011.
- Ulbrich, C. W.: Natural variations in the analytical form of the raindrop-size distribution, *J. Climate Appl. Meteorol.*, 22, 1764–1775, doi:10.1175/1520-0450(1983)022<1764:NVITAF>2.0.CO;2, 1983.
- Vasić, Z., Lin, C. A., Zawadzki, I., Bousquet, O., and Chaumont, D.: Evaluation of precipitation from numerical weather prediction models and satellites using values retrieved from radars, *Mon. Weather Rev.*, 135, 3750–3766, doi:10.1175/2007MWR1955.1, 2007.
- Vulpiani, G., Montopoli, M., Delli Passeri, L., Gioia, A. G., Giordano, P., and Marzano, F. S.: On the use of dual-polarized C-band radar for operational rainfall retrieval in mountainous areas, *J. Appl. Meteor. Clim.*, 51, 405–425, doi:10.1175/JAMC-D-10-05024.1, 2012.
- Wang, H., Sun, J., Zhang, X., Huang, X.-Y., and Auligné, T.: Radar Data Assimilation with WRF 4D-Var. Part I: System Development and Preliminary Testing, *Mon. Weather Rev.*, 141, 2224–2244, doi:10.1175/MWR-D-12-00168.1, 2013.
- Ward, J. H. J.: Hierarchical Grouping to Optimize an Objective Function, *J. Am. Stat. Assoc.*, 58, 236–244, doi:10.1080/01621459.1963.10500845, 1963.
- Wenshuo, G., Xiaoguang, Z., Lei, Y., and Huizhong, L.: An improved Sobel edge detection, *Computer Science and Information Technology (ICCSIT), 2010 3rd IEEE International Conference on*, 5, 67–71, doi:10.1109/ICCSIT.2010.5563693, 2010.
- Wernli, H., Paulat, M., Hagen, M., and Frei, C.: SAL - A novel quality measure for the verification of quantitative precipitation forecasts, *Mon. Weather Rev.*, 136, 4470–4487, doi:10.1175/2008MWR2415.1, 2008.
- White, A. B., Gottas, D. J., Strem, E., Ralph, F. M., and Neiman, P. J.: An Automated Bright-band Height Detection Algorithm for Use with Doppler Radar Spectral Moments, *J. Atmos. Oceanic Technol.*, 19, 687–697, doi:10.1175/1520-0426(2002)019<0687:AABHDA>2.0.CO;2, 2002.
- Wicker, L. J. and Skamarock, W. C.: Time-splitting methods for elastic models using forward time schemes, *Mon. Weather Rev.*, 130, 2088–2097, doi:10.1175/1520-0493(2002)130<2088:TSMFEM>2.0.CO;2, 2002.
- Wolfensberger, D., Scipion, D., and Berne, A.: Detection and characterization of the melting layer based on polarimetric radar scans, *Q. J. R. Meteorol. Soc.*, 142, 108–124, doi:10.1002/qj.2672, 2016.
- Xu, Y.-l.: Electromagnetic scattering by an aggregate of spheres, *Appl. Opt.*, 34, 4573–4588, doi:10.1364/AO.34.004573, 1995.

- Xue, M., Droegemeier, K. K., and Wong, V.: The Advanced Regional Prediction System (ARPS); A multi-scale nonhydrostatic atmospheric simulation and prediction model. Part I: model dynamics and verification, *Meteorol. Atmos. Phys.*, 75, 161–193, doi:10.1007/s007030070003, 2000.
- Zawadzki, I., Szyrmer, W., Bell, C., and Fabry, F.: Modeling of the melting layer. Part III: the density effect, *J. Atmos. Sci.*, 62, 3705–3723, doi:10.1175/JAS3563.1, 2005.
- Zeng, Y.: Efficient Radar Forward Operator for Operational Data Assimilation within the COSMO-model, Ph.D. thesis, Karlsruhe Institute of Technology, URL <https://www.ksp.kit.edu/download/1000036921>, 2013.
- Zeng, Y., Blahak, U., Neuper, M., and Jerger, D.: Radar Beam Tracing Methods Based on Atmospheric Refractive Index, *J. Atmos. Oceanic Technol.*, 31, 2650–2670, doi:10.1175/JTECH-D-13-00152.1, 2014.
- Zeng, Y., Blahak, U., and Jerger, D.: An efficient modular volume-scanning radar forward operator for NWP models: description and coupling to the COSMO model, *Q. J. R. Meteorol. Soc.*, pp. n/a–n/a, doi:10.1002/qj.2904, 2016.
- Zrnic, D. S. and Ryzhkov, A. V.: Polarimetry for weather surveillance radars, *Bull. Amer. Meteor. Soc.*, 80, 389–406, doi:10.1175/1520-0477(1999)080<0389:PFWSR>2.0.CO;2, 1999.



# Daniel WOLFENSBERGER

## PERSONAL DATA

---

PLACE AND DATE OF BIRTH: Wetzikon, Switzerland | 31 May 1988  
ADDRESS: Rue du Collège 11, 1400 Yverdon-les-Bains, Switzerland  
PHONE: +41 787178152  
EMAIL: [daniel.wolfensberger@epfl.ch](mailto:daniel.wolfensberger@epfl.ch)

## EDUCATION

---

- JULY 2013 Master of Science in ENVIRONMENTAL ENGINEERING, EPFL, Switzerland  
Final grade 5.63/6.0 | Minor: Computational Science and Engineering  
Thesis: "Automatic detection and characterization of intense rainfall cells embedded within the melting layer" | Advisor: Prof. Alexis BERNE
- JULY 2011 Bachelor in Science in ENVIRONMENTAL ENGINEERING  
Final grade 5.27/6.0, EPFL, Switzerland
- JULY 2006 Gymnase d'Yverdon, Yverdon-les-Bains | Final Grade: 5.5/6.0

## WORK EXPERIENCE

---

- |                     |  |
|---------------------|--|
| Current<br>JAN 2014 | <p>PhD Student at EPFL, Switzerland<br/><i>PhD in the Environmental Remote Sensing Laboratory (LTE)</i></p> <p>The goal of my PhD is to develop new ways of evaluating numerical weather simulations with radar data. My work focuses on three topics: (1) the detection and characterization of the melting layer of precipitation, (2) the design of a polarimetric forward radar operator able to simulate various types of radar observations based on model simulations, (3) the use of multifractals to characterize and compare precipitation and water contents fields.</p>  |
| FEB 2013-JUL 2017   | <p>Various Teaching Assistant tasks at EPFL,</p> <p>During my studies at EPFL I have accomplished numerous tasks as a Teaching assistant in the following courses: <i>Quantitative methods II, Signals, instruments and systems, Linear Algebra</i> (3 times), <i>Statial statistics and analysis</i> (3 times), <i>Environmental bioprocess engineering, Remote Sensing</i> (3 times). I have also been responsible of designing and supervising new computer exercises in QGIS and Matlab for Prof. Alexis Berne's <i>Remote Sensing</i> lectures. In 2014 I have also supervised a semester project by Oscar Urio involving the intercomparison of precipitation intensities from COSMO, GPM and the Swiss radar QPE.</p> |
| JUL-OCT 2012        | <p>Internship at ilu AG (Uster) and TK Consult (Zürich), Uster/Zürich, Switzerland<br/><i>Simulation of groundwater flows</i></p> <p>Finite element modelling of the groundwater flow under landfills in the canton Zug. Study of the impact of hypothetical riverdams on the groundwater level along the Rhone river between Chur and Lustenau.</p>   |

## SCIENTIFIC PUBLICATIONS

---

Wolfensberger, D., Scipion, D. and Berne, A. (2016), Detection and characterization of the melting layer based on polarimetric radar scans. Q.J.R. Meteorol. Soc., 142: 108–124. doi:10.1002/qj.2672

Wolfensberger, D., Gires, A., Tchiguirinskaia, I., Schertzer, D., and Berne, A.: Multifractal evaluation of simulated precipitation intensities from the COSMO NWP model, Atmos. Chem.

Phys. Discuss., <https://doi.org/10.5194/acp-2017-73>, in review, 2017.

Wolfensberger, D., and Berne, A.: A forward polarimetric radar operator for the COSMO NWP model, QJ.R. Meteorol. Soc., in review, 2017.

## AWARDS

---

- SEPT. 2016 Best Oral Presentation by a young scientist at the European Radar Conference in Antalya, Turkey
- SEPT. 2013 Winner of the Luce Grivat Price for my Master Thesis. The Luce Grivat price rewards the best EPFL Master project that provides an important, innovative and of high quality contribution to the field of Environmental Sciences and Engineering.

## LANGUAGES

---

- FRENCH: Common language  
GERMAN: Fluent (Mothertongue)  
ENGLISH: Fluent

## COMPUTER SKILLS

---

- Extended Knowledge: Python, Matlab, R, Linux,  $\LaTeX$ , QGIS  
Intermediate Knowledge: C++, C, Java, PostgreSQL, HTML/CSS

## OTHER ACTIVITIES

---

I like outdoor activities such as hiking, sailing, mountain-biking and ski-touring. I am also an aspiring member of the volunteer firefighters in Yverdon.

